Physik-Department
Technische Universität München

Development of neutron optical components for PERC

Alexander Hollering

Vollständiger Abdruck der von der Fakultät für Physik der Technischen Universität München zur Erlangung des akademischen Grades eines

Doktors der Naturwissenschaften (Dr. rer. nat.)

genehmigten Dissertation.

Vorsitzender: Prof. Dr. Lorenzo Tancredi

Prüfende der Dissertation:

1. Prof. Dr. Bastian Märkisch
2. Prof. Dr. Martin Fertl

Die Dissertation wurde am 10.01.2022 bei der Technischen Universität München eingereicht und durch die Fakultät für Physik am 25.04.2022 angenommen.

Abstract

The decay of the free neutron is a powerful tool to test the Standard Model of particle physics and search for potential deviations. By measuring the correlations between the particles involved in this decay, the weak interaction is characterized.
As part of the blinded analysis of the first direct and energy-dependent measurement of the proton asymmetry with PERKEO III, the beam polarization is analysed.
The next generation instrument PERC is equipped with an eight meter long neutron guide as active volume within a magnetic field of about 1.5 T. PERC aims to measure the correlation coefficients of the neutron decay with an accuracy of 10^{-4}. This requires neutron spin control on the same level. A non-depolarizing Cu/Ti neutron supermirror with m = 2 and excellent reflectivity of 92% at critical angle of reflection is presented. To perform measurements with polarized neutrons, it is planned to use a novel solid-state technique. The successful proof of principal measurements of Fe/Si supermirror coatings in normal and inverted layer sequence on glass, silicon and quartz substrate is provided. For further beam preparation, a high transmission solid-state neutron collimator with $^{10}B_4C$ coating could be used. Based on the reflectivity curves of our supermirrors, the beamline setup is discussed with Monte-Carlo simulations.

Zusammenfassung

Der Zerfall des freien Neutrons eignet sich bestens um das Standard Modell der Teilchenphysik zu prüfen und nach Abweichungen davon zu suchen. Durch die Messung der Korrelationskoeffizienten der am Zerfall beteiligten Teilchen, wird die schwache Wechselwirkung untersucht.
Als Teil der verblindeten Analyse der ersten direkten und energieabhängigen Messung der Proton Asymmetrie mit PERKEO III, wird die Strahlpolarisation ausgewertet.
Das Instrument der nächsten Generation namens PERC ist mit einem acht Meter langen Neutronenleiter in einem Magnetfeld von etwa 1.5 T ausgestattet. PERC hat das Ziel, die Korrelationskoeffizienten des Neutronenzerfalls mit einer Genauigkeit im Bereich von 10^{-4} zu messen. Dafür muss der Neutronenspin auf dem selben Niveau kontrollierbar sein. Es wird ein nicht-depolarisierender m = 2 Superspiegel aus Cu/Ti mit einer exzellenten Reflektivität von 92% am Grenzwinkel vorgestellt. Um Messungen mit polarisierten Neutronen durchführen zu können, wird die neue Festkörpertechnologie genutzt. Erfolgreiche Machbarkeitsstudien von Fe/Si Superspiegeln in normaler und umgekehrter Schichtfolge auf Glas, Silizium und Quarz Substraten werden diskutiert. Für weitere Strahlvorbereitungen kann ein hochtransmittierender Festkörper-Neutronenkollimator mit $^{10}B_4C$ Beschichtung genutzt werden. Basierend auf den gemessenen Reflektivitäten unserer Superspiegel, wird die Strahlführung für PERC anhand von Monte-Carlo Simulationen festgelegt.

Contents

Introduction

The weak interaction is one of the four fundamental forces in physics. It has a great impact on Earth, as it is this force, which lays the foundation of nuclear fusion in the Sun. In the proton-proton-cycle one proton is transformed into a neutron via β^+-decay, while emitting a positron and an electron neutrino. The neutron and another proton are forming deuterium, which is further reacting to helium in an exothermic way. As the proton-proton-reaction is a slow one, the Sun has been releasing energy for the last 4.5 billion years and makes life on earth possible.

In our direct environment, we experience the weak interaction in terms of radioactive β^+ and β^--decays. In a β^--decay, a neutron decays into a proton, an electron and an electron-antineutrino. β^--decays occur for neutron rich isotopes and β^+-decays occur for proton rich isotopes in contrast.

The range of the weak interaction is, compared to the other forces, with about $10^{-18}\,\mathrm{m}$ rather small. This is due to the heavy charged $\mathrm{W}^{\pm}$ ($\approx 80\,\mathrm{GeV/c^2}$) and uncharged Z^0 ($\approx 91\,\mathrm{GeV/c^2}$) mediator bosons. The P-violation (parity), which was first discovered by Wu [1–3] and the CP-violation (charge conjugation parity) are two main characteristics of weak interaction.

The decay of the free neutron is the simplest example of a semi-leptonic decay and gives the opportunity to perform measurements of the angular correlation coefficients with highest precision and to search for physics beyond the Standard Model.

Instruments like Perkeo II [4–6] and Perkeo III [7] are limited to an accuracy of 10^{-3} for angular correlation coefficient measurements. The analysis of neutron beam polarization for the proton asymmetry measurement performed with Perkeo III in 2014 is presented in this work. The successor called Proton Electron Radiation Channel (PERC) is a high precision instrument, which aims to measure correlation coefficients in neutron beta decay with a precision on the lower 10^{-4} level. It will be installed in the new neutron guide hall east at the research neutron source Heinz Maier-Leibnitz (FRM II) in Garching. PERC will be fed with cold neutrons with an expected flux density of $2\cdot 10^{10}\,\mathrm{n\,cm^{-2}\,s^{-1}}$ by a 40 m long neutron guide. One of the main parts of the instrument is its 12 m long superconducting magnet system with an on-axis magnetic field varying between 1 T and typically 6 T. A non-depolarizing supermirror neutron guide made from hundreds of layers of paramagnetic titanium (Ti) and diamagnetic copper (Cu) will be installed inside the instrument. Using these materials ensures constant neutron polarization of the incoming neutron beam throughout the whole instrument and is therefore minimizing systematic uncertainties.

This thesis focuses on the development of non-depolarizing neutron guide coatings based on the work of N. Rebrova [8]. We present a m = 2 supermirror consisting of 190 layers and excellent reflectivity of ≈ 92% at the critical angle of reflection.
The supermirror can be baked out at 100 °C, which is beneficial for vacuum conditions inside the instrument.
Furthermore, a well-known and high degree of polarization of the incoming neutron beam is necessary to perform precision measurements in neutron beta decay. By choosing an appropriate substrate material, it is feasible to use a novel solid-state neutron polarizer, offering the features of small size combined with high neutron polarization even in low angle of incidence region. In this work, different substrate materials and layer sequences of Fe/Si supermirrors are presented.
The design and characterization of a compact high transmission neutron collimator based on an $^{10}B_4C$ absorber deposited on single crystal silicon wafers completes the experimental research of neutron optics for PERC.
Finally, the beamline setup for PERC is discussed. Neutron Monte-Carlo simulations were performed using our experimental results as input parameters.

1 Slow Neutron Interactions

Slow neutrons have wavelengths of more than 2 Å ($v < 2000\,\mathrm{m/s}$) with $\lambda = 2\pi/|\vec{k}| \approx \frac{\hbar}{m_n p} \approx \frac{3956}{v}\,[\mathrm{m\,Å\,s^{-1}}]$, where $\vec{k}$ is the wave vector of neutrons with energy $E = \hbar\omega$. These wavelengths are comparable to the inter atomic scales inside matter. Interaction of slow neutrons with matter, which is described in the following in more detail, is often summarized under the term neutron optics. The neutron β-decay is also a great platform for precision searches for physics beyond the standard model and is therefore of great interest for physicists around the world. Here we focus on the relevance of this thesis to the field of neutron particle physics. The different types of interactions of neutrons based on standard literature [9–12] are described.

1.1 Weak Interaction Neutron Beta Decay

The neutron itself consists of two down and one up-type quarks. It has spin 1/2 and is electrically neutral [13, 14]. The free neutron β-decay is described completely by only three free parameters within the standard model. They have to be determined experimentally. The Fermi coupling constant G_F is known with very high precision from muon decay [15]. The axial- and vector-coupling constants of the ratio $\lambda = g_A/g_V$ are most precisely determined by the parity-violating beta asymmetry. Together with a measurement of the neutron lifetime the element V_{ud} of the Cabibbo-Kobayashi-Matrix can be determined. For a recent review on precision experiments of the free neutron decay see Ref. [16]. Currently, the average neutron lifetime is $879.4 \pm 0.6\,\mathrm{s}$ [17]. Figure 1 shows the neutron decay as a Feynman-diagram and it can be written as

$$n \rightarrow p + e^- + \overline{\nu}_e + 782\,\mathrm{keV}. \tag{1.1}$$

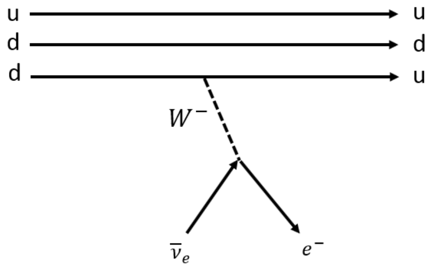

Figure 1: The decay of the free neutron via the weak interaction.

Because of the high mass of the W^--boson, the weak interaction is a short-range force. In the standard model of particle physics, this decay is described by semi-leptonic vector g_V and g_A axial vector currents.

V_{ud}, the first element of the quark mixing matrix (CKM-matrix) is given by

$$|V_{ud}|^2 = \frac{(5024.7)\,\mathrm{s}}{\tau_n(1+3\lambda^2)\,(1\,+\,\Delta_R^V)}\ , \tag{1.2}$$

where $\lambda = g_A/g_V$ is the ratio of the coupling constants, τ_n the lifetime of free neutron and Δ_R^V the inner or universal electroweak radiative corrections (RC). Using the current world averages for τ_n and λ it leads to $V_{ud} = 0.9733(3)_{\tau_n}(3)_\lambda(1)_{RC}$ [17]. Within the scope of effective field theories [18, 19], also deviations from the V - A theory of the standard model are tested by neutron beta decay measurements. Examples are right handed currents or hypothetical scalar and tensor couplings. The differential decay width of the neutron $d\Gamma_n$ is given in terms of momentum, energy and spin by [20]:

$$\begin{aligned} &d\Gamma_n(E_e,\Omega_e,\Omega_\nu,\langle\sigma_n\rangle)dE_e d\Omega_e d\Omega_\nu = \\ &\frac{1}{32\pi^5}\,\rho(E_e)\,\xi\left[1+a\frac{\vec{p}_e\vec{p}_\nu}{E_eE_\nu}+b\frac{m_e}{E_e}+\langle\vec{\sigma}_n\rangle\left(A\frac{\vec{p}_e}{E_e}+B\frac{\vec{p}_\nu}{E_\nu}+D\frac{\vec{p}_e\times\vec{p}_\nu}{E_eE_\nu}\right)\right]\ . \end{aligned} \tag{1.3}$$

Here E_e, E_ν, p_e and p_ν are the electron (neutrino) total energies and momenta. m_e is the electron mass, σ_n the neutron spin, $\rho(E_e)$ is the phase space density and the Ω_i denote solid angles. The coefficient ξ describes the influence of the coupling constants on the decay rate. Within the standard model ξ is denoted by $(1\,+\,3\lambda^2)$. The neutron spin dependent coefficients A (beta asymmetry), B (neutrino asymmetry) and D (triple correlation) describe the correlations between different particle momenta and are P (Parity) or T (Time reversal) violating. The electron neutrino angular correlation a and the Fierz interference term b are observed for unpolarized neutrons. A non-zero Fierz interference term would imply novel scalar or tensor interactions. The proton asymmetry $C = -x_C(A\,+\,B)$ stands for the preferred recoil direction of the proton with respect to the neutron spin. It is a linear combination of A and B combined with a kinematical factor $x_C = 0.27484$ [21, 22]. Table 1 shows the current measured values of the different correlation coefficients from neutron beta decay. In the past, mainly cold neutrons were used for measurements.

The first measurements of these correlation coefficients have been performed in the 1960s. Despite the problem of low statistics, also ultracold neutrons (UCN) with energies in the range of neV are used and can give competitive results. Several instruments for measuring these parameters with cold and ultracold neutrons are already existing or under construction. Examples are Nab (SNS) [26, 27], aCorn (NIST) [28–30], PERKEO III (ILL) [7, 25, 31, 32], aSPECT (ILL) [33, 34], UCNA/B (LANSCE) [35–37] and PERC (FRM II) [8, 38–40]. In the following, the instruments PERKEO III and PERC are highlighted and the importance of this work, especially

Table 1: Average of experimental determinations of correlation coefficients and the neutron lifetime and their dependence on λ within the Standard Model [23, 24]. Data taken from Particle Data Group book [17].

Corr. coeff.	Expression	Exp. value	Description
a	$\frac{1-\lvert\lambda\rvert^2}{1+3\lvert\lambda\rvert^2}$	-0.1059 ± 0.0028	Angular correlation $e - \overline{\nu}_e$
b	0	0.017 ± 0.027 [25]	Fierz interference
A	$-2\frac{\lvert\lambda\rvert^2+Re(\lambda)}{1+3\lvert\lambda\rvert^2}$	-0.11958 ± 0.00028	n-spin e-momentum corr. coeff.
B	$2\frac{\lvert\lambda\rvert^2-Re(\lambda)}{1+3\lvert\lambda\rvert^2}$	0.9807 ± 0.0030	n-spin $\overline{\nu}_e$-momentum corr. coeff.
C	$-x_C(A+B)$	-0.2377 ± 0.0026	n-spin and p-momentum corr. coeff.
D	$2\frac{Im(\lambda)}{1+3\lvert\lambda\rvert^2}$	$(-1.2 \pm 0.20) \cdot 10^{-4}$	T-odd triple product
τ	$\propto \frac{1}{1+3\lvert\lambda\rvert^2}$	$879.4 \pm 0.6\,\mathrm{s}$	neutron lifetime

for the PERC project, is explained.

Perkeo III

The Perkeo III instrument [7, 31] is the successor of former instruments called Perkeo [41] and Perkeo II [4, 42–44]. Figure 2 shows the scheme of the final Perkeo III instrument and its' beamline, as it was used in 2009 and 2014 for neutron decay measurements at the Institut Laue-Langevin (ILL) in Grenoble, France.

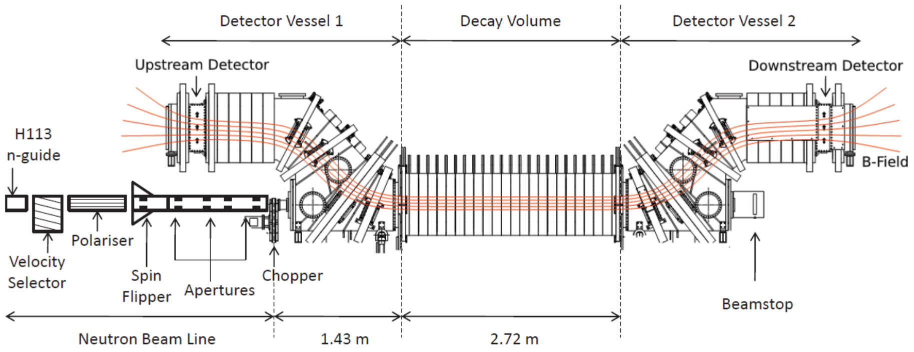

Figure 2: Scheme of the Perkeo III instrumental setup. Magnetic field lines are indicated in red. They guide the decay products, namely electrons and protons, to the detectors. Upstream of the instrument, the neutron beam preparation is shown. The beamline ends with a n-beamstop. Figure from [45].

The instrument is supplied with neutrons by the H113 guide with cold neutrons from the reactor, which is 74 m away from the instrument. The neutrons have a broad wavelength spectrum ($\approx 2 - 17$Å). Since Perkeo III uses a pulsed beam, this would lead to rapid dispersion and smearing out of the pulses. A turbine with neutron absorbing blades, called velocity selector, limits the wavelength spectrum to a range of $4.4 < \lambda < 5.6$ Å [45].

After selecting this neutron wavelength band, the neutron beam is polarized by a multichannel bender. Here the spin up neutrons perform at least two reflections on the 80 cm long polarizer channels, which are coated with a polarizing supermirror. Spin down neutrons are reflected by the coating only with very low probability and are therefore mainly absorbed. This leads to a highly polarized neutron beam at the exit of the polarizer bender. The channels of the polarizer have a width of 2 mm. The used polarizer at beam port PF1B was designed to achieve a neutron polarization of $> 98\,\%$ [46].

To be able to measure spin-asymmetries in neutron beta decay, it is mandatory to be able to flip the neutrons spin in front of the instrument. This is achieved by a so called adiabatic fast passage spin flipper (AFP) [47]. A magnetic holding field along the beamline preserves the spin direction of the transversally polarized neutrons on their way to the instrument. This holding field changes from transversal to longitudinal and matches the direction of the magnetic field inside the instrument.

A rotating disc chopper in front of the instrument converts the continuous neutron beam into a pulsed one. This makes a time resolved measurements with neutrons via time-of-flight measurements possible. The chopper itself is made of a disc with neutron absorbing ^{6}LiF plates. The disc is cut at one position with an opening window of 22.11°.

The end of its beamline is defined by the neutron beamstop. The requirements for the beamstop are not trivial. Neutrons should be absorbed and γ-radiation from the beam or conversion processes should also be suppressed. Based on previous work of Mest, the beamstop was changed from ^{6}LiF-absorber tiles to $^{10}B_4C$-tiles [48]. The reason for this can be found in neutron absorption process. Even though the ^{6}LiF produces almost no γ-radiation, it emits a high amount of delayed secondary neutrons, which are disturbing the signal within the background window of measurements. This unfavorable signal of secondary neutrons is strongly suppressed by using $^{10}B_4C$-tiles. The prompt γ signal from $^{10}B_4C$ can be seen in the electron detectors, but can be well distinguished from electron signals of the measurement and the background signal is no longer disturbed.

The charged decay particles are guided via a magnetic field from the decay volume to the two detectors. Fast energy-sensitive plastic scintillators with low sensitivity to γ-background are used. The photons coming from the scintillators are read out by photomultiplier tubes. For the measurement of the proton asymmetry C, the same detectors are used. Therefore, the protons are accelerated by a high negative voltage onto a thin carbon foil, where they emit one ore more secondary electrons, which are then accelerated onto the plastic scintillator on ground. For more details on the setup, see [49, 50]. To observe the proton asymmetry C a measurement with spin-polarized neutrons is necessary. So far, the only value for $C = 0.2377 \pm 26$ was obtained with Perkeo II [43]. In chapter 9, the neutron beam polarization analysis for the most recent measurement of C with Perkeo III in 2014 is presented.

The Proton Electron Radiation Channel PERC

PERC is our next generation instrument for studying the neutron beta decay and aims to measure a number of correlation parameters with a fractional accuracy at the 10^{-4}-level. It allows access to the parameters A, b, C, a and potentially R. This instrument follows the era of the Perkeo instruments, which were limited mainly by statistics and uncertainty of polarization to 10^{-3}-level accuracy [31, 32, 41–44, 51, 52]. The installation started in 2021 at the MEPHISTO beamsite of the Research Neutron Source Heinz Maier-Leibnitz (FRM II) [53]. The instrument will be fed by a high intensity neutron flux with an expected decay rate of $\approx 10^6$ decays per second and meter within the eight meter long decay volume [38]. Neutrons will be guided through a primary neutron guide with a curvature radius of 3 km and a diameter of $60 \,\mathrm{x}\, 106\,\mathrm{mm}^2$ from the reactor core into the new guide hall east, where the PERC instrument will be installed. A velocity selector is installed between the reactor building and hall east. Inside hall east, there will be neutron optical components like a neutron polarizer, a spinflipper and neutron guides with non-magnetic coatings in front of the actual instrument to shape and modify the wavelength and polarization of the neutron beam. Inside the instrument a neutron guide with a non-depolarizing coating of Cu and Ti will be installed.

Different guide geometries are possible and will be discussed within this thesis. Figure 3 shows a scheme of the PERC instrument. Its main component is a 12 meter long superconducting magnet, with an eight meter long decay volume inside. The incoming diverging neutron beam is guided through the decay volume by a non-depolarizing neutron guide with high reflectivity of above 90 %. This strongly increases the number of neutrons guided through the decay volume compared to former experiments.

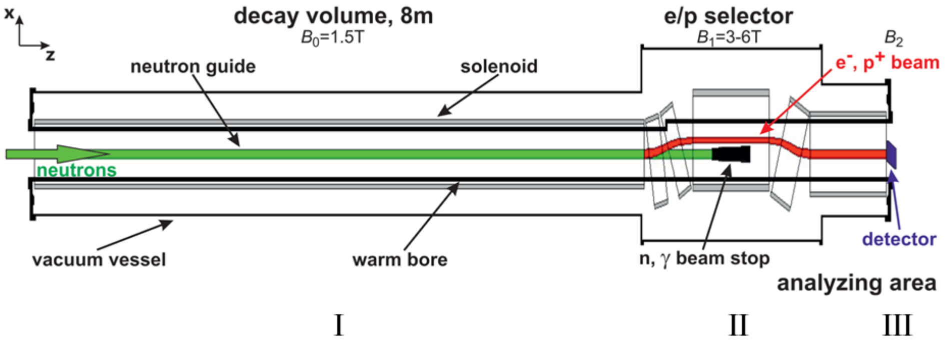

Figure 3: Scheme of the instrument PERC adapted from [39]. An eight meter long active volume (I) is followed by a filter section (II), where the charged decay products are separated from the neutron beam and a detector area (III) [54]. More details can be found in Dubbers et al. [38].

Consequently, also the number of expected decay events increases. The high reflectivity of the coating additionally suppresses the γ-background coming from potential (n,γ)-reactions inside the substrate of the neutron guide.

Inside the eight meter long decay volume area, a magnetic field of 1.5 T (B_0) is applied to collect all decay products and a slight gradient of about 10^{-2} prevents the charged particles to be trapped within the volume. In the analyzing area a magnetic filter is installed where the magnetic field can be varied from $3 - 6$ T (B_1) and the charged particles are guided around the beamstop. Variation of the magnetic field allows to vary the maximum angle of incoming particles and B_0-field. B_2 then guides the charged particles to the detector area (secondary spectrometers).

Here different detector systems can be set up, depending on the observables of interest. One possible detection system, are plastic scintillators. With such scintillators the electron energy spectrum can be measured and a proton detection with an additional conversion system is possible, similar to the system used with Perkeo II [42, 43] and Perkeo III [49, 50, 55]. Combined with the increased statistics and the special design of PERC, which allows to limit important systematics related to neutron beam polarization, magnetic field and background to the level of 10^{-4} [39], it is possible to improve the precision for correlation coefficients like A on the same level.

The required amount of data to reach a statistical accuracy on the 10^{-4} level will be achieved by two days of measurement in continuous mode or 50 days in chopped mode respectively. This estimation already includes a polarization system with only 10 % neutron transmission [38].

For the direct measurement of the Fierz interference term b, a secondary spectrometer called $NoMoS$ was investigated at the SMI, Vienna. Via the drift of charged particles inside a magnetic field and a position sensitive detector system, it is possible to measure the momentum of the particles [56]. The aim is to measure b with a precision of 10^{-3} or less [57].

For the measurement of the beta asymmetry, which will likely be the first measurement performed with PERC, several improvements in detector setup and monitoring compared to former measurements with PERKEO III can be made. These improvements concern the detector linearity and calibration, the temperature drift of the detector and the spatial response of the detector. They are addressed in detail in [55].

Within this thesis neutron polarizer supermirror coatings for PERC were improved and a novel solid-state polarizer based on the work of A. Pethukov et al. designed and tested [58, 59]. This polarizer consists of a stack of single crystal quartz wafers, where neutrons are transmitted through the material and polarized as only one spin component is reflected from the walls. The main advantage of this device is, that it is much more compact than common benders (5 cm vs. ≈ 50 cm and more) and due to the configuration of neutron optical potentials, there is almost no reflection for the wrong spin component.

For the whole measurement it is of great importance, that not only the initial polarization should be as high as possible, but also the depolarization within the whole beamline section behind the polarizer should be negligibly small. As common Ni/Ti guides have magnetic properties, they would also affect the neutron spin during wall collision leading to depolarization. Therefore, it is essential to have a completely non-magnetic supermirror coating. Based on the work of N. Rebrova, an improved neutron guide coating made of Cu/Ti with m = 2, two times the critical angle of reflection of natural nickel is shown in this thesis [8]. It has an excellent reflectivity of about 90 % at critical angle of reflection. Despite the high mobility of copper and interdiffusion, it is possible to heat these mirrors up to about 100°C without any degradation in reflectivity. This special feature will be used to improve vacuum conditions inside the PERC instrument. This neutron guide solves the problems of diverging neutron beams inside the decay volume It enables the usage of longer neutron pulses and increases the number of neutrons in the decay volume and consequently also the average decay rate.

1.2 Strong Interaction

Interaction with bulk material and single layers

Neutrons that hit a smooth surface under a very small angle of incidence, are totally reflected for most materials as the wave vector k of the neutron is changing inside the material. This is comparable to light optics, where the refractive index depends on the ratio of speed of light in vacuum and the speed of light in a material. Transferred to neutrons, it can be shown, that the coherent scattering on a material can be described by a so called Fermi potential, which is an effective optical potential of the materials surface [10, 12]

$$V_f = \frac{2\pi\hbar^2}{m_n} N b_c \ . \tag{1.4}$$

Here b_c is the coherent scattering length, N the number density of the nuclei, m_n the neutron mass and $\hbar$ the Planck constant. The refractive index can be written analogously to light optics

$$n = \frac{k_{\text{vac}}}{k_{\text{mat}}} \ . \tag{1.5}$$

With the wave vectors of the neutron in vacuum k_{vac} and in material k_{mat}. The energy of the neutron is given by

$$E = \frac{(\hbar k_{\text{mat}})^2}{2\,m_n} + V_f = \frac{(\hbar k_{\text{vac}})^2}{2\,m_n} \ . \tag{1.6}$$

By inserting this relation in equation 1.5, the refractive index for neutron can be written as

$$n = \sqrt{1 - \frac{V_f}{E}} = \sqrt{1 - \frac{2\pi\hbar^2 N b_c}{m_n} \frac{2m_n}{(\hbar k_{\text{mat}})^2}} = \sqrt{1 - \frac{\lambda^2}{\pi} N b_c} \ , \tag{1.7}$$

where $\lambda = 2\pi/|\vec{k}|$ is the neutron's wavelength in vacuum. Most materials have an at least slight positive neutron optical potential ($n \leq 1$). As shown in figure 4, it is now possible to define the conditions for total reflection of neutrons at the interface of vacuum and material.

It is obvious, that for total reflection Θ_m has to be 0 and therefore $\cos(\Theta_m) \equiv 1$. Using Snell's law $n_m \cos(\Theta_m) = n_0 \cos(\Theta_0)$ and equation 1.7, we obtain the critical (maximum) angle of total reflection:

$$\Theta_0 \ < \ \Theta_c = \lambda \sqrt{\frac{b_c N}{\pi}} \ . \tag{1.8}$$

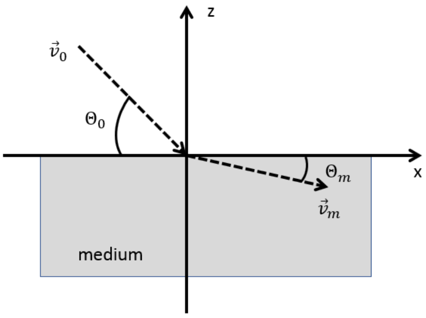

Figure 4: Refraction of neutrons at the interface of vacuum and medium ($n < 1$).

Table 2 shows potentials of most commonly used materials in neutron optics and the ones, that are important for this work.

Table 2: Neutron scattering lengths and equivalent optical Fermi potential [10, 60].

Element	b [fm]	V [neV]	Θ_c/λ [mrad/Å]
^{58}Ni	14.4	335	2.0
nat. Ni	10.3	252	1.7
Fe	9.36	207	1.59
Cu	7.6	168	1.4
Si	4.15	54	0.8
Ti	−3.34	−48	≈ 0

The critical angle of total reflection strongly depends on the material and the wavelength of the neutron. For cold neutrons only small angles of the order of several mrad can be achieved by a single layer of material.

The above considerations are based on purely coherent neutron scattering on the material, but in reality also absorption plays an important role. This can be described by an additional imaginary part in the refractive index [61]:

$$n^2 = 1 - \frac{4\pi N b_c}{k_0^2} + iN\frac{\sigma_a + \sigma_{inc}}{k_0} \ . \tag{1.9}$$

We substitute the scattering length density Nb_c with the expression ρ for following descriptions of magnetic interactions.

Interaction with multilayers (Neutron Supermirror)

Already in 1974, a monochromator of two different metals, namely manganese (Mn) and germanium (Ge) was introduced [62]. Quantum-mechanically, a neutron beam hitting the multilayer under a certain angle is reflected partially at each interface of Mn to Ge. This leads to an overlap of the arising partial waves and - equivalent to

Bragg's law for X-ray diffraction on a crystal lattice - neutrons interfere constructively if the path difference from layer to layer is a multiple of the neutron wavelength. This effect is visualized by the red graph in figure 5.

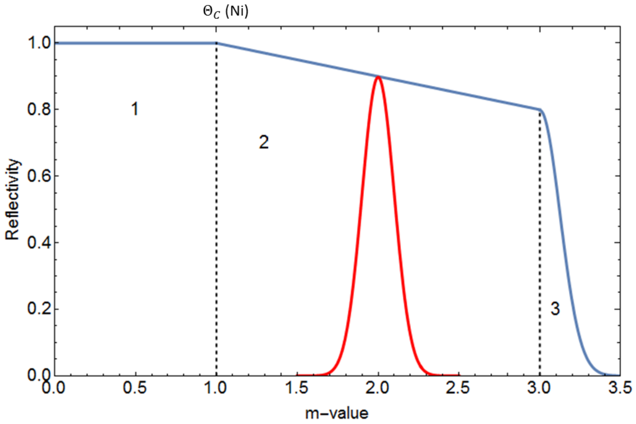

Figure 5: Scheme of reflectivity curve for neutron supermirror with m > 1, divided in 3 parts. Section (1) shows the region of total reflection. Section (2) shows a linear decrease in reflectivity and is defined by neutron interference with the stack. Section (3) defines the critical angle of reflection for neutrons. The red graph shows reflection of a double-layer system with equal thickness (monochromator).

By varying the thickness of the double-layers continuously, neutrons interfere with the stack and the critical angle of reflection can be broadened (Fig. 5 sections (1) – (3)). In other words, by this technique the peak of a monochromator can be technically turned into a continuous mirror with high reflectivity for neutrons under all angles of incidence up to a certain critical angle of reflection. Such mirrors consisting of many double-layers of two different materials are called neutron supermirrors.

The critical angle of reflection $\Theta_c/\lambda = 1.7\,\mathrm{mrad/Å}$ on natural Ni ($N = 9.13110^{28}\,\mathrm{m}^{-3}$, $b = 10.3\,\mathrm{fm}$) is defined as reference m $= 1$. The linear slope from total reflection up to the critical angle of reflection is caused by roughness and absorption inside the mirror. If there is some significant roughness growth inside the layer structure, this linear slope turns into a typical parabolic form. An example for this roughness effect is shown in chapter 5 for Cu/Ti supermirrors. At angles above the critical angle (part(3)) the reflectivity drops to zero and all neutrons hitting the mirror are transmitted through the coating and are absorbed or transmitted by the substrate.

For an existing layer structure, the theoretical reflectivity of a supermirror can be calculated by an algorithm introduced by Schelten and Mika [63]. The algorithm by Mezei and Dagleish is used to determine the optimal layer sequence for production of a supermirror [64]. A typical combination for supermirrors is Ni ($b = 10.3\,\mathrm{fm}$) and Ti

($b = -3.3\,\mathrm{fm}$). To ensure conservation of neutron polarization, it is important that the supermirror coating is non-magnetic. A supermirror of diamagnetic Cu ($b = 7.7\,\mathrm{fm}$) and paramagnetic Ti ($b = -3.3\,\mathrm{fm}$) was developed with m $=$ 2 and reflectivity of $> 90\,\%$.

When using a combination of a ferromagnetic material and a non-ferromagnetic for a supermirror, the magnetic scattering of the ferromagnetic material has to be taken into account. With these properties it is possible to built neutron polarizer supermirrors as proposed by Mezei [63] and described further in the following.

1.3 Magnetic Interaction

As a fermion, the neutron has spin 1/2, which was predicted in 1936 [65] and experimentally proven in 1949 [66]. Thus, it interacts with externally applied magnetic fields by the interaction

$$V = -\mu_n B(r) \approx 60\,\mathrm{neV/T}, \tag{1.10}$$

where μ_n is the neutron magnetic moment and the sign is defined by the relative direction of the spin and the magnetic field [10].

Considering reflection of neutrons on a material, this leads to an additional spin-dependent term in the material's effective potential in equation 1.4 [12]

$$V = V_f \pm \mu_n B\ . \tag{1.11}$$

In this context, the scattering length density (Nb_c) is used instead of the Fermi potential V_f and it is expanded by the magnetic scattering length ρ_m

$$\rho_m = \frac{m_n}{2\pi\hbar^2}\left|\mu_n B\right|, \tag{1.12}$$

to

$$\rho^{\pm} = \rho \pm \rho_m\ . \tag{1.13}$$

Here $\rho + \rho_m$ has to be used for the neutron spin parallel to the magnetic field and $\rho - \rho_m$ for neutron spin anti-parallel. As consequence, the critical angle of reflection for magnetic materials depends on the spin of the incoming neutron. Taking equation 1.8, the critical angle of total reflection, can now be written as

$$\Theta_c = \lambda\sqrt{\frac{\rho^{\pm}}{\pi}}. \tag{1.14}$$

The commonly used materials scattering lengths $\rho^{\pm}$ are shown in table 3.

Table 3: Neutron magnetic scattering length densities [10^{-6} Å^{-2}] for commonly used materials in neutron polarizers. Standard bulk densities were used to convert the scattering lengths from [60] into ρ. $\rho^{\pm}$ can be calculated with the absolute magnetic saturation, a field strength which differs for different materials. For iron it is $\approx 2.2\mu_B$, for cobalt $\approx 1.8\mu_B$ and for Ni $\approx 0.62\mu_B$ [67, 68].

	Fe	Si	Co	Ti	Ni	SiO_2	Al_2O_3	Gd
ρ	8.02	2.08	2.27	−1.93	9.4	4.19	5.72	$2.24 - i0.325$
ρ^+	13.12		6.43		10.85			
ρ^-	2.93		−1.90		7.98			

That the critical angle of reflection depends on the neutron spin, opens up a relatively simple way to obtain a polarized neutron beam by reflecting them on magnetic saturated materials preferably made of a supermirror structure. In this case neutrons with one spin component are reflected by the mirror, whereas the other is transmitted and absorbed afterwards.

The first supermirror polarizer was proposed by Mezei and Dagleish in 1977 [64]. Following their work, many devices have been planned and constructed in the past in order to get polarized neutron beams [64, 69–73]. One of the most common and effective designs of a polarizer for cold neutrons is the bender design, shown in figure 6.

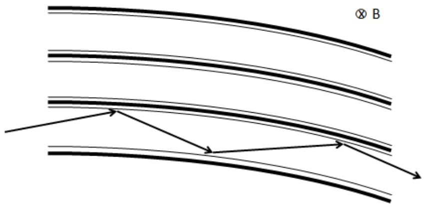

Figure 6: Scheme of a cold neutron polarizer. Typical values are a length of about 1 m, 50 channels with double sided supermirror coating with $m = 3$ on borated float glass and a curvature radius of $20 - 50$ m.

This device consists of many plates of thin glass as substrate and air gaps of same thickness in between. These glass plates are coated on top and bottom with polarizing supermirrors in order to reflect one spin component of neutrons. The radius of the channels ensure that each neutron passing this device has to perform at least one reflection on the mirror. Consequently, neutrons with the “right” spin direction are reflected on the coating and can be transmitted to the exit of the polarizer. Neutrons with the “wrong” spin direction are not reflected by the supermirror and pass through till they either hit the substrate or are absorbed by an appropriate absorption layer.

Typically a layer of Gd with a thickness of few hundred nanometers is used as absorber due to its' high neutron capture cross-section.

Besides the high degree of polarization, this design also has some disadvantages. As the substrate, typically borofloat glass, is not transparent for neutrons, all neutrons hitting the front face at the entrance are absorbed independent of spin orientation. As the surface ratio of air gap and substrate is typically 1 : 1 at the front face, 50 % of the neutron flux is absorbed already ab initio. Also it has to be considered, that glass has a finite lifetime when it is exposed to neutron radiation. With increasing number of neutrons hitting the substrate, the glass gets porous due to neutron capture reactions in boron and emission of high energy γ-radiation (2.8 MeV). The glass gets brittle and can break after a certain time [74]. If this happens, the whole polarizer needs to be exchanged, maybe even more components, if they have been contaminated by the broken glass or dust.

Also important is the choice of the materials, that are used for the supermirror coating. In the past, generally a combination of Co/Ti was used for some reasons: As the contrast in neutron optical potentials or scattering length density respectively is quite large for this material combination, a high neutron reflectivity can be achieved. For the spin up component, this difference is about $\rho^+(Co) - \rho^+(Ti) = 8.36 \cdot 10^{-6}\text{Å}^{-2}$. The potentials for the spin down component, have only a small difference of $\rho^-(Co) - \rho^-(Ti) = -1.00 \cdot 10^{-6}\text{Å}^{-2}$, which is still preferable, as reflection of neutrons with spin down is suppressed on a negative potential step (values from table 3). The only point, where neutrons with the wrong spin component are reflected in this configuration is at the interface of the first layer of supermirror and substrate, as glass has a positive scattering length density and therefore also a positive potential step with reflection of neutrons with the wrong spin in low angle region. This effect can be suppressed by the mentioned Gd absorption layer.

Still, alternatives need to be found, as the Co layers capture neutrons, producing ^{60}Co. Due to the high build-up of ^{60}Co and its long half-life of $T_{1/2} \approx 5.27$ years requires special shielding around the polarizer, resulting in difficult working conditions for changes on the device as well as very high disposal costs.

I present the proof of principle tests concerning a new type of polarizer. Based on the work of A. Petukhov et al. possible substrates and first supermirror coatings were tested for a solid state polarizer design [58]. In this type of polarizer, neutrons are transmitted through the substrate and hit the supermirror coating afterwards. It has a more compact structure, no total reflection of neutrons with wrong spin component and higher total neutron transmission.

2 Surface Coating

This chapter gives an overview of coating processes in general and commonly used ones in neutron optics. The characteristics of each technique are presented and the process of magnetron sputtering is described in more detail as it was used to produce the mirrors shown in this thesis.

2.1 Surface Coating Processes

The two main processes for surface coating are in general divided into chemical vapor deposition (CVD) and physical vapor deposition (PVD). Chemical vapor deposition uses the deposition of atoms or molecules of a certain material either by high temperature reduction or decomposition of a chemical vapor precursor species [75]. For further reading on CVD some standard literature is suggested [75–81].

Physical vapor deposition (PVD) is defined as an atomistic process, in which a material is vaporized from solid or liquid form. This can be achieved by bombarding the target material with high energetic ions. The ions, which normally are noble gas ions, like argon, are created by an electric field between the target and a shield. This electric field also causes the ions to be accelerated onto the target surface, where they deposit their energy by a number of elastic and inelastic collisions. With a certain probability, the target atoms gain enough energy in the collisions to overcome the binding energy and be ejected from the target. The vaporized atoms are then transported in low gas pressure of about 10^{-2}-10^{-3} mbar as a gas to the substrate, where they condense and form a thin film [75, 77].

Typical thicknesses of single layers vary from few nanometers up to several hundreds of nanometers. The multilayer constructs produced within this work are mainly based on copper (Cu), titanium (Ti), nickel (Ni), iron (Fe) and silicon (Si) and have total thicknesses of up to 3 µm. Just like for CVD, also PVD can be separated into several categories, which are called vacuum deposition, arc vapor deposition, ion plating and sputter deposition.

Vacuum Deposition or Vacuum Evaporation

In figure 7, the setup for vacuum evaporation is shown. The main feature of this technique is, that material from a vaporization source reaches the substrate with only very few collisions with gas molecules. This means that the particle trajectories can be considered to be straight lines. For a starting pressure in the high vacuum range $10^{-5} - 10^{-9}$ mbar, contaminations in the deposited layers can be kept at a very low level. In general thermal vaporization is done by heating the source material with tungsten wire coils or with a high energetic electron beam above their vaporization point. Typical applications are for example optical interference and mirror coatings or decorative coatings [75]. Typical film thicknesses are in the range of hundreds of nanometers. As film thicknesses of only few nanometers are difficult to control with this technique, it is not suitable for production of neutron supermirrors. Another disadvantage is, that the density of the deposited layers is well below that of the bulk material because the kinetic energy of evaporated atoms is too low to form dense films.

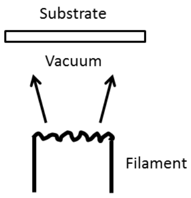

Figure 7: Principle of a vacuum evaporation setup. The filament, typically a tungsten wire, is equipped with the coating material and is then heated above its vaporization point by a high electric current.

Arc Vapor Deposition

Figure 8 shows the principle of arc vapor deposition. The applied voltage between cathode and anode needs to be near the ionization potential of the gas, typically about 25 V. As a consequence of the low voltage but high current passing through the vapor or gas, the ions bombard the cathode and the electrons bombard the anodes, hereby heating the electrodes. The ejected material consists of thermally evaporated atoms, which are mostly ionized afterwards due to the high electron density in the gas.

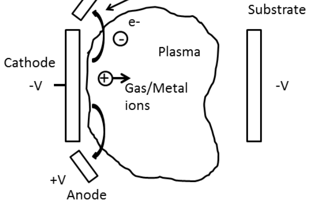

Figure 8: Principle of cathodic arc deposition. A low voltage but high current arc is causing thermal evaporation of the cathode material. By applying an additional bias voltage to the substrate, the ionized atoms and droplets from the cathode are accelerated onto the substrate and physical properties can be tuned.

Two types of arc vapor deposition can be distinguished, namely the ”vacuum arc”, where the arc is established in good vacuum between two close packed electrodes and the ”gaseous arc”, where the arc is established between two electrodes in low or high pressure environments [82]. While vacuum arcs are used in PVD, the gaseous arc technique is mainly used in processes like plasma spraying or arc welding [80]. Further information on the long history of arc vapor deposition, starting from the deposition of carbon and metal films, can be found e.g. in Refs. [83–85].

Sputter Deposition

The physical sputter process is not thermal and therefore clearly differs from the previously described processes. The sputter process is achieved by bombardment of the target with high energetic ions with enough kinetic energy to evaporate surface atoms due to momentum transfer. Usually these energetic particles are ionized inert gas particles (e.g. argon), accelerated by an electric field. Figure 9 shows the sputtering configuration with an external magnetic field on the right and without on the left.

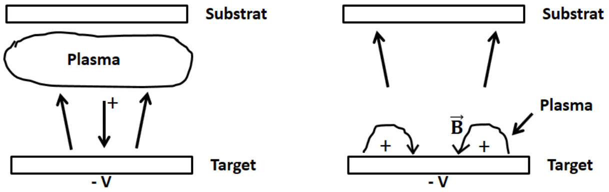

Figure 9: Principle of different sputter deposition methods. By a high negative voltage applied to the cathode, an inert gas (typically argon) is ionized and accelerated onto the target surface. There the argon ions evaporate target atoms due to momentum transfer. Left: Sputter setup without magnetic field. Right: Sputter setup with magnetic field.

Nowadays the most common type of sputtering is the so called magnetron sputtering, which uses an additional magnetic field to bind electrons on trajectories near the target surface. By this technique the electron and ion density close to the target can be increased, which leads to higher sputtering rates. Due to the fact that magnetron sputtering only requires a relatively poor vacuum, the history of sputtering already started in the 19th century and was first reported by Wright in 1877 [86]. It was used in industry from then on for highly reproducible coating processes [87].

Ion Plating or Bias Sputtering

Ion plating or bias sputtering is a variant of sputtering, where the substrate is bombarded with ions from the sputtering gas [88]. This is achieved by applying a negative voltage to the substrate and consequently accelerating positive ions on its surface. This affects the layer growth and properties in many ways. For example loosely bound particles on the surface from rest gases in the chamber (e.g. H) are removed by the ion bombardment. Furthermore, a better desorption of reactive gases can be achieved, the density of the deposited films increases, and the surface roughness is decreased [77].

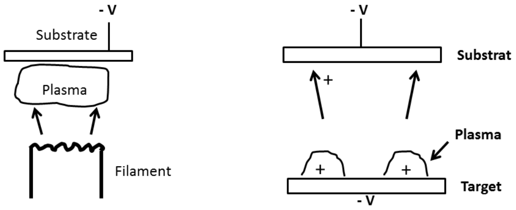

Figure 10: Principle of different bias supported deposition configurations. The additional bias voltage accelerates a part of the positive ions in the plasma onto the substrate. Depending on the applied voltage, this can have different effects. Possible layer modifications are e.g. in-situ polishing or an increased layer density. The vacuum chamber is on ground potential.

This technique is not limited to magnetron sputtering, but can be used for evaporation and the cathodic arc deposition as well, with similar effects of film modifications (Fig. 10). In the scope of this work, bias sputtering was applied to significantly reduce the surface and interface roughness of films deposited by magnetron sputtering. A detailed evaluation of the effects from bias sputtering onto the deposited Cu/Ti neutron supermirror structures can be found in chapter 5.

In the following magnetron sputtering is described in more detail and important properties and parameters such as vacuum pressure, particle energies and characteristic sputter yield are addressed.

2.2 Magnetron Sputtering

Under a noble gas pressure of about 10^{-2} - 10^{-3} mbar, it is possible to create a plasma by applying an electric field which accelerates ionized gas atoms onto the target. By adding a magnetic field near the target, the plasma can be shaped and even limited to special areas or just be confined directly above the target. The magnetic field interacts with the electric field and increases the electron density near the cathode (target), which leads to a higher ionization rate. The principle is shown in figure 11.

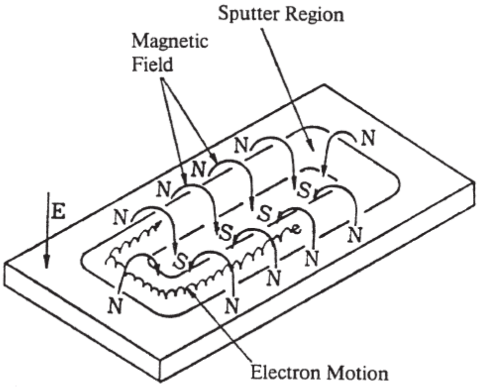

Figure 11: Schematic view of a planar magnetron electrode, showing the electric field, the magnetic field and a trace of a moving electron [89].

The higher ionization rate can be used to decrease the Ar-pressure in the chamber and therefore decrease the amount of collisions with gas atoms during sputtering for both, Ar-ions on their way to the target and target atoms on their way to the substrate. This leads to higher deposition rates with smoother film growth at the same time.
In order to understand the formation of plasma and the effect of the magnetic fields it is enough to treat the particles with one particle theory. The force acting on charged particles moving in a magnetic field, commonly created by an arrangement of permanent magnets, is the Lorentz force F

$$\vec{F} = q(\vec{E} + \vec{v} \times \vec{B}) = m\dot{\vec{v}} \; . \tag{2.1}$$

Because of this relation, a charged particle in a homogeneous field gyrates around the magnetic field lines. From equation 2.1 it follows directly, that the magnetic field only influences the perpendicular component of the particles velocity $\vec{v}_\perp$. This gyration frequency is also called Larmor frequency and is given by

$$\omega_L = \frac{|q|\,B}{m} \; . \tag{2.2}$$

The corresponding Larmor radius is

$$r_L = \frac{|\vec{v}_\perp|}{\omega_L} = \frac{|\vec{v}_\perp|\, m}{|q|\, B} \ . \tag{2.3}$$

Comparing the two main ion species, the masses of an electron ($m_e = 0.511\,\mathrm{MeV/c^2}$) and an Ar$^+$-ion ($m_{Ar} = 16.8\,\mathrm{GeV/c^2}$) differ more than four orders of magnitude resulting in largely different Larmor radii.

Therefore, considering a magnetic field of 0.1 T at the targets surface and a kinetic energy of 100 eV, the Larmor radius for electrons is $r_L = 0.3\,\mathrm{mm}$ and for argon $r_L = 90\,\mathrm{mm}$.

The magnetic field, additional to the electric field, has several advantages. With the gyration of the electrons, the probability of hitting and ionizing argon atoms increases and therefore the plasma density gets higher and the gas pressure can be decreased. This leads to a more stable plasma configuration during sputtering.

By applying an electric and magnetic field simultaneously, the equations of motion split into a term parallel to the magnetic field and one orthogonal to it

$$m\dot{v}_{\|} = qE_{\|} \ , \tag{2.4}$$

$$m\dot{v}_\perp = q\left(E_\perp + v_\perp \times B\right) \ . \tag{2.5}$$

Therefore the charged plasma particles move with an average velocity of

$$\vec{v} = \frac{\vec{E} \times \vec{B}}{B^2} \ , \tag{2.6}$$

perpendicular to $\vec{E}$ and $\vec{B}$ [90]. This so called $\vec{E} \times \vec{B}$ drift is independent of the mass of the charge carrier. It leads to a homogeneous plasma flow perpendicular to the planes spanned by $\vec{E}$ and $\vec{B}$. This effect can be used to increase plasma density near the surface area of the target and keeping the plasma away from surrounding material and chamber walls [89].

Concerning the energy transfer from the bombarding ions onto the target atoms, the masses of the materials play an important role. From conservation of energy and conservation of momentum laws, the transferred energy E_t for physical collision between hard spheres can be described by the following relation [75]

$$\frac{E_t}{E_i} = \frac{4 M_i M_t \cos^2\Theta}{(M_i + M_t)^2} \ , \tag{2.7}$$

where i describes the incident particle, t the target particle and Θ the incidence angle of the ions onto the target surface. A maximum in the energy transfer between the particles can be directly derived from equation 2.7 and is given for $M_i = M_t$ and $\cos^2 \Theta = 1$, which means that Θ should be zero.

Noble gases are preferably used for sputtering to prevent chemical reactions between the sputtering gas and the target atoms. In this thesis argon ($m_{\mathrm{Ar}} = 40\,\mathrm{u}$) with a purity of 99.999 % (5N) is used for sputtering copper, titanium, iron and silicon, as the masses are reasonably close to each other and it is a rather cheap inert gas compared to others like krypton ($m_{\mathrm{Kr}} = 83\,\mathrm{u}$) or xenon ($m_{\mathrm{Xe}} = 131\,\mathrm{u}$).

When the bombarding ions hit the target's surface, there are different interactions that can occur as shown in figure 12. The incoming ions generally interact near the surface. These can either be single collisions together with reflection or a collision cascade, where the ions physically penetrate into the target material and deposit their complete energy step by step in many serial collisions. During these collisions the energy transfer might be high enough for target atoms to overcome their binding energy and be ejected (sputtered).

Most of these collisions take place in the surface and near surface region and cause heating of the target's surface. A certain quantity of ejected particles is backscattered to the surface and has to be ejected a second time. Also implementation of inert gas into the target material is possible. Therefore, it is helpful to use noble gases, that do not form bonds with the target material. Secondary electrons from collisions help to stabilize the plasma due to additional ionization of inert gas and are therefore essential for magnetron sputtering.

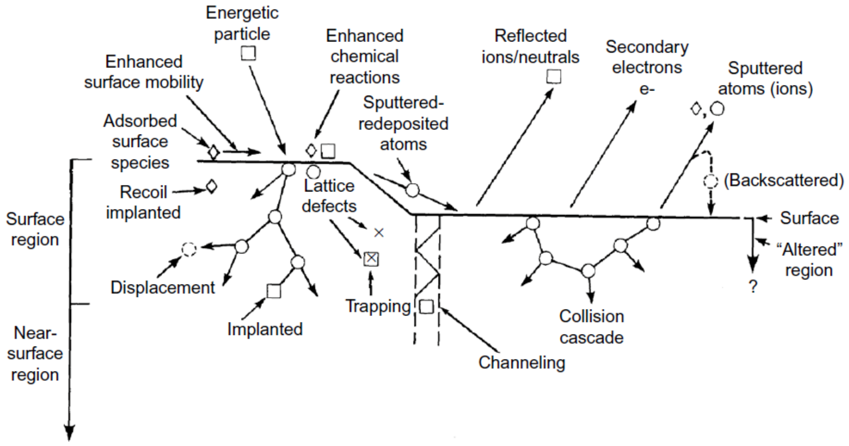

Figure 12: Surface effects that occur on the target when bombarded with high energetic atoms/ions (e.g. Ar^+)[75].

Direct Current (DC) Magnetron Sputtering

Figure 13 shows the most common used magnetron type for direct current (DC) sputtering. It is called planar and is typically equipped with an array of magnets under the target. Secondary electrons coming from the cathode are therefore trapped near the target surface by the magnetic field (see Fig. 11). This racetrack of electrons leads to a higher degree of ionization and consequently to a higher growth rate of the layer by up to one order of magnitude [91]. An advantage is for example, that the working pressure can be decreased significantly to the region of $\approx 5{\cdot}10^{-3}$ mbar.

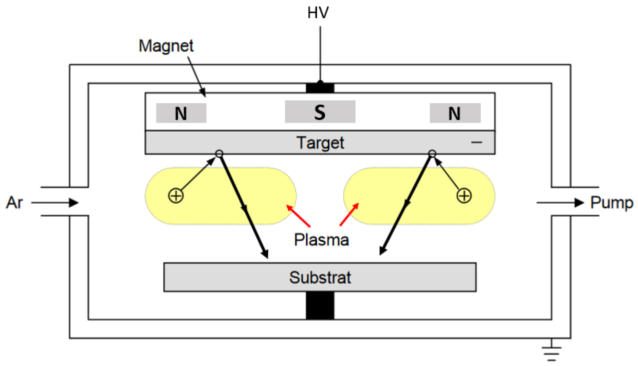

Figure 13: Theoretical operating principle of a planar magnetron with permanent magnet system behind the target. Scheme adapted from [92].

Pulsed Power (PDC) Magnetron Sputtering

The pulsed power magnetron sputtering technique can be divided in unipolar or bipolar waveform types, which are operating at frequencies between $50 - 250$ kHz [93]. The unipolar operation mode can be compared to a DC power supply, which is turned on and off at a certain frequency. In the bipolar mode, the power supply switches the polarity every few milliseconds, which consequently reduces charge build-up at the target surface and decreases arcing on the target. Therefore this operation mode is commonly used for weakly conducting target materials as well as metals as sputtering conditions are slightly different. Within this thesis, all PDC sputtered samples were produced in bipolar mode with 50 kHz frequency.

Radio Frequency (RF) Sputtering

If the frequency of the power supply exceeds 500 kHz, the mobility of Ar-ions is not sufficient anymore to follow the change in potential. They feel an attractive potential towards the cathode. Electrons on the other hand are able to follow the potential changes and acquire enough energy to ionize atoms of the sputter gas. This results in plasma generation throughout the whole space between the electrodes, which also means, that more ions are available and the working pressure can be decreased significantly in comparison to DC or PDC mode. In radiofrequency mode the target's surface is coupled capacitively to the field and feels alternately a positive and negative potential.

In the negative potential period, Ar-ions are accelerated onto the target with enough energy gain to cause sputtering, whereas in the positive potential period, electrons are attracted to the target's surface and prevent charge build-up. This is a very important feature, as it permits to also sputter insulator materials. Doing so, it has to be kept in mind, that insulator materials (like SiO2) are often brittle, have low thermal conductance and are sensitive on thermal expansion. This means that with these materials only low power and sputter rates are realizable as they would otherwise break.

Frequencies used for RF-sputtering vary typically from 0.5 to 30 MHz, with 13.56 MHz commonly used as industrial standard. In this work RF-sputtering was mainly used for deposition of Cu as the sputter rates in DC and PDC mode were too high for our application. Deposition in RF-mode showed positive effects in the sputter rate as well as significant lower roughness growth during deposition, which is of great importance for the produced neutron mirrors.

2.3 Reactive Sputtering

Reactive sputtering with a pure target distinguishes the reaction of the sputtered species with gases like oxygen or nitrogen, or the reaction with an adsorbed species, or the reaction with a co-deposited element like carbon to form compounds [94]. In 1961 the first patent on reactive sputtering was published by R.W. Berry, who produced Ta_2N resistor films with this technique [95]. Reactive sputtering is an extremely powerful tool to influence, modify and shape thin film coatings to fulfill special requirements. These are for example material specific properties like interdiffusion barrier or hardness, optical properties like transparency, crystallographic aspects like the crystal orientations and many more. In this thesis, reactive sputtering is an essential part of the research. In the first Cu/Ti neutron supermirrors produced within this work, the interdiffusion between those two materials was too high. It caused a smearing of the multilayer system and increased the interface roughness. Neutron reflectivity measurements showed a lower optical contrast than calculated and very low temperature stability of the mirrors. Therefore, by adding nitrogen to the Ti-layers, a diffusion barrier for Cu and Ti-layers was developed. The detailed results are discussed in chapter 5.

During sputtering from an elemental target, a certain amount of reactive gas (like N_2, O_2) is added to the Ar sputtering gas. This gas may also be activated in advance (N, O, N^+, O^+ etc.) to be chemically more reactive [81]. The presence of Ar results in Penning ionization and excitation processes, which activates the reactive gas and splits molecules into atoms. This is why also non-activated reactive gas can be guided into the chamber as well [96–98].

The so called “poisoning” of the sputter target has the most important impact on the process parameters. A target turns into a poisoned state, when there is enough reactive gas available to form a compound layer on the target’s surface. In this case, the sputtering rate and efficiency decrease rapidly. To get back into metallic sputtering mode with higher sputtering rate, the surface has to be cleaned by the plasma. Depending on the power density, this can take several minutes up to hours. For configurations with high sputtering rate (e.g. PDC instead of RF), the process is easier to control. The reactive sputtering process can be controlled by monitoring the partial pressure of the reactive gas by mass spectrometry [99, 100]. Measuring the impedance of the plasma or an optical absorption spectrometry of the plasma, are two additional methods to control a reactive sputtering process [101–103].

Figure 14 shows an example of reactive sputtering with oxygen. The graph shows the partial pressure as a function of the oxygen flow. Modifying the O_2 flow in the way of the arrows leads to a typical hysteresis curve. Starting at zero oxygen flow (1), sputtering is in metallic mode. Letting a small amount of O_2 inside the chamber, the sputtered material will getter almost all of the gas and form chemical bonds. Therefore the pressure stays at low level (1 → 2).

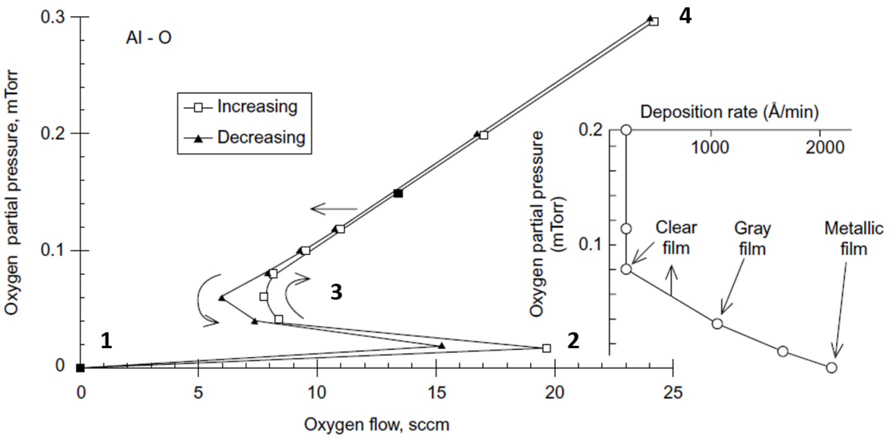

Figure 14: The graph shows the partial oxygen pressure versus its gas flow during reactive sputtering process [75].

The amount of reactive gas, that can be filled into the chamber until the saturation point strongly depends on the process parameters. Important parameters are the power density at the target, the target material itself, the operation mode (DC, PDC, RF) and Ar working pressure. Once the saturation point is reached and the reactive gas flow is further increased (3), the target surface is poisoning. In this case, the sputter rate decreases suddenly, less target element atoms are available and therefore less reactive gas can be gettered. As a consequence, the chamber pressure is increasing rapidly and from there on linearly with the reactive gas flow ($3 \rightarrow 4$). If the reactive gas flow is decreased again, the target surface first has to be sputter cleaned, before the reactive mode with high sputter rates can be entered again. Depending on the used materials, it is possible to modify even optical properties like shown in figure 14. Within this thesis, an interdiffusion barrier for Cu was formed by sputtering TiN_x at low reactive gas flows (0.5 sccm - 2 sccm).

Concurrent ion bombardment (ion plating or bias sputtering), which is used to flatten thin layers in-situ, has an important impact on the reactive sputtering process. Normally mainly Ar^+-ions are accelerated from the plasma onto the substrate surface, as the substrate is on negative potential. This enhances chemical reactions on the substrate surface, because adatom (adsorbed atom) mobility is increased. Furthermore, the bombardment leads to to the formation of a film with increased density. Experimental studies and results concerning bias voltage are shown in more detail in chapter 4.3.

2.4 Sputtering Yield and Layer Growth

To describe the number of ejected particles during the sputtering process, the so called sputtering yield is defined as the ratio of incoming ions of the sputtering gas to the amount of atoms vaporized from the target material as:

$$S = \frac{N_{\text{Vaporized atoms}}}{N_{\text{Incoming ions}}} . \tag{2.8}$$

The sputtering yield strongly depends on parameters like sputter gas, target material and ion energy. For a certain configuration of inert gas and target material, the sputtering yield for energies below 1 keV can be described by the following relation [78]

$$S(E) = \frac{3}{4\pi^2} \alpha \frac{4 M_1 M_2 E}{(M_1 + M_2)^2 \Delta H} . \tag{2.9}$$

Here $S(E)$ is the sputtering yield dependent on the ion energy E, the masses of the incoming ion M_1 and the target material M_2 and the sublimation heat ΔH needed to evaporate a target atom. The coefficient α depends on the mass ratio.

In order to describe the layer growth under certain conditions during sputtering, structure zone models are of great interest. In 1969 Movchan und Demchishin developed a model for evaporated Ni, Ti, W, Al_2O_3 and ZrO_2 layers with thicknesses between $0.3 - 2$ mm [104], dividing the layer growth roughly into three different zones (see Fig. 15). They focused mainly on the homologous temperature T/T_m, where T is the substrate temperature and T_m the melting point of the sputtered material. This model was extended by an axes for sputtering gas pressure by Thornton in 1974 [105, 106], as the energy range of ejected particles is much higher for sputtering $4 - 40\,\text{eV}$ than for evaporation $0.1 - 0.2\,\text{eV}$.

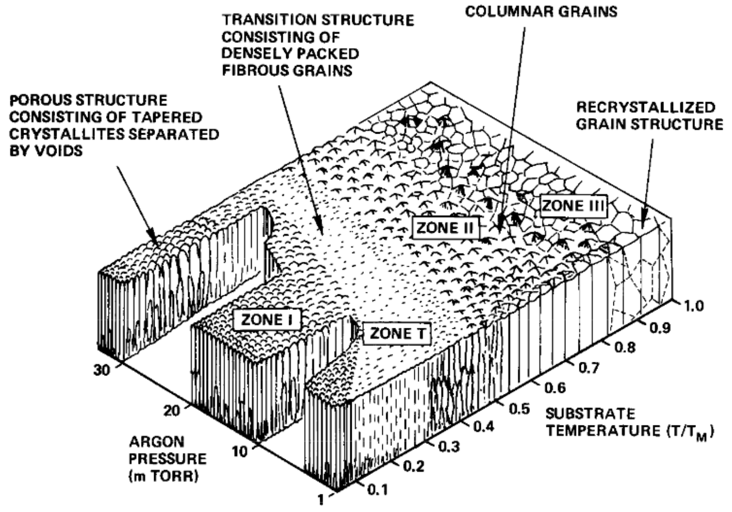

Figure 15: Structure zone model with different layer growth dependent on the homologous temperature T/T_m and the argon pressure [107].

Zone 1: This region is characterized by conical crystallites and gaps between the grain boundaries, which are the result of very low adatom mobility on the surface. This leads to shadowing effects and holes in the layer. These porous layers tend to have tensile stress inside, due to attractive forces at the grain boundaries.

Zone T: This zone is called the transition zone. In this zone, grains are very thin and close-packed. The layer's surface is very smooth. Layers of zone 1 can be converted in zone T by high energy ion bombardment, as the granular type peaks can be smoothened and particles can be pushed between the grain boundaries.

Zone 2: Layers in this zone have pronounced grain boundaries and fibers are thicker than in the transition zone. The homologous temperature is high enough to let the grain boundaries move and surface diffusion effects appear. In these layers compressive stress can be found, which can be reduced by annealing techniques. In this zone the packing density is high and surface roughness is low.

Zone 3: In this zone, bulk diffusion processes are dominating leading to high densities and large grain sizes. Effects like recrystallization and recombination reduce stress and strain within these layers.

By applying an additional bias voltage to the substrate, the growing layers are bombarded with high energetic ions from a plasma and can be compressed and the surface is smoothened [108, 109]. It can be derived, that the border between zone 1 and zone T is shifted to lower T/T_m with increasing ion energy [110]. For applications, where the substrate cannot be heated up to a certain level, applying a negative bias voltage to the substrate is a promising alternative to reach layer growth of zone T.

Structure zone models as shown above describe principles quantitatively, but cannot make quantitative statements about thin layer growth in a certain facility.

Besides the argon pressure, power density and material, the actual layer parameters in a sputtering facility also depend on several other parameters like residual rest gases, distance between magnetron and substrate or applied bias voltage. This makes it difficult to make an exact forecast and machine parameters have to be evaluated and characterized.

In this work, magnetron sputtering was used to produce all neutron optical components, because this process is highly reproducible and stable even for layer thicknesses in the range of only a few nanometers. By using the PDC-mode and the RF-mode for different materials, single layers with smooth surfaces were produced. By combining this with reactive sputtering, it was possible to produce multilayer systems with effective interdiffusion barriers. In order to decrease the roughness within the multilayer structure further, the ion plating technique was successfully implemented in the facility.

3 Measurement Methods

This chapter gives an overview of the main measurement methods used in this thesis. Important layer properties for production of high quality neutron mirrors are surface and interlayer roughness, layer growth and composition. Among others, these values strongly depend on the used machine parameters like deposition mode, power and pressure.

3.1 Neutron Reflectometry

The theory of neutron reflection and interaction with matter is briefly described in chapter 1.2. The red curve in figure 16 shows the neutron reflection on Si (substrate) with its material specific critical angle of total reflection. When exceeding this angle, the transmitted part of the neutron wave increases and the reflected one decreases. Depositing a single layer (e.g. Ni or Cu) with thickness d onto the substrate, interference effects can occur between the reflected waves at the vacuum-layer and layer-substrate interfaces. The optical path length difference of the two beams is

$$\Delta \;=\; 2d\,\sin(\Theta)\ . \tag{3.1}$$

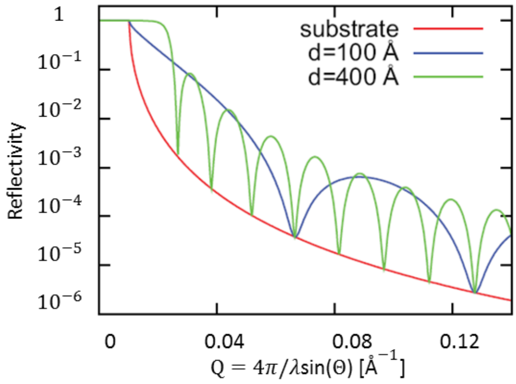

Figure 16: Neutron reflectivity of Si substrate and two Ni single layers of different thicknesses on top [111]. Q represents the momentum transfer during the scattering process.

Two interference maxima occur for a path length difference of one wavelength

$$\lambda \;=\; 2d\cdot\delta\sin(\Theta) \;\approx\; 2d\cdot\delta\Theta\ . \tag{3.2}$$

Therefore the distance of two interference peaks is decreasing with increasing layer thickness.

When measuring real surfaces, there is always a certain surface or interface roughness present. To describe this effect theoretically, the model of a one-dimensional square well potential at an interface is changed into a certain transition, which is damping the reflectivity. The roughness model used in this thesis is described later in more detail. On the left of figure 17 one observes, that the influence of roughness is dominant for angles of incidence greater than two times the critical angle of total reflection. On the right side four different scenarios are presented, which can be well differentiated.

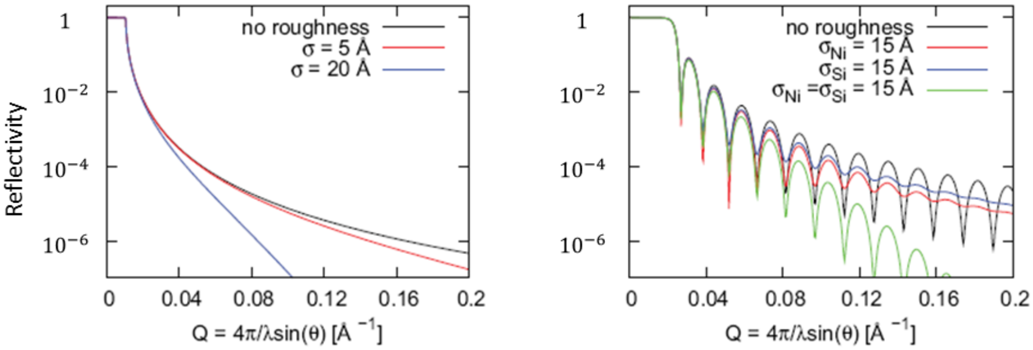

Figure 17: Left: Calculated neutron reflectivity at the interface between vacuum and Si. Right: Calculated neutron reflectivity of a 40 nm thick Ni layer on a Si substrate for different roughnesses σ [111].

If one of the two interfaces is rough, only the interference pattern at large angles of incidence is suppressed. If both surfaces are rough, the reflectivity decreases faster, because the amount of diffuse scattered neutrons is increasing.

It has to be mentioned, that interface roughness and interdiffusion between layers have the same effect on the measured neutron reflectivity and it is therefore not possible to distinguish between them.

The principle of the neutron reflectivity measurement setup of TREFF is shown in Figure 18. The instrument is supplied with neutrons coming from a graphite (PG 002) double monochromator with a resulting wavelength of $\lambda = 4.8\,\text{Å}$. For measurements with polarized neutrons, a polarizer can be inserted into the beam. This polarizer is a Si wafer coated with a Fe/Si supermirror, where the neutron spin component parallel to the magnetic field is reflected out of the beam and neutrons anti-parallel are transmitted through the wafer. The resulting polarized neutron beam is then guided under a magnetic holding field through an RF-spin flipper to the pivoted sample table. This table is adjustable in height, tilting angle and angle of incidence. With a maximal top weight of 500 kg it is possible to mount additional equipment like a sample holder or even a cryostat on top of the sample table. After interaction with the sample

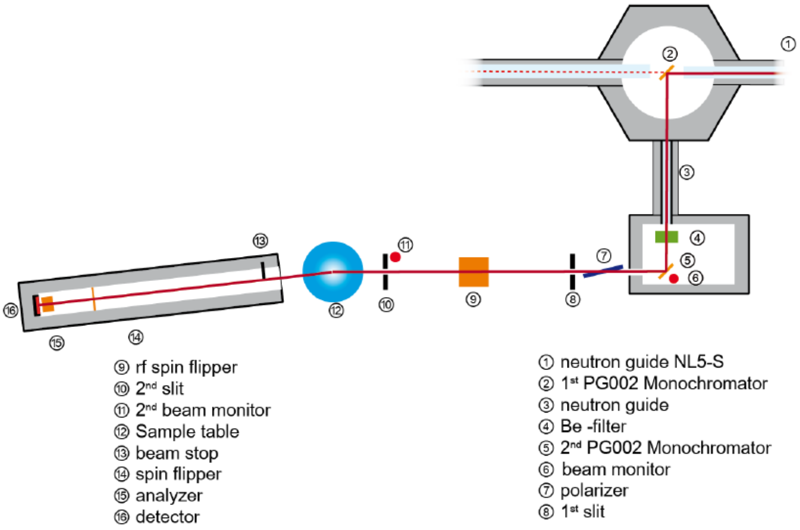

Figure 18: Schematic layout of TREFF reflectometer for measurement with polarized neutrons [112].

a multichannel polarization analyzer can be used to retrieve information about the angle of magnetization in a magnetic sample, like used e.g. in Ref. [113]. Besides the analyzer, the pivoted detector arm is equipped with a Mezei spin flipper and a two dimensional position sensitive detector, which is described in more detail in Ref. [114]. Such detector allows to measure specular and off-specular reflection and grazing incidence small angle scattering.

3.2 X-ray Reflectometry (XRR) and Diffraction (XRD)

X-Ray Reflectometry (XRR)

To determine layer thickness and surface roughness we used X-ray reflectometry to investigate thin films in the range of few nanometers up to a few hundreds of nanometers. In 1930 Kiessig discovered the effect of constructive and destructive interference of X-rays above the critical angle of total reflection [115]. The interference effects are caused by the splitting of a beam into a reflected and a refracted one at each interface of two materials or layers. The refractive index for X-ray is mainly determined by the material's density and is slightly smaller than one.

The interference pattern gives precise information about the layer thickness, material density and surface roughness. For a multilayer system even the interface roughness can be determined by an appropriate fitting routine. In this thesis, a setup similar to figure 19 was used to perform X-ray reflectometry (XRR) measurements.

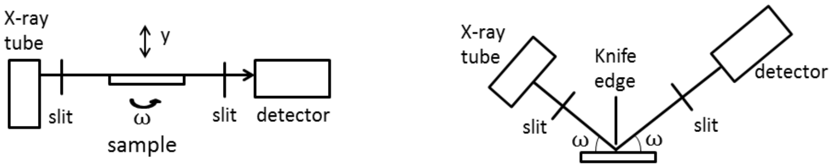

Figure 19: Left: Reflectometer setup consisting of X-ray source, slits, pivoted sample holder and detector. Right: Setup in reflection mode.

The left side of figure 19 shows the setup for sample alignment. The beam divergence can be adjusted by slits in front and behind the sample and the y- and ω-axes can be moved to align the sample surface normal to the rotational axes of the reflectometer. On the right side of figure 19, an additional knife edge is used to improve the angular resolution of the XRR measurement.

With XRR it is possible to determine layer thicknesses with high precision at an absolute scale in a non-destructive way. The X-ray refractive index $n = 1 - \mathrm{pot_{re}} - i\,\mathrm{pot_{im}}$ for a certain material depends on a real and an imaginary part [116]. The real and imaginary optical potential of every material for X-rays can be calculated by

$$\mathrm{pot_{re}} = n \cdot r_e \cdot (Z + fp) \qquad \text{and} \qquad \mathrm{pot_{im}} = n \cdot r_e \cdot fpp\ . \tag{3.3}$$

Here n describes the particle density, $r_e = 2.181 \cdot 10^{-15}\,\mathrm{m}$ is the classical electron radius, Z the atomic number, fp the anomalous scattering factor of forward scattering and fpp is the absorption of the material.

The routine, which was used to fit the reflectivity and transmission of X-rays and neutrons, is a program called Supermref written by Ulrich Schmidt. It assumes, that each layer is described by a one-dimensional rectangular square-well potential with material specific height (see appendix A). Therefore it is possible to fit reflectivity curves of single- and multilayers. For a multilayer structure, the program calculates reflectivity and transmission of the incoming wave for each interface. Doing so, it is possible to describe the measured reflectivity curve by interference of all reflected waves. The roughness at each layer interface is strongly affecting the total external reflectivity and is also taken into account in the program.

In this work, XRR was used to calibrate the sputtering rates of the coating facility prior to coating and for consistency and roughness studies afterwards. Several calibration and test samples were produced each time before producing a neutron mirror. Figure 20 shows a measured XRR curve of a single Cu layer deposited onto a glass substrate together with the corresponding fitted curve.

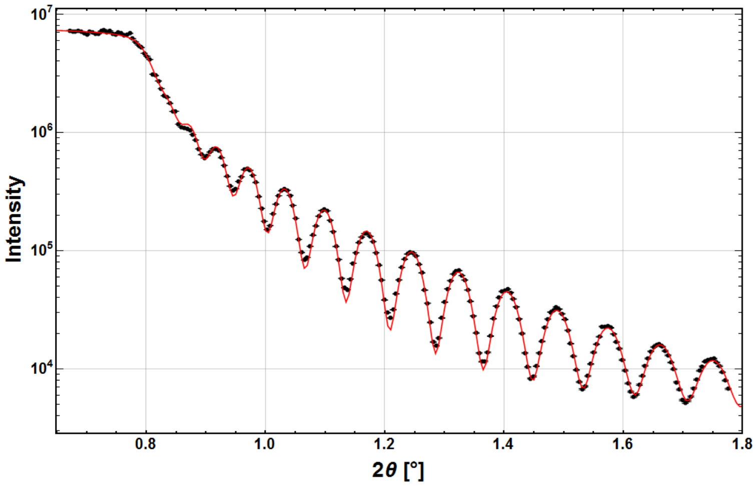

Figure 20: The plot shows a measured XRR spectrum (black points) of a 88 nm thick Cu layer compared with the corresponding fitted curve (red curve).

The fitted curve agrees well with the measured data and shows, that it is possible to determine the parameters thickness and surface roughness with high accuracy. In this example, the Cu layer has a thickness of 87.80 ± 0.04 nm and a surface roughness of 1.65 ± 0.02 nm. A definition of the term roughness in this context can be found in appendix A.

X-Ray Diffraction (XRD)

By X-ray diffraction (XRD) it is possible to qualitatively determine the nitrogen content in a certain material mix. In this work, this was used to determine the amount of nitrogen in reactively sputtered Ti layers, which were used as diffusion barrier. In the following the underlying principles are described briefly.

Figure 21 shows an example of two X-rays reflected by the (110) planes of an orthorhombic structure.

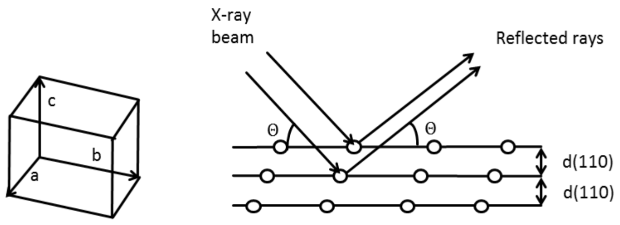

Figure 21: Left: Presentation of one P unit cell with orthorhombic structure. Right: The typical paths of two X-rays reflected on the (110) planes of the orthorhombic structure.

The penetration depth depends on the material's mass attenuation coefficient μ and ranges up to millimeters for X-rays with high angle of incidence. The penetration in material follows

$$I(d) = I_0 \cdot \exp\left(-\frac{\mu}{\rho}\rho d\right) \;, \tag{3.4}$$

where μ/ρ is the material specific mass attenuation coefficient, I the intensity and d the penetrated layer thickness. For XRD, d has to doubled, as X-rays have to leave the material again to reach the detector. For Cu μ/ρ_{Cu} 52.55 g/cm^2 (for Cu$_{K_\alpha}$) [117] and for Ti μ/ρ_{Ti} 202.3 g/cm^2 [118]. For a Cu/Ti supermirror (total thickness $\approx$ 2 µm), the X-rays can completely penetrate the layers and even the substrate is visible. To investigate only layers near the surface, it is possible to perform an GID (Gracing Incidence Diffraction) measurement, where X-rays hit the surface of the sample under a small angle of incidence (typically $0.5 - 3°$). Due to the small angle of incidence, X-rays have a long effective path inside the material, but only a small penetration depth ($\approx$ nm).

Figure 22 shows an example measurement of a TiN layer on Ti bulk material. This measurement is used as reference spectrum for determination of the peak positions from Ti and TiN$_x$ layers in this work.

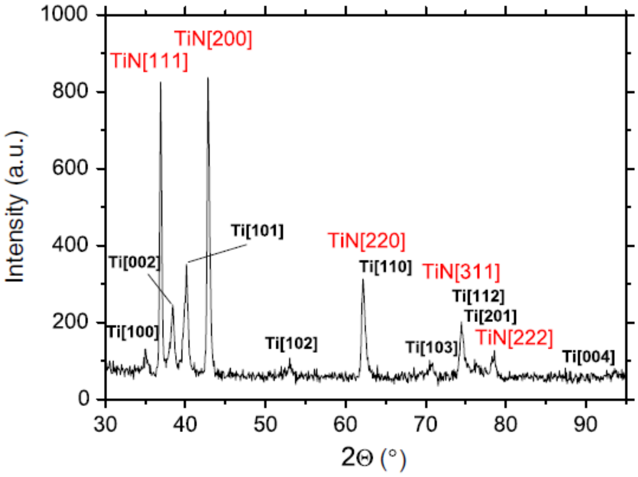

Figure 22: Grazing incidence spectrum of a TiN sample on top of Ti bulk material measured at angle of incidence of 3° [119]. In addition to the peaks of the Ti crystal phases, peaks of the TiN compound crystal phases are measureable.

A peak shift from Ti [002] orientation towards TiN [111] can be observed by increasing the nitrogen flow during deposition. In this work it is shown, that changing the crystal orientation can improve the barrier properties of sputtered TiN$_x$ layers, see chapter 5.4.1.

3.3 Elastic Recoil Detection (ERD)

With this technique it is possible to analyze samples with a depth resolution at the surface of about 10 nm and an element concentration analysis in the range of percentage [120].

For the measurements the Q3D magnetic spectrograph at the MLL was used. Figure 23 shows the geometrical arrangement for an ERD measurement [121]. The basic idea is elastic scattering of incoming high energy and heavy ions with the target material. The reactions can be assumed to be point-like and many-body interactions are weak and are corrected for. The recoil ions are scattered off in forward direction and detected. Using heavy ions (e.g. Iodine) instead of light ones (e.g. He) has the advantages, that the number of projectiles scattered into the detector is significantly lower and that the momentum transfer is high enough to detect and identify all elements by time-of-flight, energy versus energy loss, magnetic or electrostatic analysis.

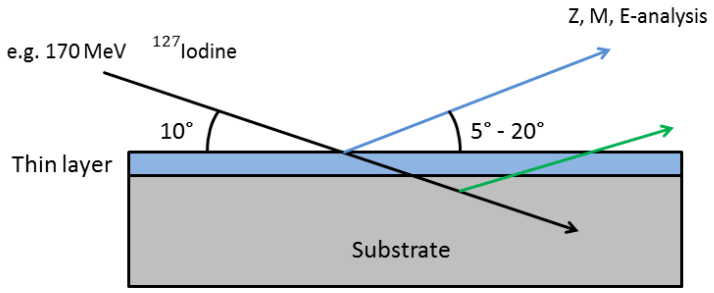

Figure 23: Geometry for elastic recoil detection (ERD) measurement. The blue arrow represents recoil atoms from a thin layer and the green arrow represents atoms coming from the substrate.

In order to determine the detected recoil atoms within an ERD measurement, often a second signal besides the energy signal from the ions is recorded by the detector. This principle is called two stage detector. The detector at Q3D can be seen in figure 24. This detector consists of an ionization chamber for the measurement of the energy loss ΔE of the recoil particles and a position sensitive silicon detector for the residual energy E_{res} [122].

For ion velocities below the Bohr velocity $v_B \cdot Z^{2/3}$ with $v_B = e^2/\hbar \approx 2.19 \cdot 10^6$ m/s, the energy loss of the particles is proportional to their velocity and therefore almost identical for every element. This results in an almost linear curve, when plotting ΔE versus the total energy $E_{tot} = \Delta E + E_{res}$ and the elements can not be separated anymore. Ions above the Bohr velocity do have a specific energy loss in the detector

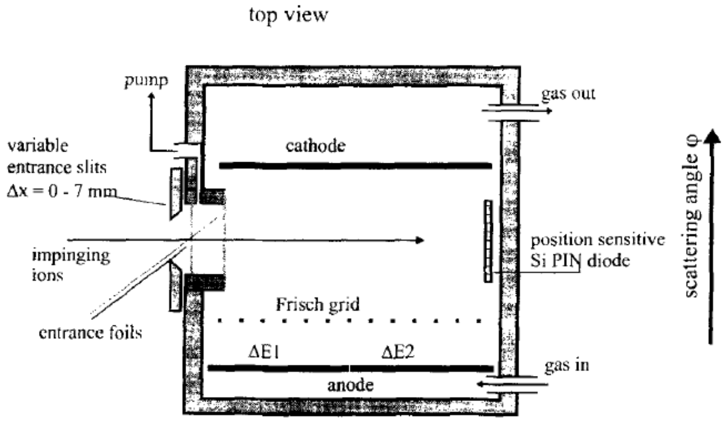

Figure 24: Detector layout for ERD measurement [122]. The Frisch grid separates the collector region in front of the anode from the sensitive volume. The element specific energy loss is measured by the plate capacitor, while the position sensitive detector measures the rest energy of the ejected particles.

gas [123, 124]. For velocities above this value, the specific energy loss follows the condition

$$\Delta E \propto \frac{MZ^2}{E_{tot}} \cdot \ln(E_{tot}) \ , \tag{3.5}$$

where M is the mass of the recoil atom.

By measuring the energy loss and the rest energy in the detector, it is possible to identify the recoil ions. In order to achieve a high sensitivity, a large solid angle of detection of a few msr ($1\,\mathrm{sr} \approx 65.54°$ opening angle) is required for a typical ERD measurement. This means a large opening angle dΦ is required in the scattering plane and has to be corrected for, because the energy of the recoil particles strongly depend on the scattering angle. This effect is called kinematic shift and can be described by [121]:

$$\mathrm{d}E/E = -2\tan\Phi\,\mathrm{d}\Phi\, + \text{ (higher orders in d}\Phi) \tag{3.6}$$

This effect can be overcome by using a position sensitive setup. Then it is possible to measure particle energies and identify different particle species [122]. Figure 32 in chapter 5.2 shows an example of an ERD measurement, which is already corrected for the kinematic shift.

As input, the energy profile of every element from the ΔE-E spectrum is generated and projected to the energy axes. The code then calculates the concentration of every measured element layer by layer, starting at the surface, where the energy for every element is given by calibration measurements.

The energy resolution of such system is mainly limited by the statistics of creating electron hole pairs in the silicon detectors, by the ionization probability in the ionization chamber and by electronic noise. The typical energy resolution of our measurements was about 1 % of total energy which equals about 10 nm in depth resolution.
It is important to keep in mind that the investigated samples suffer from irradiation damages due to the impinging ion beam. Examples for radiation damages are defects and further damage mainly due to Coulomb explosions [125] and thermal spike effects [126]. Therefore, one needs to repeatedly check the depth profile over time and stop as soon as the profile is changing.

4 Production of Neutron Optical Coatings

For production of neutron optical components (see chapters 5, 6 and 7), the sample preparation as well as the facility itself can have a major influence on the resulting coating. In this chapter, the sputtering setup is described briefly and it will be shown how it was upgraded to be able to produce high reflectivity neutron supermirrors made from copper and titanium with the help of a bias voltage applied to the substrate.

4.1 Sample Preparation

To produce neutron supermirror coatings with strong adhesion on the substrate's surface, a clean and smooth surface of the substrate is of great importance [81]. The Cu/Ti supermirror samples were deposited onto "Borofloat 33" glass with thicknesses of 5 mm and 10 mm. Before these glass samples can be loaded into the facility for coating, they have to undergo a cleaning process to guarantee adequate surface properties [75]. Contaminations that need to be removed are for example adsorbed hydrocarbon layers, which cover the whole surface or particles and fingerprints, which are localized. One very important point is, that the cleaning process does not change the surface in an undesired or uncontrolled way. This requires reproducible surface treatment, associated handling and storage techniques. For our glass samples the following cleaning procedure was performed.

The first step is cleaning the samples in an ultrasonic bath, filled with a 2 % solution of Mucasol® in purified water [127]. This solution is alkaline with a pH-value of about 11.7. At a base temperature of 65°C and ultrasonics turned on, it is able remove impurities of oil, grease, silicone and others. After approximately ten minutes in this bath, the samples can be removed and washed with purified water. The second step is another ultrasonic bath, this time in isopropanol with a temperature of 70°C. Isopropanol has good degreaser properties and slowly removing the samples after a 5 minutes bath in this solution results in samples with a clean surface and without any schlieren as the isopropanol is vaporizing quickly on air.

This is the so called pre-cleaning process and as a last step the samples and mirrors are cleaned in the sputtering facility with an ion source directly before coating. In the atmosphere, one or more monolayers of water can condensate on the substrate's surface, depending on several factors, like humidity, sample temperature and ambient temperature. This type of water can typically not be removed mechanically outside the machine, as it would return before loading the substrate into the facility. This is why an in-situ technique under vacuum conditions is applied. Therefore, a special ion source is used, which is in principle designed like a normal rectangular magnetron, but with grounded cathode and the positive charged anode below. With this configuration the positively charged Ar-ions are accelerated onto the substrate's surface and have enough energy to remove weakly bound including these water films. After this step, the substrate's surface is ready to be coated. The ion source can even be used to remove previous coatings. This could be important in case of machine failure during production or sudden ventilation of the facility. Using this tool, a potential oxide layer can be removed easily and the coating process can be continued.

The silicon and quartz wafers only required part of the cleaning process, as the supplier produced the wafers under cleanroom conditions. Here, only the in-situ cleaning with the ion source was performed. All samples cleaned with this cleaning process showed good adhesion and it was therefore verified as sufficient for our samples.

4.2 Setup

The used sputter facility consists of two vacuum chambers that can be separated from one another by a plate valve. The smaller one is the loading chamber and the bigger one the coating chamber. For sputtering a gas pressure of $< 10^{-6}$ mbar is necessary to prevent the inclusion of unintentional impurities and at least one load lock, where samples can be changed without having to ventilate the whole sputtering chamber is required. This results in clean conditions in the sputtering chamber and pumping time decreases as the volume of the load lock can be pumped within hours, while pumping the whole setup after ventilating takes about one day.

The sputtering chamber itself is equipped with an ion source in order to finish the cleaning process of the samples in-situ. With it, the substrates can be bombarded by Ar-ions, which removes weakly bounded particles on the surface of the substrate (see ion-plating). In general, these weakly bound particles, which remain even after precleaning, consist of some monolayers of water, coming from ambient air outside the setup. After treatment with the ion-source, the substrate is ready to be coated.

The setup consists of four rectangular magnetrons in total, which can be equipped with one target material each. In principal a combination of multilayers with four different materials can be produced. For our purposes, we need two different materials for the Cu/Ti supermirrors and three for the Fe/Si polarizer coatings when adding a Gd/Ti anti reflection layer at the bottom. All mirrors in this work were produced with this setup, as it is possible to be used in DC, the PDC and RF mode.

The chamber in total is about 7 m long and 0.5 m wide. Samples up to a size of 1200 mm length, 300 mm width and 20 mm in height can be coated as one piece. For the planned guide geometry of 1000 mm length, 200 mm width and 10 mm in height, the setup would be sufficient. Figure 25 shows a photo of the setup and figure 26 shows its working principle.

Figure 25: Picture of the used sputter facility. The clean room tent with the loading section of the facility is located behind the door.

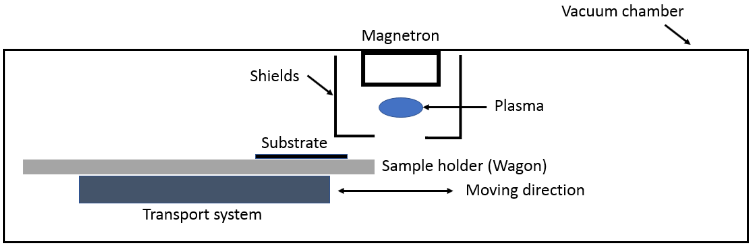

Figure 26: The layout of the sputter facility used. The substrate steadily passes the magnetron in order to achieve a homogeneous and well defined layer thickness.

The substrate lies flat on a wagon, which can be loaded into the deposition chamber via a load lock onto a transport system. Once, the wagon is inside the deposition chamber, the lock can be closed and the substrate can be moved under the magnetrons from one side to the other via the transport system. Due to the continuous movement of the substrate past the magnetrons, very homogeneous layers ($\pm 0.5\,\mathrm{nm}$ over the whole wagon width and length) can be deposited. The shields on both sides make sure that deposition takes place only at a very specific area. This opens the possibility to determine a specific deposition rate per iteration.

4.3 Setup Upgrade

To fulfill the requirements on surface roughness and layer separation, the setup was upgraded within the work of this thesis to include a system to apply a negative bias voltage. This technique allows to use ion plating resulting in smoother surfaces and layers with higher density [99, 108, 109, 128].

The main challenge was to apply bias voltage only to the transport wagon and therefore to the substrate. The coating chamber stays on ground level. Wherever electrical isolation inside the chamber was required, polyether ether ketone (PEEK) was used, as it is an isolator and suitable to be used under vacuum condition. The whole setup is shown in figures 27 and 28.

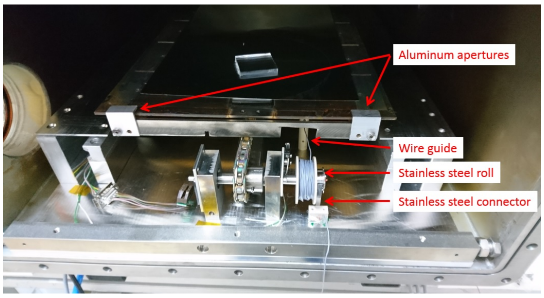

Figure 27: The wire guide and feeding roll are made of electrically isolating PEEK. Two aluminium apertures ensure the isolation between substrate holder and transport wagon as the connection point is shadowed.

To ensure electrical isolation of the substrate holder and the transport system, two aluminium apertures were mounted to shadow their connection point. From outside of the chamber, the bias voltage is connected to the feeding roll by a stainless steal sliding contact.

The photo in figure 28 shows the transport wagon at its furthermost position, hitting the chamber end switch. The wire feeding roll is connected to the copper plate on top of the transport wagon. The copper plate and the transport wagon are electrically separated from each other by a PEEK slice.

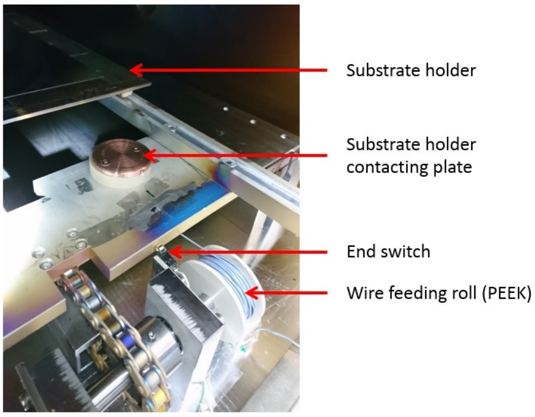

Figure 28: The copper plate acts as contact station for the substrate holder on top and is electrically isolated to the transport wagon below by a PEEK plate.

Figure 29 shows a stainless steel sheet at the bottom of the transport wagon, which is contacting the copper plate on the transport wagon. The substrate wagon itself is isolated from the transport wagon by two PEEK rails on the bottom.

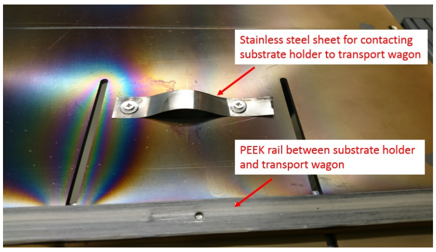

Figure 29: The substrate holder is equipped by a stainless steel stripe at the bottom to contact the copper plate on the transport wagon.

The first tests showed, that the wire guide from figure 27 was insufficient to keep the wire reliable on the feeding role. Therefore in the second iteration, a housing for the feeding roll was made by the in-house workshop of the TUM physics department. With this setup, substrate bias voltages up to 300 V were possible, allowing for in situ polishing.

5 Neutron Supermirror Coating with Copper and Titanium

Conventionally used neutron supermirrors consist of a Ni/Ti multilayer structure. To suppress magnetization, an alloy of nickel and molybdenum (NiMo) can be used instead of pure Ni [129]. Figure 30 shows the neutron reflectivity curve of a m = 3 NiMo/Ti supermirror produced within this thesis.

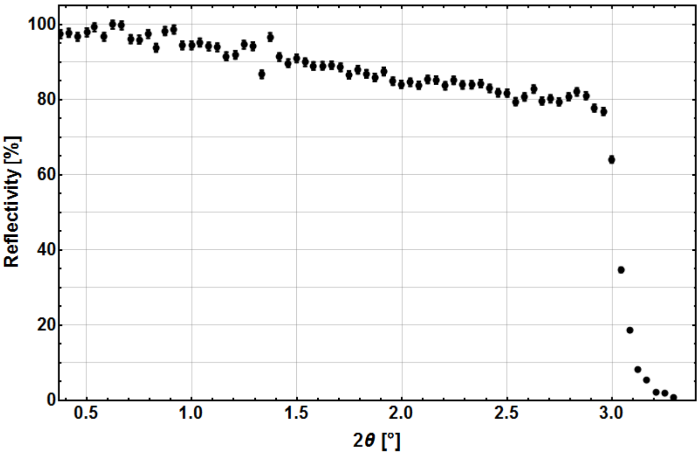

Figure 30: Neutron reflectivity measurement of a m = 3 NiMo/Ti supermirror consisting of 701 layers with reflectivity > 78 %.

Although, high reflectivity and m-values can be achieved with this material combination, neutron depolarization could be present, even for Ni alloys [130]. To prevent depolarization, we use diamagnetic Cu and paramagnetic Ti. For the implementation in the PERC instrument, the supermirror ideally has to fulfill additional requirements:

- m = 2
- Reflectivity > 80 % at critical angle of reflection
- Mildly heat resistant < 80 °C

We used neutron reflectometry, elastic recoil detection, X-ray reflectometry and X-ray diffraction to characterize and develop our Cu/Ti supermirrors. The results described in this chapter are published in [131].

5.1 Previous Work

In her Phd thesis, N. Rebrova proved, that it is possible to produce a non-depolarizing neutron supermirror with Cu and Ti, despite the previously found high interdiffusion [8]. Figure 31 shows the reflectivity curve for the supermirror with the highest reflectivity that could be achieved at this time.

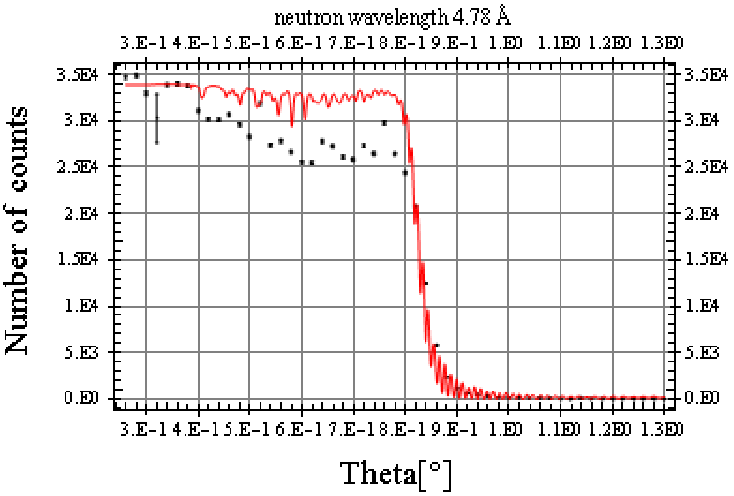

Figure 31: The experimental neutron reflectivity of a Cu/Ti sample (119 layers) with m = 1.7 (black points) and the calculated curve in red are shown [8]. The data was obtained using the TREFF reflectometer at the FRM II in Garching.

The measured reflectivity is ≈ 20 % below the calculated one. N. Rebrova made high interlayer roughness and interdiffusion of both materials responsible for this result. In her conclusion she is referring to an optimization process, which was used to produce the Ni/Ti supermirrors. There the gain in reflectivity was achieved by implanting impurities of e.g. nitrogen, oxygen or air [132] into the Ni layers (An overview of this technology can be found in [133] and citations inside [72, 134–136]). This is done by reactive sputtering of the pure materials. The result is a formation of an interdiffusion barrier between the two different materials together with a smooth interlayer surface and consequently higher neutron reflectivity.

Interdiffusion effects and impurity implementations for Cu and Ti have not been considered in her work and are investigated within this work.

5.2 Target Material

The target material is an essential aspect for the production of non-depolarizing supermirrors. Every magnetic impurity (e.g. iron) that is bound in the target material will also be deposited and incorporated in the supermirror structure. These magnetic impurities can form magnetic clusters, which lead to depolarization effects, when used in high magnetic fields as it is the case for the PERC instrument. Therefore, an element analysis via elastic recoil detection (ERD) has been performed at the Maier-Leibnitz-Laboratory (MLL) to investigate the element composition of the deposited layers in our supermirror structures. Figure 32 shows such ERD measurements with the total energy $E_{tot} = \Delta E + E_{res}$ of the recoil particles plotted versus its energy loss ΔE in a gas chamber. See chapter 3.3 for a brief introduction to ERD.

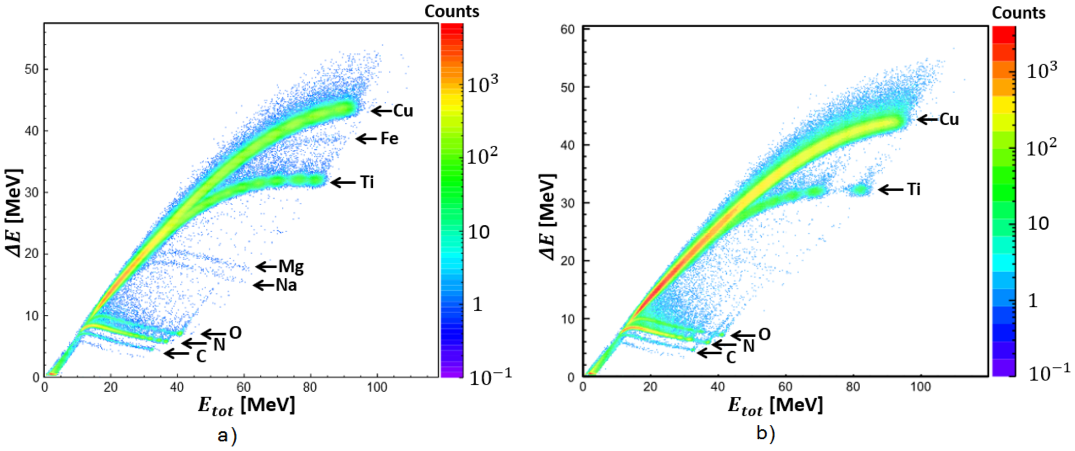

Figure 32: Element identification via ERD measurement using a $\Delta E - E_{res}$−detector telescope. **a)** Cu/Ti supermirror with target purities of 99.95 % for Cu and 99.6 % for Ti. Na, Mg and Fe were detected. Especially Fe is a critical impurity due to its magnetic properties.
b) Measurement of a Cu/Ti supermirror with target purities of 99.995 % for Cu and 99.999 % for Ti. Here no Fe is detectable. Both plots are corrected by the kinematic shift and represent the top ≈ 300 nm.

In figure 32 a) a neutron supermirror with m = 2 is shown that was produced with sputter targets of 99.95 % purity for Cu and 99.6 % for Ti. Several impurities, including iron, are detected. In figure 32 b), the target purities were 99.995 % for Cu and 99.999 % for Ti and no impurities are detectable.

The result shown in figure 32 can be explained by the production process of the Ti targets. Pure Ti can rarely be found in nature, it is mostly bound in titanium iron ore and has to be extracted. The most common process of extracting Ti from ilmenite ($FeTiO_3$) and rutile (TiO_2) is the so called Kroll process [137].

When both base materials are present, first the ilmenite is reduced to rutile by an arc and addition of carbon.

$$\mathrm{FeTiO_3} \rightarrow \mathrm{Fe} + \mathrm{TiO_2} + \mathrm{CO} \tag{5.1}$$

The iron can then be separated from the TiO_2, which is converted with chloride and coke to titanium tetrachloride at temperatures up to 100°C.

$$\mathrm{TiO_2} + 2\,\mathrm{C} + 2\,\mathrm{Cl_2} \rightarrow \mathrm{TiCl_4} + 2\,\mathrm{CO} \tag{5.2}$$

The pure $TiCl_4$ is then reduced to pure Ti under a protective gas atmosphere at high temperatures of about 900°C with addition of Mg or Na.

$$\begin{aligned} &\mathrm{TiCl_4} + 2\,\mathrm{Mg} \rightarrow \mathrm{Ti} + 2\,\mathrm{MgCl_2} \\ &\text{or} \\ &\mathrm{TiCl_4} + 4\,\mathrm{Na} \rightarrow \mathrm{Ti} + 4\,\mathrm{NaCl} \end{aligned} \tag{5.3}$$

In conclusion, the traces of Fe stem from natural contamination, whereas those of Mg and Na are caused by the production process.

From the ERD data no exact percentage of the Fe content in the Ti layers could be determined, as also all other materials, especially Cu, contribute to the overall composition that was measured. The datasheet of the target supplier claims impurities of 0.08 wt% Fe and 0.3 wt% of other elements (e.g. Mg and Na) for the Ti target with 99.6% purity.

All magnetic impurities can be avoided by using highly pure targets (99.995% for Cu and 99.999% for Ti). To achieve this degree of purity, Ti is produced by another procedure called Van-Arkel-de-Boer-procedure, where gaseous TiI_4 is separated at a glowing Wolfram wire under low pressure and high temperatures of about 800°C [138]. Following these results, only highly pure Ti and Cu targets were used to avoid depolarization of the neutron beam.

5.3 Roughness Investigations with X-rays

The surface roughness of one single layer has to be investigated and minimized first, to be able to keep roughness small even for multilayer structures. For neutron supermirrors in general the surface roughness of each deposited layer plays an important role for the overall reflectivity of the mirror. As we are working with neutron with wavelengths around 5 Å , a surface roughness of a few nm already causes a critical amount of diffuse scattering and therefore serious reduction of specular reflection of the mirror.

In general, smooth surfaces for single layers are achieved by sputtering at the lowest possible gas pressure, as interaction between sputtering gas atoms and vaporized target material is reduced. Another crucial aspect is the applied sputtering power. With increasing power, the deposition rate increases and deposited target atoms build up pyramids [106]. Therefore, the approach to find the optimal conditions is to vary the applied power and Ar working pressure using different sputtering modes [81].

The layer parameters like thickness and roughness were characterized at the X-ray diffractometers of the FRM II and the Movatec GmbH. Both X-ray sources are equipped with a monochromatic X-ray source with a wavelength of 1.54 Å (Cu $K_{\alpha 1}$), two apertures and an X-ray detector. The beam hits the surface under an angle of incidence Θ and is detected at 2Θ, which is typically drawn on the x-axis. The reflected intensity is shown on the y-axis. For Cu, the incoming waves are totally reflected up to a critical angle of 0.75°. For Ti, this critical angle of reflection is at 0.55° due to a smaller optical potential seen by X-rays. The X-ray samples shown in the following were deposited on 4 mm thick borofloat glass (substrate roughness $\approx 0.6 \pm 0.2$ nm), unless specified otherwise.

5.3.1 Single Surface Roughness

Figure 33 shows a measured X-ray reflectivity curve of a single Cu layer sputtered in PDC-mode with a power of 1 kW and at a working pressure of $5.4 \cdot 10^{-3}$ mbar, with an uncertainty of $\approx 2 \cdot 10^{-4}$ mbar from the baratron. The measured data is described well by the fit.

The Ar-flow was set to 9 sccm and the sample is moved underneath the magnetron at a speed of 10 mm/s. The sample passed the magnetron five times.

Table 4: Layer parameters of a Cu single layer sputtered in PDC-mode (1 kW). The thickness and roughness are optimized to fit the X-ray data in Figure 33.

Layer number	Thickness [nm]	Roughness [nm]	Rounds
1	87.80 ± 0.04	1.65 ± 0.02	5

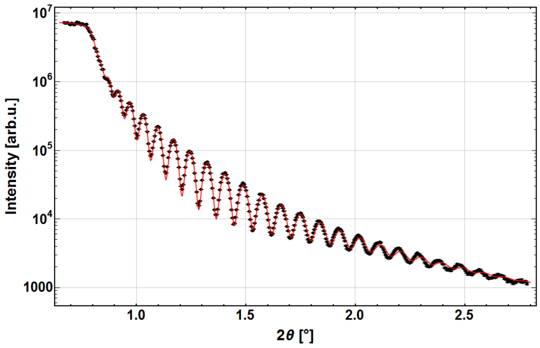

Figure 33: X-ray reflectivity spectrum with characteristic Kiessig fringes obtained from a thin Cu layer with thickness of 88 nm. It was produced in PDC-mode with a power of 1 kW. The measurement (black points) is described well by the fit (red curve).

Subtracting 0.6 nm for the average sample surface roughness leads to a roughness growth of about 0.12 Å/nm, which is too high for supermirror production. The fit results shown in table 4 yield a deposition rate of $\approx$ 17.5 nm per round at a power of 1 kW for Cu. This is also too high, as the thinnest layers for a Cu/Ti supermirror are in the range of 5 nm (for a m = 2 supermirror). Unfortunately, it is not possible to increase the speed of the holder to achieve a 5 nm thick layer, as this would put strain on the mechanical components and decrease the accuracy.

Therefore, the power at the magnetron was decreased for the next Cu sample. With the lower deposition rate we also expect roughness growth to decrease. Figure 34 shows the XRR of a Cu sample sputtered with the same parameters as before but with a power of 350 W. This is the lowest possible power to keep the plasma burning at stable conditions. The sample passed the magnetron four times. The values from the fit are shown in table 5.

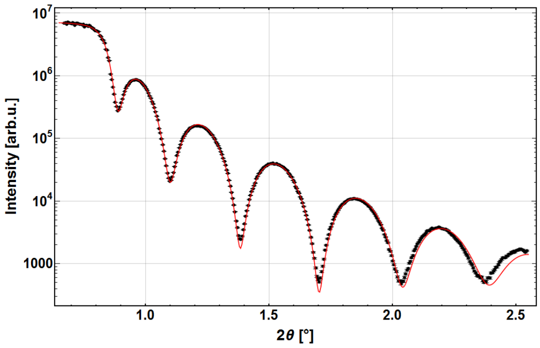

Figure 34: The XRR spectrum obtained from a Cu layer with a thickness of 23 nm. It was produced in PDC-mode with a power of 350 W. The measurement (black points) agrees well with the simulation (red curve).

Table 5: Layer parameters of a Cu single layer sputtered in PDC-mode (350 W).

Layer number	Thickness [nm]	Roughness [nm]	Rounds
1	23.48 ± 0.02	1.08 ± 0.04	4

The calculated roughness growth of about 0.2 Å/nm is even higher than before.

For Cu samples deposited in DC-mode, the deposition rate and roughness growth were determined analogously and found out to be even higher (roughness > 0.2 Å/nm at deposition rates of $>$ 8 nm/round, at 350 W).

All further attempts for Cu layers in DC- and PDC-mode to reduce the roughness growth via changing the gas pressure, the magnetron power and the bias voltage for in situ polishing did not improve the layer parameters.

The deposition of Cu in RF-mode on the other hand, resulted in significantly lower roughness as extracted from XRR measurements. In this mode, the Ar-flow was reduced from 9 sccm to 4 sccm, which corresponds to a chamber pressure of $1.9 \cdot 10^{-3}$ mbar and leads to a smoother arrangement of the atoms at the surface. Additionally, the whole plasma cloud is located much further away from the target's surface and the radiofrequency field causes some ions and electrons to be accelerated onto the substrate's surface. This results in a small in-situ polishing effect on the deposited surface. The sputtering power was set to 500 W and the speed of the substrate holder was kept at 10 mm/s. Figure 35 shows the result of the XRR measurement with the corresponding fit.

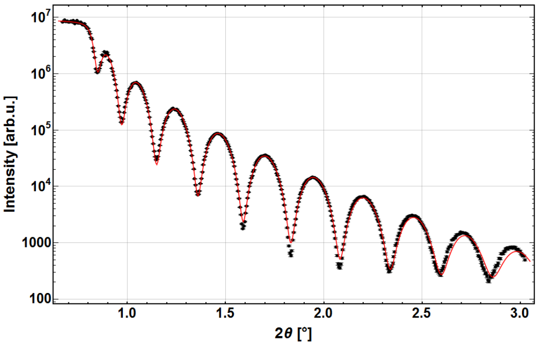

Figure 35: The XRR spectrum obtained from a 32 nm thick Cu layer deposited in RF-mode (500 W). The measurement (black points) agrees well with the simulation (red curve).

Table 6 presents the fit results for the Cu layer sputtered in RF-mode. The corresponding roughness growth of about 0.06 Å/nm is significantly smaller than for deposition in DC- and PDC-mode. This result was reproduced several times, so the RF-mode

Table 6: Layer parameters of a Cu single layer sputtered in RF-mode (500 W).

Layer number	Thickness [nm]	Roughness [nm]	Rounds
1	32.13 ± 0.02	0.803 ± 0.05	8

was chosen to deposit the Cu layers of the supermirrors.

For Ti, the effects of the sputter parameters on the roughness growth were investigated similarly. The lowest surface roughness growth for pure Ti was found using PDC-mode. The layer was deposited at 9 sccm Ar-flow at a working pressure of $5.4 \cdot 10^{-3}$ mbar and a power of 500 W, with no additional reactive gas or substrate bias voltage. Figure 36 shows the XRR spectrum of this sample and table 7 the values extracted from the fit.

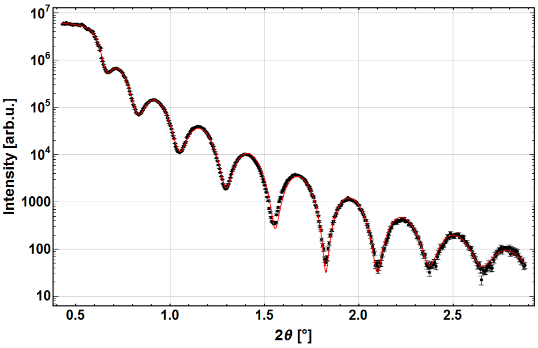

Figure 36: The XRR spectrum obtained from a pure 31 nm thick Ti layer sputtered in PDC-mode (500 W). The measurement (black points) agrees well with the simulation (red curve).

Table 7: Fitresult of a Ti layer sputtered in PDC-mode (500 W).

Layer number	Thickness [nm]	Roughness [nm]	Rounds
1	30.72 ± 0.03	1.22 ± 0.01	10

This corresponds to a roughness growth of about 0.2 Å/nm for the sample deposited in PDC-mode. These were the best results achieved for pure Ti.

In addition to the Cu and Ti surface analysis, I investigated how a bias voltage applied to the substrate affects the surface roughness growth of TiN_x layers. TiN_x is used as an interdiffusion barrier to the supermirror structure to increase reflectivity, as is discussed in chapter 5.4.

Figure 37 shows the roughness versus the bias voltage for ion plating for TiN_xx layers (Ti:N = 3.3 : 1). The six samples have the same thickness of 32 ± 0.5 nm and were sputtered under identical conditions (Ar-flow 9 sccm, N_2-flow 2 sccm, power 500 W).

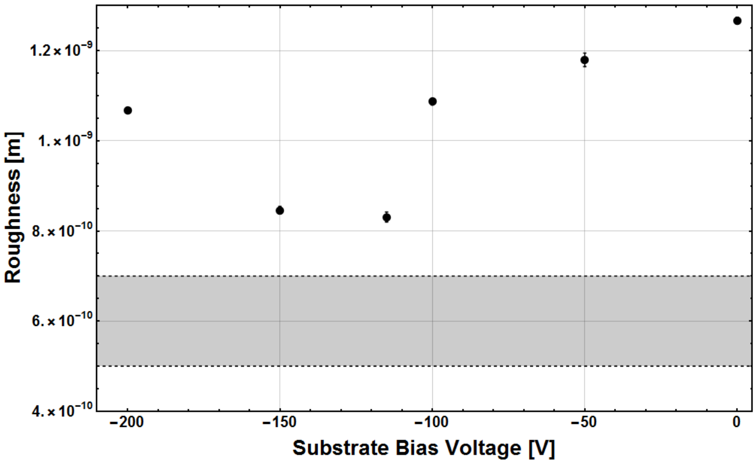

Figure 37: Surface roughness values of TiN_x single layers sputtered under the same conditions but with different substrate bias voltage (Power 500 W, Ar-flow 9 sccm, N_2-flow 2 sccm). All samples have a thickness of 32.5 ± 0.5 nm. The data points show a broad minimum in surface roughness from −150 V till −110 V. The grey region marks the typical surface roughness of our borofloat glass substrates. Taking the roughness of the substrate into account, the roughness of the TiN_x layer is decreased by a factor of three compared to sputtering without bias voltage.

It is clear, that applying an additional bias voltage to the substrate has a serious impact on the deposited layers. Subtracting the average substrate roughness of 0.6 nm leads to a surface roughness reduction by a factor of three, when comparing the sample without bias voltage and the sample with −150 V or −110 V. For bias voltages between −110 V and 0 V the ion energy is probably high enough to remove some rest gases from the surface, but not enough to flatten the surface actively. For voltages exceeding −150 V the energy of the Ar-ions is high enough to kick out material (here Ti/TiN_x) from the deposited material on the substrate. This effect is called re-sputtering and leads to an increase in surface roughness of the deposited layer and decreases the sputtering rate, as a certain amount of material is removed again from the layer directly after it was deposited [99]. In the region with minimum surface roughness, Ar-ions have enough energy to remove loosely bound particles, as well as flatten bumps, without causing re-sputtering. The result is a very smooth surface together with a sputtering rate, which is almost the same as without bias voltage.

Applying these results, it was further investigated how the surface roughness grows with thickness. Two samples with identical thickness of 165 nm were produced. The first one without bias voltage applied, the second one with − 150 V. The Ar and N_2-flow were 9 sccm and 2 sccm respectively. Figure 38 shows both XRR spectra in direct comparison. From the Kiessig fringes in figure 38 it can be seen, that applying an additional bias voltage for deposition of TiN$_x$ reduces the roughness growth drastically.

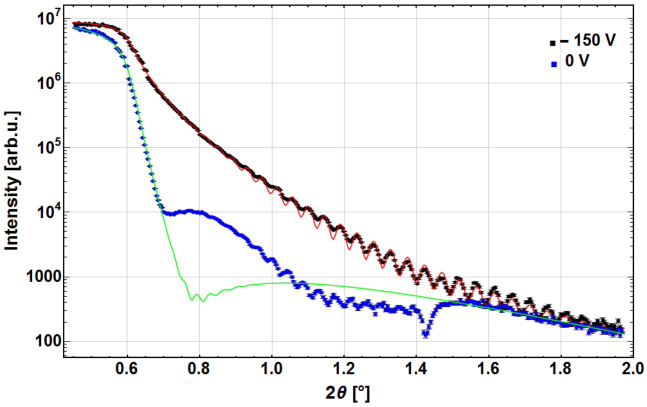

Figure 38: XRR spectra of TiN$_x$ samples with and without bias voltage. The fit for the sample with bias voltage agrees well with the data and yields a layer thickness of 167 ± 1 nm and a roughness of 2.15 ± 0.03 nm. For the sample without bias voltage the surface roughness is too high to perform a reliable fit, as the routine is only valid up to approximately 4 nm. The second fit corresponds to a thickness of about 165 nm and a roughness of 6.5 nm.

The steep decrease of X-ray reflectivity for the sample deposited without bias voltage is caused by high surface roughness of more than 6.5 nm. An additional transition layer of approximately 7 nm causes the difference between the measured and the calculated curves. Such a roughness value for a layer thickness of 165 nm would result in unacceptable high roughness values for neutron supermirrors, as they consist of approximately 1 µm TiN$_x$ plus 1 µm Cu. The increased diffuse scattering would lead to a low specular reflectivity, as is seen in chapter 5.4.2. The fit to the sample sputtered with applied bias voltage yields a thickness of 167 nm and a roughness of 2.15 nm. Subtracting 0.6 nm for the average sample surface roughness leads to a roughness growth of only 0.09 Å/nm, assuming linear roughness growth.

Table 8 summarizes the sputtering parameters and conditions, with which the lowest surface roughness values were achieved.

Table 8: Sputter parameters for the deposition of Cu and Ti layers with minimized surface roughness.

	Dep. mode	Ar-flow [sccm]	Working pressure [mbar]	Bias voltage [V]
Cu	RF (13.56 MHz)	4	$1.9 \cdot 10^{-3}$	0
Ti	PDC (50 kHz)	9	$5.4 \cdot 10^{-3}$	– 150

5.3.2 Influence of Multilayer Roughness

To investigate interface roughness growth, stability of machine parameters and reproducibility, several multilayer structures of Cu/Ti were sputtered. Three of them are presented here as an example. Sample 1 was sputtered without applying additional bias voltage and consists of a five layer structure (TiN_x (13 nm) / Cu (10 nm) / TiN_x (13 nm) / Cu (10 nm) / TiN_x (13 nm)). The layer sequence of sample 2 is equivalent to sample 1, but the TiN_x layers were sputtered with an additional bias voltage of −150 V, in order to investigate the roughness minimization via in situ polishing. Sample 3 consists of a monochromator, meaning a layer structure of 40 double layers of Cu (6.9 nm)/TiN_x (6.6 nm). For the sputtering parameters see appendix B.2.

The XRR spectra of sample 1 and 2 are shown in figure 39 together with the fitted curves.

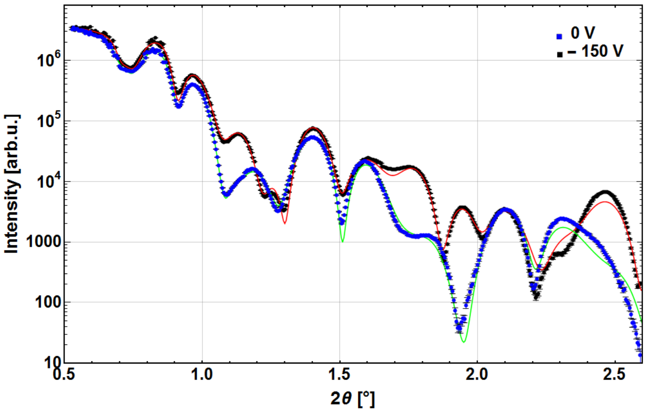

Figure 39: XRR spectra of a five layer structure without bias voltage (Blue), with additional bias voltage of −150 V (Black) and its fitted curves. The fit results are listed in table 9.

In table 9 the layer parameters for samples 1 and 2 are listed, showing only slight differences in the layer thicknesses of the structures. The roughness of both samples is compared in figure 40, showing significantly higher roughness growth for sample 1, which was produced without additional bias voltage.

For sample 1, the roughness visibly grows from one TiN_x-layer to the next, whereas for Cu the surface is even polished. When calculating the roughness growth from layer 1 to 3 we get 0.4 Å/nm and for layer 3 to 5 0.3 Å/nm, which coincides well with the average roughness growth of 0.36 Å/nm extracted from the XRR measurement of the TiN_x layer deposited without bias voltage (figure 38).

The slightly thicker first layer of sample 2 can be explained by the fact, that the sample was located too close to the magnetron during plasma cleaning of the target and was already coated with ≈ 2 nm of TiN_x. For sample 2, a top layer roughness of

Table 9: Layer parameters of a Cu/Ti five layer structure without and with additional bias voltage of −150 V when sputtering TiN_x.

Sample 1 (0 V)	Material	Thickness [nm]	Roughness [nm]
1	TiN_x	12.8 ± 0.2	0.6 ± 0.05
2	Cu	10.4 ± 0.04	0.5 ± 0.07
3	TiN_x	12.6 ± 0.04	1.0 ± 0.08
4	Cu	10.4 ± 0.04	0.9 ± 0.05
5	TiN_x	13.0 ± 0.05	1.3 ± 0.03
Sample 2 (−150 V)	**Material**	**Thickness [nm]**	**Roughness [nm]**
1	TiN_x	14.9 ± 0.1	0.5 ± 0.06
2	Cu	9.4 ± 0.2	0.5 ± 0.06
3	TiN_x	13.3 ± 0.03	0.3 ± 0.07
4	Cu	9.7 ± 0.2	0.6 ± 0.05
5	TiN_x	13.7 ± 0.04	0.7 ± 0.03

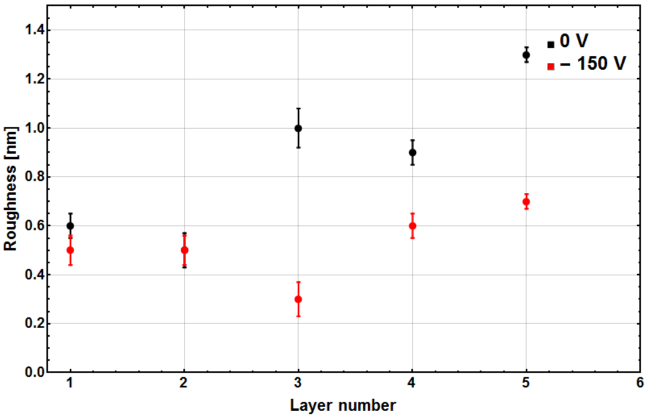

Figure 40: Roughness obtained from fits to XRR data of Cu/Ti multilayers with five layers, produced without and with bias voltage. Without bias voltage, each Ti layer (1, 3, 5) shows a significant roughness increase, whereas Cu (2, 4) even shows a small polishing effect (See layers 2, 4). With additional bias voltage, roughness is kept near substrate level for the whole structure.

only 0.7 ± 0.05 nm was obtained (total thickness 61 nm), which is in the same range as the glass substrate roughness.

Sample 3 is a monochromator consisting of 80 single layers of Cu/Ti. Like sample 2, it was produced with reactive sputtering of Ti with 2 sccm N_2 and additional bias voltage of −150 V. With these parameters, it is possible to produce mirrors with many layers keeping the interlayer roughness at a low level. The XRR spectrum and the corresponding fit are shown in figure 41.

For the fit, it was assumed, that all Cu layers and all TiN_x layers respectively have the same thickness. Therefore, there is only one thickness and one roughness value

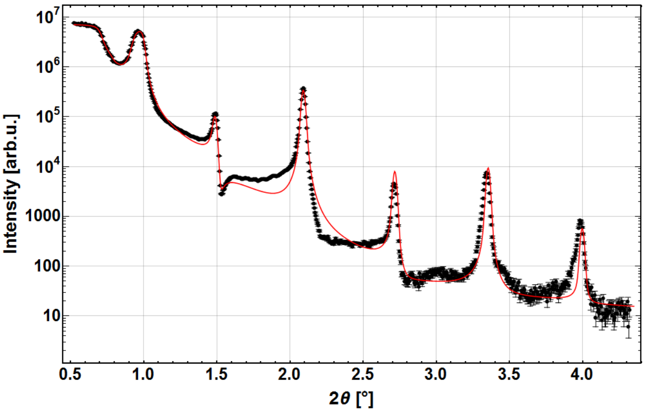

Figure 41: XRR spectrum of a Cu/Ti monochromator (40 double layers of Cu = 6.9 nm and TiN_x = 6.6 nm) with additional bias voltage of −150 V during sputtering of TiN_x. For the fit in red, the thickness and roughness values were averaged over all Cu and TiN_x layers. With this technique, the roughness growth is minimized at least for the first 100 layers.

for Cu and TiN_x. We obtain a thickness of 6.59 ± 0.1 nm for the Cu layers and 6.87 ± 0.1 nm for the TiN_x layers. The two roughness values are 0.91 ± 0.02 nm for Cu and 0.69 ± 0.02 nm for TiN_x, both of which are very low for a multilayer system of 80 layers and a total thickness of approximately 540 nm. This result shows that both, interdiffusion and interlayer roughness growth, can be kept at a very low level using reactive sputtering with additional bias voltage.

Several other Cu/TiN_x supermirrors have been studied under XRR, but did not result in reasonable fits, as their surface roughness exceeded 3 nm.

5.4 Neutron Supermirror

The overall performance of a neutron supermirror is mainly influenced by the strongly correlated parameters interlayer roughness, interdiffusion and crystal growth. Only by an optimized interaction of all three parameters, meaning minimized interdiffusion and interlayer roughness as well as preferably only one crystal orientation per material, supermirrors with high neutron reflectivity can be produced. Unfortunately, tuning one parameter after another is not possible due to the strong correlation. For example, reactive sputtering of Ti with nitrogen forms effective interdiffusion barriers and increases the neutron reflectivity of a mirror [133]. But the added nitrogen can also increase the crystal growth in random orientations, which leads to a stronger roughness growth and therefore a lower reflectivity again. For the optimization process of our supermirror coatings neutron reflectometry, ERD, XRR and XRD were used.

5.4.1 Influence of Impurities

In the previous chapters reactive sputtering of Ti with N_2 was used to optimize the roughness of single and multilayers. The influence on our neutron supermirrors was investigated by neutron reflectometry using the TREFF instrument at the FRM II with a neutron wavelength $\lambda = 4.8\,\text{Å}$. The x-axis of the reflectivity measurements can be transformed to momentum transfer by the relation $q = 4\pi \sin(\Theta)/\lambda$. Figure 42 shows the neutron reflectivity of three monochromators, deposited with different N_2 flow. With increasing N_2 flow $0 - 2\,\text{sccm}$ during Ti deposition, an increasing reflectivity was observed.

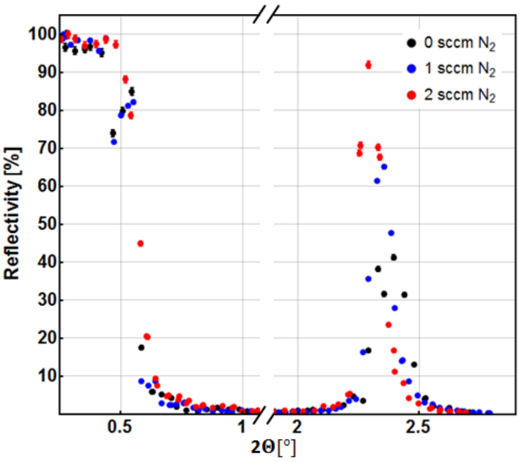

Figure 42: Neutron reflectivity of three Cu/Ti monochromators (40 double layers of Cu$=$ 6.9 nm and TiN$_x =$ 6.6 nm) sputtered with different N_2 flows for Ti. Total reflection is present up to 0.5°. Between 0.8° and 2.1° the reflectivity drops to zero as neutrons are not reflected by the mirror. For this layer sequence, constructive interference appears around 2.4°.

We obtain different shapes for the monochromator's interference peaks in terms of height and width, dependent on the varying N_2 flow during sputtering. We explain these results by the two effects interdiffusion and interlayer roughness, which have very similar impact on the neutron reflectivity and cannot be distinguished with this measurement method. The high neutron reflectivity above 90 % and the smallest peak width of the monochromator sputtered with 2 sccm N_2 indicates, that both interlayer roughness and interdiffusion are the lowest for this sample. The broadening of the interference peak for lower reactive gas flows is caused by an increasing amount of diffuse scattered neutrons. The shift to higher angles of Bragg reflection, that we obtain for 0.5 sccm and 1 sccm is explained by an effectively thinner layer "seen" by the incoming neutrons, when high interdiffusion is present.

Following these results, a supermirror was produced with a N_2 flow of 2 sccm and showed high neutron reflectivity besides a dip at 0.7° due to a missing Cu top layer. The supermirror as well as the monochromators were deposited with low purity targets of 99.95 % for Cu and 99.6 % for Ti. Figure 43 shows the neutron reflectivity of this supermirror. It was confirmed, that it is possible to produce a neutron supermirror with m ≈ 2 with Cu/Ti and additional reactive sputtering.

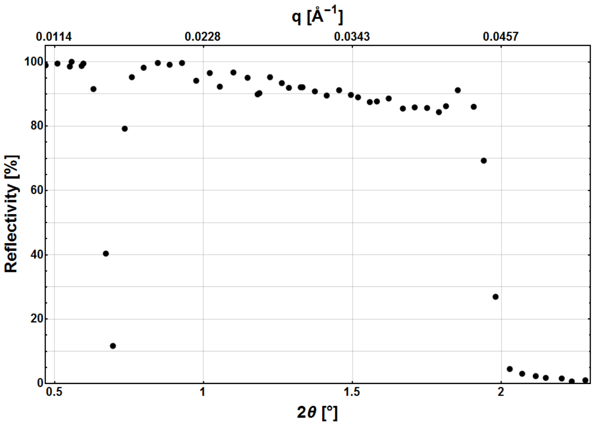

Figure 43: Reflectivity curve of a Cu/Ti (purity Cu 99.95%, Ti 99.6%) neutron supermirror with $m = 1.95$, measured at the TREFF spectrometer with a neutron wavelength of 4.8 Å. Cu was sputtered in RF mode with a power of 500 W. Ti was sputtered reactively with a power of 500 W and an additional N_2 flow of 2 sccm.

To determine the N_2 content, we used ERD and complementary the more easily accessible XRD technique. With XRD it is also possible to determine the crystal orientations inside the coatings. Figure 32 a) (page 45) shows the measurement with the $\Delta E - E_{res}$-detector telescope. Using that dataset and the computer code KONZERD [122], the $E - \Delta E$-spectrum is projected on the energy axes and a depth profile is calculated, which shows the layer structure. This depth profile includes all elements contained in the supermirror shown in figure 44.

From layer number 3, 5 and 7, the Ni:Ti ratio was evaluated to be $\approx 1 : 3.3$. With ERD measurements, it is possible to calibrate any sputter facility to get the right nitrogen ratio and reproduce the results anywhere, where reactive sputtering is possible. The statistical uncertainty for the concentration measurement is below 1%. The ERD measurement also gives insight to what happened during the production and helps to explain the neutron reflectivity, which is shown in figure 43. The ERD measurement shows, that the Cu top layer is missing completely and the second Cu layer is too thin, which results in a drastic dip of reflectivity. Noticeable is also, that the top Ti layer is almost completely oxidized, up to a depth of ≈ 10 nm. Furthermore, hydrogen

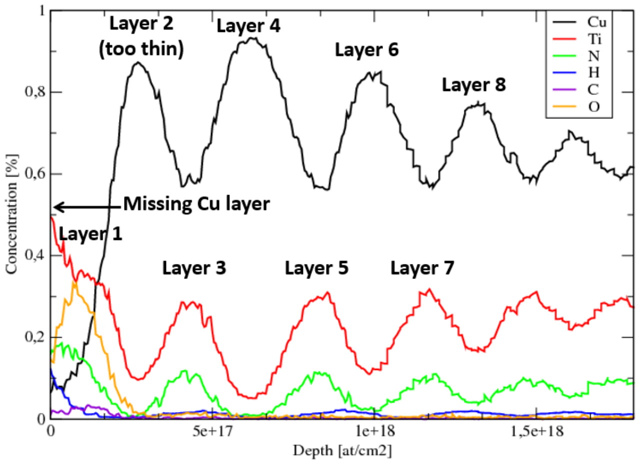

Figure 44: Depth-resolved element analysis of a Cu/Ti m = 2 neutron supermirror from ERD detection. Ti was sputtered reactively with a N_2 flow of 2 sccm resulting in a ratio N:Ti of 1 : 3.3. The top ≈ 300 nm are shown, given in atoms/cm^2.

from the surface is penetrating up to the middle of the layer (≈ 3 nm). On a side note, the ERD measurement only shows the top ≈ 300 nm of the supermirror (2 µm total thickness), with decreasing accuracy in depth. The depth resolution of the measurement setup is about 10 nm at the surface and therefore insufficient to evaluate the interdiffusion of the layers (for comparison, the thickest Ti layer is only 12 nm).

The nitrogen content can also be evaluated via XRD. From the XRD measurement one gets the intensity of refracted X-rays depending on the angle of diffraction. This spectrum shows the peaks respective of the crystal planes and their orientation. To determine the peak positions and to verify the crystal phases within the material, a linear combination of Lorentzian functions was used. The model for fitting the data is a linear combination of the form

$$\begin{aligned} \text{Model} &= \sum_{i=1}^{n} g(x_i, a_i, \mu_i, \sigma_i) + B \\ \text{with} \quad g(x, a, \mu, \sigma) &= \frac{a}{1 + \frac{(x-\mu)^2}{\sigma^2}} \end{aligned} \tag{5.4}$$

with an additional background parameter B. Here a is the peak amplitude, μ is the peak position, σ describes the peak width, x is the actual angle and n the number of diffraction peaks.

The position of the TiN_x peak from the (111) plane is strongly dependent on the amount of nitrogen built in the Ti layers during the sputtering process and therefore a precise, reproducible and clearly defined nitrogen content can be determined from the data. Figure 45 shows the XRD spectrum of a pure Ti target 99.999 % and table 10 lists the peak positions.

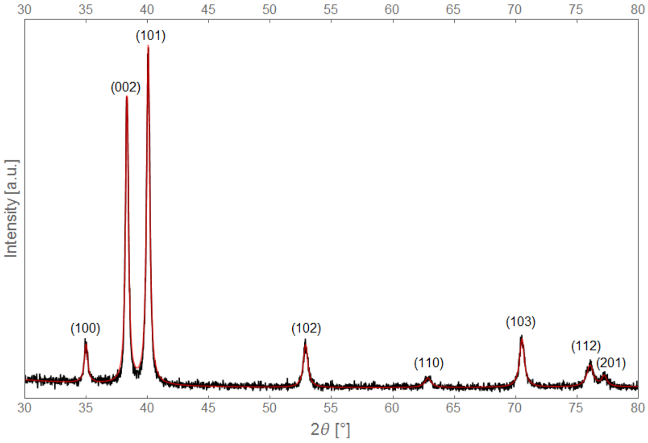

Figure 45: XRD spectrum of a Ti-target with purity of 99.999% measured at an angle of incidence of 2°.

Table 10: Width and position of each peak shown in figure 45 are listed with their standard error.

Index	$\mu[°]$	$\sigma[°]$
1	34.985 ± 0.005	0.163 ± 0.008
2	38.321 ± 0.001	0.1362 ± 0.0009
3	40.052 ± 0.001	0.1514 ± 0.0009
4	52.880 ± 0.006	0.217 ± 0.008
5	62.84 ± 0.03	0.31 ± 0.04
6	70.510 ± 0.005	0.235 ± 0.007
7	76.06 ± 0.01	0.32 ± 0.02
8	77.22 ± 0.02	0.26 ± 0.04

By comparing this XRD spectrum with the spectrum in figure 22 (page 34) (taken from [119]), the peaks for the different phases were identified. A detailed XRD peak analysis is a complex topic, as the peak intensities depend on many contributing factors, like the material specific multiplicity factor, the Debye-Waller factor, the volume of one unit cell and reflecting power, only to mention a few. Some of these parameters would need separate measurements and evaluations, which is beyond the scope of this thesis. The procedure of a detailed peak analysis can be found in [139–141].

Figure 46 shows the XRD analysis of TiN_x single layers with a thickness of $\approx 300\,\mathrm{nm}$ produced with different N_2 flows. The diffraction peak of pure Ti[002] at an angle of 38.321° shifts to TiN[111] peak at 37.188°. We note that the reactively sputtered layers consist of a composition of only two crystal phases, which is favorable in terms of roughness control. These are the Ti[002] and the TiN[111] phase.

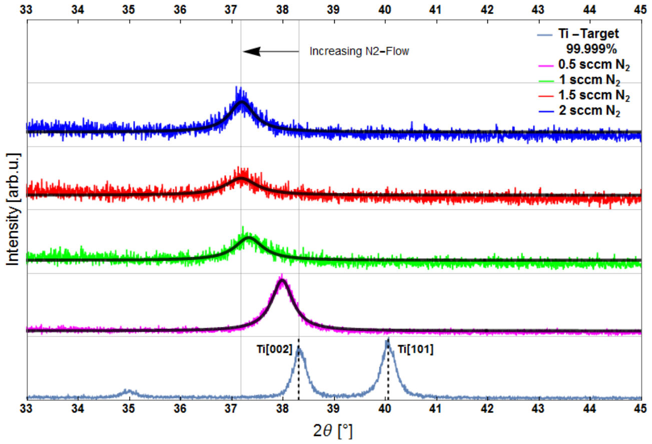

Figure 46: XRD measurement of TiN_x single layers with a thickness of ≈ 300 nm. The peak of pure Ti[002] clearly shifts towards the TiN[111] peak with increasing nitrogen flow during deposition. The fit results for the peak positions are presented in table 11. The samples were sputtered using a Ti-target with purity a of 99.6% at a working pressure of $5.4 \cdot 10^{-3}$ mbar, a power of 500 W and different nitrogen flow (given in sccm).

Table 11: XRD peak positions of TiN_x single layers with 300 nm thickness.

Nitrogen Flow [sccm]	Peak Position	SE
0	38.321	0.001
0.5	37.978	0.003
1	37.326	0.020
1.5	37.173	0.031
2	37.187	0.015

This result shows, that a transition of phases can be achieved by varying the nitrogen flow during deposition of the layers and gives a qualitative impression of the amount of nitrogen built into the layers.

Therefore, XRD offers a way to check for layer composition and impurities. Figure 47 shows the XRD measurement of a Cu/Ti m = 2 supermirror (target purity 99.95% for Cu and 99.6% for Ti) and from 2020 (target purity 99.995% for Cu and 99.999% for Ti) in comparison.

The main peaks (Cu[111]) differ significantly in intensity, due to the missing top Cu layer (≈ 70 nm) of the 2017 supermirror. Looking at Table 12 it can be noticed, that the positions of the Cu[111]-phase are identical within the uncertainty. The Cu[200] peak is inconsistent within the uncertainty, which could be explained by the lower purity of the 2017 targets, as impurities and defects can change lattice parameters

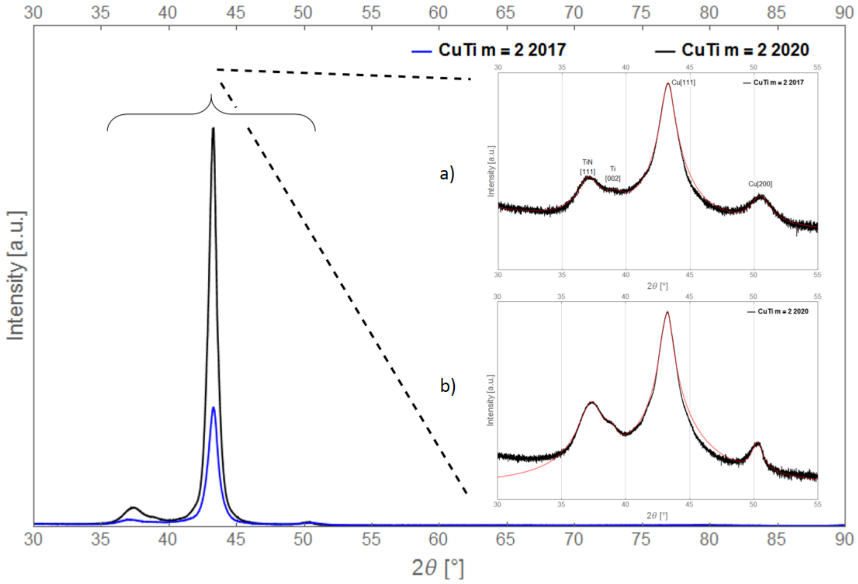

Figure 47: XRD spectra of the two Cu/Ti neutron supermirrors with m = 2 with the highest achieved neutron reflectivities. The target purities of the 2017 supermirror were 99.95% for Cu and 99.6% for Ti, and those for the 2020 supermirror were 99.995% for Cu and 99.999% for Ti. In a) and b) the intensity is plotted on a logarithmic scale. The positions of the main peaks are shown in table 12.

Table 12: XRD peak positions of Cu/Ti neutron supermirrors produced in 2017 and 2020 with different target purities.

	2017		2020	
	Peak Pos.	SE	Peak Pos.	SE
TiN[111]	37.090	0.009	37.337	0.010
Ti[002]	39.043	0.036	38.840	0.034
Cu[111]	43.2620	0.0002	43.279	0.001
Cu[200]	50.500	0.013	50.250	0.029

and therefore shift the peaks. For the Ti[002] peak the same argument applies. The shift of the TiN[111] peak is due to the change in the amount of nitrogen in the layer. By adjusting the N_2 content in the Ti layers, effective interdiffusion barriers can be produced, but if the amount of nitrogen is too high, an increasing roughness growth from layer to layer is causing diffuse neutron scattering.

The effect of diffuse neutron scattering was also observed for supermirrors sputtered without reactive gases. Here, the diffuse scattering of the neutrons is explained by an increased interdiffusion. The reflectivity was measured using the position sensitive detector at TREFF. Figure 48 compares the detector images of two supermirrors. The left side shows the neutron reflectivity of a supermirror sputtered without implementation of N_2 and the detector image at $2\Theta = 1.56°$, where diffuse scattering is present. The right shows the neutron reflectivity and detector image of a supermirror sputtered with the optimal N_2 content.

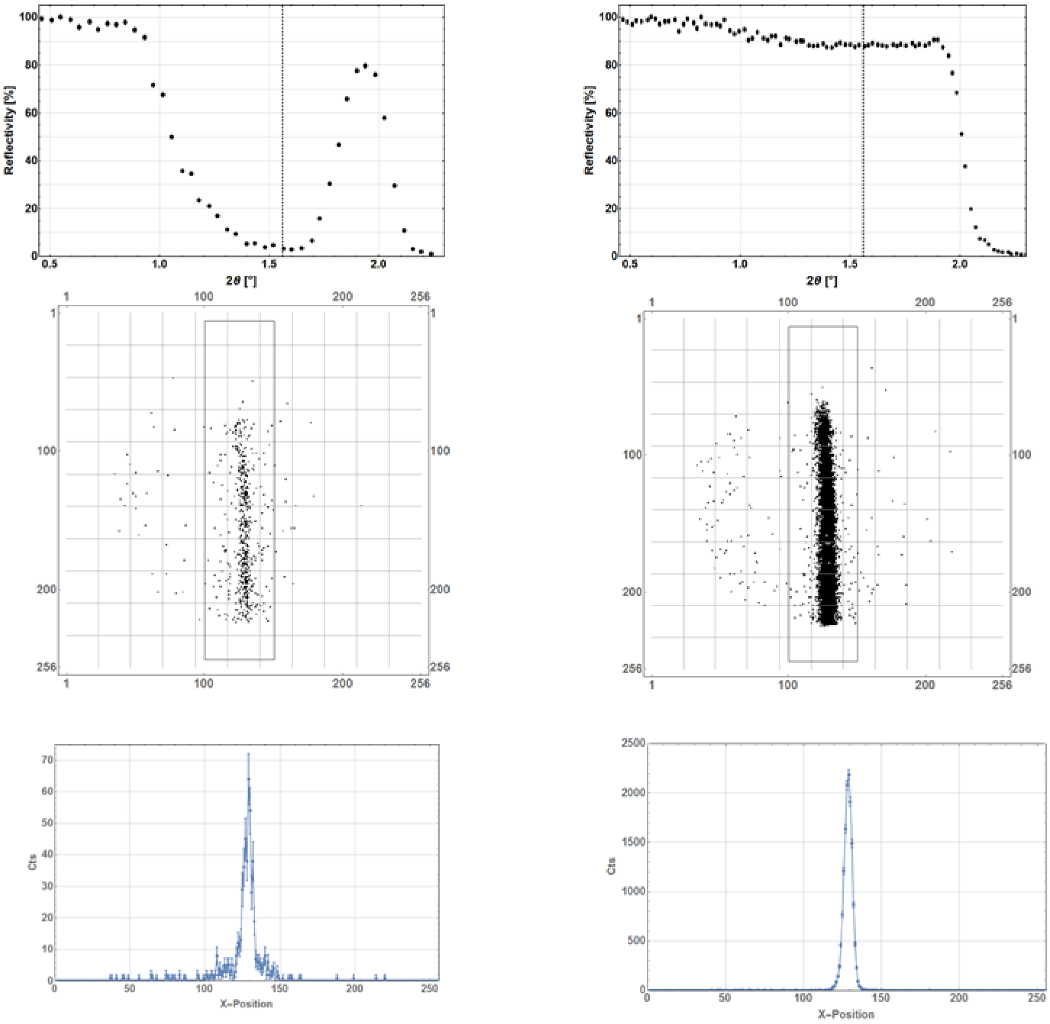

a) b)

Figure 48: Recorded detector images at an angle of incidence of $2\Theta = 1.56°$ for two different Cu/Ti m = 2 neutron supermirrors. The rectangle marks the signal window of the detector, on which the neutrons are reflected specularly. a) Example of a Cu/Ti supermirror with high interlayer roughness. Cu and Ti were sputtered in metallic mode (without N_2) and with additional bias voltage. The ratio of specular to diffuse reflection is low and the neutron reflectivity was $\approx 4\,\%$. b) Example of a Cu/Ti supermirror with low interlayer roughness. The mirror was sputtered with N_2 for TiN_x layers and additional bias voltage. The signal to noise ratio is quite high and the neutron reflectivity is $\approx 88\,\%$.

The rectangle in figure 48 defines the region of specular reflection at the detector, used to determine the ratio of specularly to diffusely reflected neutrons. Considering perfect specular reflection, every neutron reflected from the supermirror should be detected in this window (Channels: $100 < x < 150$; $5 < y < 250$). The ratio of counts inside the window to the rest of the detector is $\approx$ 14 for figure 48a) and $\approx$ 121 for figure 48b). The difference is almost a factor of 10, which is a clear indication of the negative influence of the interlayer roughness to the neutron reflectivity.

By using bias sputtering for in-situ polishing, the interfaces could be smoothened and several m = 2 Cu/TiN$_x$ supermirrors with constantly high reflectivity values, but without the magnetic impurities were produced. Figure 49 shows the resulting reflectivity curves for these mirrors. Cu was sputtered in RF mode with a generator power of 500 W and a pressure of $1.9 \cdot 10^{-3}$ mbar. Ti was sputtered in PDC mode reactively with an additional N$_2$ gasflow varying from 1.5 - 2.3 sccm at a pressure $5.4 \cdot 10^{-3}$ mbar and a power of 500 W. A negative bias voltage of 150 V was applied during production of the TiN$_x$ layers.

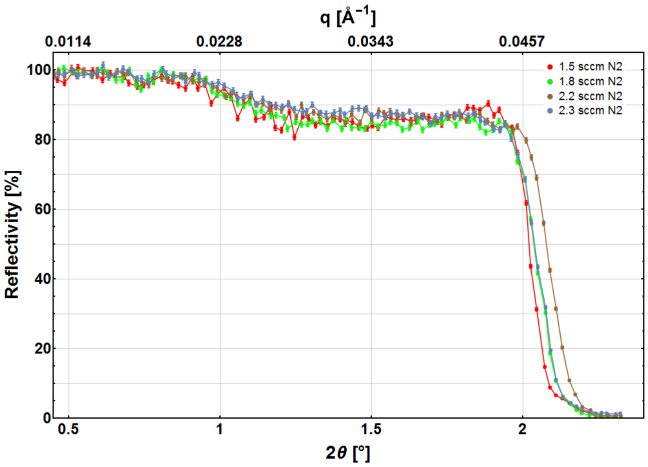

Figure 49: Neutron reflectivity curves for m = 2 Cu/Ti supermirrors sputtered with different additional N$_2$ gasflow and with highly pure target materials. The reflectivity is affected by the amount of nitrogen. The data points are joined for better visualization.

Figure 50 shows the reflectivity of the neutron mirror with highest reflectivity achieved in 2017 with low target purities and the best one produced in 2020 with high purity targets, additional N$_2$ gasflow of 2 sccm and a substrate bias voltage of -150 V for TiN$_x$ layers.

Comparing the curves it can be seen, that the drop due to the too thin Cu layer can be be eliminated completely by depositing the right layer sequence and thicknesses. Also

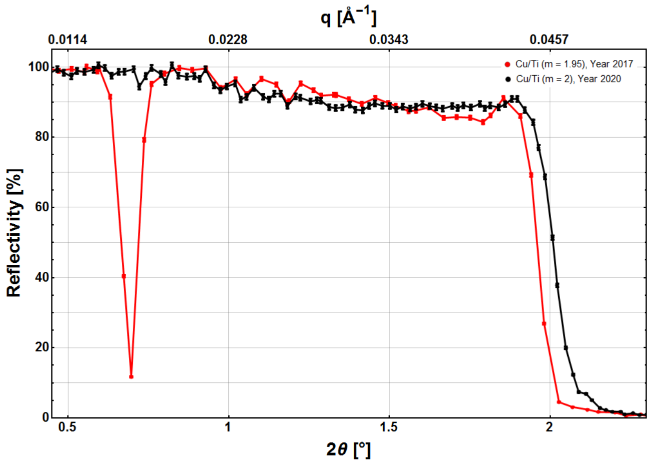

Figure 50: The reflectivity curve of the neutron mirror with the highest achieved neutron reflectivities from 2017 (from Fig. 43) and from 2020. The target purity was increased for Cu from 99.95% to 99.995% and for Ti from 99.6% to 99.999%.Both supermirror were produced by reactive sputtering of Ti with 2 sccm N_2 and the 2020 supermirror with additional -150 V bias voltage for TiN_x layers. The data points are joined for better visualization.

the critical angle of reflection of the 2020 mirror is about 0.05° higher and matches the theoretical value of the $m = 2$ layer sequence very well. It has a reflectivity above 90 %, making it the best Cu/Ti supermirror, which has so far been produced.

5.4.2 Heat Treatment and Long-term Stability

Cu has a high diffusion mobility and, if heated, may diffuse into the Ti layers through the barrier formed by the TiN_x [142, 143]. As the warm bore of the PERC instrument will be baked in order to reach the vacuum requirements, this includes the supermirror. The temperature has to be at least 80 °C for over 24 hours to clean the internal surfaces and remove residual rest gases from the instrument.

In a series of test measurements, the sample was first baked in a vacuum oven ($p \approx 5 \cdot 10^{-3}$ mbar) at 80° C for 12 hours. Then its reflectivity was measured. Afterwards, the sample was baked at 100°C for 12 hours and measured again. This procedure was repeated for temperatures of 80°C, 100°C, 150°C, 200°C, 300°C. Figure 51 shows the neutron reflectivity curve of the Cu/Ti supermirror with $m = 2$, consisting of 190 layers, after each baking.

A significant drop in reflectivity was expected, especially for high angles of incidence where the crucial layers get thinner, but the reflectivity barely decreases. After baking the sample at 200° C, the reflectivity only decreased by maximally 5 %. Even after

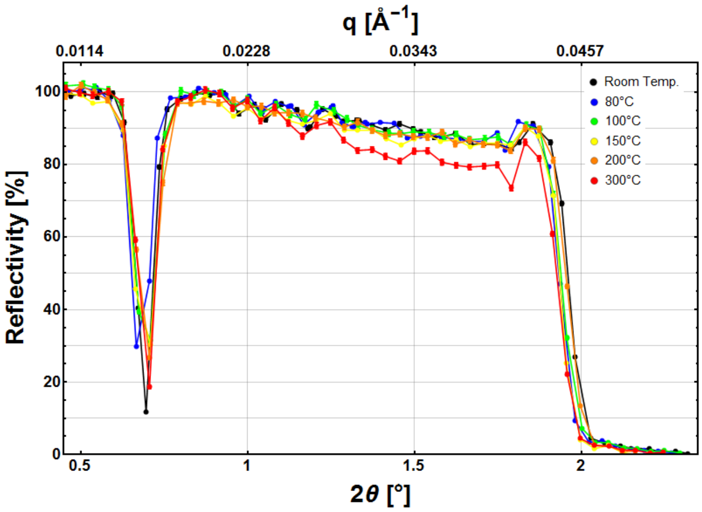

Figure 51: Reflectivity curves of Cu/Ti (m = 1.95, from Figure 43) measured at TREFF reflectometer with a neutron wavelength of 4.8Åafter different baking temperatures. The supermirror coating is highly temperature resistant, as the reflectivity shows only small decrease up to 200°C and even after 300°C it decreases only ≈ 7%.The data points are joined for better visualization.

baking the mirror at 300° C, the reflectivity decreased only ≈ 7 % compared to room temperature. The coating itself was optically not influenced and the mirror was still sticking on the glass substrate. This proves, that the neutron guide can be baked out up to at least 100° C without any losses in neutron reflectivity.

After the analysis in chapter 5.4.1, highly pure targets (Cu 99.995%, Ti 99.999%) were used for sputtering, as the others showed magnetic impurities, which would cause depolarization inside PERC.

To be sure, that the supermirrors produced with the new targets are also heat resistant on the level of interest, one mirror was baked for 48 h at 100° C in the vacuum oven. Figure 52 shows the neutron reflectivity curve before and after baking. The comparison shows no change in reflectivity, which means that the new mirrors are also suitable for the application in PERC.

Another important factor is the time stability of the supermirror coating. Therefore, the reflectivity of the supermirror produced in 2017 was measured again almost three years later. The mirror shown in figure 51, which had already been baked once at 300° C for 12 h, was measured again in 2020. The resulting reflectivity curve is shown in figure 53.

The direct comparison shows only very small changes in reflectivity. This proves the stability of the supermirror coating for at least three years even after a heat treatment at 300° C. The slight tendency towards higher reflectivity values could be explained

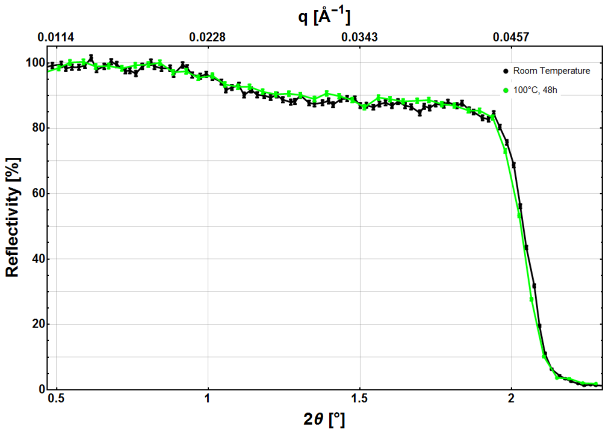

Figure 52: The reflectivity curve of a m = 2 Cu/TiN$_x$ supermirror produced in 2020, before and after 48 h of baking at 100°C. There is no noticeable change in reflectivity. The data points are joined for visualization.

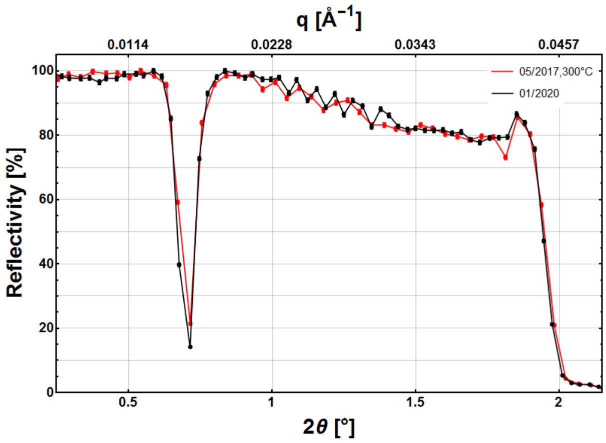

Figure 53: Reflectivity measurements of a Cu/Ti m = 1.95 supermirror, which had been baked at 300° C for 12 h in 2017 and 2020, two years and eight months later. The measured angles of the 2020 measurement were corrected by 0.05° due to misalignment of the reflectometer. There is no significant decrease in reflectivity after nearly three years of storage at room temperature and in atmosphere. The data points are joined for visualization.

by small chemical changes in the interlayers by forming energetically more favorable bonds, which smoothed the interfaces and therefore lead to higher reflectivities at some angles (e.g. at 1.8°).

5.4.3 Roughness Growth Model

In practice, it is impossible to produce perfectly smooth layers without any interdiffusion. In order to be able to produce supermirrors with higher m-values, it is necessary to understand the process of roughness growth during production. In her thesis, N. Rebrova [8] developed a model, which was expanded within this work. The present a model describes the roughness growth inside our supermirrors precisely. Here, the roughness of the i-th layer is given by:

$$r_i = r_{\text{sub}} + r_{\text{diff}} + r \cdot \left(\frac{d_i}{d_{\text{tot}}} \right)^p , \tag{5.5}$$

where r_{sub} is the roughness of the glass substrate, r_{diff} is the diffusion roughness, r is the roughness accretion, d_i and d_{tot} are thicknesses of the i-th layer and all layers below respectively and p is the power of roughness growth ($p = 0.5$ corresponds to purely statistical roughness growth).

$p = 0.5$ is the case for purely statistical roughness growth, as it is the case for sputtering without ion plating. By applying an additional substrate bias voltage, the Ar ions a accelerated onto the substrate's surface, which results in an in-situ polishing and consequently $p > 1$.

The roughness growth model in Equation 5.5 was implemented to the fitting routine Supermref and used to determine the roughness growth for our Cu/Ti neutron supermirrors. A double sided decaying exponential describes the diffusion roughness. The interface roughness is the standard deviation of a Gaussian function, folded over the step functions of the neutron optical potentials. The supermirror with the highest achieved neutron reflectivity (produced in 2020) is shown in figure 54 together with the fitted curve.

The input parameters for the fitting routine are the sputtering parameters of Appendix B.1, the glass roughness (0.8 nm) and the background (10 Counts). Table 13 shows the fit results of the free parameters.

The actual roughness values dependent on the layer number in the supermirror are shown in figure 55.

The surface roughness is building up from layer to layer, but with a total roughness at the top of ≈ 4 nm (consisting of $r_{\text{sub}} + r_{\text{diff}} + r$) it is still very small, when taking into account that the total thickness of the coating is ≈ 2 µm. The exponent of the roughness growth is slightly above one, which means that the roughness is growing slower during the first layers and tending to grow faster with increasing thickness.

The roughness of 1.6 nm for the first layers of the supermirror is a little bit higher than expected. One possible explanation is, that a thin metal layer is needed on

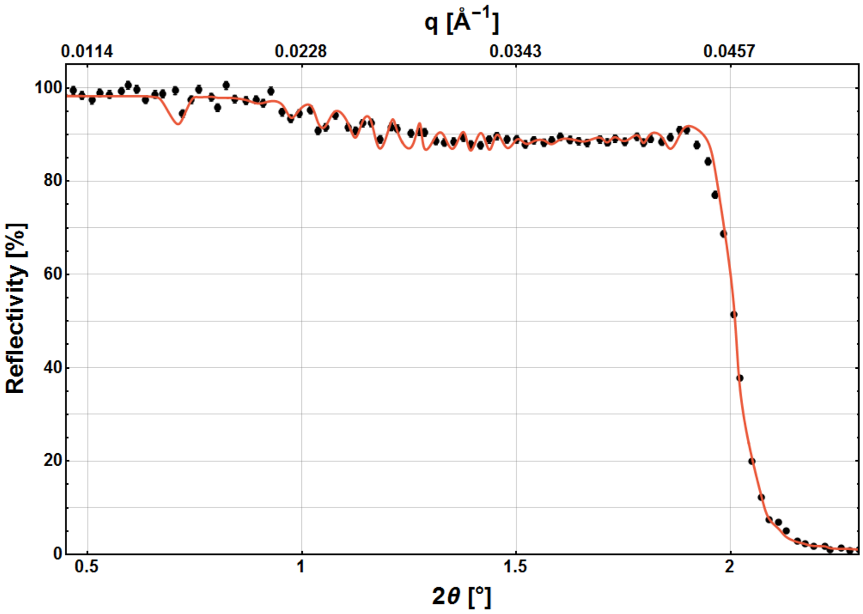

Figure 54: Neutron reflectivity measurement of a m = 2 CuTi neutron supermirror with a reflectivity above 90% and the corresponding fit. Given the systematic uncertainties which are not considered in the model like variation of single layer thicknesses and the missing experimental resolution in the model, the agreement is reasonable despite a reduced χ^2-value of 6.8.

Table 13: The free parameters for the CuTi (m = 2, 190 layers) neutron supermirror shown in figure 54. Parameters r_{sub}, r, r_{diff}, p define the roughness growth from layer to layer.

Neutron optical potential Cu [m^{-2}]	Re: $6.01 \cdot 10^{14}$, Im: $9.38 \cdot 10^{10}$
Neutron optical potential Ti [m^{-2}]	Re: $-2.15 \cdot 10^{14}$, Im: $1.55 \cdot 10^{11}$
Amplitude [Cts]	14613 ± 26
Thickness scaling factor Cu	1.063 ± 0.001
Thickness scaling factor Ti	0.975 ± 0.001
r_{sub} [nm]	0.80 ± 0.02
r [nm]	2.41 ± 0.09
r_{diff} [nm]	0.79 ± 0.02
p	1.41 ± 0.06
χ^2-value fit	6.8

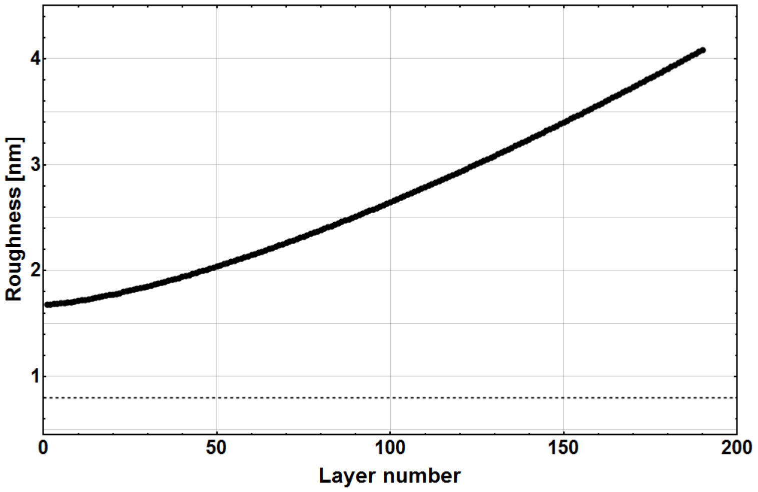

Figure 55: The graph shows the roughness values inside the m = 2 CuTi neutron supermirror from Figure 54 dependend on the layer number in the supermirror. The values are calculated using equation 5.5 and the fit results shown in table 13. The roughness increases with the power $p = 1.41$, with the low final roughness of about 4 nm at the total material thickness of 2 µm.

the substrate's surface to contact it to the transport wagon and initialize the in situ polishing.

In conclusion, we present a model which enables a realistic statement about the roughness growth inside our supermirrors which can also be used for the development of mirrors with a higher number of layers.

5.5 Results of Cu/Ti Development

This chapter showed, that impurities in the target are also implanted in the deposited layers, as we expected. Therefore, it is mandatory to use highly pure targets for the production of non-magnetic neutron supermirrors. The roughness and interdiffusion of single and multilayers can be influenced positively by the deposition process. With the presented set of parameters for Cu and Ti it is possible to deposit multilayer structures with minimized roughness growth. Besides the classical sputtering parameters like working pressure, sputtering mode and power, we used reactive sputtering and substrate bias voltage for the layer optimization. We showed, that XRD can be used for the determination of the nitrogen content inside the reactively deposited TiN_x layers as well as ERD.

In conclusion, we demonstrate for the first time a m = 2 supermirror based on Cu/Ti. It shows an excellent reflectivity above 90 %, which is only slightly inferior to state of the art Ni/Ti mirrors [144]. Hence, the neutron capture induced background inside PERC will be low. Due to the excellent heat stability of our mirrors, baking of the neutron guide in the warm bore of PERC can be realized [54] to obtain clean high vacuum conditions. The fit of our extended model for the roughness growth inside the supermirror describes the measured reflectivity excellently and can be used for further optimization processes.

6 Solid-State Neutron Polarizer based on Iron and Silicon

This chapter deals with the development of a novel solid-state neutron polarizer. This device is used to polarize an incoming neutron beam and can be used with a broad spectrum range. A polarizer is essential for PERC, as neutron spin dependent measurements will be performed. Challenges, which have to be met concerning such polarizer are namely a high degree of neutron polarization, together with lowest possible neutron losses. We investigate the solid-state polarizer concept, which is based on the work of A. Pethukov et al. [58]. We focused on the most promising substrate materials and the development of high reflectivity supermirrors.

6.1 Motivation

For details on the working principle of neutron polarizers, see chapter 1.3. Figure 56 shows a comparison of the classical polarizer design (e.g. Cobalt (Co)/Titanium (Ti) supermirror on glass substrate) and the solid-state concept (Fe/Si supermirror on quartz substrate).

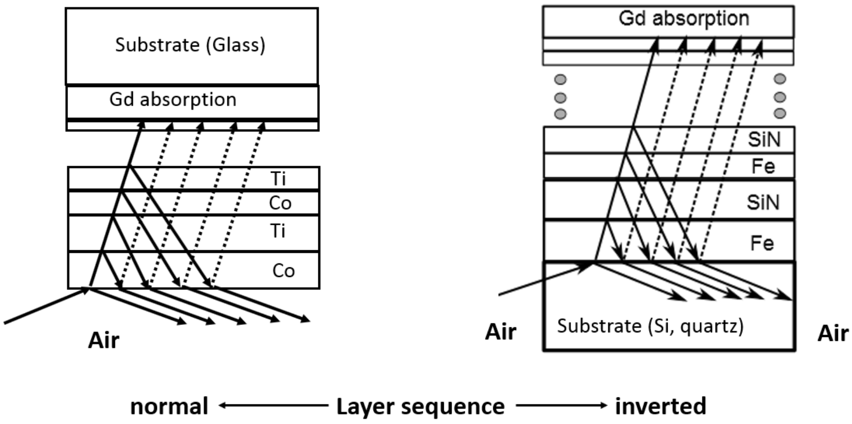

Figure 56: Left: Example of Co/Ti supermirror with normal layer sequence deposited on glass substrate. The neutrons hit the mirror from air/vacuum side. Right: Principle of a solid state polarizer based on FeSiN$_x$ supermirror coating with inverted layer sequence. The incoming neutrons are transmitted by the substrate and hit the mirror from substrate side.

The classical design using a Co/Ti supermirror on glass substrate has several disadvantages. The most critical one is the production of the radioactive isotope Co^{60} during operation by neutron capture. Its long half-life of $T_{1/2} \approx 5.27$ years requires special shielding around the polarizer, resulting in difficult working conditions for changes on the device as well as very high disposal costs. Furthermore, half of the incoming neutrons hit the glass substrate and get absorbed by it. The neutron capture reactions with the contained boron with emission of alpha- and Lithium particles and high energy γ-radiation (2.8 MeV), damage the substrate. Mainly due to the alpha- and Lithium particles, the glass gets brittle and breaks after a certain time in the neutron beam. This limits the operation time of such polarizers. Another disadvantage is the total reflection of neutrons with both spin components in low q-region, induced by the positive neutron optical potential step from the last Co layer to the glass substrate.

The solid-state polarizer consists of a Fe/Si supermirror deposited on a substrate material, that is nearly transparent for neutrons (e.g. Si, quartz). Depending on the substrate material, the radiation damage can be reduced compared to the classical design and also the size of the device can be reduced from at least 50 cm to around 10 cm only.

The polarizer design is based on the material specific scattering length density, introduced in chapter 1.3 and shown in table 3 on page 14. The SLD for quartz is $\rho(\mathrm{SiO_2}) = 4.19 \cdot 10^{-6}\text{Å}^{-2}$ and $\rho(\mathrm{Al_2O_3}) = 5.72 \cdot 10^{-6}\text{Å}^{-2}$ for sapphire. For the reflection of spin down neutrons (spin anti parallel to the magnetic field) on Fe the SLD is $\rho^{-}(\mathrm{Fe}) = 2.93 \cdot 10^{-6}\text{Å}^{-2}$. Neutrons passing from quartz or sapphire on Fe see a negative step in SLD. Hence there is no total reflection, even in low-q region. As neutrons are no longer entering the supermirror from air/vacuum but from the substrate, the layer sequence has to be inverted for the solid-state design. Inverting the layer sequence is trivial in terms of calculation but not in production as the thickest layer is now the first layer of the supermirror, leading to larger roughness from the beginning of production.

Inside the Fe/Si supermirror structure, the SLD difference should be zero for the spin down component and high for the spin up component. For the spin up component of Fe and Si the difference in SLD is $\rho^{+}(\mathrm{Fe}) - \rho^{+}(\mathrm{Si}) = 11.04 \cdot 10^{-6}\text{Å}^{-2}$, which is even higher than for Co/Ti. For the spin down component the SLD of Fe is $\rho^{-}(\mathrm{Fe}) = 2.93 \cdot 10^{-6}\text{Å}^{-2}$ and is slightly higher than for Si $\rho^{-}(\mathrm{Si}) = 2.08 \cdot 10^{-6}\text{Å}^{-2}$. This would lead to a small fraction of neutrons with spin down reflected. For this case, the potential of Si has to be matched to that of Fe.

6.2 Experiments with Polarized Neutrons

We used the TREFF instrument to characterize the polarizing supermirrors. It is equipped with a transmission polarizer, two spin-flippers and a multichannel analyzer.

In the following, the instrument and the supermirror characterizations are presented in detail.

6.2.1 TREFF Analyzer

To perform measurements with polarized neutrons at TREFF, a magnetic sample holder was constructed and assembled. Without such holder neutrons could depolarize on their way from the polarizer to the detector. It can be used to measure wafers or alternatively any substrate with a maximal height of about 120 mm and a width of maximum 100 mm. The special feature of this holder is a homogeneous magnetic holding field with a strength of 100 mT, which was measured with a Hall-probe and is a factor of three stronger than existing sample holders at the TREFF instrument. This magnetic holding field ensures magnetization of the supermirror coating and therefore enables the magnetic splitting in reflectivity of the coating. The sample holder and a Si wafer coated with a Fe/SiN$_x$ supermirror are shown in figure 57.

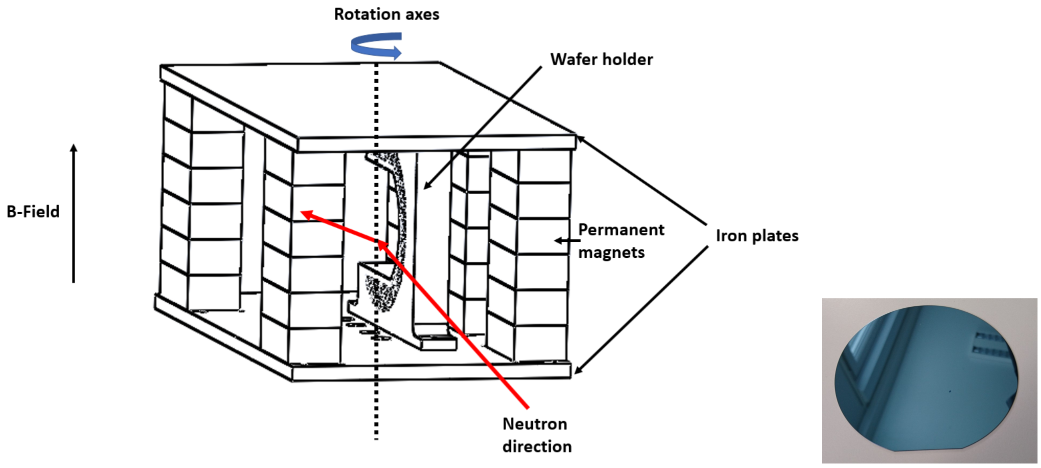

Figure 57: On the left side, the sample holder for reflectivity measurements with polarized neutrons at the TREFF instrument is shown. The right shows an example of a Si wafer coated with a m = 2 Fe/SiN$_x$ supermirror.

To check the performance of the instrument's polarizing components, a 200 nm thick Fe layer deposited on a Si wafer was measured once with the polarizer and once with the analyzer. When the devices are working properly, the count rates should be comparable. The reflectivity curves $R^{\pm}$ for spin up and down neutrons are shown in figure 58.

The measurement shows an intensity difference of a factor of almost 10 for the same setup, which indicates significant absorption inside the analyzer device.

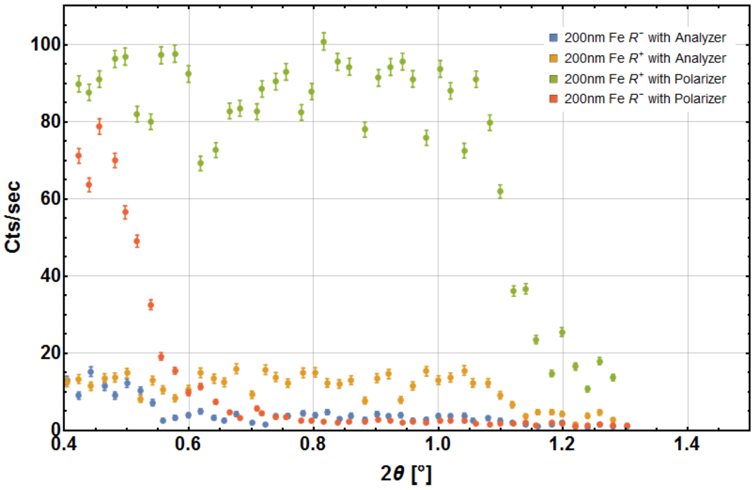

Figure 58: Reflectivity measurement of a pure Fe layer with spin up and spin down neutrons with the polarizer and the analyzer. The measurement with the analyzer (polarizer moved out of the beam) shows a significantly lower count rate than with the polarizer and otherwise unchanged instrument settings.

The product AFP is the analyzing power (TREFF analyzer) times flipper efficiency times polarizing power (our Fe mirror). It can be extracted for the polarizer and the analyzer from the reflectivity curves and is defined as

$$\mathrm{AFP} = \frac{R^+ - R^-}{R^+ + R^-} \,. \tag{6.1}$$

The standard deviation for the detected neutrons is given by the Poisson distribution. For an amount of neutrons greater than ≈ 20, this statistic is well described by the Gaussian distribution. The standard deviation for the product AFP is given by

$$\sigma_{\mathrm{AFP}} = 2 \cdot \frac{R^+ \cdot R^-}{(R^+ + R^-)^2} \cdot \sqrt{\frac{1}{R^+} + \frac{1}{R^-}} \,. \tag{6.2}$$

The product AFP for TREFF's polarizer and analyzer are shown in figure 59.

These measurements show that the multichannel analyzer provides only low neutron transmission and no reliable neutron polarization. One possible reason for this is shown in Ref. [113], where some broken lamella are visible. This is causing an inhomogeneous intensity distribution in vertical direction .

Following these results, we kept the instrument's analyzer in non-polarizing transmission mode and measured only with the polarizer. We used our polarizing samples as analyzer and were able to determine the products AFP for different supermirrors.

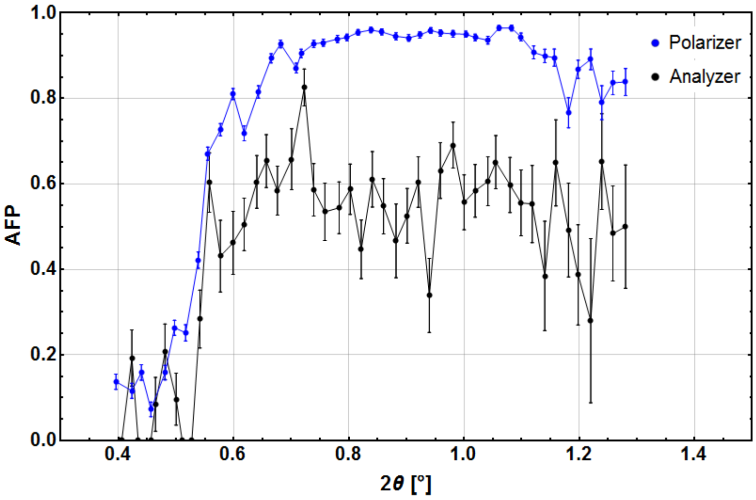

Figure 59: AFP for a pure Fe layer measured at TREFF with the polarizer and the analyzer separately.

6.2.2 Matching Si and Fe

To match the SLD of Fe for spin down neutrons with that of Si, the SLD of our Si layers was increased by adding N_2 during the production. Figure 60 shows reflectivity curves of a pure polished 4" Si wafer with thickness of 0.525 mm, of a 200 nm thick Fe layer deposited on borofloat glass and of a 100 nm thick SiN_x layer on a Si wafer.

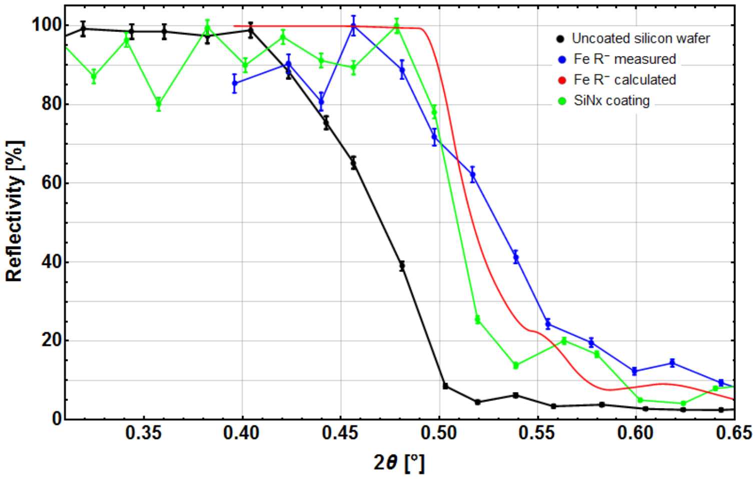

Figure 60: Neutron reflectivity curves for the spin down component of pure Si, a SiN_x layer matched to Fe and a 200 nm thick Fe layer. The SiN_x layer was produced by reactive sputtering of Si with 1 sccm N_2.

The Fe and SiN_x layers were deposited with parameters described in Appendix B.3. The graph of the SiN_x layer shows, that the addition of 1 sccm N_2, increased the critical angle of reflection from $2\Theta = 0.4°$ to $2\Theta = 0.5°$, which is matching the reflectivity of Fe very well.

6.2.3 Influence of Different Substrates on the Fe/Si System

This chapter describes the development of Fe/SiN$_x$ supermirror coatings on different substrates. For each substrate, namely borofloat glass, silicon and quartz we present the reflectivity measurements with polarized neutrons performed at the TREFF reflectometer. The supermirror deposited on borofloat glass was additionally measured at the Helmholtz-Zentrum Berlin (HZB) for comparison of the instrument performances. The supermirror on glass was deposited in normal layer sequence (Appendix B.3), whereas the supermirrors on a Si wafer and on polycrystalline quartz were deposited with the inverted layer sequence.

Figure 61 shows the reflectivity curves for spin up and spin down neutrons at TREFF and HZB together with the calculated reflectivities.

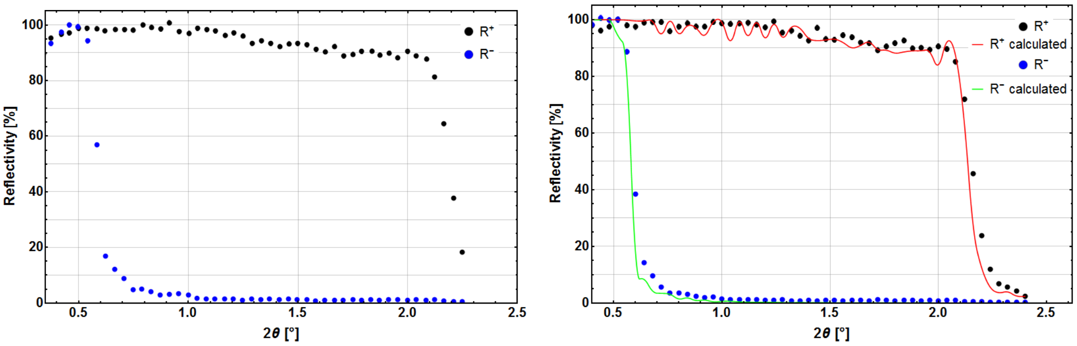

Figure 61: Left: Neutron reflectivity measurement $R^{\pm}$ of a $m = 2.2$ Fe/SiN$_x$ supermirror on borofloat glass (TREFF). Right: Neutron reflectivity measurement of the same sample at HZB and its calculated reflectivity.

The data analysis showed, that the analyzer at TREFF instrument still has an influence on the spin down component, as the count rate in the low q-region (total reflection) is on average 5 % lower than that of the spin up component. In principle, the count rates for both components should be equal in this region. For the calculation of the reflectivities, the roughness growth model from chapter 5.4.3 was used. The calculated curves correspond to roughness values of $r_{\text{sub}} = 0.5$ nm for the substrate roughness, $r = 2.0$ nm for roughness of the layers, $p = 0.12$ and zero interdiffusion roughness. The value of p indicates, that the roughness is approaching quickly the value of r and is then growing only slowly.

Figure 62 shows the resulting AFP values for the two measurements of the supermirrors.

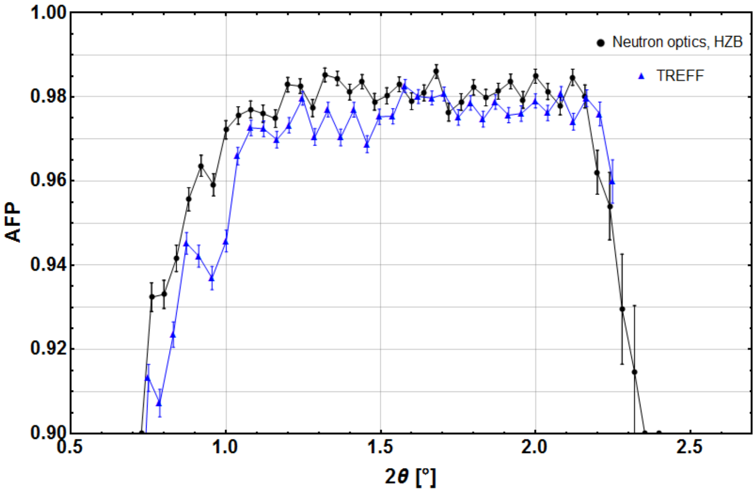

Figure 62: AFP values of a m = 2.2 FeSiN$_x$ supermirror on borofloat glass, measured at TREFF and the HZB.

The average AFP value at the TREFF instrument is 0.9760 ± 0.0038 in the region $1.1° - 2°$, whereas a value of 0.9810 ± 0.0031 was measured at HZB. Possible explanations for the lower average AFP at TREFF are either a smaller neutron polarization, a lower flipper efficiency or an influence of some analyzer plates. Nevertheless, it was possible to successfully characterize different substrates for a solid-state polarizer as well as Fe/SiN$_x$ supermirror coatings in normal and inverted layer sequence.

The inverted layer sequence was firstly tested on a Si wafer, which was polished on both sides, had a diameter of 100 ± 0.5 mm, a crystal orientation [100] and a thickness of 525 ± 20 µm. Figure 63 shows the raw data of the reflectivity measurement of a m = 2 Fe/SiN$_x$ supermirror coating in inverted layer sequence on the wafer. As we measured only one thin Si wafer, the effective path length of the incoming neutrons inside the mirror strongly depend on their angle of incidence (AOI).

This means, that for higher angles, neutrons travel a shorter length inside the material and therefore the overall absorption is lower. For a narrow beam neutrons travel the whole way through the wafer up to a critical AOI, which is given by

$$\Theta < \arctan\left(\frac{d}{r}\right) \approx 0.6° \ , \tag{6.3}$$

for radius $r = 50$ mm, thickness $d = 0.525$ mm). Here, the path length is approximately constant. For higher AOI $\Theta > 0.6°$ the neutron's path length L traveled in the wafer decreases

$$L = 2 \cdot (d/\sin(\Theta)) \ . \tag{6.4}$$

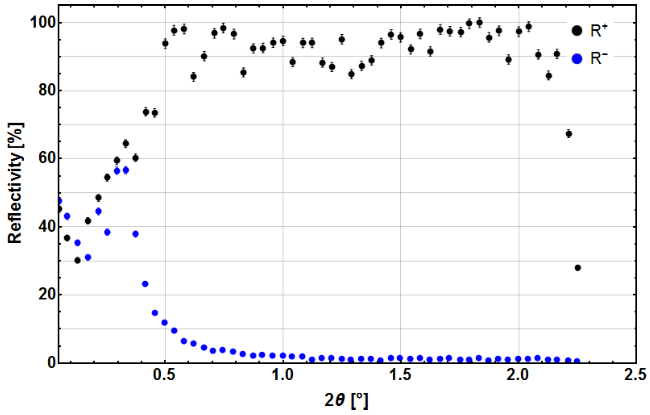

Figure 63: Uncorrected reflectivity curve of a m $= 2$ Fe/SiN$_x$ inverted supermirror on a 0.525 mm thin Si wafer. In the shown raw data it seems, that the reflectivity of R^+ is constantly between 90 %-100 %, which is not the case in reality. Therefore, corrections were applied, which are explained in the text.

Figure 64 shows the principle and the path length of neutrons inside the substrate dependent on the AOI.

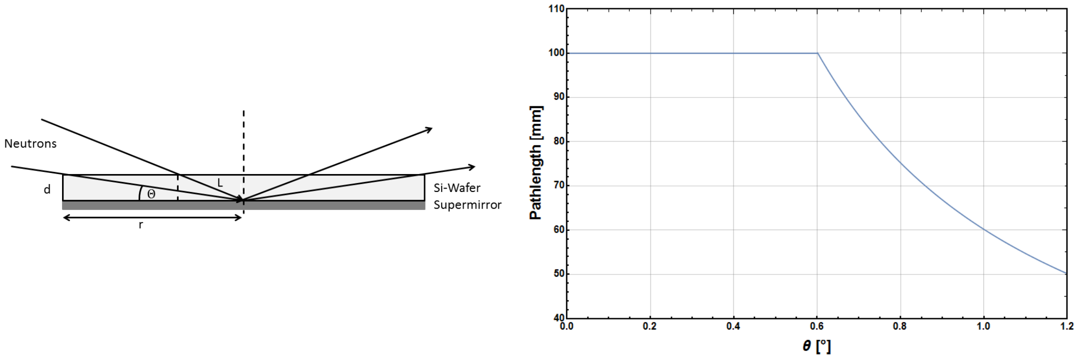

Figure 64: Left: Setup for the reflectivity measurement. Incoming neutrons under small angles of incidence are transmitted through the whole wafer length, whereas the path inside the substrate material for neutrons under higher angles of incidence is reducing. Right: The actual calculated neutron path length inside the substrate dependent on the angle of incidence.

The effective penetration length of neutrons inside the substrate is decreasing with increasing AOI, which would lead to an increased count-rate, as scattering and absorption are less present. But here the count-rate is nearly constant. This is explained by the fact, that the reflectivity of the supermirror is decreasing for AOI above critical angle of total reflection (see Fig. 5) and hence decreases the measured count-rate again. Therefore, the measured data was normalized to a path length in the substrate of 100 mm using equ. 6.3 and 6.4 and the cross sections for Si. The capture cross section of Si is $\sigma_{\text{abs}} = 0.171$ barn, the coherent scattering cross section is $\sigma_{\text{coh}} = 2.163$ barn and the cross section for incoherent scattering is $\sigma_{\text{inc}} = 0.004$ barn [60].

Figure 65 shows the normalized reflectivity curve. Now, the reflectivity R^+ is decreasing much faster, which can be explained by the inverted supermirror layer sequence. Here the thickest layer of the supermirror is deposited as first layer, which consequently increases the roughness of the mirror.

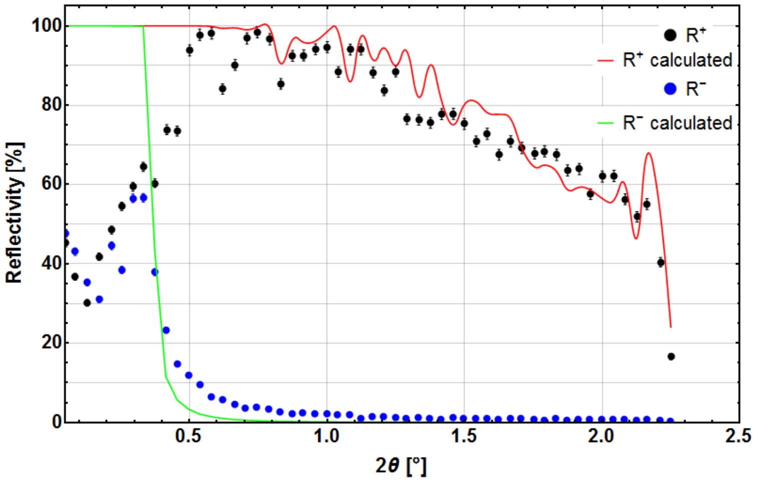

Figure 65: Corrected reflectivity curve of a m = 2 Fe/SiN$_x$ inverted supermirror on a Si wafer. Reflectivity values were corrected in terms of actually passed path length through the substrate material.

The correction of the effectively traveled path of neutrons inside the substrate is only needed to calculate the theoretical reflectivity curve to determine the roughness values. Here $r_{\text{sub}} = 0.5$ nm, $p = 0.12$ and zero r_{diff} are the same as for the supermirror on borofloat glass. The value for roughness $r = 3.1$ nm is more than 1 nm bigger, which is again explained by the inverted layer sequence. As this comparatively high roughness value is building up already within the first layers, the reflectivity curve drops faster for higher angles of incidence. Hence, a supermirror with inverted layer sequence and more than 50 % reflectivity at critical angle of reflection is shown. The corrections do not affect the AFP values of this mirror, which are shown in Figure 66. The positive potential step from the substrate to the Fe's spin-down component is smaller for Si than for borofloat glass. Therefore, the polarization in the low-q region is better and the polarization of 80 % is already reached at $2\Theta \approx 0.5°$ instead of $2\Theta \approx 0.6°$ for glass. The average degree of polarization is not influenced by the inversion of the layer sequence.

In addition to the Si substrate, also a material with higher SLD than the Fe's spin-down component was investigated. Single crystal quartz was one of the most promising

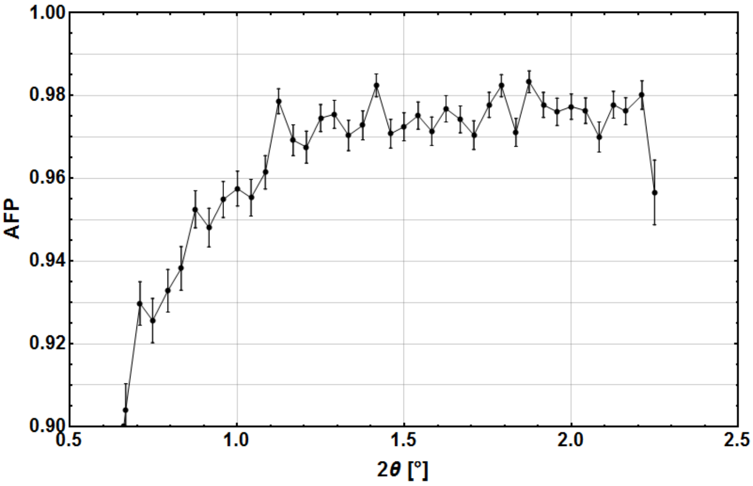

Figure 66: AFP of a m = 2 Fe/SiN$_x$ inverted supermirror on a Si wafer.

substrate materials, but due to the high costs we decided to use polycrystalline quartz for first tests.

For quartz (SiO$_2$) also the coherent cross section of oxygen $\sigma_{\mathrm{coh}} = 4.232$ barn and the incoherent $\sigma_{\mathrm{inc}} = 8 \cdot 10^{-4}$ barn have to be taken into account. This increases the overall cross section and makes transmission slightly worse than for Si. The lower transmission is compensated by the fact, that the reflectivity curve R$^-$ drops to zero from lowest angles of incidence, because of the negative potential step from the substrate to the coating. Figure 67 shows the reflectivity curves $R^{\pm}$ for a m = 2 Fe/SiN$_x$ neutron supermirror deposited in inverted layer sequence on quartz. The substrate plate had a thickness of 5 mm, so that all incoming neutrons within the given angular range passed through the whole substrate length.

The reflectivity curve of R^+ proceeds similar to that shown in figure 65, which shows on the one hand, that it is possible to produce this kind of coating in inverted layer sequence and on the other hand confirmed, that the corrections made for the thin Si wafer were necessary. The values used to calculate the theoretical reflectivity curves are $r_{\mathrm{sub}} = 0.5$ nm, $r_{\mathrm{diff}} = 0.05$ nm, $r = 3.05$ nm and $p = 0.03$. With these parameters, the layer roughness at the top layer is 3.1 nm, exactly as for the supermirror coated on Si substrate. The lower value of p claims that the overall roughness is reached even more quickly for the quartz substrate compared to Si.

The AFP values shown in figure 68 clearly show the benefit of this material, which is a high polarization even in the low-q region.

The absolute value of AFP strongly depends on the reflectivity of the R^- component. As there is no region of total reflection for the quartz R^- component, the reflectivity

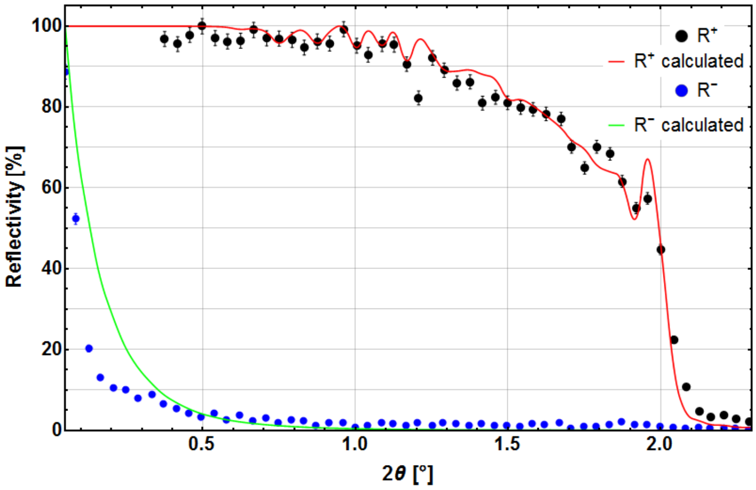

Figure 67: Reflectivity curve for Fe/SiN$_x$ m = 2 supermirror with inverted layer sequence on polycrystalline quartz substrate. All neutrons passed the substrate on the full length.

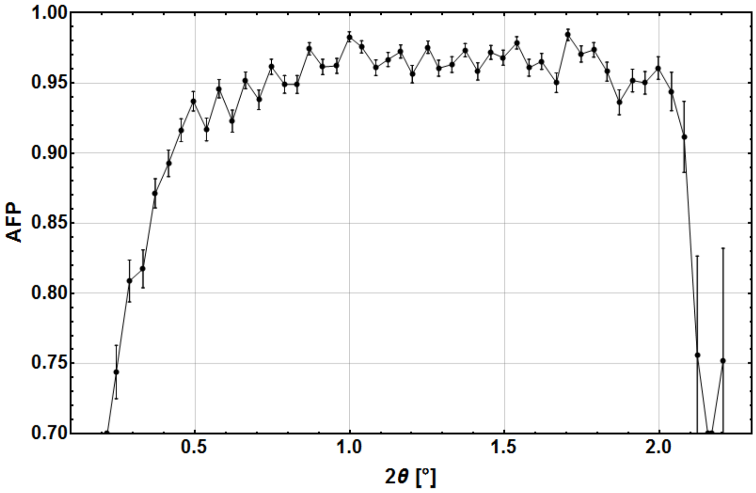

Figure 68: AFP of a m = 2 Fe/SiN$_x$ inverted supermirror on quartz plate. As the neutron optical potential for quartz is slightly higher than that of Fe down component, there is almost no region of total reflection for R^-. Consequently, there is a high degree of polarization even in the low-q region.

of this component was determined by the point of zero reflection at high angles of incidence ($2\Theta = 2.3°$).

The resulting AFP for Fe/SiN$_x$ coating on quartz substrate shows values of $> 90\,\%$ for a wide angular range from $\approx 0.4° - 2.1°$, which is a great improvement in comparison to classical borofloat glass substrate. The direct comparison of the three evaluated substrates with it's AFP values are presented in figure 69.

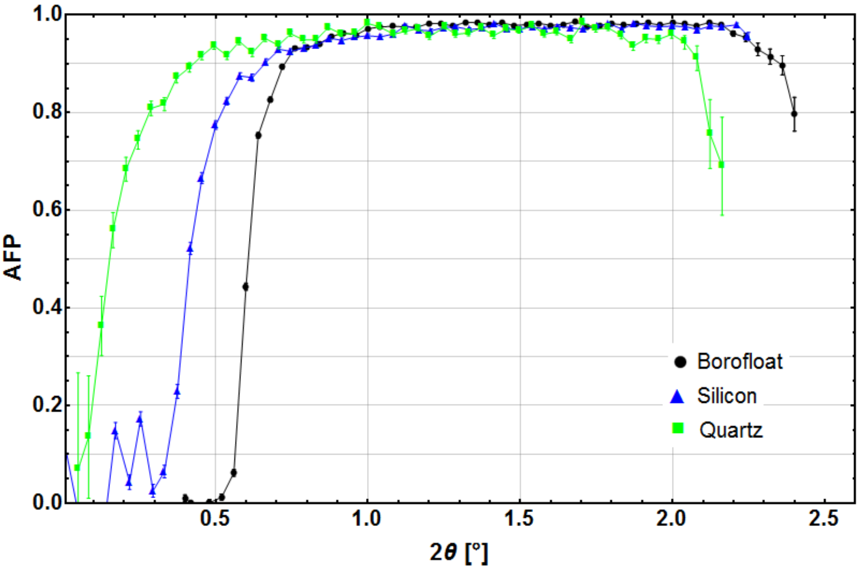

Figure 69: The AFP values of three Fe/SiN$_x$ supermirrors on different substrates. It is clearly visible, that the degree of polarization especially in the low-q regon can be strongly influenced by the choice of substrate material.

The graph shows a significant improvement in achievable AFP values in the low q-region. Setting the critical value of AFP to $90\,\%$ the critical angle of incidence could be decreased from $2\Theta \approx 0.7°$ for a normal supermirror on borofloat glass to $2\Theta \approx 0.4°$ for an inverted supermirror on quartz. The main advantages of quartz are a significantly wider angular range of polarization and a more compact design as devices of $5 - 10\,\text{cm}$ length are usually sufficient. This also enables to build the bracket with the magnetic field in a more compact way and the resulting field is higher. The stronger magnetic field in the range of $> 300\,\text{mT}$ results in an improved magnetic saturation the supermirrors coating. In Ref. [59] a factor 2 higher transmission compared to a classical Co/Ti bender [145] is proposed. In there, an additional Gd/Si antireflection and absorption layer is deposited on top of the Fe/Si supermirror to capture neutrons, that are transmitted through the supermirror.

In conclusion, the main requirements concerning choice of substrate material and supermirror coating were investigated within this work. With the good reflectivity curves of the supermirrors with inverted layer sequence a solid-state polarizer can be designed. Applying the technique of substrate biasing, which was described in detail in chapter 5, could probably improve the supermirrors reflectivity further. A higher neutron reflectivity is directly related to a higher total neutron transmission, which would be a crucial improvement of the whole device. Such polarizer is not curved and hence does not increase the beam divergence, which makes it highly favorable for PERC.

7 Characterization of a High Transmission Neutron Collimator

A high degree of neutron beam collimation is important for PERC for the measurements of neutron beta decay correlation coefficients. It is from great interest to shape the neutron beam already in front of the instrument. Neutron beam collimators are usually built from a radial system [146], acid-etched glass with micro channels [147], a sequence of diaphragms or are of Soller-type [148]. These devices strongly reduce the beam intensity and are commonly built as Soller slit collimators, consisting of many parallel ordered absorbing plates, that are separated in a supporting structure [149]. We present a compact Soller-type slit collimator consisting of a stack of silicon wafers with a thin boron $^{10}B_4C$ absorption layers on both sides of each wafer. The advantage of this absorber material is much softer neutron capture γ-radiation. This simplifies the radiation shielding for the device considerably. The neutron transmission is optimized by replacing every second wafer with a spacer of equal height. The presented almost perfect triangular transmission curves are in good agreement with Monte-Carlo simulations.

7.1 Prototype Preparation

The performance of a Soller-type collimator depends on a few characteristics. These are the thickness of the absorber T, the separation of the layers S and its length L. For a parallel incident beam and totally absorbing plates, the peak transmission through the collimator is given by the fraction of the absorbing plates' frontal area and is proportional to $(S - T)/S$. For substrate plates consisting of a material, which is transparent for incoming neutrons, like silicon coated with $^{10}B_4C$, neutrons are also transmitted through the substrate. The consequence is a higher overall neutrons transmission of the device. Since surface roughness and ripples increase neutron scattering on the surface, the transmission strongly depends on the flatness of the substrate. The reachable full-width at half-maximum (FWHM) is given by $\operatorname{atan}((S - T)/L)$. The transmission of such a collimator strongly depends on the properties of the incoming neutron beam concerning neutron energy and divergence. Clearly, the maximum can be achieved for an infinitesimal thin substrate coated with an absorber, which eliminates all neutrons above a certain angle of incidence.

The required absorber thickness t is roughly estimated by [150]:

$$t_{opt} = k_1 \frac{\alpha}{\rho\sigma} log_{10}(k_2 L) \ , \tag{7.1}$$

here α is the calculated minimal FWHM (defined by device geometry), ρ is the scattering center density, σ the total cross section of the absorber for neutrons, L the length of the collimator and $k_1 = 3.28$, $k_2 = 4.72 \cdot 10^5$ are constants.

This formula gives only a rough approximation of the optimal absorber thickness and gives a value in the range of 1 µm for the material specific values in table 14. From transmission measurements on single $^{10}B_4C$ layers, we estimated an absorber thickness of 650 nm $^{10}B_4C$ to be sufficient for the collimation of a neutron beam with a wavelength of 4.8 Å at TREFF. Our device consists of 48 rectangular silicon wafers (30 mm wide, 50 mm long, each 0.275 mm thick), coated on both sides with $^{10}B_4C$ absorber. The plates were assembled in an aluminum support structure. With these dimensions a L/S ratio of about 90 is achieved, where L is the length of the device and S the layer separation. The assembled device is shown in Figure 70.

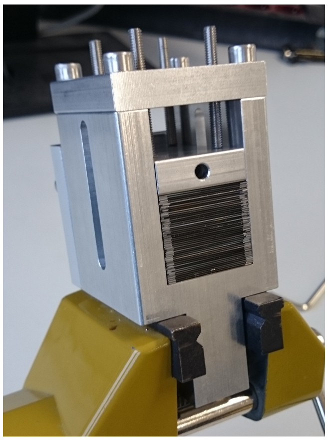

Figure 70: Assembled collimator in the aluminium supporting structure. Every second wafer was removed to maximize transmission. The wafers are double-sided coated with 650 nm $^{10}B_4C$ via magnetron sputtering.

The frontal area of the support structure was covered by borated rubber for the measurements to prevent neutrons from entering the aluminum and scattering back into the collimated beam.

For the Monte-Carlo simulations the neutron wavelength is fixed to $\lambda = 4.8$ Å, the beam is non divergent and the dimensions of the silicon wafers are taken from above. The material properties for the simulations are listed in table 14.

Table 14: Used substrate and absorber parameters concerning the frontal area of the collimator. The absorption cross section is given for thermal neutrons. Values used for Monte-Carlo simulations.

Substrate	Si	$^{10}B_4C$
Density [g/cm^3]	2.329	2.52
Atomic mass [au]	28.0855	10.4019
$\sigma_{\text{scattering}}$ [barn]	2.167	3.59
$\sigma_{\text{absorption}}$ [barn]	0.171	3068.
Thickness [m]	$0.275 \cdot 10^{-3}$	$650 \cdot 10^{-9}$

With these material parameters, the transmission through the substrate material can be calculated [151]:

$$T(L) = e^{-\sigma_i N L} \tag{7.2}$$

Here L is the length of the transmitted material, σ_i is the total cross-section of the material at a given neutron wavelength, and N the number density. With our design, we omit every second substrate leaving just an air gap. For a parallel neutron beam, the maximum transmission through the collimator for 4.8 Å is hence given by

$$\begin{aligned} T &= \frac{D_{Si}}{2\,S} T_{Si}(L) + \frac{D_{gap}}{2\,S} T_{gap}(L) + \frac{D_{abs}}{S} T_{abs}(L) \\ &= 93.7\,\% \end{aligned} \tag{7.3}$$

using the dimensions given in table 14, the substrate thickness equal to the gap thickness $D_{Si} = D_{gap}$, the layer spacing S, a calculated transmission of single crystal Si substrate of $T_{Si}(L = 5\text{cm}) = 87.9\,\%$ and an assumed transmission of the gaps $T_{gap} = 1$.

7.2 Neutron Studies and Results

The first measurement was performed at TREFF instrument at the research neutron source Heinz Maier-Leibnitz (FRM II) in Munich. The incoming beam was collimated by the instruments apertures to a divergence of $\approx 0.011°$ (horizontal apertures 0.2mm), which is smaller then the theoretical collimators FWHM. The measured and the simulated rocking are presented in figure 71.

The rocking curve shows a full-width half-maximum of FWHM = 0.272°. Due to the fact, that the incoming beam has a divergence of only $\approx 0.011°$, the profile of the rocking curve is triangular. The simulation contains all material specific parameters

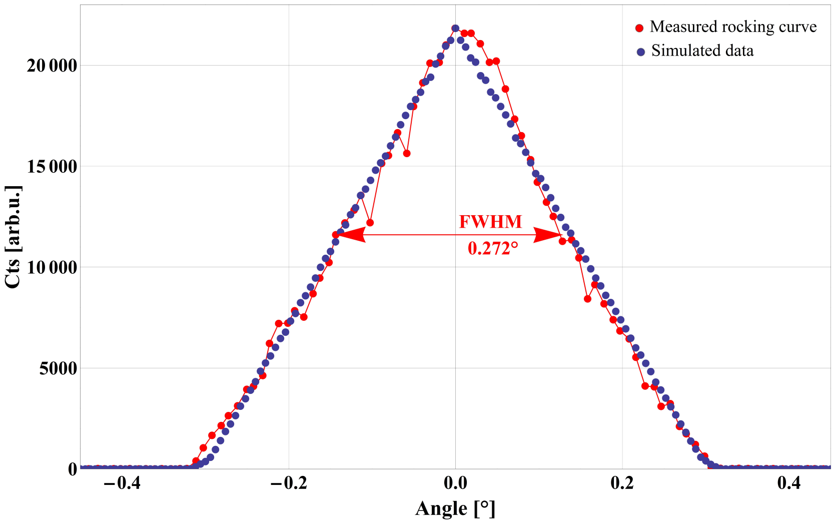

Figure 71: Rocking curve of the collimator measured at a neutron wavelength of 4.8 Å at TREFF. The measured data agrees well with the simulation. A FWHM of about 0.27° is achieved for a narrow incoming neutron beam. The statistical error bars are smaller than the points shown on the graph.

and agrees well with the measurement. This result confirmed our expectation, that an absorber thickness of 650nm $^{10}B_4C$ is sufficient for this setup.

Two more rocking curves were recorded for neutrons with 1 Å, 1.5 Å monochromatic neutrons at the RESI instrument of the FRM II beamline SR8b. For the monochromatic beam a Germanium Ge-511,25′ mosaic deformed wafer stack is used for 1.5 Å neutrons and a Cu-422, 20′ mosaic for 1 Å neutrons [152]. The corresponding rocking curves are shown in figures 72 and 73. As the beam profile of the incoming neutron beam is unknown, there is no simulated data. A Gaussian-broadening coming from an unknown divergence profile of the incoming neutron beam was found. The rocking curves have a FWHM of $0.399 \pm 0.009°$ for 1Å and $0.44 \pm 0.01°$ for 1.5Å. Even for a neutron wavelength of 1Å, a signal to background ratio of ≈ 74 can be achieved with 650 nm $^{10}B_4C$, which is better than expected.

The total transmission for 1.5Å was measured by dividing the count rate in the peak maximum and the count rate without collimator. The resulting peak transmission of $72.623 \pm 0.037\%$ for a beam size of $5x5$ mm^2 is smaller than the theoretical value calculated with equ. 7.3. The smaller transmission indicates, that the device is collimating the incoming neutron beam. Nevertheless, the broadening of the FWHM and the decreasing signal to background ratio can be explained by an increasing number of neutrons transmitted through the absorber.

The high transmission of $72.623 \pm 0.037\%$ for 1.5Å could only be achieved by replacing every second wafer by an air gap and the lower background is achieved by replacing

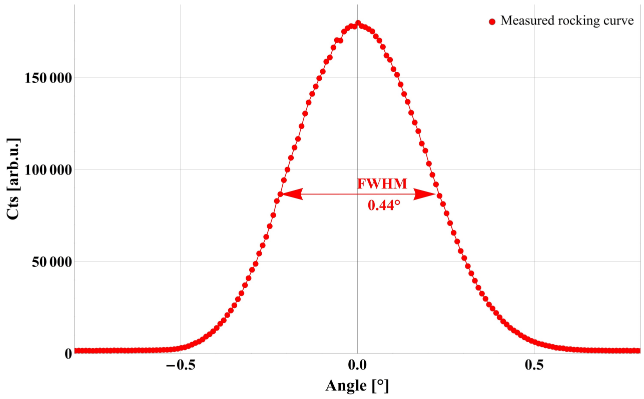

Figure 72: The rocking curve for a neutron wavelength of 1.5Å. The FWHM increased from 0.27° at 4.8 Å to a value of 0.44 ± 0.01° at 1.5 Å, because of the unknown beam divergence and the smaller neutron wavelength of 1.5Å, which leads to higher transmission probability through the absorber material. The signal to background ratio decreased to a value of 120.61 ± 0.02 due to higher energy of the incoming neutrons.

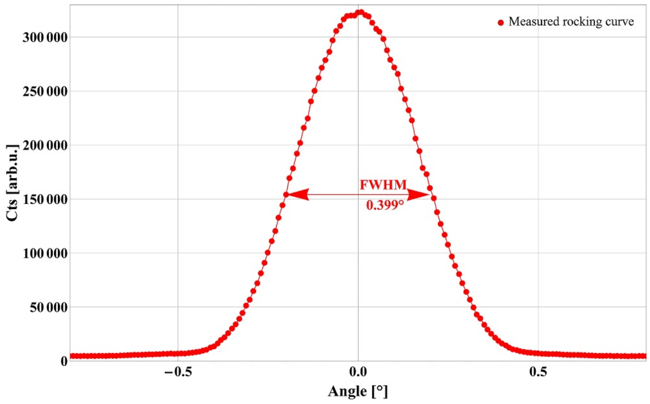

Figure 73: Measurement of the collimator rocking curve for a neutron wavelength of 1Å. The FWHM broadened to 0.399 ± 0.009°. The signal to background ratio is still ≈ 74. Hence, the device can also be used in beams with higher neutron energies.

gadolinium as absorber material by $^{10}B_4C$. Compared to standard collimators with gadolinium coated foils have typically a length of 100 mm and more. Our collimator is by a factor of two smaller. Another advantage is, that the absorber layer coated by magnetron sputtering has a much smaller frontal area compared to gadolinium or boron enriched paint, as the thickness of $^{10}B_4C$ coating can be kept below 1 μm in our configuration. A high signal to noise ratio was measured and analyzed to be 1834.2 ± 2.6 for a neutron wavelength of 4.8Å.

In conclusion, we present an improved collimator in terms of transmission and γ-background level, based on already introduced principle of using silicon wafers for compact neutron collimators [149].

This device can be further improved in terms of transmission and signal to background ratio. Concerning transmission, the triangular shaped curve can be modified to be rectangular, by coating the top of the absorber surface with a nickel layer, as it is proposed by L.D. Cussen et al. [153]. A Ni-layer at the interface would increase the critical angle of reflection of incoming neutrons. The transmitted beam profile would therefore change from triangular to rectangular, dependent on the used material or technique. By using a Ni/Ti neutron supermirror, this critical angle can even be increased, which also leads to an increase of the rectangular width. For smaller neutron wavelengths a certain optimum for the absorber thickness can be evaluated, which is described in [150] by L. D.Cussen. As our absorber thickness was optimized for a wavelength of around 5Å, the signal to background ratio is decreasing in our measurements for wavelengths below 5 Å. In general the use of Si wafers and $^{10}B_4C$ as absorber is superior to absorber paint, as the neutron scattering and therefore background level is much lower. A relatively simple dimension adjustment, production and assembly are further advantages of such a device. For beam ports, which require a highly collimated incoming neutron beam with low γ background because of γ sensitive detectors, this type of Soller collimator could be important and affordable upgrade.

8 Design of the PERC Beamline

The new neutron beta decay facility PERC is introduced briefly in chapter 1.1. The instrument is currently under construction at the FRM II. The instrument will be fed by a high flux cold neutron beam guided from the reactor via a primary neutron guide to the guide Hall East. Figure 74 shows the instrument at its final position.

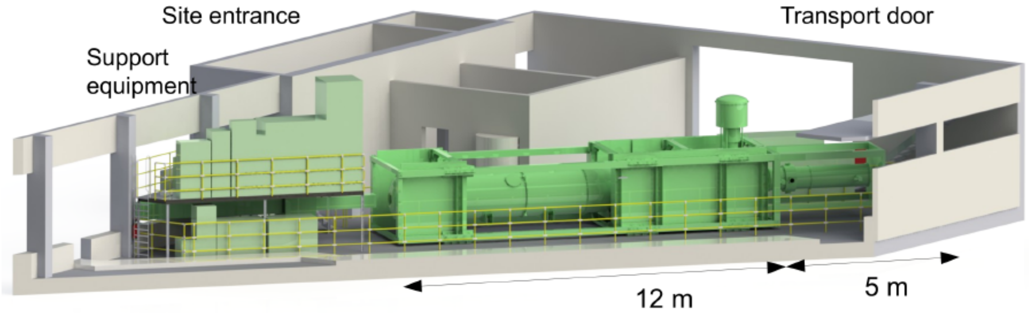

Figure 74: The PERC setup at the beam port MEPHISTO in the Hall East of the research reactor FRM II [154].

The primary guide was optimized by C. Klauser. She used McStas as simulation method [40]. Based on her results, the primary guide was designed and produced with a Ni/Ti supermirror coating with m = 2.5, a cross section of $60 \times 106\,\mathrm{mm}^2$ and a curvature radius of 3 km. The curvature reduces fast neutron background and γ - radiation. The simulated thermal equivalent flux density is $2 \cdot 10^{10}\,\mathrm{n\,cm^{-2}\,s^{-1}}$ with a mean wavelength of 4.5 Å [53]. The primary guide is to be installed at the beam port SR-4b. A Dornier neutron velocity selector is located at the end of the primary guide. It typically gives way to neutrons around 5 Å with a resolution of $\frac{\Delta\lambda}{\lambda} = 11\%$ [155]. It is placed outside of the Hall East. The technical data of this device is shown in table 15.

Table 15: Technical data of the Dornier selector at a neutron wavelength of 5 Å[155].

Blade length	250 mm
Blade width	0.4 mm
Amount of blades	72
Total length of selector	400 mm
Torsion angle	48.27°
Window width	150 mm
Window height	65 mm
Frequency	425 Hz

All components and beamline parts following the MEPHISTO guide are considered here. The actual PERC beamline will consist of a polarization system, a spin flipper and a chopper, before neutrons enter the decay volume. Within this work, several options of the layout of the beamline have been considered and optimized. All neutron optical devices can be installed in a gap of ≈ 8 m between the wall of Hall East and the entrance of the PERC decay volume. The section between the selector and the decay volume will be coated with the non-depolarizing Cu/Ti supermirror coating in order to preserve the neutron spin coming from the polarizing device and to reduce unwanted neutron losses and background creation due to a possible change in the coatings m-value near the entrance of the decay volume. Reproducible and stable neutron guide coatings with m = 2 from Cu/Ti are shown in chapter 5.

The optimization was done for the beamline section in front of PERC and the inner guide. Geometrical considerations and optimizations were carried out in order to reduce neutron losses, especially directly in front of the instrument. The design of the inner neutron guide has special requirements, as the whole section has to be pumped down to ultra-high vacuum. Considerations, results and discussion of the performed Monte-Carlo simulations are presented.

8.1 The Monte-Carlo Software McStas

Monte-Carlo simulations are a powerful tool to optimize beamline parameters, such as neutron flux, guide design and dimensions or background estimations. The simulations on the neutron beam within this thesis were carried out using the neutron ray tracing program McStas, version 2.3 [156]. McStas is a meta language, that allows the user to easily build up and investigate a neutron beamline with the help of preconfigured components such as guides. The software is based on Monte-Carlo (MC) method written in ISO-C.

MC itself is mathematically an application of the law of large numbers [157]. For a function, that is finite continuous integrable, the theorem claims, that the sum of this function in a certain interval converges to the integral over the same interval. For randomly sampled values within this interval, this is the MC technique. As random generators are still not perfect, for McStas it can be described as quasi-Monte-Carlo technique. This quasi-MC technique can be even accelerated significantly by attributing each neutron a weight factor, which indicates the probability of the neutron's existence at a certain point. The weight of the neutron is adjusted after each beamline component or interaction partner. This eliminates calculation power for simulation of neutrons, that would never hit the relevant place (detector or sample).

In the simulations presented here, gravity effects were not considered and neutrons are unpolarized. The simulations are based on previous work and results of already existing simulations of the primary guide (MEPHISTO-beam port) performed by J. Klenke [158] and C. Klauser [40].

8.2 Development of a New “Source”-Component

The guide system from the reactor core to the Neutron Guide Hall East at FRM II in Munich is approximately 30 m long. The section of the beamline that is optimized here, is located behind this guide. Simulating the entire guide from reactor to the instrument would need huge calculation power and would slow down the overall optimization process. To be able to perform fast and flexible simulations, the results from former simulations were used to create a new source component in McStas. Therefore, the beam profile at the end of MEPHISTO-guide was studied and used to create a source component that has a quasi-identical beam profile in terms of neutron flux, wavelength-, position-, and divergence distribution. The new McStas component, is called “PERC_source.comp”.

Figure 75 shows on the left side the neutron flux density profile with a mean neutron wavelength of 4.5 Å and a maximum at 3.3 Å. The corresponding capture flux is presented in black and is gives an overall flux density of $\approx 2 \cdot 10^{10}\,\mathrm{n\,cm^{-2}\,s^{-1}}$.

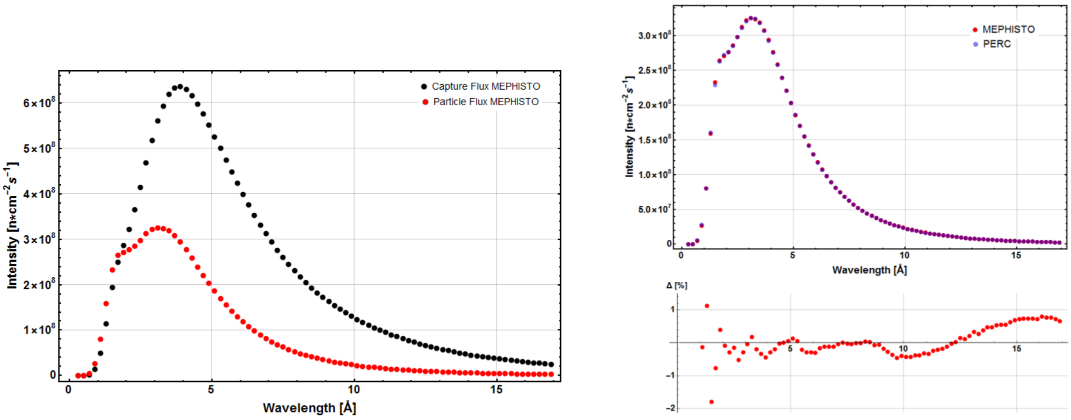

Figure 75: Left: Simulated neutron particle and capture flux from simulations of the primary guide. Right: The particle flux from simulations of the primary guide and from “PERC_source.comp”. The two profiles coincide within ±2% for the whole wavelength spectrum.

The right side shows the neutron particle flux profile of the primary guide and the profile coming from “PERC_source.comp”. The plot of the residuals shows that the two spectra coincide within ± 2%, which is sufficient for the following considerations. To approximate the neutron flux, a fit was performed using a linear combination of five

Maxwell-distributions. Each Maxwell-distribution is parameterized by five different intensity values (I_{1-5}) and five temperatures (T_{1-5}).

Because of the curvature of the primary guide, the neutron distribution inside the guide is not homogeneous. Therefore, the data from the position sensitive detectors (PSD) at the end of the primary guide were analyzed. Figure 76 shows on the left a cut through three different positions of the detector in y-direction and on the right side the neutron intensity profile of the primary guide in x-direction.

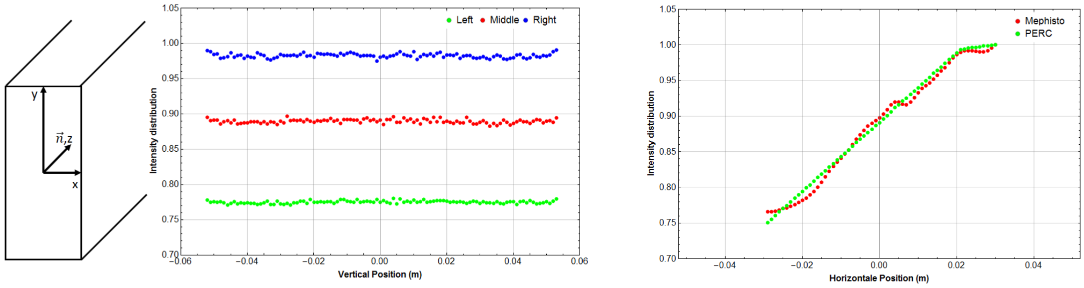

Figure 76: The beam intensity profile in x- and y-direction. Left: Scheme of a neutron guide and the coordinate system with neutron flight direction pointing in z-direction. Middle: A linear intensity distribution in y-direction at three different x-positions (left, middle, right). Right: The intensity profile in x-direction (at $y = 0$). For the PERC source component, a combination of two linear curves was used to approximate the intensity profile of the MEPHISTO guide. The two intensity profiles coincide within ± 2%.

The number of neutrons from garland reflections (neutrons with many reflections along the outside of the neutron guide) is higher on the right side of the guide. On the left (inner wall of curvature), the main fraction consists of specular reflected neutrons and almost no garland reflected neutrons are detected. The exact intensity distribution in terms of position is therefore strongly dependent on the neutron guide geometry.

The cut through the three vertical positions shows, that the intensity profile in y-direction can be estimated to be constant. In x-direction, the profile is increasing almost linearly. To keep the complexity of the new source component low, we describe the intensity profile of the neutron beam in x-direction by a combination of two linear functions. The two profiles coincide within ± 2 %. The corresponding values for the linear functions are implemented in the source code as modification of the neutron weight factor (p-value) for each neutron.

The horizontal and the vertical divergence are considered separately. The different analysis steps are similar, so we will only show it in detail for the horizontal divergence. Figure 77 shows the divergence of the beam for different neutron wavelengths.

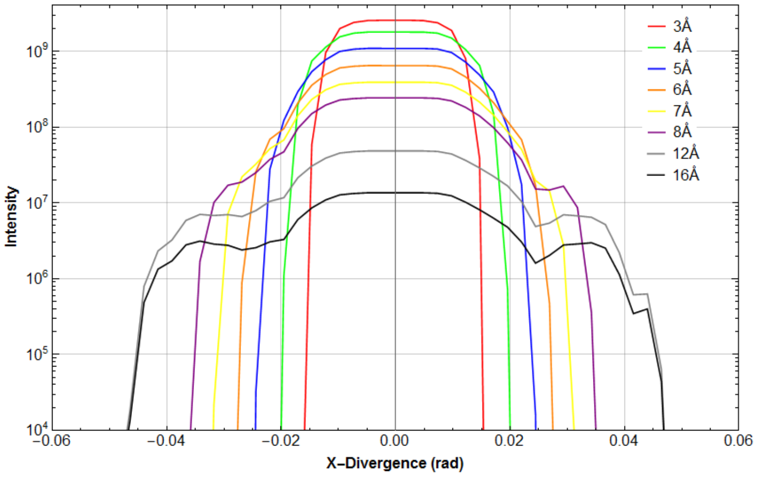

Figure 77: Cut through horizontal divergence plotted in rad for different wavelengths.

To efficiently parametrize the beam divergence, we need a function which describes it well enough and is quite simple to compute. The corresponding fit model, which was chosen is:

$$\mathrm{Div}_{\mathrm{x}} = a_n \cdot \exp\left(-(b_n \cdot x)^4\right) \ . \tag{8.1}$$

Here a_n is the amplitude and b_n is the divergence specific parameter, which was used later to define a model for the whole wavelength band $(0.3 - 17\text{Å})$. Figure 78 shows the resulting fit for the horizontal divergence of neutrons with a wavelength of 5 Å with the parameters $a_5 = (1.103 \pm 0.003) \cdot 10^9$ and $b_5 = 63.40 \pm 0.17$.

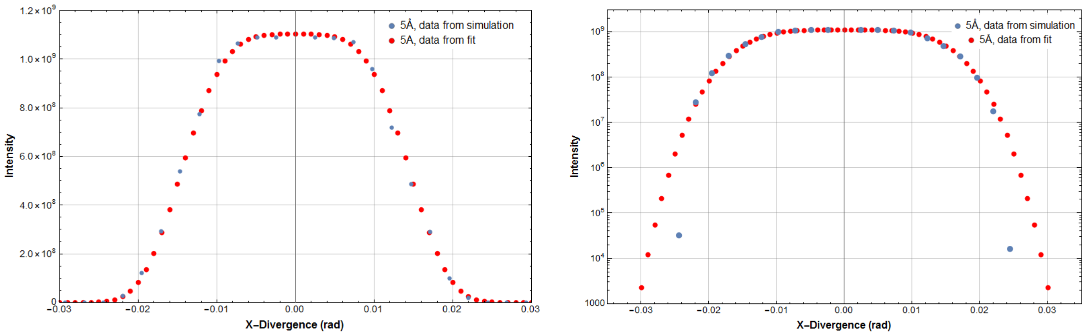

Figure 78: Left: Comparison of the horizontal divergence in rad for neutrons with a wavelength of 5 Å obtained from data from end of primary guide and as described by our model. Right: The same plot in logarithmic intensity scale.

For the divergence distribution of the whole neutron wavelength spectrum in horizontal direction, the fit parameters from the fits above (Fig. 78) for (3, 4, 5, 6, 7, 8, 12, 16 Å) were plotted against the neutron wavelength and again fitted to get the parameters for each wavelength for the source component. The used model is

$$\mathrm{Div}_{\mathrm{x-end}} = b_1 \cdot \exp(-t_1 \cdot \lambda) + b_2 \cdot \exp(-t_2 \cdot \lambda) \ , \tag{8.2}$$

with the parameters $b_1 = 301.52 \pm 55.03$, $t_1 = 0.83 \pm 0.08$, $b_2 = 61.80 \pm 5.24$ and $t_2 = 0.012 \pm 0.008$. The corresponding plot is shown in figure 79.

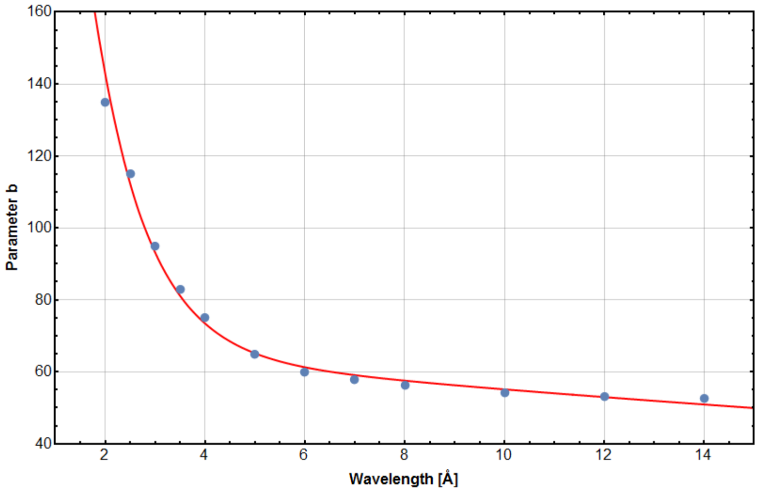

Figure 79: Determination of parameters of the horizontal divergence model dependent on the wavelength. The model used for the fit is shown by equation 8.2.

These values were used for determination of the horizontal divergence and are implemented in the PERC source component.

The same analysis was used to describe the neutron beam divergence at certain wavelength in y-direction. Here, a simpler fit function could be applied

$$\mathrm{Div}_{\mathrm{y}} = 1 - y \cdot |x^{2.5}| \ . \tag{8.3}$$

The vertical divergence for any wavelength can be determined by fitting the results from equation 8.3 with the function

$$\mathrm{Div}_{\mathrm{y-end}} = a_1 \cdot \exp(-f_1 \cdot x) + a_2 \cdot \exp(-f_2 \cdot x) \ . \tag{8.4}$$

Here the parameter values are $a_1 = (8.07 \pm 0.18) \cdot 10^5$, $f_1 = 1.21 \pm 0.06$, $a_2 = (5.21 \pm 0.18) \cdot 10^5$ and $f_2 = 0.29 \pm 0.06$. Figure 80 shows the result as a function of the neutron wavelength.

Combining the horizontal and vertical divergence functions from above and implementing them in the McStas PERC source component results in a good agreement in the overall description of divergence in x- and y-direction. The discrepancy of the old

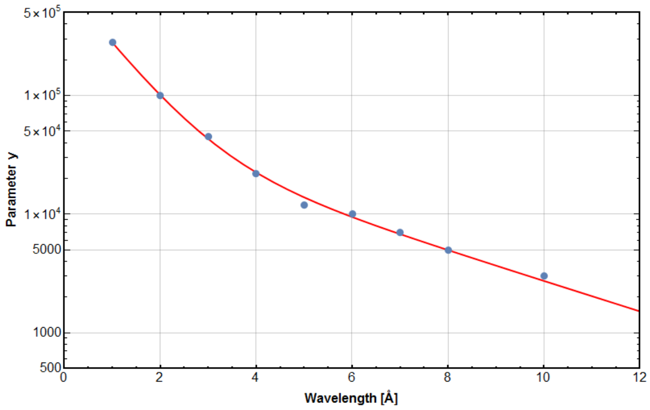

Figure 80: Determination of parameters for vertical divergence. The model used for the fit is shown by equation 8.4.

simulations of the primary guide and the new simulation results performed with the PERC source component show a maximum discrepancy below 4 %. Hence, the new component was used for further simulations concerning the beamline of the PERC instrument.

8.3 Beamline Optimization

The beamline simulation starts with the new source component with the same cross section as the MEPHISTO neutron guide of $60 \times 106\,\mathrm{mm}^2$. The source is followed by an adjustable slit to simulate different guide geometries. The next component is the Dornier velocity selector, which is described by the component "v_selector.comp" in McStas. The transmission of neutrons with small wavelengths through the selector is not taken into account. Such transmission is present in reality due to weaker absorption in the device's lamella. When working with a neutron wavelength of 4.5 Å the technical data sheet of the selector assumes a neutron suppression of $< 5 \cdot 10^4$. The selector is followed by a 8.75 m long neutron guide section. The simulations of the guide geometry are performed for unpolarized neutrons, since the geometry of the polarizer is not fixed yet. The simulations are carried out for a continuous beam.

After this 8.75 m long neutron guide, there is an approximately 1.3 m long gap between the neutron guide and the inner guide of PERC. This gap is unavoidable due to the structure of the magnetic shielding of the cryostat. The setup is shown in figure 81.

One main interest of the simulations was the neutron flux inside PERC depending on the guide geometry in front of the gap. The aim was to find a compromise between maximal neutron flux and minimal neutron losses directly in front of the instrument in order to avoid unwanted background due to neutron absorption processes.

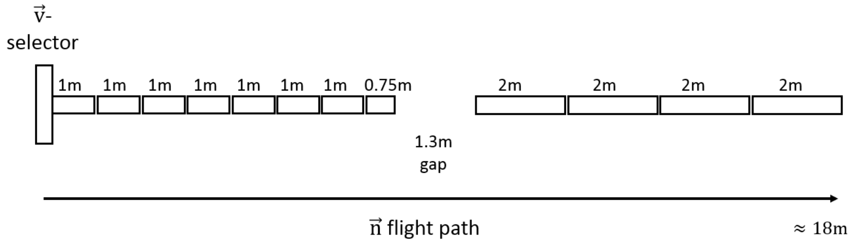

Figure 81: The beamline consisting of the velocity selector, 8.75 m neutron guide, 1.3 m gap in front of the inner neutron guide of PERC and the 8 m long inner guide. The inner guide is not yet determined and shown in 2 m pieces here.

The gap is followed by the 8 m long neutron guide in PERC. The exact geometry of this guide is not determined yet. For the current study, the dimensions of the inner guide are varied to investigate their influence on the neutron flux. Additional aspects are the segmentation of the guide in different segments and the implementation of pumping slits with minimized neutron losses.

For the simulation of neutron guides, the reflectivity of each guide wall has to be determined. This is commonly described using a model as shown in figure 82. Its parameters are the m-value (i.e. the maximum angle of reflection), the reflectivity in the region of total reflection R_0, the momentum transfer of total reflection Q_c, the slope of the reflectivity curve α and the width at critical angle of reflection W. These values were determined by the measured reflectivity curve of a Cu/Ti supermirror m = 1.95 of the year 2017.

- m-value = 1.95
- $R_0 = 0.995$
- $Q_c = 0.01946$
- $\alpha = 7.905$
- $W = 0.0043$

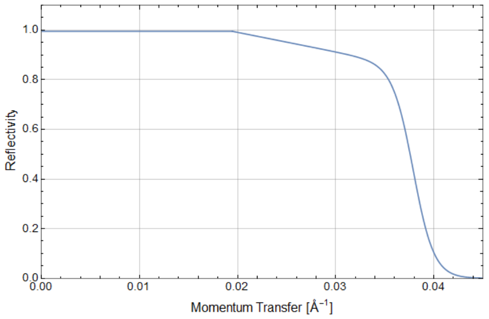

Figure 82: Reflectivity curve of the PERC Cu/Ti guide used for McStas simulations and the corresponding parameters. The curve is based on the experimental results shown in chapter 5.

8.3.1 Beam Preparation

For the guide in front of PERC, the height and width were considered separately to investigate corresponding divergence effects independently. By investigating the loss of neutrons in the 1.3 m gap, it is possible to find reasonable guide geometries.

Determination of guide width effects

To exclude effects caused by vertical divergence, the height of the 8.75 m long neutron guide was left constant at 20 mm and the width was varied from 30 mm to 70 mm for neutron flux evaluation. Table 23 shows the results for a neutron wavelength of 4 Å(Appendix C.1). The first column contains the guide geometry, followed by the neutron loss in the 1.3 m gap, the gap transmission and the total flux at the end of the PERC instrument. The McStas code for the corresponding simulation is shown in appendix C.1, together with the tables for 6 Å and 8 Å neutrons. Each table shows the result of several simulations.

There is no loss in the gap for smaller guide widths than 34 mm due to the maximal beam divergence of about 0.02 rad for 4 Å. For guide widths larger than 60 mm, the total flux at the end of the instrument begins to decrease again (marked red). This can be explained by the fact, that the MEPHISTO guide in front is also only 60 mm broad. Therefore, it is not recommended to increase the width of the guide between the MEPHISTO exit and the inner PERC guide to more than 60 mm. Figure 83 shows the behavior of the neutron flux along the beamline for the different guide widths in front of PERC.

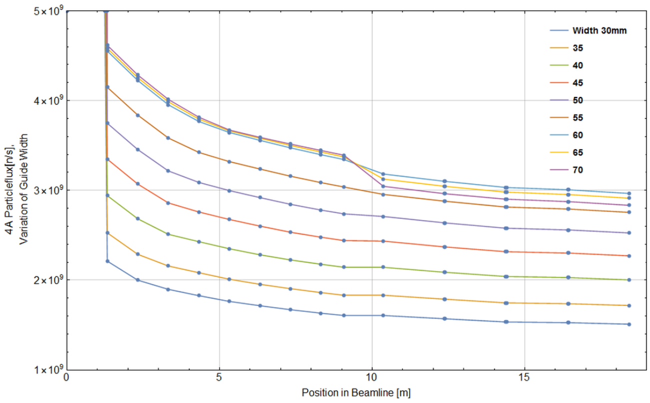

Figure 83: Particle flux in neutrons per second versus position in beamline for different neutron guide widths in front of PERC. Only every fifth simulation is shown for clarity.

The drop at about one meter comes from the slit, which is limiting the beam to the defined geometry. The shape of the curves look quite similar in the “free flight” (1 m − 9 m) section and only the intensity differs. It can be seen, that till a guide width of 34 mm there is no neutron loss in the gap. For higher neutron guide widths, losses start to increase due to divergence effects and the gap length of 1.3 m. The corresponding gap transmission for 4 Å is presented in figure 84. It shows, that the transmission is nearly 1 up to a width of 40 mm and is then decreasing. For a width of 70 mm, it is only 90 %.

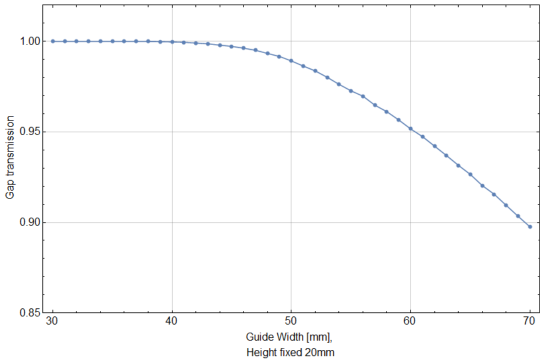

Figure 84: The gap transmission in front of PERC instrument for different guide widths and constant height of 20 mm. The neutron wavelength is 4 Å. Even for a width of 70 mm the loss is only about 10 %.

Figure 85 shows, that the total flux at the end of the instrument is decreasing for widths over 60 mm.

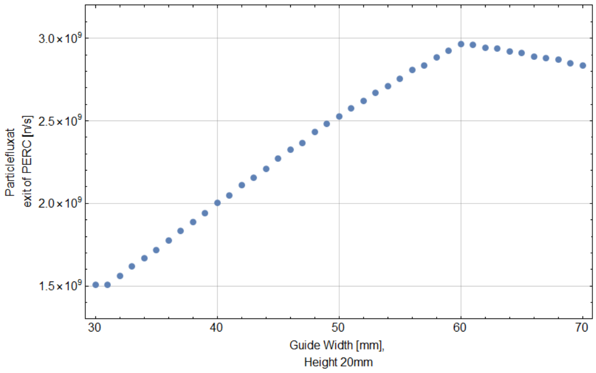

Figure 85: Total flux in neutrons per second at the exit of PERC instrument for varying guide width and constant height of 20 mm. The neutron wavelength is 4 Å.

For higher neutron wavelengths, like 6 Åor 8 Å, the transmission through the gap decreases more with larger guide widths. This is explained by a larger beam divergence for these wavelengths.

Determination of guide height effects

For the investigation of the guide height the procedure is similar. The width is held constant and the height is varied from 20 mm to 70 mm to investigate the influence of divergence effects.
From table 26 (appendix C.1) it can be derived, that there is no neutron loss in the gap up to a height of 26 mm. Compared to the width considerations, there is no maximum of the flux at the end of PERC, because the MEPHISTO guide in front has a height of 106 mm, which is always larger than the beam height and the flux in y-direction is distributed uniformly.
Figure 86 shows the flux distribution for certain guide heights. The graphs for neutron wavelengths of 6 Å and 8 Å can be found in appendix C.1.

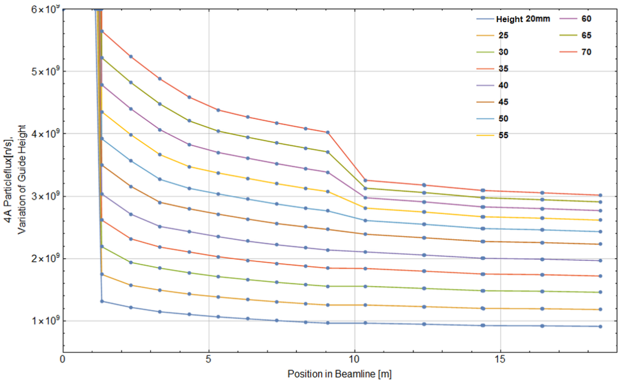

Figure 86: The particle flux in neutrons per second (y-axis) versus position in beamline (x-axis) for different neutron guide heights in front of PERC. Only every fifth simulation is plotted for clarity.

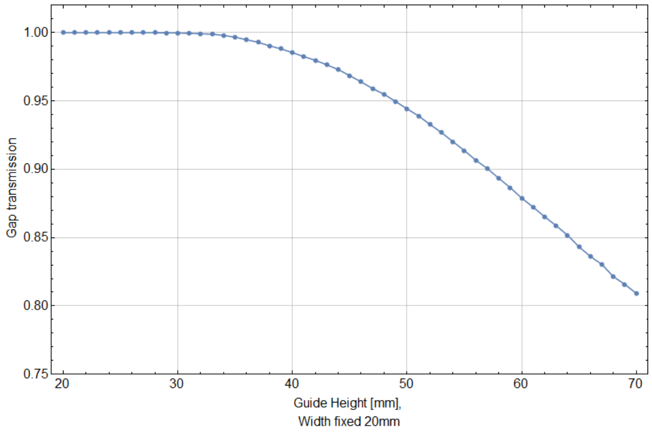

Figure 87: The transmission through the gap in front of the PERC instrument as a function guide height and constant width of 20 mm. The simulated neutron wavelength is 4 Å.

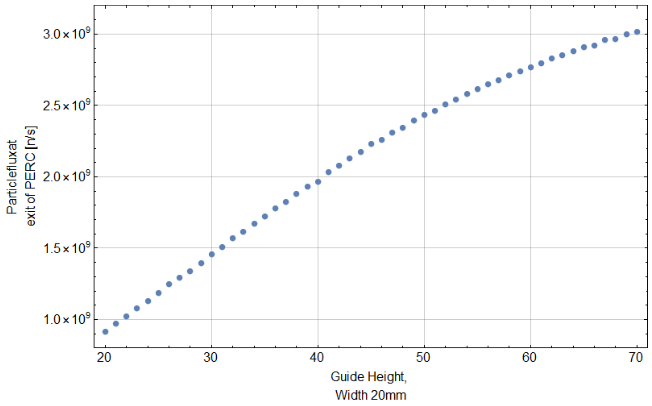

Figure 88: The total flux in neutrons per second at the exit of the PERC instrument for different guide height and constant width of 20 mm. The simulated neutron wavelength is 4 Å.

Reasonable guide geometry in front of PERC

The results from above were used to determine preferable guide geometries of the guide in front of PERC. Table 16 shows the simulation results for these guide geometries. The values for the guide height and width were chosen, that the losses in the gap increase by approximately 5 % from one to another.

To suppress neutron losses and therefore the background almost completely, a very small guide of 34 x 26 mm^2 has to be chosen. In contrast this would decrease the

Table 16: Wavelength 4 Å. Simulations of different geometries of the guide in front of PERC.

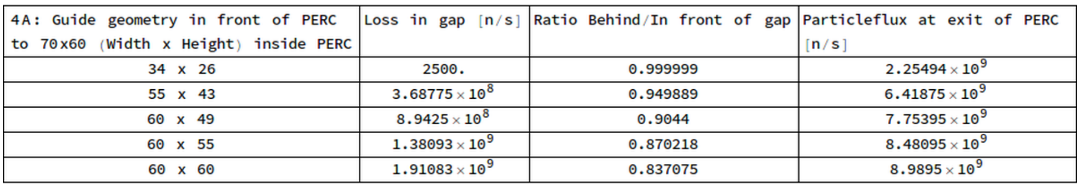

4A: Guide geometry in front of PERC to 70x60 (Width x Height) inside PERC	Loss in gap [n/s]	Ratio Behind/In front of gap	Particleflux at exit of PERC [n/s]
34 x 26	2500.	0.999999	2.25494×10^9
55 x 43	3.68775×10^8	0.949889	6.41875×10^9
60 x 49	8.9425×10^8	0.9044	7.75395×10^9
60 x 55	1.38093×10^9	0.870218	8.48095×10^9
60 x 60	1.91083×10^9	0.837075	8.9895×10^9

neutron flux at the exit by a factor of 4 compared to a guide with 60 x 60 mm^2. Every neutron that is not transmitted to the inner neutron guide of PERC has to be absorbed by shielding around. The maximum allowed background level defines the final guide geometry in front of PERC.

8.3.2 Guide in PERC

In the following, some possible geometries of the PERC inner guide (decay volume) are discussed. The focus lies on the achievable neutron flux at the exit of the decay volume. Different designs in terms of guide length, pumping slits between two guide elements and guide extension from one guide piece to the next will be presented. The aim of the extension in horizontal direction from one guide piece to another is neutron loss reduction in the pumping slit between the two pieces, which is needed to be able to pump down the decay volume to UHV-region. The extension of the guide in horizontal direction was designed, so that almost the whole divergence spectrum of the beam is transmitted to the next guide section. The slits on top and bottom are minimized to reduce neutron losses in pumping slits as much as possible. Figure 89 shows the top view onto two guide pieces. The guides are extended in width and the sides are open for pumping.

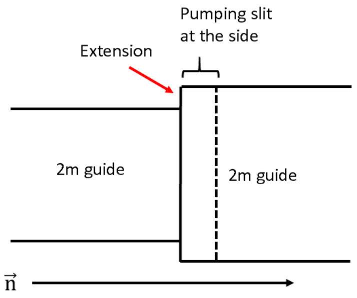

Figure 89: The top view onto two guide segments inside PERC. The second guide segment is 2 mm broader in order to reduce losses in the 20 mm long pumping slits on both sides of the guide.

In McStas, it is not possible to define different lengths for the top and bottom plates of one guide element. Therefore, they were simulated by two additional mirrors with same reflectivity. In reality this top and bottom plates could be realized by simply making the top and bottom plates of the neutron guide 20 mm longer than the side plates.

In the following, four different geometries were investigated in order to determine a geometry of the decay volume with optimized neutron flux at the exit.

- Eight 1 m long guide segments inside PERC with 10 mm gap for pumping, with an initial cross section of 60 × 60 mm^2
- Eight 1 m long guide segments inside PERC with 10 mm gap for pumping, with an initial cross section of 60 × 60 mm^2. Subsequent segments are each 1 mm wider.
- Four 2 m long guide segments inside PERC with 20 mm gap for pumping, with an initial cross section of 60 × 60 mm^2. Subsequent segments are each 2 mm wider.
- Four 2 m long guide segments inside PERC with 20 mm gap for pumping, with an initial cross section of 70 × 60 mm^2. Subsequent segments are each 2 mm wider.

A neutron wavelength of 5 Å was used for the following simulations. Figure 90 shows the neutron flux at the exit of PERC dependent on the guide geometry in front of the instrument and the inner guide.

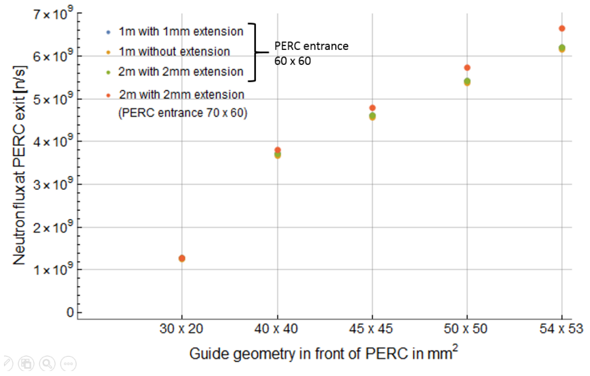

Figure 90: The neutron flux at the exit of PERC for different guide geometries in front of PERC and different geometries of the inner guide. The neutron wavelength is 5 Å.

As expected, the neutron flux at the exit of PERC with an inner guide geometry of $60 \times 60\,\text{mm}^2$ is increasing with increasing diameter of the guide in front. A further flux optimization is achieved by increasing the cross section of the decay volume from $60 \times 60\,\text{mm}^2$ to $70 \times 60\,\text{mm}^2$. For a front guide with cross section $50 \times 50\,\text{mm}^2$, the neutron flux at the exit could be increased from $\approx 5.4 \cdot 10^9\,\text{n/s}$ (Fig. 90, green point) to $\approx 5.8 \cdot 10^9\,\text{n/s}$ (Fig. 90, red point). Although the neutron flux at the exit is increasing with increasing diameter of the front guide, the neutron losses in the 1.3 m gap also get significantly larger. For an initial cross section in PERC of $60 \times 60\,\text{mm}^2$ for example, the neutron loss in the gap is only about 6 % for a guide geometry of $40 \times 40\,\text{mm}^2$ in front of PERC and already about 25 % for $60 \times 60\,\text{mm}^2$ (see table 29 in appendix C.2). Here, again a compromise between flux and background has to be made.

For a comparison of the four different possibilities of the inner guide, the results are shown separately. We compare the relative neutron flux at the exit of PERC and define the flux with the highest value as 1.

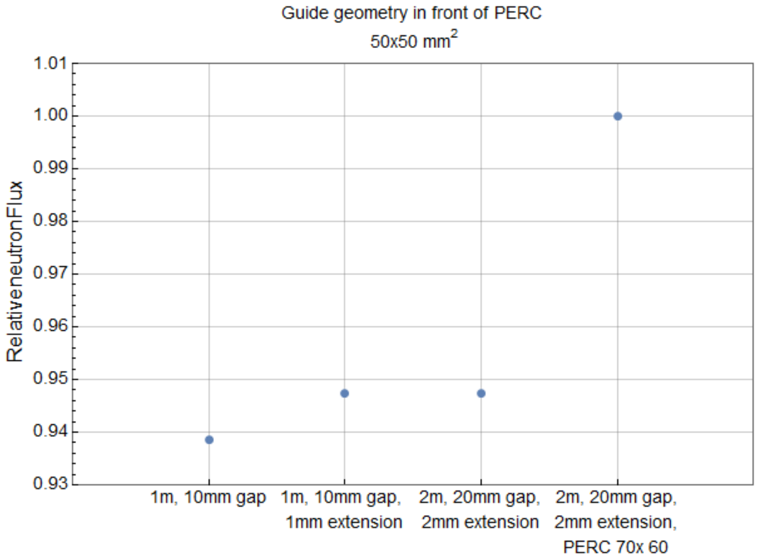

Figure 91: Comparison of the neutron flux at the exit of PERC dependent on the inner guide geometry. With a $50 \times 50\,\text{mm}^2$ guide in front of PERC, the neutron loss inside the gap is about 15 % for the $60 \times 60\,\text{mm}^2$ inner guide and about 15 % for $70 \times 60\,\text{mm}^2$ inner guide.

The presented simulation results show, that the difference in neutron flux for the different geometries is in the range of only few percent. Here, the neutron flux can be increased by $\approx 1\,\%$ compared to simple slits by broadening the neutron

guide after each guide segment. This is explained by a larger angular acceptance for neutrons in the following guide segment. As expected, the effect is identical for the segmentation of 1 m and 2 m, because the angle from one piece to the next is $\alpha = \arctan(1/10) = \arctan(2/20) = 0.099\,\mathrm{rad}$. The simulation of the $70 \times 60\,\mathrm{mm}^2$ shows the highest flux at the exit. This broadening of 10 mm of the first inner neutron guide decreases the losses in the gap from 15 % to 10 %. The width and height of the inner guide are limited to a maximum of $70 \times 60\,\mathrm{mm}^2$ by the size of the warm bore.
In conclusion, the presented simulations show several geometrical considerations, which can be used to choose a neutron flux optimized and background minimized geometry for the instruments beamline. It is recommended to choose the maximal possible guide size for the inner guide of PERC to minimize neutron losses in front of PERC and maximize the neutron flux at the exit at once. The geometry of the guide in front of PERC has to be chosen after the consideration of the maximum allowed background in the gap.

For example, considering a neutron guide with a cross section of $60 \times 60\,\mathrm{mm}^2$ in front of PERC and an inner guide with the same cross section, one would have a neutron loss of 25 % through the gap (see table 29). This equals a simulated neutron flux $\approx 2.5 \cdot 10^9\,\mathrm{n\ s}^{-1}$. Choosing a decay volume, consisting of eight 1 m pieces, with a 10 mm gap and 1 mm extension after each piece, one would end up with a high neutron flux of $7.2 \cdot 10^9 \mathrm{n\ s}^{-1}$ at the exit of the PERC instrument.

9 Analysis of the Beam Polarization of the Measurement of the Proton Asymmetry with Perkeo III

In 2014/2015 Perkeo III was installed at the ILL to measure the proton asymmetry parameter $C = -x_C(A + B)$, which allows new cross-checks within the standard model (see chapter 1.1 for details). For the first time, an improved measurement setup allowed to determine the parameter C as a function of the proton energy. Here, a polarized and pulsed beam of cold neutrons was used. The same detectors were used for protons and electrons, as the protons are converted to electrons by ultra-thin carbon foils in front of the detectors.

To avoid expectation bias during analysis, the data analysis was blinded and performed by the different collaboration partners. The major parts of the analysis like detector characterization, background treatment and other systematic effects are finished and presented with scaled values e.g. in Refs. [49, 50]. The neutron beam polarization is linearly related to the proton asymmetry and is therefore one of the most important corrections. Its detailed analysis is shown in the following. Also the result presented here is scaled by a blinding factor, as not all other systematic effects have been analyzed completely yet.

9.1 Polarization Analysis with a flip-able Analyzer

^{3}He offers a strong neutron spin-dependent absorption cross-section and is therefore often used as polarized He spin filter [159]. For the polarization measurements here, the beamstop was replaced by a cell, filled with polarized ^{3}He gas, inside a “magic box” and a detector behind it. The “magic box” is a compact magnetostatic cavity, which provides a very homogeneous magnetic environment for the polarized ^{3}He cell [160]. This device allows to transport or host the spin filter on a beam line. Due to the strong spin-dependence of neutron absorption cross-section, ^{3}He cells are used for high precision polarization analysis with cold neutrons [145]. Incoming neutrons with spin parallel to the spin of the ^{3}He gas are transmitted through the cell. This state is called “white” in the following. If the neutron spin is anti-parallel to the ^{3}He spin, neutrons are absorbed inside the cell. Such state is called “black”. By flipping the magnetic holding field of the “magic box”, also the spin of the ^{3}He gas flips. This allows to continuously skip between black and white state of the cell during a measurement. The setup is shown in figure 92.

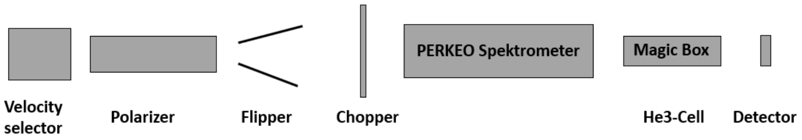

Figure 92: Setup of the polarization measurement: The neutrons fly from left to right. With a time-of-flight measurement, a π-flipper and a flip-able analyzer, the polarization can be determined as a function of wavelength.

When working with the shown setup, the following measurements are used to define the polarization of a neutron beam:

$$\begin{aligned}
n_{w0} &= \epsilon T_A I(1+AP) \text{ (}^3\text{He white, flipper off} \rightarrow \text{high count rate)} && (9.1)\\
n_{w1} &= \epsilon T_A I(1-AFP) \text{ (}^3\text{He white, flipper on} \rightarrow \text{low count rate)} && (9.2)\\
n_{b0} &= \epsilon T_A I(1-AP) \text{ (}^3\text{He black, flipper off} \rightarrow \text{low count rate)} && (9.3)\\
n_{b1} &= \epsilon T_A I(1+AFP) \text{ (}^3\text{He black, flipper on} \rightarrow \text{high count rate)} && (9.4)
\end{aligned}$$

Here ϵ is the detector efficiency, T_A is the spin independent transmission, I the beam intensity, P the polarization, A the analyzing power and F the flipper efficiency. Without using the neutron flipper, the product AP_{13} (calculated from states of equ. 9.1 and 9.3) can be determined

$$AP_{13} = \frac{n_{w0} - n_{b0}}{n_{w0} + n_{b0}} \ , \tag{9.5}$$

with

$$\Delta(AP_{13}) = \frac{2}{(n_{w0} + n_{b0})^2} \cdot \sqrt{(n_{b0}\Delta n_{w0})^2 + (n_{w0}\Delta n_{b0})^2} \ . \tag{9.6}$$

To obtain the observables described in equ. 9.2 and 9.4 the neutron spin is flipped upstream by a fast adiabatic spin-flipper. The efficiency of such flipper is given by its flipping ratio and can be extracted by

$$F = \frac{n_{w0} - 2n_{w1} + n_{b0}}{n_{w0} - n_{b0}} \ , \tag{9.7}$$

$$\begin{aligned}\Delta F =&\frac{2}{(n_{w0} - n_{b0})^2} \cdot \\ &\cdot \sqrt{((n_{w1} - n_{b0})\Delta n_{w0})^2 + ((n_{w0} - n_{b0})\Delta n_{w1})^2 + ((n_{w0} - n_{w1})\Delta n_{b0})^2} \ .\end{aligned} \tag{9.8}$$

The transmission of a polarized ^{3}He cell is given by

$$T_{He}(\lambda) = T_{cell}(\lambda)\exp(-Olp\lambda(1 \pm P_{He})) \ , \tag{9.9}$$

with

$$O \equiv \frac{N_A \frac{\sigma_{th}}{\lambda_{th}}}{\mathrm{V}_m \frac{T}{T_0}} = 7.34 \cdot 10^{-2} \frac{1}{\mathrm{cm} \cdot \mathrm{bar}} \ . \tag{9.10}$$

T_{cell} is the transmission of the empty cell with $T_{cell} < 1$, due to absorption in the entrance and exit window. l is the length of the cell volume, p the ^{3}He pressure and P_{He} the ^{3}He polarization. The minus sign is used for neutrons with spin anti-parallel to that of ^{3}He and plus for neutrons with spin parallel to ^{3}He. The values used to calculate O are the temperatures $T = 295.15\,\mathrm{K}$ (reference temperature), $T_0 = 273.15\,\mathrm{K}$, $\mathrm{V}_m = 22.414\,\mathrm{l/mol}$ and $\sigma_{th} = 5316\,\mathrm{barn}$ for the thermal cross-section of the reaction ^{3}He(n,p)t [161].

With the expression for the transmission of a ^{3}He cell and Equ. 9.1 and 9.3 the expressions for the intensity and the product AP can be written as

$$I_{rel} \equiv n_{w0} + n_{b0} = 2\epsilon I T_{\mathrm{cell}} \exp(-Olp\lambda) \cosh(Olp\lambda P_{\mathrm{He}}) \ , \tag{9.11}$$

$$AP_{13} \equiv \frac{n_{w0} - n_{b0}}{n_{w0} + n_{b0}} = P \tanh(Olp\lambda P_{\mathrm{He}}) \ . \tag{9.12}$$

Taking into account, that the ^{3}He polarization is decreasing with time

$$P_{\mathrm{He}}(t) = P_{\mathrm{He},0} \exp\left(-\frac{t}{t_0}\right) \tag{9.13}$$

and considering a finite wavelength resolution parameter σ as a consequence of time-of-flight measurement with a chopper and velocity selector, the time-dependent intensity is given by

$$\begin{aligned} I_{\mathrm{rel}}(t) &= n_{w0}(t) + n_{b0}(t) \\ &= 2\epsilon I T_{\mathrm{cell}} \exp\left(-Olp\lambda_0 \left(1 - \frac{Olp\sigma^2}{\lambda_0} \frac{1 + (P_{\mathrm{He},0}\exp(-t/t_0))^2}{2}\right)\right) \times \\ &\quad \cosh\left(Olp\lambda_0 \left(1 - \frac{Olp\sigma^2}{\lambda_0}\right) P_{\mathrm{He},0} \exp(-t/t_0)\right) \ . \end{aligned} \tag{9.14}$$

The parameters O, l, p, λ_0 and σ are known or were measured. The transmission T_{cell} of the empty cell is mainly limited by the entrance and exit windows, which in this case are made of 1 cm Si each and can be calculated by

$$T_{\mathrm{cell}} = \exp\left(-\frac{\rho}{M} N_A \Sigma(\lambda) L\right) \ . \tag{9.15}$$

Here $\rho = 2.33\,\mathrm{g/cm}^3$ is the mass density of Si, $M = 28\,\mathrm{u}$ the molar mass, N_A the Avogadro number, $L = 2\,\mathrm{cm}$ the thickness of both windows together and $\Sigma(\lambda)$ the total cross-section per atom. The values for $\Sigma(\lambda)$ were taken from [59]. The calculated cell transmission as a function of the neutron wavelength is shown in figure 93.

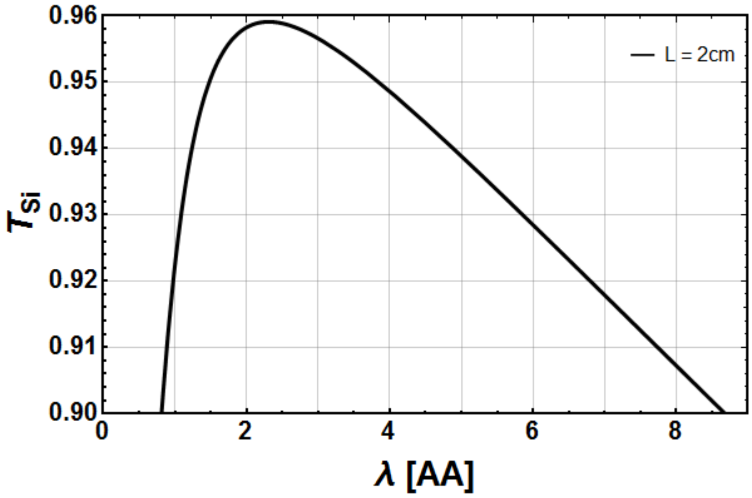

Figure 93: Resulting transmission of the two cell windows with 1 cm thickness each. Equ. 9.15 was used for the calculation.

The relaxation times of the ^{3}He cells were determined by a fit using Equ. 9.14 with I and t_0 being free parameters. The value for t_0 is then used to determine the time-dependent analyzing power of each cell by

$$A_{\mathrm{He}}(t) = \tanh\left(Olp\lambda_0 P_{\mathrm{He},0} \exp\left(-\frac{t}{t_0}\right)\right) \ . \tag{9.16}$$

The detector setup with the ^{3}He-cells mounted on a moveable table because the detector itself did not cover the whole beam. The measurement of the time-dependent intensity was always performed at the same horizontal position. The fit results of the used cells labelled with number $4-7$ and the corresponding time-dependent analyzing powers are shown in figures 94 - 97. The results of the fits with I and t_0 as free parameters are used for the further analysis. The higher χ^2_{red}-value in figure 94 could be explained by the significant longer measurement time, where the fixed cell parameters gain influence. An additional systematic effect, like background variation, would also gain influence at longer times where measurement rates get lower.

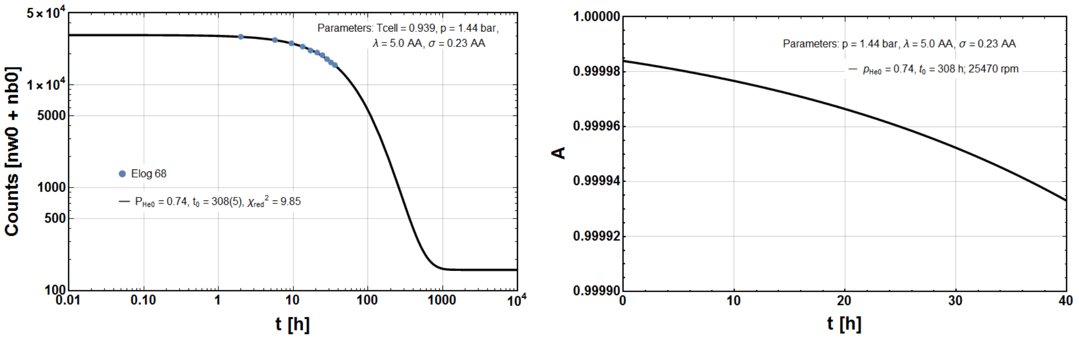

Figure 94: The cell relaxation for the polarization measurement behind PERKEO III, central scan (Elog #68). Left: Fit with I and t_0 as free parameters for the measured intensity at reference point $x = 0$ and a selector velocity of 25470 rpm corresponding to a central nominal neutron wavelength of 5 Å. Right: Resulting time evolution of the analyzing power for the fit results in the left plot. The difference is well below 10^{-4} for $t < 40\,\mathrm{h}$, which is the operation time of the cell within the measurements.

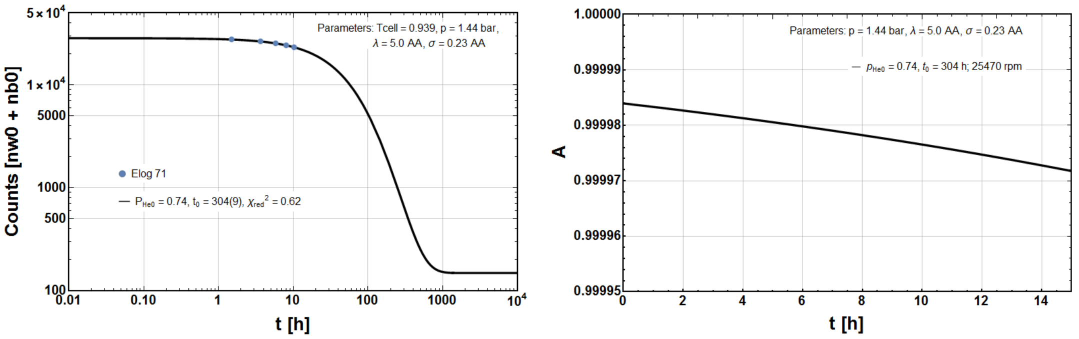

Figure 95: The cell relaxation for the polarization measurement behind PERKEO III, central scan shifted for systematic check (Elog #71). Left: Fit with I and t_0 as free parameters for the measured intensity at reference point $x = 0$ and a selector velocity of 25470 rpm. Right: Resulting time evolution of the analyzing power for the fit results in the left plot. The difference is well below 10^{-4} for $t < 15\,\mathrm{h}$, which is the operation time of the cell within the measurements.

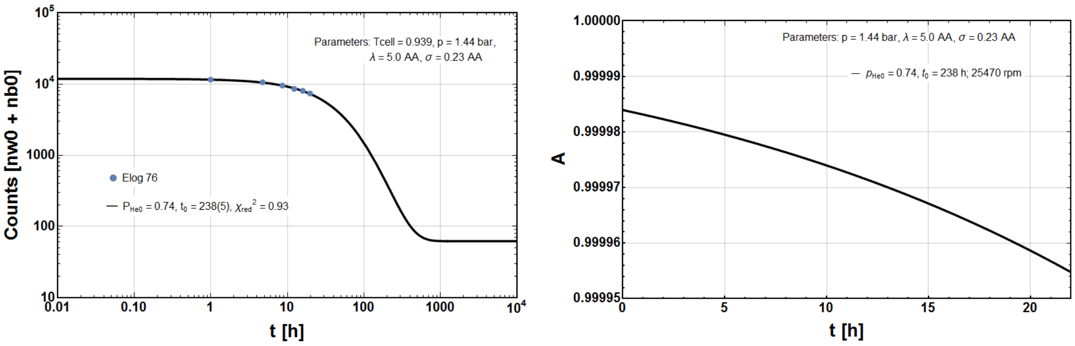

Figure 96: The cell relaxation for the polarization measurement behind Perkeo III, lower scan (Elog #76). Left: Fit with I and t_0 as free parameters for the measured intensity at reference point $x = 0$ and a selector velocity of 25470 rpm. Right: Resulting time evolution of the analyzing power for the fit results in the left plot. The difference is well below 10^{-4} for $t < 24\,\text{h}$, which is the operation time of the cell within the measurements.

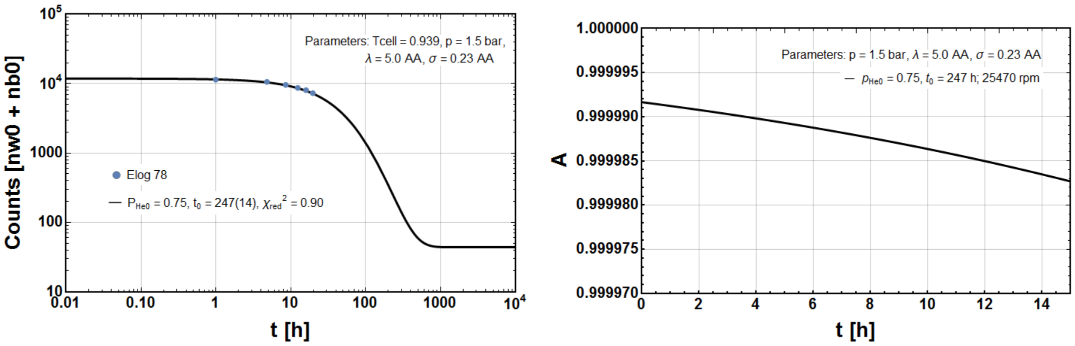

Figure 97: The cell relaxation for the polarization measurement behind Perkeo III, upper scan (Elog #78). Left: Fit with I and t_0 as free parameters for the measured intensity at reference point $x = 0$ and a selector velocity of 25470 rpm. Right: Resulting time evolution of the analyzing power for the fit results in the left plot. The difference is well below 10^{-5} for $t < 15\,\text{h}$, which is the operation time of the cell within the measurements.

9.2 Measuring Procedure

For the measurement of the beam polarization with a ^{3}He cell as flip-able analyzer, the cross-section of the beam was divided in 18 sections with a size of $5 \times 8\,\text{cm}^2$ owing to the input aperture of the cell. Figure 98 shows the segmentation of the beam for the polarization measurements. Scanning the beam in three horizontal positions (top, center, bottom), characterizes the complete neutron beam. The red rectangles (I - VII) indicate a measurement shifted by one half of the aperture width as a systematic test.

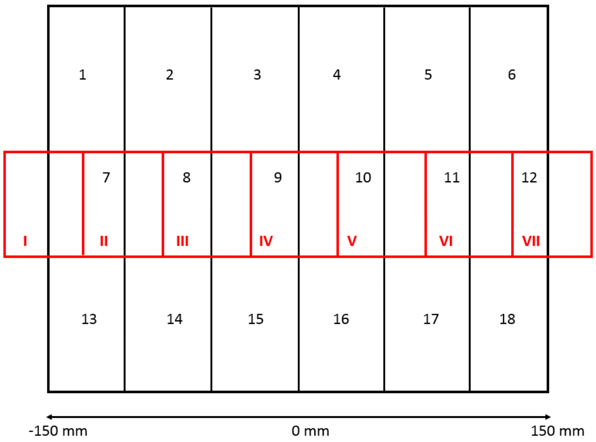

Figure 98: The small rectangles represent the input aperture $5 \times 8\,\mathrm{cm}^2$ of the ^{3}He cell. By scanning at three horizontal levels ($1-6$ top, $7-12$ center and $13-18$ bottom), the whole beam is characterized. The red rectangles (I - VII) represent a measurement series shifted by one half of the aperture width as a systematic test.

To characterize the complete neutron beam, four polarization measurements were carried out, using four different ^{3}He cells:

- Cell 4 (Elog #68): Measurement in central row (Fig 98, $7-12$) for $\lambda = 4.5\,\text{Å}; 5.0\,\text{Å}; 5.5\,\text{Å}$
- Cell 5 (Elog #71): Measurement in central row shifted by one half of the aperture width (Fig 98, I - VII) for $\lambda = 5.0\,\text{Å}$
- Cell 6 (Elog #76): Measurement in bottom row (Fig 98, $13-18$) for $\lambda = 4.5\,\text{Å}; 5.0\,\text{Å}; 5.5\,\text{Å}$
- Cell 7 (Elog #78): Measurement in top row (Fig 98, $1-6$) for $\lambda = 4.5\,\text{Å}; 5.0\,\text{Å}$ (flipper not working for $5.5\,\text{Å}$)

Table 17: Datasets of the polarization measurements. The chopper frequency is 76 Hz for the measurements. The Neutron velocity selector has a finite wavelength resolution assuming a FWHM of 10.8 %.

Measurement	Data file number	Vertical position	Selector frequency [rpm]
Elog #68, Cell 4	42222 – 42764	Central	23154, 25470, 28300
Elog #71, Cell 5	42793 – 43165	Central, shifted	25470
Elog #76, Cell 6	43249 – 43621	Bottom	23154, 25470, 28300
Elog #78, Cell 7	43627 – 44011	Top	25470, 28300

The total measurement time in each case file is 480 seconds. The "white (w)" state of the ^{3}He cell is the one with high neutron transmission, when the spin flipper is off and the "black (b)" state is the one with low neutron transmission, when the spin flipper is off. For each case in terms of position and selector speed, a sequence of states of the ^{3}He cell "w-b-b-w-b-w-w-b" was measured. For each state, the spin-flipper is turned on and off several times. The sequence for "white" state (Off-On [s]) is: $20 - 200 - 20 - 100 - 40 - 100$. For statistical sensitivity, the states with low neutron transmission are measured 400 s, whereas the others are measured 80 s. For "black" orientation this sequence is given by (Off-On [s]): $100 - 40 - 100 - 20 - 200 - 20$.

9.3 Results of the Measurements

Intensity scans for the three heights and the x-positions covering the horizontal range ($-150 \dots 150$ mm) were performed to determine the region of interest of the beam and to be able to calculate an intensity weighted average beam polarization in the end. The intensity measurements were performed for selector velocities of 23154 rpm, 25470 rpm and 28300 rpm, which corresponds to central neutron wavelengths of 5.5 Å, 5 Å and 4.5 Å. It was measured via a detector with a nominal efficiency of $5 \cdot 10^{-5}$, which changes with v_0/v. Hence, the capture intensity was measured, which is proportional to the decay probability of neutrons inside the decay volume. Figure 99 shows the result for 25470 rpm. The measurement region represents almost the complete beam, as the intensities in the outer regions are close to 0.

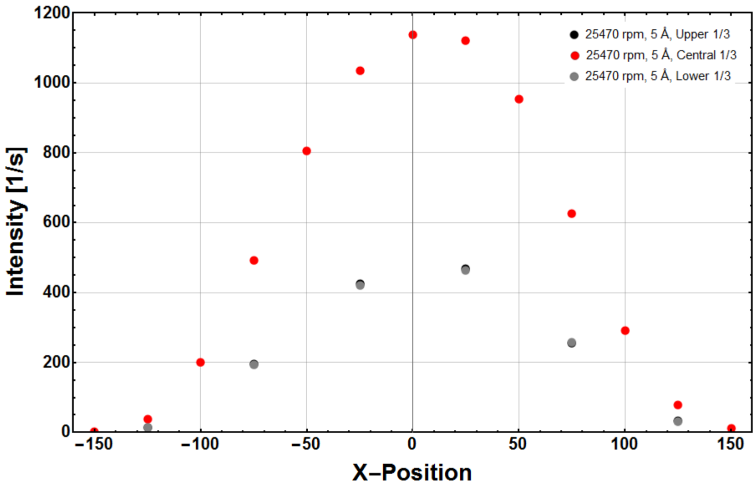

Figure 99: Intensity scans at different heights and horizontal positions for a selector velocity of 25470 rpm (Elog 73, 75, 79). The error bars are smaller than the markers.

For each TOF measurement and combination of ^{3}He cell orientation (white and black) and flipper (on, off), the following spectra were extracted:

- Uncorrected spectra $N(i)$. This is the sum of identical flipper and cell combinations in counts per bin.
- Uncorrected normalized spectra $n(i)$. This is the sum of identical flipper and cell combinations in counts per bin.
- Dead time corrected spectra $n_{Dt,Cor}$ in [neutrons/bin · s] for a detector dead time of 2 µs.
- Background subtracted spectra $n_{Bg,Cor}$ in [neutrons/bin · s].
- Dead time and background corrected spectra $n_{Dt,Bg,Cor}$ in [neutrons/bin · s].
- Separate intensity spectra in [neutrons/s] at the different measurement positions. These intensities were used to calculate the polarization at a certain point and its normalization.

Figure 100 shows the uncorrected spectra of the configurations ^{3}He cell in white mode with spin flipper off and ^{3}He cell in black mode with spin flipper off for a measurement time of 80 seconds (Elog #71). A high signal to background ratio is noticeable for both cases.

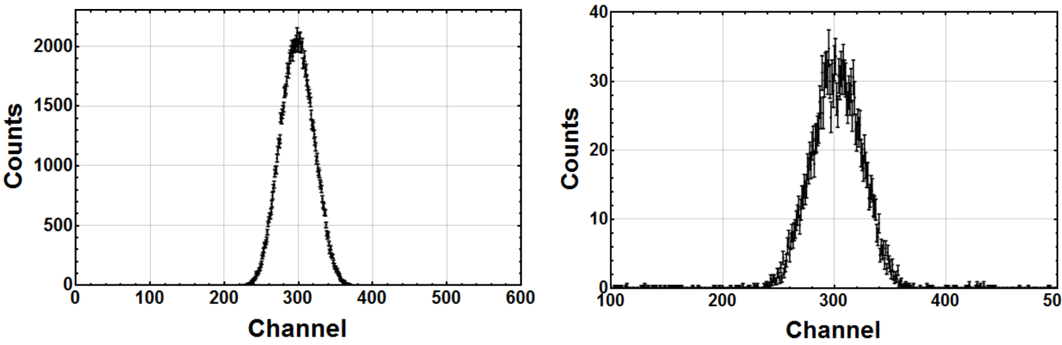

Figure 100: Uncorrected raw spectra in counts per bin for the configurations ^{3}He cell in white mode with spin flipper off and ^{3}He cell in black mode with spin flipper off. Each time channel has a width of 20 µs.

The uncorrected normalized spectra $n(i)$ [n/(bin*s)] were obtained by dividing $N(i)$ by the measured time per bin i. This is the product of the total measuring time in the state in seconds, the chopper frequency in pulses per seconds and the bin width in seconds. Figure 101 shows such spectra for the different horizontal positions at central height (Cell 5, shifted) of the beam.

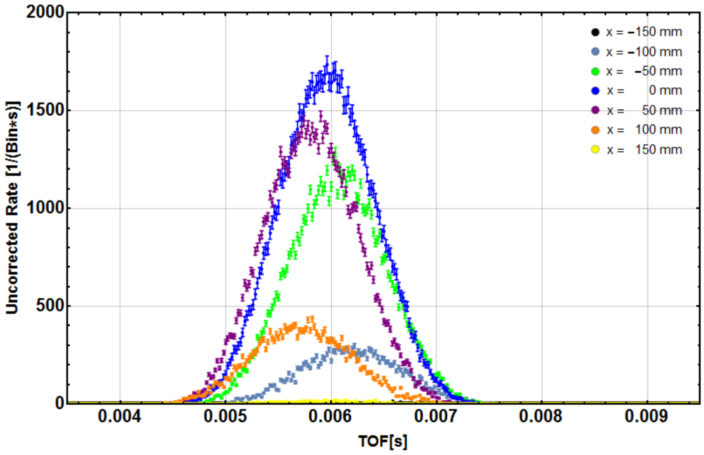

Figure 101: Horizontal scan in central height with the standard aperture of 50 x 80 mm^2 for a selector velocity of 25470 rpm (Cell 5).

The dead time corrected spectra $n_{\mathrm{Dt,Cor}}(i)$, assuming a detector dead time of 2 µs, were obtained by

$$n_{\mathrm{Dt,Cor}}(i) = \frac{n(i)}{1-n(i)\tau}, \text{ with } \delta n_{\mathrm{Dt,Cor}}(i) = \frac{\delta n(i)}{1-n(i)\tau} \; . \tag{9.17}$$

In this relation no systematic uncertainty of the dead time is included. Figure 102 presents the effect of the dead time correction on the spectrum with maximum rate at $x = 0$. The effect is small. The maximum correction (at the point of highest count-rate) is 0.35 %.

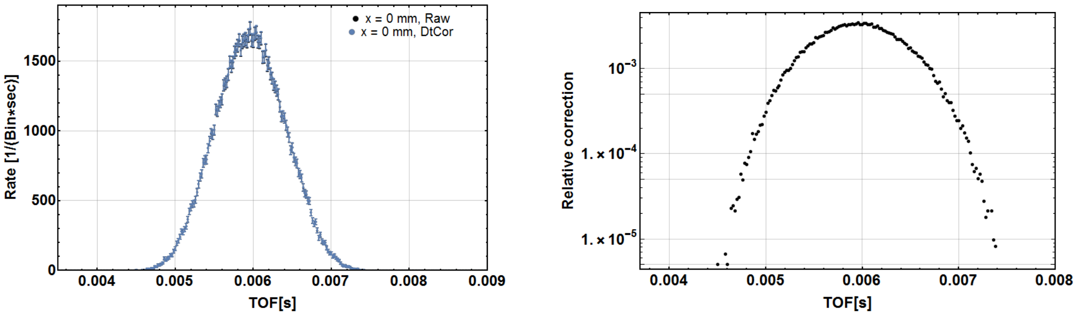

Figure 102: Left: The effect of dead time correction for the scan point at $x = 0$ (Elog #71, chopper frequency 76 Hz, selector velocity 25470 rpm). Right: The corresponding small relative correction.

The background for the measurement was determined by averaging the normalized spectra $n(i)$ over two background windows. One is before the neutron pulse (bins 1 − 200) and the other is after it (bins 450 − 490). The background was then subtracted bin wise. In the single bins with a small width, negative rates were accepted. The result is presented in figure 103.

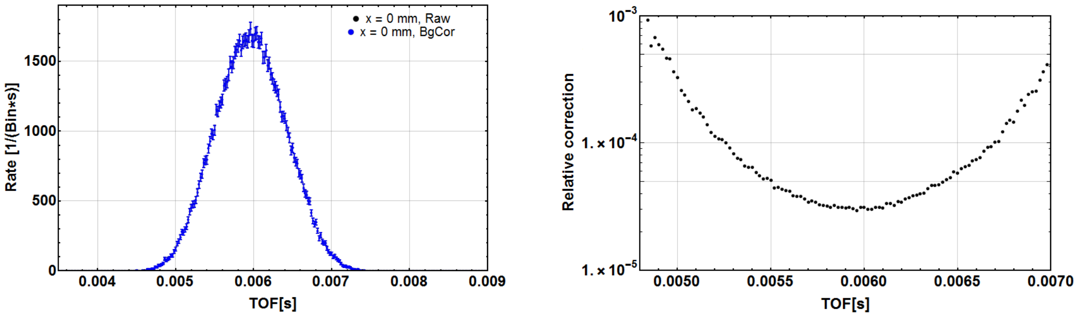

Figure 103: Left: The effect of background correction for the scan point at $x = 0$ (Elog #71, chopper frequency 76 Hz, selector velocity 25470 rpm). Right: The corresponding relative correction shows, that the background is negligible.

For AP values very close to one, there is still the possibility of a negative pulse integral due to statistical fluctuation. If the intensity of a neutron pulse integral is negative, the resulting AP value above one would be unphysical. In the presented analysis, this was only the case at the beam corners with low statistical weight. AP values greater than one were accepted within this analysis, as the correction of this effect will be carried out in subsequent analysis steps with an approach like it is described in Ref. [162]. A neutron spin dependence of the background was excluded by comparing the background of the measurements in white state with spin flipper off and in black state with spin flipper off. The background values for both configurations were identical within statistical uncertainties.

The dead time and background corrected spectra $n_{\mathrm{DtCor,BgCor}}(i)$ were obtained by subtracting the background from the dead time corrected spectra. Figure 104 shows the effect of both corrections on the data.

These corrections were applied to each measurement of the 4 configurations n_{w0}, n_{w1}, n_{b0} and n_{b1} from Equ. 9.1-9.4 for the different selector velocities and positions. With the corrected spectra and Equ. 9.5, AP_{13} is obtained for each rectangle of the beam $(1-18$, see Fig. 98).

Since the decay probability of the neutrons is proportional to the beam intensity, the intensity weighted average beam polarization is determined. To do so, one has to weigh the measured polarization with the beam intensity at that point. Then the intensity weighted average beam polarization can be calculated. Alternatively, it would be possible to sum up the events of both spin-states over the full beam to calculate the average beam polarization. The major difficulty here is, that the time dependent neutron transmission of the ^{3}He cell has to be taken into account. For

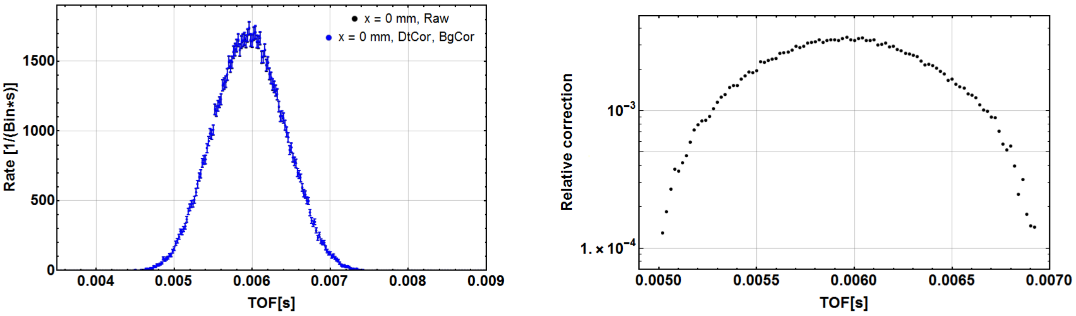

Figure 104: Left: The effect of dead time and background correction for the scan point at $x = 0$ (Elog #71, chopper frequency 76 Hz, selector velocity 25470 rpm). Right: The corresponding relative correction shows, that the combined influence of both effects is still small.

the analysis presented here, the first option was used. The following graphs show the measured polarization at each measurement point for a certain selector velocity and its intensity weighted average. The values shown, are modified with an offset, as the analysis is still blinded at the time of writing.

Figure 105 compares the product AP_{13} for the raw data and for the dead time and background corrected data. It can be seen, that after applying the corrections, the polarization at each point increases. As expected, the corrections have the strongest influence in the outer regions, where the statistics get worse.

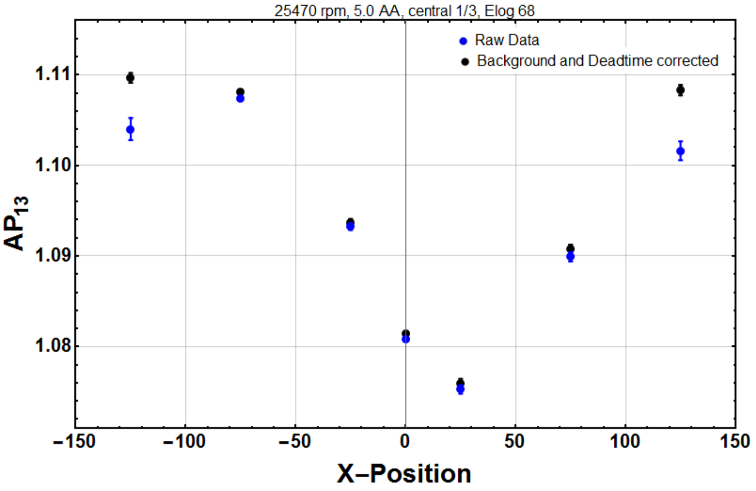

Figure 105: Polarization measurement behind PERKEO in central height (Elog #68). Comparison of raw polarization and with dead time and background correction applied. The selector velocity was 25470 rpm. The shown values are blinded with an offset.

For a systematic check, the polarization measurement with cell 4 (Elog #68) for a selector velocity of 25470 rpm in central height, was repeated with cell 5 (Elog #71) at positions shifted by 25 mm. Figure 106 shows, that the corresponding intensity weighted average polarization coincides very well, which was expected.

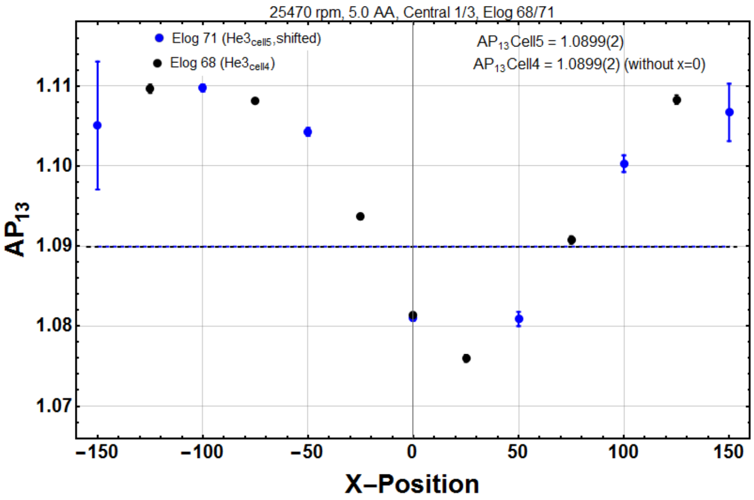

Figure 106: Polarization measurement behind Perkeo in central height (Elog #68/71) measured at the standard positions, as well as shifted by 25 mm. The selector velocity was 25470 rpm. The shown values are blinded with an offset.

For the central height, the polarization was measured for two more selector velocities (23154 rpm and 28300 rpm) to determine the wavelength dependence of the polarization. The corresponding position dependent polarization measurements with the averaged values are shown in figure 107.

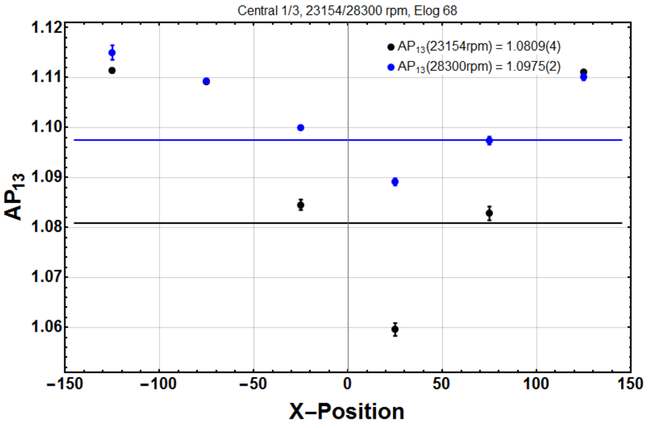

Figure 107: Polarization measurement behind Perkeo III in central height (Elog #68) for a selector velocity of 23154 rpm and 28300 rpm. It shows the wavelength dependent polarization which is increasing with selector velocity. The shown values are blinded with an offset.

Figure 108 shows the average polarization values dependent on the selector velocity of the full beam. For the top part of the beam, the measurement at the selector velocity of 23154 rpm is missing, because the neutron flipper was not working at this time. The degree of polarization is increasing with the selector frequency. This effect is explained by the geometry of the neutron beam coming from the $H113$ guide and the polarizer bender adjustment.

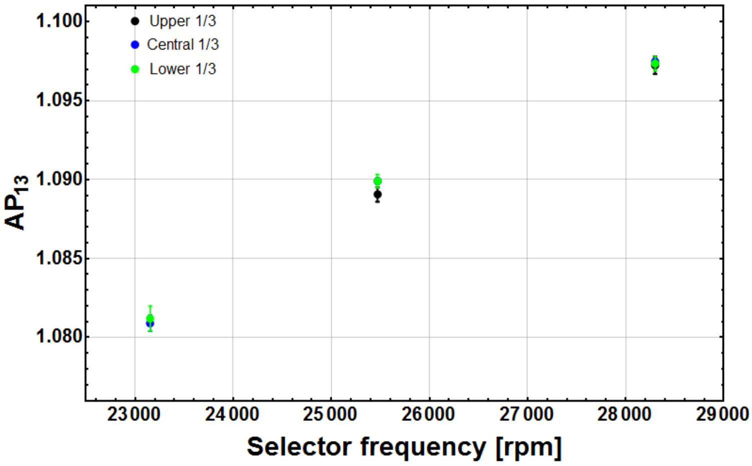

Figure 108: Average polarization behind PERKEO III at the bottom, top and center (Elog #68, 76, 78), measured at standard positions and with different selector velocities (23154 rpm, 25470 rpm, 28300 rpm). There is no data point for 23154 rpm at the top, because the neutron flipper did not work during the measurement. The shown values are blinded with an offset.

Table 18 summaries the polarization measurements. The intensity weighted average polarization values of the full beam for the different selector velocities are obtained similarly to the partial measurements. The polarization of each measurement is weighted by the intensity at this point and then the average of the full beam was calculated.

As expected, the polarization values in general do not show a significant height dependence for a given selector velocity. The left-right asymmetry is expected from the curvature of the bender polarizer and the geometry of the beam line. During the proton measurement the detectors only covered a fraction of the beam due to production and transport issues of the large carbon conversion foils, see [49, 50]. Due to the divergence of the beam this might result in a time-dependent correction as function of time-of-flight of the neutron through the PERKEO instrument. This weighting is determined with the help of simulations, which are not part of this work, but part of subsequent analysis [163]. The overall statistical accuracy of the proton measurement will be in the range of percent [49].

Table 18: Summary of the neutron polarization measurements behind Perkeo III. The intensity weighted average polarization values are shown for the different selector velocities and scan ranges. Only the statistical uncertainties are shown. All polarization values are blinded by addition of a certain offset.

Selector [rpm], Scan range	Bottom	Central	Top	Full Beam
23154 (5.5 Å) −125....125	1.0812(8)	1.0809(4)	———	1.081(3)
25470 (5.0 Å) −125....125	1.0899(4)	1.0899(2)	1.0891(5)	1.0896(1)
25470 (5.0 Å) −150....150	———	1.0899(2)	———	———
28300 (4.5 Å) −125....125	1.0972(5)	1.0975(2)	1.0972(5)	1.0973(1)

Hence, it suffices to treat the systematic uncertainties of the polarization measurement on the level of 10^{-3}. For the time-dependent analyzing power of the ^{3}He cells no corrections were applied, as the difference is $< 10^{-4}$ (see Fig. 94 - 97). The systematic uncertainty of the background is estimated to be of the same order of its correction, which is $0.3 \cdot 10^{-4}$. For the systematic uncertainty of the dead time, we use a conservative approach with half of the size of the correction. This contributes to the systematical uncertainty with $0.3 \cdot 10^{-4}$. The depolarization of the instruments exit window made of AlMg3 was measured in a previous beam time in 2008. The depolarization effect here was found to be small with a systematical uncertainty of $2.2 \cdot 10^{-4}$ [164]. Also the effect of non perfect spin transport through the instrument was evaluated in [164] and found to have a systematic uncertainty of only $1.4 \cdot 10^{-4}$. Hence, the total systematic uncertainty is $< 5 \cdot 10^{-4}$.

10 Summary

Precision experiments on neutron beta decay are used to determine parameters of the Standard Model of particle physics and to search for new physics beyond it. Combining the determination of the ratio of axial- and vector-couplings $\lambda = g_A/g_V$ via the beta asymmetry with a measurement of the neutron lifetime, allows to precisely determine the first element of the CKM-matrix V_{ud}. Within the scope of effective field theories, deviations from the V-A theory like right handed currents or hypothetical scalar and tensor couplings are tested by neutron beta decay studies. Some of the observables of neutron beta decay like the beta asymmetry A or the neutrino asymmetry B depend on the neutron spin. Studying these parameters with PERC requires a well designed beamline and several neutron optical components like an efficient neutron polarizer and most important, a completely non-depolarizing neutron guide.

Within this work, for the first time non-depolarizing supermirrors consisting of diamagnetic Cu and paramagnetic Ti with a maximum angle of reflection corresponding to m = 2 and excellent properties were produced. The choice of the right sputtering technology and reactive sputtering with ion plating were two key aspects in this development. Combining both allows to control the roughness growth and interdiffusion during sputtering of the supermirrors. A new roughness growth model describes measured data well and can be used for further optimization processes. A reflectivity of ≈ 92 % at the critical angle of reflection has been experimentally measured and clearly exceeds the desired reflectivity of 80 %. Additionally, these mirrors are long-term stable and can be baked out at 100 °C, which is beneficial for the vacuum conditions inside the PERC instrument. The mirrors fulfill all requirements for a non-depolarizing neutron guide inside PERC and its beamline in front.

For the beam polarization in front of PERC Fe/SiN$_x$ supermirrors are the most promising candidate. An inverted layer sequence of the supermirror opens the possibility to apply the novel solid-state technique. The great advantages of such a device compared to classical bender design are a more compact design, no increase of neutron beam divergence combined with a high degree of neutron polarization. Within this thesis, m = 2.2 supermirrors were produced in normal layer sequence with high reflectivity of ≈ 90 % at the critical angle of reflection and a very high polarization of more than 98 %. It is shown experimentally, that a high polarization of the neutron beam of 97 % and 95 % for neutron transmission through Si and quartz and inverted layer sequence are reached. The high polarization even in the low q-region compensates the lower reflectivity in the high q-region and makes this kind of polarizer design highly suitable for PERC.

Another neutron optical component produced and characterized within this thesis, is a high transmission collimator. Due to its small size it is very versatile and has a wide field of application. The high signal to noise ratio of more than 1800 for a neutron wavelength of 4.8 Å combined with a high transmission, make this a promising device, wherever a defined beam divergence is needed.

Real life conditions of the PERC beamline were simulated using the neutron ray-tracing program McStas. The final beamline was defined by evaluation of the most important parameters like neutron guide cross-section, neutron loss during transport and guide segmentation for pumping of the guide. The segmentation of the decay volume contains slits after each guide segment which are necessary to effectively pump down the full decay volume to UHV. The corresponding work on the vacuum pump system for PERC is described in Ref. [165]. The production of the beamline defined within this work will begin in 2022.

One of the planned measurements with PERC is the proton asymmetry parameter $C = -x_C(A + B)$, which is sensitive to right-handed currents. A recent measurement of C performed with PERKEO III at the ILL is currently analysed. Within this thesis, the average neutron beam polarization, which is linearly related to the proton asymmetry, was determined. To avoid any systematical bias within the data analysis, the analysis was split and distributed to three independent groups. The overall statistical accuracy of the proton measurement will be in the range of percent [49]. The statistical uncertainty of the polarization measurement is $1 \cdot 10^{-4}$ and the systematical uncertainties are below $5 \cdot 10^{-4}$. The analysis performed in this thesis will be used as guideline for future measurements with PERC.

The important developments in neutron optics, the definition of the beamline for PERC and the data analysis of the C measurement will make a large contribution to improve the precision of several correlation coefficients in neutron beta decay studies with PERC on the 10^{-4} level.

References

[1] Wu, C. S. and Ambler, E. and Hayward, R. W. and Hoppes, D. D. and Hudson, R. P. “Experimental Test of Parity Conservation in Beta Decay”. In: *Phys. Rev.* 105 (4 1957), pp. 1413–1415. DOI: `10.1103/PhysRev.105.1413`.

[2] Jerome I. Friedman and V. L. Telegdi. “Nuclear Emulsion Evidence for Parity Nonconservation in the Decay Chain $\pi^+ \to \mu^+ \to e^+$”. In: *Phys. Rev.* 106 (6 1957), pp. 1290–1293. DOI: `10.1103/PhysRev.106.1290`.

[3] Richard L. Garwin, Leon M. Lederman, and Marcel Weinrich. “Observations of the Failure of Conservation of Parity and Charge Conjugation in Meson Decays: the Magnetic Moment of the Free Muon”. In: *Phys. Rev.* 105 (4 1957), pp. 1415–1417. DOI: `10.1103/PhysRev.105.1415`.

[4] H. Abele et al. “A measurement of the beta asymmetry A in the decay of free neutrons”. In: *Physics Letters B* 407.3 (1997), pp. 212 –218. ISSN: 0370-2693. DOI: `10.1016/S0370-2693(97)00739-9`.

[5] H. Abele et al. “Is the Unitarity of the Quark-Mixing CKM Matrix Violated in Neutron β-Decay?” In: *Phys. Rev. Lett.* 88 (21 2002), p. 211801. DOI: `10.1103/PhysRevLett.88.211801`.

[6] C. Plonka. “Verbesserung der Lichtausopplung zur Messung der Neutrinoasymmetry mit PERKEO II”. Diploma Thesis. Ruprecht-Karls-Universität, Heidelberg, Jan. 2000.

[7] Bastian Martin Märkisch. “Das Spektrometer PERKEO III und der Zerfall des freien Neutrons”. PhD thesis. Universität Heidelberg, 2006. DOI: `10.11588/heidok.00006927`.

[8] N. Rebrova. “Development of a non-depolarizing neutron guide for PERC”. PhD thesis. University of Heidelberg, 2014.

[9] M. Utsuro and V. K. Ignatovich. *Handbook of Neutron Optics.* WILEY-VCH Verlag GmbH & Co. KGaA, 2010.

[10] R. Golub, D. Richardson, S. K. Lamoreaux. *Ultra-Cold Neutrons.* Adam Hilger, Bristol, Philadelphia, New York, 1991.

[11] I. I. Gurevich, L. V. Tarasov. *Physics of Low Energy Neutrons.* Nauka, Moscow, 1965.

[12] Varley F. Sears. *Neutron optics, an introduction to the theory of neutron optical phenomena and their applications.* Oxford University Press, 1989.

[13] R. F. Bacher and E. U. Condon. “The Spin of the Neutron”. In: *Phys. Rev.* 41 (5 1932), pp. 683–685. DOI: `10.1103/PhysRev.41.683.2`.

[14] J. Chadwick. “Possible Existence of a Neutron”. In: *Nature* 129 (1932), p. 312. DOI: `10.1038/129312a0`.

[15] D. M. Webber et al. “Measurement of the Positive Muon Lifetime and Determination of the Fermi Constant to Part-per-Million Precision”. In: *Phys. Rev. Lett.* 106 (4 2011), p. 041803. DOI: `10.1103/PhysRevLett.106.041803`.

[16] Dirk Dubbers and Bastian Märkisch. “Precise Measurements of the Decay of Free Neutrons”. In: *Annual Review of Nuclear and Particle Science* 71.1 (2021), pp. 139–163. DOI: `10.1146/annurev-nucl-102419-043156`.

[17] P.A. Zyla et al. “Review of Particle Physics”. In: *PTEP* 2020.8 (2020), p. 083C01. DOI: `10.1093/ptep/ptaa104`.

[18] Falkowski, Adam, Gonzalez-Alonso, M. & Naviliat-Cuncic. “Comprehensive analysis of beta decays within and beyond the Standard Model”. In: *Journal of High Energy Physics* 2021.126 (2021), p. 4. DOI: `10.1007/JHEP04(2021)126`.

[19] Tanmoy Bhattacharya et al. “Probing novel scalar and tensor interactions from (ultra)cold neutrons to the LHC”. In: *Phys. Rev. D* 85 (5 2012), p. 054512. DOI: `10.1103/PhysRevD.85.054512`.

[20] J. D. Jackson, S. B. Treiman, and H. W. Wyld. “Possible Tests of Time Reversal Invariance in Beta Decay”. In: *Phys. Rev.* 106 (3 1957), pp. 517–521. DOI: `10.1103/PhysRev.106.517`.

[21] S. B. Treiman. “Recoil Effects in K Capture and β Decay”. In: *Phys. Rev.* 110 (2 1958), pp. 448–450. DOI: `10.1103/PhysRev.110.448`.

[22] F. Glück. “The proton asymmetry in neutron decay”. In: *Physics Letters B* 376.1 (1996), pp. 25–28. ISSN: 0370-2693. DOI: `https://doi.org/10.1016/0370-2693(96)00290-0`.

[23] Hartmut Abele. “The neutron. Its properties and basic interactions”. In: *Progress in Particle and Nuclear Physics* 60.1 (2008), pp. 1 –81. ISSN: 0146-6410. DOI: `10.1016/j.ppnp.2007.05.002`.

[24] Dirk Dubbers and Michael G. Schmidt. “The neutron and its role in cosmology and particle physics”. In: *Rev. Mod. Phys.* 83 (4 2011), pp. 1111–1171. DOI: `10.1103/RevModPhys.83.1111`.

[25] H. Saul et al. “Limit on the Fierz Interference Term b from a Measurement of the Beta Asymmetry in Neutron Decay”. In: *Phys. Rev. Lett.* 125 (11 2020), p. 112501. DOI: `10.1103/PhysRevLett.125.112501`.

[26] Dinko Pocanic et al. “Nab: Measurement principles, apparatus and uncertainties”. In: *Nuclear Instruments and Methods in Physics Research Section A: Accelerators, Spectrometers, Detectors and Associated Equipment* 611.2 (2009). Particle Physics with Slow Neutrons, pp. 211–215. ISSN: 0168-9002. DOI: `10.1016/j.nima.2009.07.065`.

[27] Fry, J. et al. “The Nab experiment: A precision measurement of unpolarized neutron beta decay”. In: *EPJ Web Conf.* 219 (2019), p. 04002. DOI: `10.1051/epjconf/201921904002`.

[28] F.E. Wietfeldt et al. “aCORN: An experiment to measure the electron- antineutrino correlation in neutron decay”. In: *Nuclear Instruments and Methods in Physics Research Section A: Accelerators, Spectrometers, Detectors and Associated Equipment* 611.2 (2009). Particle Physics with Slow Neutrons, pp. 207–210. ISSN: 0168-9002. DOI: `10.1016/j.nima.2009.07.064`.

[29] Md T. Hassan and aCORN Collaboration. “Recent results from the aCORN experiment”. In: *APS Division of Nuclear Physics Meeting Abstracts.* Vol. 2020. APS Meeting Abstracts. Jan. 2020, SG.002.

[30] M. T. Hassan et al. “Measurement of the neutron decay electron- antineutrino angular correlation by the aCORN experiment”. In: *Phys. Rev. C* 103 (4 2021), p. 045502. DOI: `10.1103/PhysRevC.103.045502`.

[31] B. Märkisch et al. “The new neutron decay spectrometer Perkeo III”. In: *Nuclear Instruments and Methods in Physics Research Section A: Accelerators, Spectrometers, Detectors and Associated Equipment* 611.2 (2009). Particle Physics with Slow Neutrons, pp. 216 –218. ISSN: 0168-9002. DOI: `10.1016/j.nima.2009.07.066`.

[32] Roick, Christoph et al. “Undetected electron backscattering in Perkeo III”. In: *EPJ Web Conf.* 219 (2019), p. 04005. DOI: `10.1051/epjconf/201921904005`.

[33] O Zimmer and J Byrne and M.G.D van der Grinten and W Heil and F Glück. “”aSPECT” - a new spectrometer for the measurement of the angular correlation coefficient a in neutron beta decay”. In: *Nuclear Instruments and Methods in Physics Research Section A: Accelerators, Spectrometers, Detectors and Associated Equipment* 440.3 (2000), pp. 548 –556. ISSN: 0168-9002. DOI: `10.1016/S0168-9002(99)01035-9`.

[34] M. Simson et al. “Measuring the proton spectrum in neutron decay - Latest results with aSPECT”. In: *Nuclear Instruments and Methods in Physics Research Section A: Accelerators, Spectrometers, Detectors and Associated Equipment*

611.2 (2009). Particle Physics with Slow Neutrons, pp. 203–206. ISSN: 0168-9002. DOI: `10.1016/j.nima.2009.07.068`.

[35] X. Sun et al. “Search for dark matter decay of the free neutron from the UCNA experiment: $n \to \chi + e^+e^-$”. In: *Phys. Rev. C* 97 (5 May 2018), p. 052501. DOI: `10.1103/PhysRevC.97.052501`.

[36] A. T. Holley et al. “A high-field adiabatic fast passage ultracold neutron spin flipper for the UCNA experiment”. In: *Review of Scientific Instruments* 83.7 (2012), p. 073505. DOI: `10.1063/1.4732822`.

[37] Leah Broussard and UCNB Collaboration. “UCNB: The neutrino asymmetry in polarized ultracold neutron decay”. In: *AIP Conference Proceedings* 1560.1 (2013), pp. 149–151. DOI: `10.1063/1.4826741`.

[38] D. Dubbers et al. “A clean, bright, and versatile source of neutron decay products”. In: *Nuclear Instruments and Methods in Physics Research Section A: Accelerators, Spectrometers, Detectors and Associated Equipment* 596.2 (2008), pp. 238 –247. ISSN: 0168-9002. DOI: `10.1016/j.nima.2008.07.157`.

[39] G Konrad et al. “Neutron Decay with PERC: a Progress Report”. In: *Journal of Physics: Conference Series* 340 (2012), p. 012048. DOI: `10.1088/1742-6596/340/1/012048`.

[40] Christine Klauser. “High Precision Neutron Polarization For PERC”. PhD thesis. Technical University of Vienna, 2013.

[41] P. Bopp and E. Klemt and J. Last and H. Schütze and D. Dubbers and S.J. Freedman. “The superconducting neutron decay spectrometer PERKEO”. In: *Nuclear Instruments and Methods in Physics Research Section A: Accelerators, Spectrometers, Detectors and Associated Equipment* 267.2 (1988), pp. 436 –447. ISSN: 0168-9002. DOI: `10.1016/0168-9002(88)90485-8`.

[42] Schumann, M. and Soldner, T. and Deissenroth, M. and Glück, F. and Krempel, J. and Kreuz, M. and Märkisch, B. and Mund, D. and Petoukhov, A. and Abele, H. “Measurement of the Neutrino Asymmetry Parameter B in Neutron Decay”. In: *Phys. Rev. Lett.* 99 (19 2007), p. 191803. DOI: `10.1103/PhysRevLett.99.191803`.

[43] Schumann, M. and Kreuz, M. and Deissenroth, M. and Glück, F. and Krempel, J. and Märkisch, B. and Mund, D. and Petoukhov, A. and Soldner, T. and Abele, H. “Measurement of the Proton Asymmetry Parameter in Neutron Beta Decay”. In: *Phys. Rev. Lett.* 100 (15 2008), p. 151801. DOI: `10.1103/PhysRevLett.100.151801`.

[44] D. Mund et al. “Determination of the Weak Axial Vector Coupling $\lambda = g_A/g_V$ from a Measurement of the β-Asymmetry Parameter A in Neutron Beta Decay”. In: *Phys. Rev. Lett.* 110 (17 2013), p. 172502. DOI: `10.1103/PhysRevLett.110.172502`.

[45] X. Wang. “The Free Neutron β-Decay: A Powerful Tool for the Investigation in Particle Physics”. PhD thesis. Technische Universität München, 2013.

[46] T. Soldner et al. “Installation and first tests of the new PF1b polariser”. In: *Tech. rep. ILL03SO10T. Institut Laue-Langevin, Grenoble, France* (2002).

[47] A.N. Bazhenov et al. “An adiabatic resonance spin-flipper for thermal and cold neutrons”. In: *Nuclear Instruments and Methods in Physics Research Section A: Accelerators, Spectrometers, Detectors and Associated Equipment* 332.3 (1993), pp. 534 –536. ISSN: 0168-9002. DOI: `10.1016/0168-9002(93)90311-5`.

[48] H. F. Mest. “Measurement of the Beta-Asymmetry in the Decay of Free Polarized Neutrons with the Spectrometer PERKEO III”. PhD thesis. Ruprecht-Karls-Universität, Heidelberg, June 2011.

[49] Christoph Roick. “Particle Detection and Proton Asymmetry in Neutron Beta Decay”. Dissertation. München: Technische Universität München, 2018.

[50] Lukas Raffelt. “Measurement of the Proton Asymmetry (C) in free neutron β-decay with PERKEO III”. PhD thesis. Universität Heidelberg, 2016. DOI: `10.11588/heidok.00022095`.

[51] J. Reich and H. Abele and M.Astruc Hoffmann and S. Baeßler and P.v. Bülow and D. Dubbers and V. Nesvizhevsky and U. Peschke and O. Zimmer. “A measurement of the beta asymmetry in neutron decay with PERKEO II”. In: *Nuclear Instruments and Methods in Physics Research Section A: Accelerators, Spectrometers, Detectors and Associated Equipment* 440.3 (2000), pp. 535 –538. ISSN: 0168-9002. DOI: `10.1016/S0168-9002(99)01032-3`.

[52] B. Märkisch et al. “Measurement of the Weak Axial-Vector Coupling Constant in the Decay of Free Neutrons Using a Pulsed Cold Neutron Beam”. In: *Phys. Rev. Lett.* 122 (24 2019), p. 242501. DOI: `10.1103/PhysRevLett.122.242501`.

[53] H. M.-L. Zentrum, et al. “MEPHISTO: Facility for particle physics with cold neutrons”. In: *Journal of large-scale research facilities* 1.A21 (2015). DOI: `10.17815/jlsrf-1-48`.

[54] Wang, Xiangzun et al. “Design of the magnet system of the neutron decay facility PERC”. In: *EPJ Web Conf.* 219 (2019), p. 04007. DOI: `10.1051/epjconf/201921904007`.

[55] Heiko Saul. “Energy Dependence of the Beta Asymmetry in Neutron Beta Decay”. Dissertation. München: Technische Universität München, 2018.

[56] X. Wang, G. Konrad, and H. Abele. “RxB drift momentum spectrometer with high resolution and large phase space acceptance”. In: *Nuclear Instruments and Methods in Physics Research Section A: Accelerators, Spectrometers, Detectors and Associated Equipment* 701 (2013), pp. 254 –261. ISSN: 0168-9002. DOI: `10.1016/j.nima.2012.10.071`.

[57] D Moser et al. “Recent design studies for the novel momentum spectrometer NoMoS”. In: 1643 (2020), p. 012005. DOI: `10.1088/1742-6596/1643/1/012005`.

[58] A.K. Petukhov. “Advanced broad-band solid-state supermirror polarizers for cold neutrons”. In: *Instrumentation and Detectors (physics.ins-det)* (2016). DOI: `10.1016/j.nima.2016.09.023`.

[59] A. K. Petukhov et al. “A project of advanced solid-state neutron polarizer for PF1B instrument at Institut Laue-Langevin”. In: *Review of Scientific Instruments* 90.8 (2019), p. 085112. DOI: `10.1063/1.5114796`.

[60] Varley F. Sears. “Neutron scattering lengths and cross sections”. In: *Neutron News* 3.3 (1992), pp. 26–37. DOI: `10.1080/10448639208218770`.

[61] O. Schaerpf. “Comparison of theoretical and experimental behaviour of supermirrors and discussion of limitations”. In: *Physica B: Condensed Matter* 156-157 (1989), pp. 631 –638. ISSN: 0921-4526. DOI: `10.1016/0921-4526(89)90750-3`.

[62] B. P. Schoenborn, D. L. D. Caspar, and O. F. Kammerer. “A novel neutron monochromator”. In: *Journal of Applied Crystallography* 7.5 (1974), pp. 508–510. DOI: `10.1107/S0021889874010302`.

[63] J. Schelten and K. Mika. “Calculated reflectivities of super-mirrors”. In: *Nuclear Instruments and Methods* 160.2 (1979), pp. 287 –294. ISSN: 0029-554X. DOI: `10.1016/0029-554X(79)90605-0`.

[64] F. Mezei, P.A. Dagleish. “Corrigendum and first experimental evidence on neutron supermirrors”. In: *Communications on Physics (London)* 2.2 (1977), pp. 41 –43.

[65] F. Bloch. “On the Magnetic Scattering of Neutrons”. In: *Phys. Rev.* 50 (3 1936), pp. 259–260. DOI: `10.1103/PhysRev.50.259`.

[66] O. Halpern. “Double refraction and polarization of neutron beam”. In: *Physical Review* 75 (1949).

[67] H. Danan, A. Herr, and A. J. P. Meyer. “New Determinations of the Saturation Magnetization of Nickel and Iron”. In: *Journal of Applied Physics* 39.2 (1968), pp. 669–670. DOI: `10.1063/1.2163571`.

[68] D. Jiles. *Introduction to magnetism and magneticmaterials.* Chapman and Hall, New York, 1991.

[69] Drabkin, G.M., et.al. “Polarizing neutronguide on the base of multilayer mirrors”. In: *Zhurnal Tekhnicheskoj Fiziki* 47.1 (1977), pp. 203 –208.

[70] Schärpf O. “Properties of beam bender type neutron polarizers using supermirrors”. In: *Physica B: Condensed Matter* 156 - 157 (1989), pp. 639 –646. ISSN: 0921-4526. DOI: `10.1016/0921-4526(89)90751-5`.

[71] O. Schärpf and N. Stuesser. “Recent progress in neutron polarizers”. In: *Nuclear Instruments and Methods in Physics Research Section A: Accelerators, Spectrometers, Detectors and Associated Equipment* 284.1 (1989), pp. 208 –211. ISSN: 0168-9002. DOI: `10.1016/0168-9002(89)90283-0`.

[72] C.F. Majkrzak. “Advances in polarized neutron reflectometry”. In: *Physica B: Condensed Matter* 213-214 (1995), pp. 904 –909. ISSN: 0921-4526. DOI: `10.1016/0921-4526(95)00319-5`.

[73] F. Mezei T. Krist A. Teichert and L. Rosta. *Modern developments in Xray and neutron optics.* Springer-Verlag, Berlin, Heidelberg, 2008. DOI: `ISBN978-3-540-74560-0`.

[74] R. Boffy, et.al. “Why neutron guides may end up breaking down? Some results on the macroscopic behaviour of alkali-borosilicate glass support plates under neutron irradiation”. In: *Nuclear Instruments and Methods in Physics Research Section B: Beam Interactions with Materials and Atoms* 358 (2015), pp. 179 –187. ISSN: 0168-583X. DOI: `10.1016/j.nimb.2015.06.017`.

[75] Donald M. Mattox. *Handbook of Physical Vapor Deposition (PVD) Processing.* 2nd. Elsevier, 2010.

[76] H.K. Pulker. *Coatings on Glass.* 2nd. Elsevier Science, 1999.

[77] Krishna Seshan, ed. *Handbook of thin film deposition processes and technologies.* Vol. 2. William Andrew, 2002.

[78] K.Wasa, I. Kanno, and H. Kotera. *Handbook of Sputter Deposition Technology: Fundamentals and Applications for Functional Thin Films, Nano-materials and MEMS.* p. 67 -68. William Andrew Publishing, 2012.

[79] K. Wasa, I. Kanno, and H. Kotera. *Handbook of Sputter Deposition Technology: Fundamentals and Applications for Functional Thin Films, Nano-materials and MEMS*. William Andrew, 2012.

[80] G. Bruckmann, H.Scholz. *Handbook of Vacuum Arc Science and Technology*. Ed. by L. Raymond, R.L. Boxman, P.J. Martin, D.M. Sanders (Eds.) Chapter 4. Noyes Publications, 1996.

[81] D.M. Mattox. *Handbook of Physical Vapor Deposition (PVD) Processing*. Materials Science and Process Technology. Elsevier Science, 1998.

[82] J.W. Lafferty. *Vacuum Arcs: Theory and applications*. 1980.

[83] A. Anders. *A Brief History of Cathodic Coatings, Cathodic Arcs: From Fractal Spots to Energetic Condensation*. Ed. by in: A. Anders. Chapter 2. Springer, 2009.

[84] B.J. Massey. "Production of Self-supporting Carbon Films". In: *Pergamon Press* in: S. Komiya, N. Yagi (Eds.), Transactions of 8th AVS National Symposium (1962). p. 922.

[85] M.S.P. Lucas, C.R. Vail, W.C. Stewart, H.A. Owen. "A New Deposition Technique for Refractory Metal Films". In: *Pergamon Press* in: S. Komiya, N. Yagi (Eds.), Transactions of 8th AVS National Symposium (1962). p. 988.

[86] A.W. Wright. "On the Production of Transparent Metal Films by the Electrical Discharge in Exhausted Tubes". In: *Am. J. Sci 13 (3rd ser.)* 1 (1877), pp. 49 –55.

[87] D.M. Mattox. *The Foundations of Vacuum Coating Technology*. p. 11. Springer, 2003.

[88] R. F. Bunshah. *Deposition technologies for films and coatings : developments and applications*. Park Ridge, N.J., U.S.A. : Noyes Publications, 1982.

[89] Mitsuharu Konuma. *Film Deposition by plasma techniques*. Ed. by Günter Ecker. Springer-Verlag, 1992.

[90] Gerhard Kienel and Klaus Röll, ed. *Vakuumbeschichtung 2 Verfahren und Anlagen*. Springer-Verlag, 1995.

[91] R. Liu. *Metallization, chapter 8 in Chang, CY and Sze, SM (Eds.), ULSI Technology*. McGraw-Hill, New York, 1996.

[92] Marcus Pritschow. "Titannitrid- und Titan-Schichten für die Nano-Elektromechanik". PhD thesis. University of Stuttgart, 2007.

[93] S. Schiller, K. Goedicke, J. Reschke, V. Rirchoff, S. Scneider, F. Milde. “Pulsed magnetron sputter technology”. In: *Surf. Coat. Technol.* 61 (1993), p. 331.

[94] W.D. Westwood. *Basics of reactive sputtering, in: W.D. Westwod, Sputter Deposition.* Ed. by of Materials Interfaces AVS: Science Technology and Processes. Vol. 2. AVS Education Committee Book Series, 2003.

[95] R.W. Berry. “Method of making a capacitor employing film-forming metal electrodes”. Pat. 2 993 266. 1961.

[96] F. M. Penning. “Über Ionisation durch metastabile Atome. (On the ionization of metastable atoms)”. In: *Die Naturwissenschaften (in German)* 15.40 (1927), p. 818. DOI: `10.1007/bf01505431`.

[97] Carlos A. Arango, Moshe Shapiro, and Paul Brumer. “Cold Atomic Collisions: Coherent Control of Penning and Associative Ionization”. In: *Phys. Rev. Lett.* 97 (19 2006), p. 193202. DOI: `10.1103/PhysRevLett.97.193202`.

[98] K. Hiraoka, H. Furuya, S. Kambara, S. Suzuki, Y. Hashimoto, A. Takamizawa. “Atmospheric-pressure Penning ionization of aliphatic hydrocarbons”. In: *Rapid Commun. Mass Spectrom.* 20.21 (2006), pp. 3213 –22. DOI: `10.1002/rcm.2706`.

[99] S. Logothetidis, I. Alexandrou, and S. Kokkou. “Optimization of TiN thin film growth with in situ monitoring: the effect of bias voltage and nitrogen flow rate”. In: *Surface and Coatings Technology* 80.1 (1996), pp. 66 –71. ISSN: 0257-8972. DOI: `10.1016/0257-8972(95)02687-8`.

[100] W.D. Sproul et al. “Advances in partial-pressure control applied to reactive sputtering”. In: *Surface and Coatings Technology* 39-40 (1989). Papers presented at the 16th International Conference on Metallurgical Coatings, pp. 499 –506. ISSN: 0257-8972. DOI: `10.1016/S0257-8972(89)80011-8`.

[101] Burmakou, A. P. and Kuleshov, V. N. “Algorithms for optical control of reactive magnetron deposition of film coatings”. In: *Journal of Applied Spectroscopy* 79.3 (July 2012), pp. 410 –415. DOI: `10.1007/s10812-012-9616-0`.

[102] J. W. Coburn and M. Chen. “Optical emission spectroscopy of reactive plasmas: A method for correlating emission intensities to reactive particle density”. In: *Journal of Applied Physics* 51.6 (1980), pp. 3134–3136. DOI: `10.1063/1.328060`.

[103] V.S. Vidyarthi et al. “Plasma emission controlled multi-target reactive sputtering for in-situ crystallized Pb(Zr,Ti)O3 thin films on 6″ Si-wafers”. In: *Thin Solid Films* 515.7 (2007), pp. 3547 –3553. ISSN: 0040-6090. DOI: `10.1016/j.tsf.2006.10.131`.

[104] B. A. Movchan und A. V. Demchishin. “Study of the structure and properties of thick vacuum condensates of nickel, titanium, tungsten, aluminum oxide and zirconium dioxide”. In: *The Physics of Metals and Metallography* 28 (1969), pp. 83–90.

[105] John A. Thornton. “Influence of apparatus geometry and deposition conditions on the structure and topography of thick sputtered coatings”. In: *Journal of Vacuum Science and Technology* 11.4 (1974), pp. 666–670. DOI: `10.1116/1.1312732`.

[106] John A. Thornton. “The microstructure of sputter-deposited coatings”. In: *Journal of Vacuum Science & Technology A* 4.6 (1986), pp. 3059–3065. DOI: `10.1116/1.573628`.

[107] John A. Thornton. “Influence of substrate temperature and deposition rate on structure of thick sputtered Cu coatings”. In: *Journal of Vacuum Science and Technology* 12.4 (1975), pp. 830–835. DOI: `10.1116/1.568682`.

[108] Geng,J. and Schüler,A. and Oelhafen,P. and Gantenbein,P. and Düggelin,M. and Mathys,D. and Guggenheim,R. “Changing TiN film morphology by ”plasma biasing””. In: *Journal of Applied Physics* 86.6 (1999), pp. 3460–3462. DOI: `10.1063/1.371229`.

[109] K. Fischer and H. Oettel. “Microstructural gradients in thin hard coatings-tailor-made”. In: *Surface and Coatings Technology* 97.1 (1997), pp. 308 –312. ISSN: 0257-8972. DOI: `10.1016/S0257-8972(97)00377-0`.

[110] R. Messier, A. P. Giri, and R. A. Roy. “Revised structure zone model for thin film physical structure”. In: *Journal of Vacuum Science & Technology A* 2.2 (1984), pp. 500–503. DOI: `10.1116/1.572604`.

[111] Brueckel, Thomas, Heger, Gernot, Richter, Dieter. *Neutron scattering Lectures.* Ed. by Roth, Georg, Zorn, Reiner. Vol. 39. Forschungszentrum Jülich GmbH, 2012.

[112] Heinz Maier-Leibnitz Zentrum et al. “TREFF: Reflectometer and instrument component test beamline at MLZ”. In: *Journal of large-scale research facilities* 3.A121 (2017). DOI: `10.17815/jlsrf-3-161`.

[113] U. Rücker, W. Bergs, B. Alefeld, E. Kentzinger, Th. Brückel. “Polarization analysis for the 2D position-sensitive detector of the HADAS reflectometer in Jülich”. In: *Physica B* 297 (2001), pp. 140 –142. DOI: `10.1016/S0921-4526(00)00856-5`.

[114] R. Engels et al. “Digital position sensitive discrimination for 2-dimensional scintillation detectors”. In: *IEEE Transactions on Nuclear Science* 44.3 (1997), pp. 506–508.

[115] Heinz Kiessig. “Interferenz von Röntgenstrahlen an dünnen Schichten”. In: *Annalen der Physik* 402.7 (1931), pp. 769–788. DOI: `10.1002/andp.19314020702`.

[116] J. Daillant and A. Gibaud. *X-ray and neutron reflectivity: principles and applications*. Springer, 1999.

[117] URL: `https://physics.nist.gov/PhysRefData/XrayMassCoef/ElemTab/z29.html`.

[118] URL: `https://physics.nist.gov/PhysRefData/XrayMassCoef/ElemTab/z22.html`.

[119] D. Höche, H. Schikora, H. Zutz, A. Emmel, R. Queitsch, P. Schaaf. “TiN-coating formation by pulsed Nd:YAG laser irradiation of titanium in nitrogen”. In: *J. Coat. Technol. Res.* 5.4 (2008), pp. 505 –512.

[120] A. Bergmaier. “Quantitative Elementanalytik an Diamantschichten mittels elastischer Vorwärtsstreuung (ERD) hochenergetischer schwerer Ionen”. PhD thesis. Shaker Verlag, 1999.

[121] G. Dollinger et al. “High resolution elastic recoil detection”. In: *Nuclear Instruments and Methods in Physics Research Section B: Beam Interactions with Materials and Atoms* 219-220 (2004). Proceedings of the Sixteenth International Conference on Ion Beam Analysis, pp. 333 –343. ISSN: 0168-583X. DOI: `10.1016/j.nimb.2004.01.079`.

[122] A. Bergmaier, G. Dollinger, and C.M. Frey. “A compact ΔE-Eres detector for elastic recoil detection with high sensitivity”. In: *Nuclear Instruments and Methods in Physics Research Section B: Beam Interactions with Materials and Atoms* 136-138 (1998). Ion Beam Analysis, pp. 638 –643. ISSN: 0168-583X. DOI: `10.1016/S0168-583X(97)00877-X`.

[123] J.P. Stoquert and G. Guillaume and M. Hage-Ali and J.J. Grob and C. Ganter and P. Siffert. “Determination of concentration profiles by elastic recoil detection with a ΔE-E gas telescope and high energy incident heavy ions”. In: *Nuclear Instruments and Methods in Physics Research Section B: Beam Interactions with Materials and Atoms* 44.2 (1989), pp. 184–194. ISSN: 0168-583X. DOI: `10.1016/0168-583X(89)90426-6`.

[124] B. Gebauer and D. Fink and P. Goppelt and M. Wilpert and Th. Wilpert. "Multidimensional ERDA measurements and depth profiling of medium-heavy elements". In: *Nuclear Instruments and Methods in Physics Research Section B: Beam Interactions with Materials and Atoms* 50.1 (1990), pp. 159–166. ISSN: 0168-583X. DOI: `10.1016/0168-583X(90)90350-4`.

[125] Ch. Dufour et al. "Sensitivity of metallic materials under irradiation with swift heavy ions". In: *Nuclear Instruments and Methods in Physics Research Section B: Beam Interactions with Materials and Atoms* 107.1 (1996), pp. 218 –222. ISSN: 0168-583X. DOI: `10.1016/0168-583X(95)01030-0`.

[126] F. Seitz. "Displacement of atoms during irradiation". In: *Solid State Physics* 2 (1956), pp. 307 –442.

[127] Schülke & Mayr GmbH. *Mucasol product information and safety data sheet.* VO (EG) 648/2004. Feb. 2021. DOI: `https://www.schuelke.com/de-de/produkte/mucasol.php`.

[128] Sung-Yong Chun. "Bias Voltage Effect on the Properties of TiN Films by Reactive Magnetron Sputtering". In: *Journal of the Korean Physical Society* 56.4 (2010), pp. 1134 –1139.

[129] R. Kovacs-Mezei and Th. Krist and Zs. Revay. "Non-magnetic supermirrors produced at Mirrotron Ltd." In: *Nuclear Instruments and Methods in Physics Research Section A: Accelerators, Spectrometers, Detectors and Associated Equipment* 586.1 (2008). Proceedings of the European Workshop on Neutron Optics, pp. 51–54. ISSN: 0168-9002. DOI: `10.1016/j.nima.2007.11.034`.

[130] U. Schmidt. Private communication. 2016.

[131] A. Hollering et al. "A non-depolarizing CuTi neutron supermirror guide for PERC". In: *Nuclear Instruments and Methods in Physics Research Section A: Accelerators, Spectrometers, Detectors and Associated Equipment* 1032 (2022), p. 166634. ISSN: 0168-9002. DOI: `https://doi.org/10.1016/j.nima.2022.166634`.

[132] M Senthil Kumar et al. "Stress minimisation in sputtered Ni/Ti supermirrors". In: *Physica B: Condensed Matter* 241-243 (1997). Proceedings of the International Conference on Neutron Scattering, pp. 95–97. ISSN: 0921-4526. DOI: `https://doi.org/10.1016/S0921-4526(97)00520-6`.

[133] Peter Böni. "Supermirror-based beam devices". In: *Physica B: Condensed Matter* 234-236 (1997). Proceedings of the First European Conference on

Neutron Scattering, pp. 1038 –1043. ISSN: 0921-4526. DOI: `10.1016/S0921-4526(96)01255-0`.

[134] Charles F. Majkrzak and John F. Ankner. “Supermirror neutron guide coatings”. In: *Neutron Optical Devices and Applications*. Ed. by Charles F. Majkrzak and James L. Wood. Vol. 1738. International Society for Optics and Photonics. SPIE, 1992, pp. 150 –158. DOI: `10.1117/12.130626`.

[135] Benedicte Ballot, Francois J. Samuel, and Bernard Farnoux. “Supermirror neutron guide”. In: *Neutron Optical Devices and Applications*. Ed. by Charles F. Majkrzak and James L. Wood. Vol. 1738. International Society for Optics and Photonics. SPIE, 1992, pp. 159 –165. DOI: `10.1117/12.130627`.

[136] O. Elsenhans and Peter Boeni and H. P. Friedli and Hans Grimmer and Philippe A. Buffat and K. Leifer and Ian S. Anderson. “Thin films for neutron optics”. In: *Neutron Optical Devices and Applications*. Ed. by Charles F. Majkrzak and James L. Wood. Vol. 1738. International Society for Optics and Photonics. SPIE, 1992, pp. 130 –140. DOI: `10.1117/12.130624`.

[137] W. Kroll. “Method for manufacturing titanium and alloys thereof”. Pat. US2205854A. 1940.

[138] A. E. van Arkel, J. H. de Boer. “Darstellung von reinem Titanium-, Zirkonium-, Hafnium- und Thoriummetall”. In: *Z. anorg, u. alg. Chem.* 148 (1925), pp. 345 –350. DOI: `10.1002/zaac.19251480133`.

[139] Lev S. Zevin, Giora Kimmel. *Quantitative X-ray Diffractometry*. Ed. by Inez Mureinik. 1st ed. Springer Verlag, 1995.

[140] Guinier Andre. *X-ray Studies of Materials*. John WIley & Sons Inc, 1963.

[141] M. F. C. Ladd, R. A. Palmer. *Structure Determination by X-Ray Crystallography*. 2nd ed. Plenum Press New York and London, 1985. DOI: `10.1007/978-1-4615-7939-7`.

[142] C.M Libanati and Sra.F Dyment. “Autodifusion de titanio alfa”. In: *Acta Metallurgica* 11.11 (1963), pp. 1263 –1268. ISSN: 0001-6160. DOI: `10.1016/0001-6160(63)90115-9`.

[143] M. Beyeler et Y. Adda. “Determination des volumes d’activation pour la diffusion des atomes dans l’or, le cuivre et l’aluminium”. In: *J. Phys. France* 29.4 (1968), pp. 345 –352. DOI: `10.1051/jphys:01968002904034500`.

[144] C. Schanzer, M. Schneider, and P. Böni. “Neutron Optics: Towards Applications for Hot Neutrons”. In: *Journal of Physics: Conference Series* 746 (2016), p. 012024. DOI: `10.1088/1742-6596/746/1/012024`.

[145] M. Kreuz et al. “The crossed geometry of two super mirror polarisers-a new method for neutron beam polarisation and polarisation analysis”. In: *Nuclear Instruments and Methods in Physics Research Section A: Accelerators, Spectrometers, Detectors and Associated Equipment* 547.2 (2005), pp. 583 –591. ISSN: 0168-9002. DOI: `10.1016/j.nima.2005.03.154`.

[146] A.F. Wright, M. Berneron, and S.P. Heathman. “Radial collimator system for reducing background noise during neutron diffraction with area detectors”. In: *Nuclear Instruments and Methods* 180.2 (1981), pp. 655 –658. ISSN: 0029-554X. DOI: `10.1016/0029-554X(81)90113-0`.

[147] A. S. Tremsin et al. “Neutron collimation with microchannel plates: calibration of existing technology and near future possibilities”. In: *IEEE Nuclear Science Symposium Conference Record.* Vol. 1. 2005, pp. 120–124. DOI: `10.1109/NSSMIC.2005.1596220`.

[148] W. Soller. “A new precision x-ray spectrometer”. In: *Phys. Rev.* 24 (1924), pp. 158 –167. DOI: `10.1103/PhysRev.24.158`.

[149] L. D. Cussen. “A design for improved neutron collimators”. In: *Nuclear Instruments and Methods in Physics Research Section A: Accelerators, Spectrometers, Detectors and Associated Equipment* 414 (1998), pp. 365 –371. DOI: `10.1016/S0168-9002(98)00664-0`.

[150] L. D. Cussen. “The optimisation of absorber thickness for neutron soller slit collimators”. In: *Nuclear Instruments and Methods in Physics Research Section A: Accelerators, Spectrometers, Detectors and Associated Equipment* 413 (1998), pp. 138 –142. DOI: `10.1016/S0168-9002(98)00489-6.`.

[151] P. M. Rinard. “Neutron interaction with matter”. In: (1997), pp. 364 –366.

[152] H. M.-L. Zentrum, et al. “RESI: Thermal neutron single crystal diffractometer”. In: *Journal of large-scale research facilities* 1.A4 (2015). DOI: `10.17815/jlsrf-3-161`.

[153] L. D. Cussen, P. Hoghoj, I. Anderson. “Neutron collimator with rectangular beam profile”. In: *Nuclear Instruments and Methods in Physics Research Section A: Accelerators, Spectrometers, Detectors and Associated Equipment* 460 (2001), pp. 374 –380. DOI: `10.1016/S0168-9002(00)01077-9`.

[154] Kathrin Lehmann. “Private Communication”. In: (2020).

[155] Daimler-Benz Aerospace. “Neutron velocity selector, blade rotor developed by dornier/gkss/ptb”. In: *Dornier Satellitensysteme GmbH* ().

[156] P. Willendrup, E. Farhi, E. Knudsen, U. Filges, K. Lefmann, J. Stein. “User and Programmers Guide to the Neutron Ray-Tracing Package McStas, version 2.3”. In: (2016).

[157] F James. “Monte Carlo theory and practice”. In: *Reports on Progress in Physics* 43.9 (1980), pp. 1145–1189. DOI: `10.1088/0034-4885/43/9/002`.

[158] Jens Klenke. “Private Communication”. In: (2016).

[159] K.P. Coulter et al. “Neutron polarization with polarized 3He”. In: *Nuclear Instruments and Methods in Physics Research Section A: Accelerators, Spectrometers, Detectors and Associated Equipment* 270.1 (1988), pp. 90–94. ISSN: 0168-9002. DOI: `10.1016/0168-9002(88)90013-7`.

[160] A.K. Petoukhov et al. “Compact magnetostatic cavity for polarised 3He neutron spin filter cells”. In: *Nuclear Instruments and Methods in Physics Research Section A: Accelerators, Spectrometers, Detectors and Associated Equipment* 560.2 (2006), pp. 480–484. ISSN: 0168-9002. DOI: `10.1016/j.nima.2005.12.247`.

[161] A.D. Carlson. “The neutron cross sectio standards, evaluations and aoolications.” In: *Metrologia* 48 (2011), p. 328.

[162] Gary J. Feldman and Robert D. Cousins. “Unified approach to the classical statistical analysis of small signals”. In: *Phys. Rev. D* 57 (7 1998), pp. 3873–3889. DOI: `10.1103/PhysRevD.57.3873`.

[163] Michael Klopf. “TBA”. PhD thesis. Atominstitut der Technischen Universität Wien, 2021.

[164] Torsten Soldner. “Polarisation of PERKEO-III A, beam time 2008/2009”. 2018.

[165] Stefan Bodmaier. “The vacuum pump system of PERC”. MA thesis. Technische Universität München, 2018.

Appendix

A Reflectivity and Transmission of X-rays and Neutrons (Program supermref)

In this Appendix, the basic assumptions and methods for calculation of X-ray and neutron reflectivity curves is presented. The analysis of measured X-ray and neutron reflectivity curves, was full filed using a program "Supermref", written by Ulrich Schmidt. The following presentation is referred to an internal report of Ulrich Schmidt in 2005.

The calculation of the reflectivity for X-rays and neutrons is based on a one-dimensional square-well potential. This means, that for every material in a multilayer structure including the substrate a certain optical potential can be calculated. In the simplest assumption, the potential is jumping at each boundary from one value to the next one, dependent on the material. With the conditions, that the neutron/X-ray wave is differentiable and continuous at this point and the substrate is propagating to infinity, the Schrödinger equation is solvable. A scheme of the configuration is shown in Figure 109, with P being the material specific potential and the number of the interface x_n.

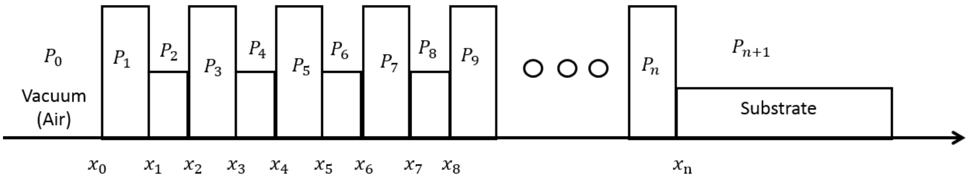

Figure 109: One-dimensional square-well potential assumption for calculation of reflectivity and transmission of neutrons and X-rays on a multilayer structure. P_0 defines the potential of vacuum or air respectively, P_1-P_n the potentials of the different materials in the multilayer and P_{n+1} the potential of the substrate seen by neutrons or X-rays. By the x values the interfaces are numbered from vacuum up to the substrate.

Unfortunately the assumption of perfectly separated layers is not valid for the situation in reality. In practice the potentials at the boundaries of two materials are smeared out caused by a production specific feature called interdiffusion. The interdiffusion at a interface can also be called roughness and will be described by a smooth transition of two potentials instead of a potential step. This transition could be approximated by many small steps but requires high computational power. Here it is interpolated by a polygonal chain, which gives adequate results with only 3 to 7 steps (compare ≈ 50 steps needed, when dividing into small steps). For angles above the critical angle of total reflection, the reflectivity drops drastically caused by the roughness. For reasons of calculation speed and computational power, the program calculates first the amplitude at a boundary for the simple one-dimensional square-well and corrects respectively to the roughness afterwards. This technique allows fast calculation of the corresponding reflectivity curve. It turned out, that the width of this polygonal chain, as well as the form at the boundary have serious impact on the actual reflectivity. Therefore two different sorts of roughness can be verified. The first one is the structural roughness, which describes the roughness from layer to layer. This kind of roughness can be compared to snow falling on a flat surface. Deposited particles fall down randomly on the substrate. This model results in a gaussian function in the height profile after deposition of one layer. The potential function can then be calculated from the integral of the height function near the boundary. We get an error-function for the potential function, which means that an following layer starts with the roughness of the layer before. The structural roughness is therefore growing from layer to layer with a certain power, which is strongly material and process specific. The second kind of roughness is called interdiffusion roughness. This value describes the smearing of two potentials caused by the solubility of two materials within each other. The derivative of the potentialfunction can then be described theoretically by an exponential function with falling slope from both sides of the boundary. This kind of roughness is independent from the layers deposited before (except for very thin layers, thickness < 2 times interdiffusion roughness).

With this method it is possible to determine the structural roughness on the level of $10^{-10}\,\mathrm{m}$ for roughness values $<\ 4\,\mathrm{nm}$ and on the level of $10^{-7}\,\mathrm{m}$, when the roughness is in the range of $4\ <\ 7\,\mathrm{nm}$. The interdiffusion roughness can be a factor of two bigger and the total roughness can be described by the sum of structural and interdiffusion roughness.

B Sputter Parameters and Layer Sequences

B.1 Cu/Ti m $=2$ Supermirror

Table 19: Sputtering conditions for m $=2$ Cu/Ti supermirror with 190 layers. The layers were deposited onto 10 mm thick borofloat glass substrate. For the Cu layers the generator power was 500 W in RF mode and the working pressure was $1.9 \cdot 10^{-3}$ mbar. The Ti layers were sputtered at a generator power of 500 W in PDC mode and the working pressure was $5.4 \cdot 10^{-3}$ mbar. Air and N2 reactive gases were added to the Ti layers with varying gas-flow from mirror to mirror. In the neutron supermirrors of the year 2020 Ti layers were sputtered with additional bias voltage of -150 V.

Layer number (from glass substrate)	Material	Velocity	Rounds	Ar gasflow [sccm]	Thickness [nm]
1	Ti	970	2	9	6.60
2	Cu	636	1	4	8.00
3	Ti	932	2	9	6.87
4	Cu	630	1	4	7.78
5	Ti	930	2	9	6.88
6	Cu	628	1	4	7.80
7	Ti	927	2	9	6.90
8	Cu	626	1	4	7.83
9	Ti	925	2	9	6.92
10	Cu	624	1	4	7.85
11	Ti	923	2	9	6.94
12	Cu	622	1	4	7.88
13	Ti	920	2	9	6.96
14	Cu	620	1	4	7.91
15	Ti	918	2	9	6.97
16	Cu	617	1	4	7.94
17	Ti	915	2	9	6.99
18	Cu	615	1	4	7.96
19	Ti	913	2	9	7.01
20	Cu	613	1	4	7.99
21	Ti	910	2	9	7.03
22	Cu	611	1	4	8.02
23	Ti	908	2	9	7.05
24	Cu	609	1	4	8.05
25	Ti	905	2	9	7.07
26	Cu	606	1	4	8.08
27	Ti	902	2	9	7.09
28	Cu	604	1	4	8.11
29	Ti	900	2	9	7.11
30	Cu	602	1	4	8.14
31	Ti	897	2	9	7.13

Layer number (from glass substrate)	Material	Velocity	Rounds	Ar gasflow [sccm]	Thickness [nm]
32	Cu	599	1	4	8.17
33	Ti	894	2	9	7.15
34	Cu	597	1	4	8.21
35	Ti	892	2	9	7.18
36	Cu	595	1	4	8.24
37	Ti	889	2	9	7.20
38	Cu	592	1	4	8.27
39	Ti	886	2	9	7.22
40	Cu	590	1	4	8.31
41	Ti	884	2	9	7.24
42	Cu	588	1	4	8.34
43	Ti	881	2	9	7.27
44	Cu	585	1	4	8.38
45	Ti	878	2	9	7.29
46	Cu	583	1	4	8.41
47	Ti	875	2	9	7.31
48	Cu	580	1	4	8.45
49	Ti	872	2	9	7.34
50	Cu	577	1	4	8.49
51	Ti	869	2	9	7.36
52	Cu	575	1	4	8.52
53	Ti	866	2	9	7.39
54	Cu	572	1	4	8.56
55	Ti	863	2	9	7.41
56	Cu	570	1	4	8.60
57	Ti	860	2	9	7.44
58	Cu	567	1	4	8.64
59	Ti	857	2	9	7.47
60	Cu	564	1	4	8.69
61	Ti	854	2	9	7.49
62	Cu	561	1	4	8.73
63	Ti	851	2	9	7.52
64	Cu	559	1	4	8.77
65	Ti	848	2	9	7.55
66	Cu	556	1	4	8.82
67	Ti	845	2	9	7.58
68	Cu	553	1	4	8.86
69	Ti	841	2	9	7.61
70	Cu	550	1	4	8.91
71	Ti	838	2	9	7.64
72	Cu	547	1	4	8.96
73	Ti	835	2	9	7.67
74	Cu	544	1	4	9.01
75	Ti	831	2	9	7.70
76	Cu	541	1	4	9.06
77	Ti	828	2	9	7.73
78	Cu	538	1	4	9.11
79	Ti	824	2	9	7.76
80	Cu	535	1	4	9.16

Layer number (from glass substrate)	Material	Velocity	Rounds	Ar gasflow [sccm]	Thickness [nm]
81	Ti	821	2	9	7.80
82	Cu	532	1	4	9.22
83	Ti	817	2	9	7.83
84	Cu	528	1	4	9.27
85	Ti	814	2	9	7.86
86	Cu	525	1	4	9.33
87	Ti	810	2	9	7.90
88	Cu	522	1	4	9.39
89	Ti	806	2	9	7.94
90	Cu	519	1	4	9.45
91	Ti	803	2	9	7.97
92	Cu	515	1	4	9.51
93	Ti	799	2	9	8.01
94	Cu	512	1	4	9.58
95	Ti	795	2	9	8.05
96	Cu	1016	2	4	9.64
97	Ti	791	2	9	8.09
98	Cu	1009	2	4	9.71
99	Ti	787	2	9	8.13
100	Cu	1002	2	4	9.78
101	Ti	783	2	9	8.17
102	Cu	994	2	4	9.86
103	Ti	779	2	9	8.22
104	Cu	986	2	4	9.93
105	Ti	775	2	9	8.26
106	Cu	979	2	4	10.01
107	Ti	770	2	9	8.31
108	Cu	971	2	4	10.09
109	Ti	766	2	9	8.35
110	Cu	963	2	4	10.18
111	Ti	762	2	9	8.4
112	Cu	954	2	4	10.27
113	Ti	757	2	9	8.45
114	Cu	946	2	4	10.36
115	Ti	753	2	9	8.5
116	Cu	937	2	4	10.45
117	Ti	748	2	9	8.56
118	Cu	929	2	4	10.55
119	Ti	743	2	9	8.61
120	Cu	920	2	4	10.66
121	Ti	738	2	9	8.67
122	Cu	910	2	4	10.77
123	Ti	733	2	9	8.73
124	Cu	901	2	4	10.88
125	Ti	728	2	9	8.79
126	Cu	891	2	4	11
127	Ti	723	2	9	8.85
128	Cu	881	2	4	11.12
129	Ti	718	2	9	8.92

Layer number (from glass substrate)	Material	Velocity	Rounds	Ar gasflow [sccm]	Thickness [nm]
130	Cu	871	2	4	11.25
131	Ti	712	2	9	8.99
132	Cu	860	2	4	11.39
133	Ti	707	2	9	9.06
134	Cu	849	2	4	11.54
135	Ti	701	2	9	9.13
136	Cu	838	2	4	11.69
137	Ti	695	2	9	9.21
138	Cu	827	2	4	11.85
139	Ti	689	2	9	9.29
140	Cu	815	2	4	12.03
141	Ti	683	2	9	9.37
142	Cu	803	2	4	12.21
143	Ti	677	2	9	9.46
144	Cu	790	2	4	12.41
145	Ti	670	2	9	9.55
146	Cu	777	2	4	12.62
147	Ti	663	2	9	9.65
148	Cu	763	2	4	12.84
149	Ti	656	2	9	9.75
150	Cu	749	2	4	13.09
151	Ti	649	2	9	9.86
152	Cu	734	2	4	13.35
153	Ti	642	2	9	9.97
154	Cu	718	2	4	13.64
155	Ti	634	2	9	10.1
156	Cu	702	2	4	13.96
157	Ti	626	2	9	10.22
158	Cu	685	2	4	14.3
159	Ti	618	2	9	10.36
160	Cu	667	2	4	14.69
161	Ti	609	2	9	10.51
162	Cu	648	2	4	15.12
163	Ti	600	2	9	10.67
164	Cu	628	2	4	15.6
165	Ti	591	2	9	10.84
166	Cu	607	2	4	16.14
167	Ti	581	2	9	11.02
168	Cu	584	2	4	16.77
169	Ti	571	2	9	11.22
170	Cu	840	3	4	17.5
171	Ti	560	2	9	11.43
172	Cu	801	3	4	18.35
173	Ti	549	2	9	11.66
174	Cu	758	3	4	19.38
175	Ti	537	2	9	11.91
176	Cu	712	3	4	20.64
177	Ti	525	2	9	12.18
178	Cu	661	3	4	22.23

Layer number (from glass substrate)	Material	Velocity	Rounds	Ar gasflow [sccm]	Thickness [nm]
179	Ti	513	2	9	12.47
180	Cu	605	3	4	24.29
181	Ti	502	2	9	12.76
182	Cu	543	3	4	27.09
183	Ti	983	4	9	13.02
184	Cu	473	3	4	31.09
185	Ti	972	4	9	13.17
186	Cu	395	3	4	37.24
187	Ti	987	4	9	12.97
188	Cu	719	7	4	47.72
189	Ti	546	2	9	11.72
190	Cu	719	11	4	68.41

B.2 Cu/Ti Monochromator

Table 20: Sputtering conditions for Cu/Ti monochromator with 80 layers. The layers were deposited onto 10 mm thick borofloat glass substrate. For the Cu layers the generator power was 500 W in RF mode and the working pressure was $1.9 \cdot 10^{-3}$ mbar. The Ti layers were sputtered at a generator power of 500 W in PDC mode and the working pressure was $5.4 \cdot 10^{-3}$ mbar. Air and N2 reactive gases were added to the Ti layers with varying gas-flow from mirror to mirror. Within the monochromators in year 2020 the Ti layers were sputtered with additional bias voltage of -150 V.

Layer number (from glass substrate)	Material	Velocity	Rounds	Ar gasflow [sccm]	Thickness [nm]
1	Ti	727	1	9	6.6
2	Cu	1097	1	4	6.9
3	Ti	727	1	9	6.6
4	Cu	1097	1	4	6.9
.					
.					
.					
77	Ti	727	1	9	6.6
78	Cu	1097	1	4	6.9
79	Ti	727	1	9	6.6
80	Cu	1097	1	4	6.9

B.3 Fe/Si m = 2 Polarizer Supermirror

In the meantime, of this work, A. Petukhov et. al. published their progress in development of a compact solid state polarizer, which was already fully assembled and characterized [59]. They describe a device, which is 5 − 10 times smaller than normal air gap benders. Based on single crystal Sapphire substrate it is claimed, that for wavelength region of $\lambda = 0.3 - 1.2$ nm one reaches a polarization of $\mathrm{P} = 0.999$ even in the low q-region. One disadvantage is simply a lower total transmission of about 15 % in total neutron transmission due to the higher absorption inside the substrate material.

Table 21: Sputtering conditions for Fe/Si polarizer supermirror with 227 layers. The layers were deposited onto 10 mm thick borofloat glass substrate. For the Fe layers the generator power was 500 W in RF mode and the working pressure was $1.9 \cdot 10^{-3}$ mbar. The Si layers were sputtered at a generator power of 500 W in PDC mode and the working pressure was $5.6 \cdot 10^{-3}$ mbar. 1 sccm N2 reactive gas was added to match the neutron optical potential from Si to the one of the Fe down component. For the solid state polarizer coated on quartz wafers, the shown layer sequence has to be inverted. This means, that layer 227 is coated at first, and layer 1 at the end of the supermirror.

Layer number (from glass substrate)	Material	Velocity	Rounds	Ar gasflow [sccm]	Thickness [nm]
1	Si	1338	3	10	7.40
2	Fe	757	2	4	7.40
3	Si	1415	3	10	7.00
4	Fe	714	2	4	7.84
5	Si	1412	3	10	7.01
6	Fe	713	2	4	7.86
7	Si	1409	3	10	7.03
8	Fe	711	2	4	7.88
9	Si	1406	3	10	7.04
10	Fe	709	2	4	7.90
11	Si	1403	3	10	7.06
12	Fe	707	2	4	7.92
13	Si	1400	3	10	7.07
14	Fe	705	2	4	7.95
15	Si	1396	3	10	7.09
16	Fe	703	2	4	7.97
17	Si	1393	3	10	7.11
18	Fe	701	2	4	7.99
19	Si	1390	3	10	7.12
20	Fe	699	2	4	8.02
21	Si	1387	3	10	7.14
22	Fe	697	2	4	8.04
23	Si	1384	3	10	7.15
24	Fe	695	2	4	8.06
25	Si	1380	3	10	7.17

Layer number (from glass substrate)	Material	Velocity	Rounds	Ar gasflow [sccm]	Thickness [nm]
26	Fe	693	2	4	8.09
27	Si	1377	3	10	7.19
28	Fe	690	2	4	8.11
29	Si	1374	3	10	7.21
30	Fe	1377	4	4	8.14
31	Si	1371	3	10	7.22
32	Fe	1372	4	4	8.16
33	Si	1367	3	10	7.24
34	Fe	1368	4	4	8.19
35	Si	1364	3	10	7.26
36	Fe	1364	4	4	8.21
37	Si	1360	3	10	7.28
38	Fe	1359	4	4	8.24
39	Si	1357	3	10	7.30
40	Fe	1355	4	4	8.27
41	Si	1354	3	10	7.31
42	Fe	1351	4	4	8.29
43	Si	1350	3	10	7.33
44	Fe	1346	4	4	8.32
45	Si	1347	3	10	7.35
46	Fe	1342	4	4	8.35
47	Si	1343	3	10	7.37
48	Fe	1337	4	4	8.38
49	Si	1339	3	10	7.39
50	Fe	1333	4	4	8.40
51	Si	1336	3	10	7.41
52	Fe	1328	4	4	8.43
53	Si	1332	3	10	7.43
54	Fe	1323	4	4	8.46
55	Si	1329	3	10	7.45
56	Fe	1319	4	4	8.49
57	Si	1325	3	10	7.47
58	Fe	1314	4	4	8.53
59	Si	1321	3	10	7.49
60	Fe	1309	4	4	8.56
61	Si	1317	3	10	7.52
62	Fe	1304	4	4	8.59
63	Si	1314	3	10	7.54
64	Fe	1299	4	4	8.62
65	Si	1310	3	10	7.56
66	Fe	1294	4	4	8.65
67	Si	1306	3	10	7.58
68	Fe	1289	4	4	8.69
69	Si	1302	3	10	7.60
70	Fe	1284	4	4	8.72
71	Si	1298	3	10	7.63
72	Fe	1279	4	4	8.76
73	Si	1294	3	10	7.65
74	Fe	1274	4	4	8.79

Layer number (from glass substrate)	Material	Velocity	Rounds	Ar gasflow [sccm]	Thickness [nm]
75	Si	1290	3	10	7.67
76	Fe	1269	4	4	8.83
77	Si	1286	3	10	7.70
78	Fe	1263	4	4	8.86
79	Si	1282	3	10	7.72
80	Fe	1258	4	4	8.90
81	Si	1278	3	10	7.75
82	Fe	1253	4	4	8.94
83	Si	1274	3	10	7.77
84	Fe	1247	4	4	8.98
85	Si	1269	3	10	7.80
86	Fe	1242	4	4	9.02
87	Si	1265	3	10	7.83
88	Fe	1236	4	4	9.06
89	Si	1261	3	10	7.85
90	Fe	1230	4	4	9.10
91	Si	1256	3	10	7.88
92	Fe	1225	4	4	9.14
93	Si	1252	3	10	7.91
94	Fe	1219	4	4	9.19
95	Si	1248	3	10	7.94
96	Fe	1213	4	4	9.23
97	Si	1243	3	10	7.96
98	Fe	1207	4	4	9.28
99	Si	1238	3	10	7.99
100	Fe	1201	4	4	9.32
101	Si	1234	3	10	8.02
102	Fe	1195	4	4	9.37
103	Si	1229	3	10	8.05
104	Fe	1189	4	4	9.42
105	Si	1224	3	10	8.09
106	Fe	1183	4	4	9.47
107	Si	1220	3	10	8.12
108	Fe	1176	4	4	9.52
109	Si	1215	3	10	8.15
110	Fe	1170	4	4	9.57
111	Si	1210	3	10	8.18
112	Fe	1163	4	4	9.63
113	Si	1205	3	10	8.22
114	Fe	1157	4	4	9.68
115	Si	1200	3	10	8.25
116	Fe	1150	4	4	9.74
117	Si	1195	3	10	8.29
118	Fe	1143	4	4	9.80
119	Si	1190	3	10	8.32
120	Fe	1136	4	4	9.86
121	Si	1184	3	10	8.36
122	Fe	1129	4	4	9.92
123	Si	1179	3	10	8.40

Layer number (from glass substrate)	Material	Velocity	Rounds	Ar gasflow [sccm]	Thickness [nm]
124	Fe	1122	4	4	9.98
125	Si	1174	3	10	8.44
126	Fe	1115	4	4	10.05
127	Si	1168	3	10	8.47
128	Fe	1107	4	4	10.11
129	Si	1832	3	10	8.52
130	Fe	1100	4	4	10.18
131	Si	1157	3	10	8.56
132	Fe	1092	4	4	10.25
133	Si	1151	3	10	8.60
134	Fe	1084	4	4	10.33
135	Si	1145	3	10	8.64
136	Fe	1077	4	4	10.40
137	Si	1139	3	10	8.69
138	Fe	1068	4	4	10.48
139	Si	1133	3	10	8.73
140	Fe	1060	4	4	10.56
141	Si	1127	3	10	8.78
142	Fe	1052	4	4	10.65
143	Si	1121	3	10	8.83
144	Fe	1043	4	4	10.74
145	Si	1115	3	10	8.88
146	Fe	1035	4	4	10.83
147	Si	1108	3	10	8.93
148	Fe	1026	4	4	10.92
149	Si	1102	3	10	8.99
150	Fe	1017	4	4	11.02
151	Si	1095	3	10	9.04
152	Fe	1007	4	4	11.12
153	Si	1088	3	10	9.10
154	Fe	998	4	4	11.23
155	Si	1081	3	10	9.16
156	Fe	988	4	4	11.34
157	Si	1074	3	10	9.22
158	Fe	978	4	4	11.45
159	Si	1067	3	10	9.28
160	Fe	968	4	4	11.57
161	Si	1059	3	10	9.34
162	Fe	957	4	4	11.70
163	Si	1052	3	10	9.41
164	Fe	947	4	4	11.83
165	Si	1044	3	10	9.48
166	Fe	935	4	4	11.97
167	Si	1036	3	10	9.55
168	Fe	924	4	4	12.12
169	Si	1028	3	10	9.63
170	Fe	912	4	4	12.28
171	Si	1020	3	10	9.71
172	Fe	900	4	4	12.44

Layer number (from glass substrate)	Material	Velocity	Rounds	Ar gasflow [sccm]	Thickness [nm]
173	Si	1011	3	10	9.79
174	Fe	888	4	4	12.61
175	Si	1002	3	10	9.88
176	Fe	875	4	4	12.80
177	Si	993	3	10	9.97
178	Fe	862	4	4	13.00
179	Si	984	3	10	10.06
180	Fe	848	4	4	13.21
181	Si	974	3	10	10.16
182	Fe	834	4	4	13.43
183	Si	964	3	10	10.26
184	Fe	819	4	4	13.68
185	Si	954	3	10	10.37
186	Fe	804	4	4	13.94
187	Si	944	3	10	10.49
188	Fe	787	4	4	14.22
189	Si	933	3	10	10.61
190	Fe	771	4	4	14.53
191	Si	922	3	10	10.74
192	Fe	753	4	4	14.87
193	Si	910	3	10	10.88
194	Fe	735	4	4	15.24
195	Si	898	3	10	11.03
196	Fe	715	4	4	15.66
197	Si	885	3	10	11.18
198	Fe	1042	6	4	16.12
199	Si	872	3	10	11.35
200	Fe	1010	6	4	16.64
201	Si	858	3	10	11.53
202	Fe	975	6	4	17.23
203	Si	844	3	10	11.73
204	Fe	938	6	4	17.91
205	Si	829	3	10	11.94
206	Fe	899	6	4	18.69
207	Si	813	3	10	12.17
208	Fe	856	6	4	19.62
209	Si	797	3	10	12.42
210	Fe	810	6	4	20.74
211	Si	780	3	10	12.69
212	Fe	760	6	4	22.12
213	Si	763	3	10	12.98
214	Fe	939	8	4	23.86
215	Si	745	3	10	13.28
216	Fe	857	8	4	26.13
217	Si	729	3	10	13.59
218	Fe	766	8	4	29.22
219	Si	714	3	10	13.86
220	Fe	997	12	4	33.69
221	Si	708	3	10	13.99

Layer number (from glass substrate)	Material	Velocity	Rounds	Ar gasflow [sccm]	Thickness [nm]
222	Fe	965	14	4	40.64
223	Si	723	3	10	13.70
224	Fe	957	18	4	52.65
225	Si	817	3	10	12.11
226	Fe	946	26	4	76.92
227	Si	817	3	10	12.11

B.4 NiMo/Ti m = 3 Supermirror

Table 22: Sputtering conditions for NiMo(75/15)/Ti neutron supermirror with 701 layers. The layers were deposited onto 10 mm thick borofloat glass substrate. For the NiMo layers the generator power was 500 W in RF mode and the working pressure was $1.9 \cdot 10^{-3}$ mbar. The Ti layers were sputtered at a generator power of 500 W in RF mode and the working pressure was $1.9 \cdot 10^{-3}$ mbar. As reactive gas 0.06 sccm was added to the Ti layers to smoothn the interlayer surfaces.

Layer number (from glass substrate)	Material	Velocity	Rounds	Ar gasflow [sccm]	Thickness [nm]
2	NiMo	1067	1	4	4.59
3	Ti	823	2	4	4.62
4	NiMo	1306	1	4	4.59
5	Ti	822	2	4	4.62
6	NiMo	1305	1	4	4.60
7	Ti	821	2	4	4.63
8	NiMo	1304	1	4	4.60
9	Ti	821	2	4	4.63
10	NiMo	1303	1	4	4.60
11	Ti	820	2	4	4.63
12	NiMo	1302	1	4	4.61
13	Ti	820	2	4	4.64
14	NiMo	1301	1	4	4.61
15	Ti	819	2	4	4.64
16	NiMo	1300	1	4	4.61
17	Ti	818	2	4	4.64
18	NiMo	1299	1	4	4.62
19	Ti	818	2	4	4.65
20	NiMo	1298	1	4	4.62
21	Ti	817	2	4	4.65
22	NiMo	1297	1	4	4.63
23	Ti	817	2	4	4.65
24	NiMo	1296	1	4	4.63
25	Ti	816	2	4	4.66
26	NiMo	1295	1	4	4.63
27	Ti	816	2	4	4.66
28	NiMo	1294	1	4	4.64
29	Ti	815	2	4	4.66
30	NiMo	1293	1	4	4.64
31	Ti	814	2	4	4.67
32	NiMo	1292	1	4	4.64
33	Ti	814	2	4	4.67
34	NiMo	1291	1	4	4.65
35	Ti	813	2	4	4.67
36	NiMo	1290	1	4	4.65
37	Ti	813	2	4	4.68
38	NiMo	1289	1	4	4.65
39	Ti	812	2	4	4.68

Layer number (from glass substrate)	Material	Velocity	Rounds	Ar gasflow [sccm]	Thickness [nm]
40	NiMo	1288	1	4	4.66
41	Ti	811	2	4	4.68
42	NiMo	1287	1	4	4.66
43	Ti	811	2	4	4.69
44	NiMo	1286	1	4	4.67
45	Ti	810	2	4	4.69
46	NiMo	1285	1	4	4.67
47	Ti	809	2	4	4.69
48	NiMo	1284	1	4	4.67
49	Ti	809	2	4	4.70
50	NiMo	1283	1	4	4.68
51	Ti	808	2	4	4.70
52	NiMo	1282	1	4	4.68
53	Ti	808	2	4	4.70
54	NiMo	1281	1	4	4.68
55	Ti	807	2	4	4.71
56	NiMo	1280	1	4	4.69
57	Ti	806	2	4	4.71
58	NiMo	1279	1	4	4.69
59	Ti	806	2	4	4.72
60	NiMo	1278	1	4	4.70
61	Ti	805	2	4	4.72
62	NiMo	1277	1	4	4.70
63	Ti	805	2	4	4.72
64	NiMo	1276	1	4	4.70
65	Ti	804	2	4	4.73
66	NiMo	1275	1	4	4.71
67	Ti	803	2	4	4.73
68	NiMo	1273	1	4	4.71
69	Ti	803	2	4	4.73
70	NiMo	1272	1	4	4.72
71	Ti	802	2	4	4.74
72	NiMo	1271	1	4	4.72
73	Ti	801	2	4	4.74
74	NiMo	1270	1	4	4.72
75	Ti	801	2	4	4.74
76	NiMo	1269	1	4	4.73
77	Ti	800	2	4	4.75
78	NiMo	1268	1	4	4.73
79	Ti	800	2	4	4.75
80	NiMo	1267	1	4	4.74
81	Ti	799	2	4	4.76
82	NiMo	1266	1	4	4.74
83	Ti	798	2	4	4.76
84	NiMo	1265	1	4	4.74
85	Ti	798	2	4	4.76
86	NiMo	1264	1	4	4.75
87	Ti	797	2	4	4.77
88	NiMo	1263	1	4	4.75

Layer number (from glass substrate)	Material	Velocity	Rounds	Ar gasflow [sccm]	Thickness [nm]
89	Ti	796	2	4	4.77
90	NiMo	1262	1	4	4.76
91	Ti	796	2	4	4.78
92	NiMo	1261	1	4	4.76
93	Ti	795	2	4	4.78
94	NiMo	1259	1	4	4.76
95	Ti	794	2	4	4.78
96	NiMo	1258	1	4	4.77
97	Ti	794	2	4	4.79
98	NiMo	1257	1	4	4.77
99	Ti	793	2	4	4.79
100	NiMo	1256	1	4	4.78
101	Ti	793	2	4	4.79
102	NiMo	1255	1	4	4.78
103	Ti	792	2	4	4.80
104	NiMo	1254	1	4	4.78
105	Ti	791	2	4	4.80
106	NiMo	1253	1	4	4.79
107	Ti	791	2	4	4.81
108	NiMo	1252	1	4	4.79
109	Ti	790	2	4	4.81
110	NiMo	1251	1	4	4.80
111	Ti	789	2	4	4.81
112	NiMo	1250	1	4	4.80
113	Ti	789	2	4	4.82
114	NiMo	1248	1	4	4.81
115	Ti	788	2	4	4.82
116	NiMo	1247	1	4	4.81
117	Ti	787	2	4	4.83
118	NiMo	1246	1	4	4.81
119	Ti	787	2	4	4.83
120	NiMo	1245	1	4	4.82
121	Ti	786	2	4	4.83
122	NiMo	1244	1	4	4.82
123	Ti	785	2	4	4.84
124	NiMo	1243	1	4	4.83
125	Ti	785	2	4	4.84
126	NiMo	1242	1	4	4.83
127	Ti	784	2	4	4.85
128	NiMo	1241	1	4	4.84
129	Ti	783	2	4	4.85
130	NiMo	1239	1	4	4.84
131	Ti	783	2	4	4.86
132	NiMo	1238	1	4	4.85
133	Ti	782	2	4	4.86
134	NiMo	1237	1	4	4.85
135	Ti	781	2	4	4.86
136	NiMo	1236	1	4	4.85
137	Ti	781	2	4	4.87

Layer number (from glass substrate)	Material	Velocity	Rounds	Ar gasflow [sccm]	Thickness [nm]
138	NiMo	1235	1	4	4.86
139	Ti	780	2	4	4.87
140	NiMo	1234	1	4	4.86
141	Ti	779	2	4	4.88
142	NiMo	1232	1	4	4.87
143	Ti	779	2	4	4.88
144	NiMo	1231	1	4	4.87
145	Ti	778	2	4	4.88
146	NiMo	1230	1	4	4.88
147	Ti	777	2	4	4.89
148	NiMo	1229	1	4	4.88
149	Ti	777	2	4	4.89
150	NiMo	1228	1	4	4.89
151	Ti	776	2	4	4.90
152	NiMo	1227	1	4	4.89
153	Ti	775	2	4	4.90
154	NiMo	1225	1	4	4.90
155	Ti	774	2	4	4.91
156	NiMo	1224	1	4	4.90
157	Ti	774	2	4	4.91
158	NiMo	1223	1	4	4.91
159	Ti	773	2	4	4.92
160	NiMo	1222	1	4	4.91
161	Ti	772	2	4	4.92
162	NiMo	1221	1	4	4.92
163	Ti	772	2	4	4.92
164	NiMo	1219	1	4	4.92
165	Ti	771	2	4	4.93
166	NiMo	1218	1	4	4.93
167	Ti	770	2	4	4.93
168	NiMo	1217	1	4	4.93
169	Ti	770	2	4	4.94
170	NiMo	1216	1	4	4.93
171	Ti	769	2	4	4.94
172	NiMo	1215	1	4	4.94
173	Ti	768	2	4	4.95
174	NiMo	1213	1	4	4.94
175	Ti	767	2	4	4.95
176	NiMo	1212	1	4	4.95
177	Ti	767	2	4	4.96
178	NiMo	1211	1	4	4.95
179	Ti	766	2	4	4.96
180	NiMo	1210	1	4	4.96
181	Ti	765	2	4	4.97
182	NiMo	1208	1	4	4.96
183	Ti	765	2	4	4.97
184	NiMo	1207	1	4	4.97
185	Ti	764	2	4	4.98
186	NiMo	1206	1	4	4.98

Layer number (from glass substrate)	Material	Velocity	Rounds	Ar gasflow [sccm]	Thickness [nm]
187	Ti	763	2	4	4.98
188	NiMo	1205	1	4	4.98
189	Ti	762	2	4	4.98
190	NiMo	1204	1	4	4.99
191	Ti	762	2	4	4.99
192	NiMo	1202	1	4	4.99
193	Ti	761	2	4	4.99
194	NiMo	1201	1	4	5.00
195	Ti	760	2	4	5.00
196	NiMo	1200	1	4	5.00
197	Ti	759	2	4	5.00
198	NiMo	1199	1	4	5.01
199	Ti	759	2	4	5.01
200	NiMo	1197	1	4	5.01
201	Ti	758	2	4	5.01
202	NiMo	1196	1	4	5.02
203	Ti	757	2	4	5.02
204	NiMo	1195	1	4	5.02
205	Ti	756	2	4	5.02
206	NiMo	1193	1	4	5.03
207	Ti	756	2	4	5.03
208	NiMo	1192	1	4	5.03
209	Ti	755	2	4	5.03
210	NiMo	1191	1	4	5.04
211	Ti	754	2	4	5.04
212	NiMo	1190	1	4	5.04
213	Ti	753	2	4	5.04
214	NiMo	1188	1	4	5.05
215	Ti	753	2	4	5.05
216	NiMo	1187	1	4	5.05
217	Ti	752	2	4	5.05
218	NiMo	1186	1	4	5.06
219	Ti	751	2	4	5.06
220	NiMo	1184	1	4	5.07
221	Ti	750	2	4	5.06
222	NiMo	1183	1	4	5.07
223	Ti	750	2	4	5.07
224	NiMo	1182	1	4	5.08
225	Ti	749	2	4	5.07
226	NiMo	1180	1	4	5.08
227	Ti	748	2	4	5.08
228	NiMo	1179	1	4	5.09
229	Ti	747	2	4	5.08
230	NiMo	1178	1	4	5.09
231	Ti	747	2	4	5.09
232	NiMo	1176	1	4	5.10
233	Ti	746	2	4	5.10
234	NiMo	1175	1	4	5.11
235	Ti	745	2	4	5.10

Layer number (from glass substrate)	Material	Velocity	Rounds	Ar gasflow [sccm]	Thickness [nm]
236	NiMo	1174	1	4	5.11
237	Ti	744	2	4	5.11
238	NiMo	1172	1	4	5.12
239	Ti	743	2	4	5.11
240	NiMo	1171	1	4	5.12
241	Ti	743	2	4	5.12
242	NiMo	1170	1	4	5.13
243	Ti	742	2	4	5.12
244	NiMo	1168	1	4	5.14
245	Ti	741	2	4	5.13
246	NiMo	1167	1	4	5.14
247	Ti	740	2	4	5.13
248	NiMo	1166	1	4	5.15
249	Ti	739	2	4	5.14
250	NiMo	1164	1	4	5.15
251	Ti	739	2	4	5.14
252	NiMo	1163	1	4	5.16
253	Ti	738	2	4	5.15
254	NiMo	1162	1	4	5.17
255	Ti	737	2	4	5.16
256	NiMo	1160	1	4	5.17
257	Ti	736	2	4	5.16
258	NiMo	1159	1	4	5.18
259	Ti	735	2	4	5.17
260	NiMo	1157	1	4	5.18
261	Ti	735	2	4	5.17
262	NiMo	1156	1	4	5.19
263	Ti	734	2	4	5.18
264	NiMo	1155	1	4	5.20
265	Ti	733	2	4	5.18
266	NiMo	1153	1	4	5.20
267	Ti	732	2	4	5.19
268	NiMo	1152	1	4	5.21
269	Ti	731	2	4	5.20
270	NiMo	1150	1	4	5.22
271	Ti	731	2	4	5.20
272	NiMo	1149	1	4	5.22
273	Ti	730	2	4	5.21
274	NiMo	1148	1	4	5.23
275	Ti	729	2	4	5.21
276	NiMo	1146	1	4	5.24
277	Ti	728	2	4	5.22
278	NiMo	1145	1	4	5.24
279	Ti	727	2	4	5.23
280	NiMo	1143	1	4	5.25
281	Ti	726	2	4	5.23
282	NiMo	1142	1	4	5.26
283	Ti	725	2	4	5.24
284	NiMo	1140	1	4	5.26

Layer number (from glass substrate)	Material	Velocity	Rounds	Ar gasflow [sccm]	Thickness [nm]
285	Ti	725	2	4	5.24
286	NiMo	1139	1	4	5.27
287	Ti	724	2	4	5.25
288	NiMo	1137	1	4	5.28
289	Ti	723	2	4	5.26
290	NiMo	1136	1	4	5.28
291	Ti	722	2	4	5.26
292	NiMo	1134	1	4	5.29
293	Ti	721	2	4	5.27
294	NiMo	1133	1	4	5.30
295	Ti	720	2	4	5.28
296	NiMo	1131	1	4	5.30
297	Ti	719	2	4	5.28
298	NiMo	1130	1	4	5.31
299	Ti	719	2	4	5.29
300	NiMo	1128	1	4	5.32
301	Ti	718	2	4	5.29
302	NiMo	1127	1	4	5.32
303	Ti	717	2	4	5.30
304	NiMo	1125	1	4	5.33
305	Ti	716	2	4	5.31
306	NiMo	1124	1	4	5.34
307	Ti	715	2	4	5.31
308	NiMo	1122	1	4	5.35
309	Ti	714	2	4	5.32
310	NiMo	1121	1	4	5.35
311	Ti	713	2	4	5.33
312	NiMo	1119	1	4	5.36
313	Ti	712	2	4	5.33
314	NiMo	1118	1	4	5.37
315	Ti	712	2	4	5.34
316	NiMo	1116	1	4	5.37
317	Ti	711	2	4	5.35
318	NiMo	1115	1	4	5.38
319	Ti	710	2	4	5.35
320	NiMo	1113	1	4	5.39
321	Ti	709	2	4	5.36
322	NiMo	1112	1	4	5.40
323	Ti	708	2	4	5.37
324	NiMo	1110	1	4	5.41
325	Ti	707	2	4	5.38
326	NiMo	1108	1	4	5.41
327	Ti	706	2	4	5.38
328	NiMo	1107	1	4	5.42
329	Ti	705	2	4	5.39
330	NiMo	1105	1	4	5.43
331	Ti	704	2	4	5.40
332	NiMo	1104	1	4	5.44
333	Ti	703	2	4	5.40

Layer number (from glass substrate)	Material	Velocity	Rounds	Ar gasflow [sccm]	Thickness [nm]
334	NiMo	1102	1	4	5.44
335	Ti	702	2	4	5.41
336	NiMo	1101	1	4	5.45
337	Ti	701	2	4	5.42
338	NiMo	1099	1	4	5.46
339	Ti	700	2	4	5.43
340	NiMo	1097	1	4	5.47
341	Ti	700	2	4	5.43
342	NiMo	1096	1	4	5.48
343	Ti	699	2	4	5.44
344	NiMo	1094	1	4	5.48
345	Ti	698	2	4	5.45
346	NiMo	1092	1	4	5.49
347	Ti	697	2	4	5.45
348	NiMo	1091	1	4	5.50
349	Ti	696	2	4	5.46
350	NiMo	1089	1	4	5.51
351	Ti	695	2	4	5.47
352	NiMo	1087	1	4	5.52
353	Ti	694	2	4	5.48
354	NiMo	1086	1	4	5.53
355	Ti	693	2	4	5.49
356	NiMo	1084	1	4	5.53
357	Ti	692	2	4	5.49
358	NiMo	1082	1	4	5.54
359	Ti	691	2	4	5.50
360	NiMo	1081	1	4	5.55
361	Ti	690	2	4	5.51
362	NiMo	1079	1	4	5.56
363	Ti	689	2	4	5.52
364	NiMo	1077	1	4	5.57
365	Ti	688	2	4	5.52
366	NiMo	1076	1	4	5.58
367	Ti	687	2	4	5.53
368	NiMo	1074	1	4	5.59
369	Ti	686	2	4	5.54
370	NiMo	1072	1	4	5.60
371	Ti	685	2	4	5.55
372	NiMo	1070	1	4	5.61
373	Ti	684	2	4	5.56
374	NiMo	1069	1	4	5.62
375	Ti	683	2	4	5.57
376	NiMo	1067	1	4	5.62
377	Ti	682	2	4	5.57
378	NiMo	1065	1	4	5.63
379	Ti	681	2	4	5.58
380	NiMo	1063	1	4	5.64
381	Ti	680	2	4	5.59
382	NiMo	1061	1	4	5.65

Layer number (from glass substrate)	Material	Velocity	Rounds	Ar gasflow [sccm]	Thickness [nm]
383	Ti	679	2	4	5.60
384	NiMo	1060	1	4	5.66
385	Ti	678	2	4	5.61
386	NiMo	1058	1	4	5.67
387	Ti	677	2	4	5.62
388	NiMo	1056	1	4	5.68
389	Ti	676	2	4	5.63
390	NiMo	1054	1	4	5.69
391	Ti	675	2	4	5.63
392	NiMo	1052	1	4	5.70
393	Ti	673	2	4	5.64
394	NiMo	1051	1	4	5.71
395	Ti	672	2	4	5.65
396	NiMo	1049	1	4	5.72
397	Ti	671	2	4	5.66
398	NiMo	1047	1	4	5.73
399	Ti	670	2	4	5.67
400	NiMo	1045	1	4	5.74
401	Ti	669	2	4	5.68
402	NiMo	1043	1	4	5.75
403	Ti	668	2	4	5.69
404	NiMo	1041	1	4	5.76
405	Ti	667	2	4	5.70
406	NiMo	1039	1	4	5.77
407	Ti	666	2	4	5.71
408	NiMo	1037	1	4	5.78
409	Ti	665	2	4	5.72
410	NiMo	1036	1	4	5.79
411	Ti	664	2	4	5.73
412	NiMo	1034	1	4	5.80
413	Ti	663	2	4	5.74
414	NiMo	1032	1	4	5.82
415	Ti	661	2	4	5.75
416	NiMo	1030	1	4	5.83
417	Ti	660	2	4	5.76
418	NiMo	1028	1	4	5.84
419	Ti	659	2	4	5.76
420	NiMo	1026	1	4	5.85
421	Ti	658	2	4	5.77
422	NiMo	1024	1	4	5.86
423	Ti	657	2	4	5.78
424	NiMo	1022	1	4	5.87
425	Ti	656	2	4	5.80
426	NiMo	1020	1	4	5.88
427	Ti	655	2	4	5.81
428	NiMo	1018	1	4	5.89
429	Ti	653	2	4	5.82
430	NiMo	1016	1	4	5.91
431	Ti	652	2	4	5.83

Layer number (from glass substrate)	Material	Velocity	Rounds	Ar gasflow [sccm]	Thickness [nm]
432	NiMo	1014	1	4	5.92
433	Ti	651	2	4	5.84
434	NiMo	1012	1	4	5.93
435	Ti	650	2	4	5.85
436	NiMo	1010	1	4	5.94
437	Ti	649	2	4	5.86
438	NiMo	1008	1	4	5.95
439	Ti	648	2	4	5.87
440	NiMo	1006	1	4	5.97
441	Ti	646	2	4	5.88
442	NiMo	1003	1	4	5.98
443	Ti	645	2	4	5.89
444	NiMo	1001	1	4	5.99
445	Ti	644	2	4	5.90
446	NiMo	999	1	4	6.00
447	Ti	643	2	4	5.91
448	NiMo	997	1	4	6.02
449	Ti	641	2	4	5.92
450	NiMo	995	1	4	6.03
451	Ti	640	2	4	5.94
452	NiMo	993	1	4	6.04
453	Ti	639	2	4	5.95
454	NiMo	991	1	4	6.06
455	Ti	638	2	4	5.96
456	NiMo	988	1	4	6.07
457	Ti	636	2	4	5.97
458	NiMo	986	1	4	6.08
459	Ti	635	2	4	5.98
460	NiMo	984	1	4	6.10
461	Ti	634	2	4	5.99
462	NiMo	982	1	4	6.11
463	Ti	633	2	4	6.01
464	NiMo	980	1	4	6.12
465	Ti	631	2	4	6.02
466	NiMo	977	1	4	6.14
467	Ti	630	2	4	6.03
468	NiMo	975	1	4	6.15
469	Ti	629	2	4	6.04
470	NiMo	973	1	4	6.17
471	Ti	627	2	4	6.06
472	NiMo	971	1	4	6.18
473	Ti	626	2	4	6.07
474	NiMo	968	1	4	6.20
475	Ti	625	2	4	6.08
476	NiMo	966	1	4	6.21
477	Ti	623	2	4	6.10
478	NiMo	964	1	4	6.23
479	Ti	622	2	4	6.11
480	NiMo	961	1	4	6.24

Layer number (from glass substrate)	Material	Velocity	Rounds	Ar gasflow [sccm]	Thickness [nm]
481	Ti	621	2	4	6.12
482	NiMo	959	1	4	6.26
483	Ti	619	2	4	6.14
484	NiMo	956	1	4	6.27
485	Ti	618	2	4	6.15
486	NiMo	954	1	4	6.29
487	Ti	617	2	4	6.16
488	NiMo	952	1	4	6.31
489	Ti	615	2	4	6.18
490	NiMo	949	1	4	6.32
491	Ti	614	2	4	6.19
492	NiMo	947	1	4	6.34
493	Ti	612	2	4	6.21
494	NiMo	944	1	4	6.35
495	Ti	611	2	4	6.22
496	NiMo	942	1	4	6.37
497	Ti	609	2	4	6.24
498	NiMo	939	1	4	6.39
499	Ti	608	2	4	6.25
500	NiMo	937	1	4	6.41
501	Ti	607	2	4	6.27
502	NiMo	934	1	4	6.42
503	Ti	605	2	4	6.28
504	NiMo	931	1	4	6.44
505	Ti	604	2	4	6.30
506	NiMo	929	1	4	6.46
507	Ti	602	2	4	6.31
508	NiMo	926	1	4	6.48
509	Ti	601	2	4	6.33
510	NiMo	924	1	4	6.50
511	Ti	599	2	4	6.34
512	NiMo	921	1	4	6.52
513	Ti	598	2	4	6.36
514	NiMo	918	1	4	6.53
515	Ti	596	2	4	6.38
516	NiMo	916	1	4	6.55
517	Ti	594	2	4	6.39
518	NiMo	913	1	4	6.57
519	Ti	593	2	4	6.41
520	NiMo	910	1	4	6.59
521	Ti	591	2	4	6.43
522	NiMo	907	1	4	6.61
523	Ti	590	2	4	6.44
524	NiMo	904	1	4	6.63
525	Ti	588	2	4	6.46
526	NiMo	902	1	4	6.65
527	Ti	587	2	4	6.48
528	NiMo	899	1	4	6.68
529	Ti	585	2	4	6.50

Layer number (from glass substrate)	Material	Velocity	Rounds	Ar gasflow [sccm]	Thickness [nm]
530	NiMo	896	1	4	6.70
531	Ti	583	2	4	6.52
532	NiMo	893	1	4	6.72
533	Ti	582	2	4	6.53
534	NiMo	890	1	4	6.74
535	Ti	580	2	4	6.55
536	NiMo	887	1	4	6.76
537	Ti	578	2	4	6.57
538	NiMo	884	1	4	6.79
539	Ti	577	2	4	6.59
540	NiMo	881	1	4	6.81
541	Ti	575	2	4	6.61
542	NiMo	878	1	4	6.83
543	Ti	573	2	4	6.63
544	NiMo	875	1	4	6.86
545	Ti	571	2	4	6.65
546	NiMo	872	1	4	6.88
547	Ti	570	2	4	6.67
548	NiMo	869	1	4	6.91
549	Ti	568	2	4	6.69
550	NiMo	866	1	4	6.93
551	Ti	566	2	4	6.71
552	NiMo	862	1	4	6.96
553	Ti	564	2	4	6.74
554	NiMo	859	1	4	6.98
555	Ti	562	2	4	6.76
556	NiMo	856	1	4	7.01
557	Ti	560	2	4	6.78
558	NiMo	853	1	4	7.04
559	Ti	559	2	4	6.80
560	NiMo	849	1	4	7.06
561	Ti	557	2	4	6.83
562	NiMo	846	1	4	7.09
563	Ti	555	2	4	6.85
564	NiMo	843	1	4	7.12
565	Ti	553	2	4	6.87
566	NiMo	839	1	4	7.15
567	Ti	551	2	4	6.90
568	NiMo	836	1	4	7.18
569	Ti	549	2	4	6.92
570	NiMo	832	1	4	7.21
571	Ti	547	2	4	6.95
572	NiMo	828	1	4	7.24
573	Ti	545	2	4	6.97
574	NiMo	825	1	4	7.27
575	Ti	543	2	4	7.00
576	NiMo	821	1	4	7.31
577	Ti	541	2	4	7.03
578	NiMo	817	1	4	7.34

Layer number (from glass substrate)	Material	Velocity	Rounds	Ar gasflow [sccm]	Thickness [nm]
579	Ti	539	2	4	7.05
580	NiMo	814	1	4	7.37
581	Ti	537	2	4	7.08
582	NiMo	810	1	4	7.41
583	Ti	534	2	4	7.11
584	NiMo	806	1	4	7.44
585	Ti	532	2	4	7.14
586	NiMo	802	1	4	7.48
587	Ti	530	2	4	7.17
588	NiMo	798	1	4	7.52
589	Ti	528	2	4	7.20
590	NiMo	794	1	4	7.55
591	Ti	526	2	4	7.23
592	NiMo	790	1	4	7.59
593	Ti	523	2	4	7.26
594	NiMo	786	1	4	7.63
595	Ti	1042	4	4	7.29
596	NiMo	782	1	4	7.67
597	Ti	1037	4	4	7.33
598	NiMo	778	1	4	7.72
599	Ti	1032	4	4	7.36
600	NiMo	773	1	4	7.76
601	Ti	1028	4	4	7.40
602	NiMo	769	1	4	7.80
603	Ti	1023	4	4	7.43
604	NiMo	764	1	4	7.85
605	Ti	1018	4	4	7.47
606	NiMo	760	1	4	7.90
607	Ti	1013	4	4	7.51
608	NiMo	755	1	4	7.94
609	Ti	1007	4	4	7.54
610	NiMo	751	1	4	7.99
611	Ti	1002	4	4	7.58
612	NiMo	746	1	4	8.04
613	Ti	997	4	4	7.62
614	NiMo	741	1	4	8.10
615	Ti	992	4	4	7.66
616	NiMo	736	1	4	8.15
617	Ti	986	4	4	7.71
618	NiMo	731	1	4	8.21
619	Ti	980	4	4	7.75
620	NiMo	726	1	4	8.26
621	Ti	975	4	4	7.80
622	NiMo	721	1	4	8.32
623	Ti	969	4	4	7.84
624	NiMo	715	1	4	8.39
625	Ti	963	4	4	7.89
626	NiMo	710	1	4	8.45
627	Ti	957	4	4	7.94

Layer number (from glass substrate)	Material	Velocity	Rounds	Ar gasflow [sccm]	Thickness [nm]
628	NiMo	704	1	4	8.52
629	Ti	951	4	4	7.99
630	NiMo	699	1	4	8.59
631	Ti	945	4	4	8.05
632	NiMo	693	1	4	8.66
633	Ti	938	4	4	8.10
634	NiMo	687	1	4	8.73
635	Ti	932	4	4	8.16
636	NiMo	681	1	4	8.81
637	Ti	925	4	4	8.22
638	NiMo	675	1	4	8.89
639	Ti	918	4	4	8.28
640	NiMo	668	1	4	8.98
641	Ti	911	4	4	8.34
642	NiMo	662	1	4	9.06
643	Ti	904	4	4	8.41
644	NiMo	655	1	4	9.16
645	Ti	897	4	4	8.47
646	NiMo	648	1	4	9.25
647	Ti	889	4	4	8.55
648	NiMo	641	1	4	9.36
649	Ti	881	4	4	8.62
650	NiMo	634	1	4	9.47
651	Ti	874	4	4	8.70
652	NiMo	626	1	4	9.58
653	Ti	865	4	4	8.78
654	NiMo	619	1	4	9.70
655	Ti	857	4	4	8.87
656	NiMo	611	1	4	9.83
657	Ti	848	4	4	8.96
658	NiMo	1806	3	4	9.96
659	Ti	839	4	4	9.06
660	NiMo	1781	3	4	10.11
661	Ti	830	4	4	9.16
662	NiMo	1754	3	4	10.27
663	Ti	820	4	4	9.27
664	NiMo	1725	3	4	10.43
665	Ti	810	4	4	9.38
666	NiMo	1696	3	4	10.61
667	Ti	800	4	4	9.50
668	NiMo	1665	3	4	10.81
669	Ti	1183	6	4	9.63
670	NiMo	1633	3	4	11.02
671	Ti	1166	6	4	9.77
672	NiMo	1599	3	4	11.26
673	Ti	1148	6	4	9.93
674	NiMo	1563	3	4	11.52
675	Ti	1130	6	4	10.09
676	NiMo	1525	3	4	11.80

Layer number (from glass substrate)	Material	Velocity	Rounds	Ar gasflow [sccm]	Thickness [nm]
677	Ti	1110	6	4	10.27
678	NiMo	1485	3	4	12.13
679	Ti	1089	6	4	10.47
680	NiMo	1441	3	4	12.49
681	Ti	1066	6	4	10.69
682	NiMo	1394	3	4	12.91
683	Ti	1042	6	4	10.94
684	NiMo	1343	3	4	13.41
685	Ti	1016	6	4	11.22
686	NiMo	1286	3	4	13.99
687	Ti	988	6	4	11.54
688	NiMo	1223	3	4	14.71
689	Ti	957	6	4	11.91
690	NiMo	1152	3	4	15.63
691	Ti	922	6	4	12.36
692	NiMo	1069	3	4	16.84
693	Ti	882	6	4	12.92
694	NiMo	969	3	4	18.58
695	Ti	836	6	4	13.64
696	NiMo	841	3	4	21.41
697	Ti	778	6	4	14.65
698	NiMo	658	3	4	27.38
699	Ti	935	8	4	16.27
700	NiMo	971	11	4	68.01
701	Ti	951	10	4	19.99

C Neutron Monte-Carlo Simulation of PERC

C.1 Width and Height Considerations

Table 23: Wavelength 4 Å. List of different guide widths for the guide after velocity selector and in front of PERC. 1.3 m gap between this guide and inner PERC guide is in focus. Loss in this gap is given in neutrons per second and in relative values. The last column shows the particle flux at the end of the PERC instrument in neutrons per second. The maximal guide size without neutron losses in the gap is marked in yellow and the maximal flux at the exit is marked in red.

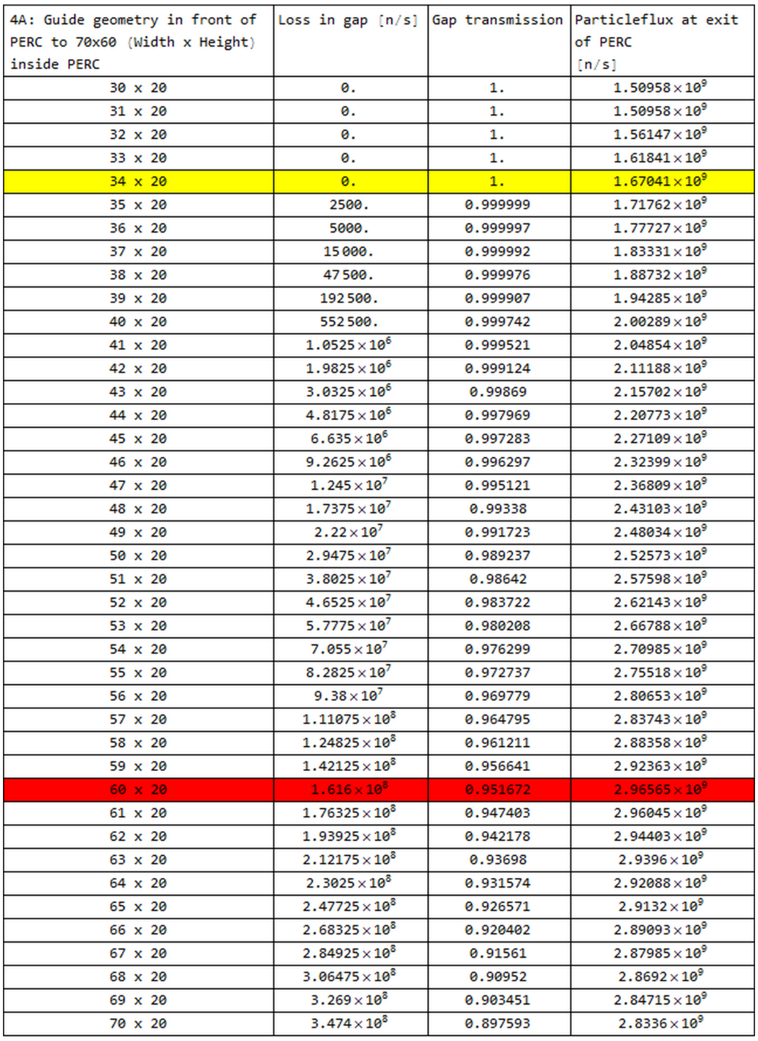

4A: Guide geometry in front of PERC to 70x60 (Width x Height) inside PERC	Loss in gap [n/s]	Gap transmission	Particleflux at exit of PERC [n/s]
30 x 20	0.	1.	1.50958×10^{9}
31 x 20	0.	1.	1.50958×10^{9}
32 x 20	0.	1.	1.56147×10^{9}
33 x 20	0.	1.	1.61841×10^{9}
34 x 20	0.	1.	1.67041×10^{9}
35 x 20	2500.	0.999999	1.71762×10^{9}
36 x 20	5000.	0.999997	1.77727×10^{9}
37 x 20	15000.	0.999992	1.83331×10^{9}
38 x 20	47500.	0.999976	1.88732×10^{9}
39 x 20	192500.	0.999907	1.94285×10^{9}
40 x 20	552500.	0.999742	2.00289×10^{9}
41 x 20	1.0525×10^{6}	0.999521	2.04854×10^{9}
42 x 20	1.9825×10^{6}	0.999124	2.11188×10^{9}
43 x 20	3.0325×10^{6}	0.99869	2.15702×10^{9}
44 x 20	4.8175×10^{6}	0.997969	2.20773×10^{9}
45 x 20	6.635×10^{6}	0.997283	2.27109×10^{9}
46 x 20	9.2625×10^{6}	0.996297	2.32399×10^{9}
47 x 20	1.245×10^{7}	0.995121	2.36809×10^{9}
48 x 20	1.7375×10^{7}	0.99338	2.43103×10^{9}
49 x 20	2.22×10^{7}	0.991723	2.48034×10^{9}
50 x 20	2.9475×10^{7}	0.989237	2.52573×10^{9}
51 x 20	3.8025×10^{7}	0.98642	2.57598×10^{9}
52 x 20	4.6525×10^{7}	0.983722	2.62143×10^{9}
53 x 20	5.7775×10^{7}	0.980208	2.66788×10^{9}
54 x 20	7.055×10^{7}	0.976299	2.70985×10^{9}
55 x 20	8.2825×10^{7}	0.972737	2.75518×10^{9}
56 x 20	9.38×10^{7}	0.969779	2.80653×10^{9}
57 x 20	1.11075×10^{8}	0.964795	2.83743×10^{9}
58 x 20	1.24825×10^{8}	0.961211	2.88358×10^{9}
59 x 20	1.42125×10^{8}	0.956641	2.92363×10^{9}
60 x 20	1.616×10^{8}	0.951672	2.96565×10^{9}
61 x 20	1.76325×10^{8}	0.947403	2.96045×10^{9}
62 x 20	1.93925×10^{8}	0.942178	2.94403×10^{9}
63 x 20	2.12175×10^{8}	0.93698	2.9396×10^{9}
64 x 20	2.3025×10^{8}	0.931574	2.92088×10^{9}
65 x 20	2.47725×10^{8}	0.926571	2.9132×10^{9}
66 x 20	2.68325×10^{8}	0.920402	2.89093×10^{9}
67 x 20	2.84925×10^{8}	0.91561	2.87985×10^{9}
68 x 20	3.06475×10^{8}	0.90952	2.8692×10^{9}
69 x 20	3.269×10^{8}	0.903451	2.84715×10^{9}
70 x 20	3.474×10^{8}	0.897593	2.8336×10^{9}

Table 24: Variation of guide width of guide in front of PERC for neutron wavelength 6 Å.

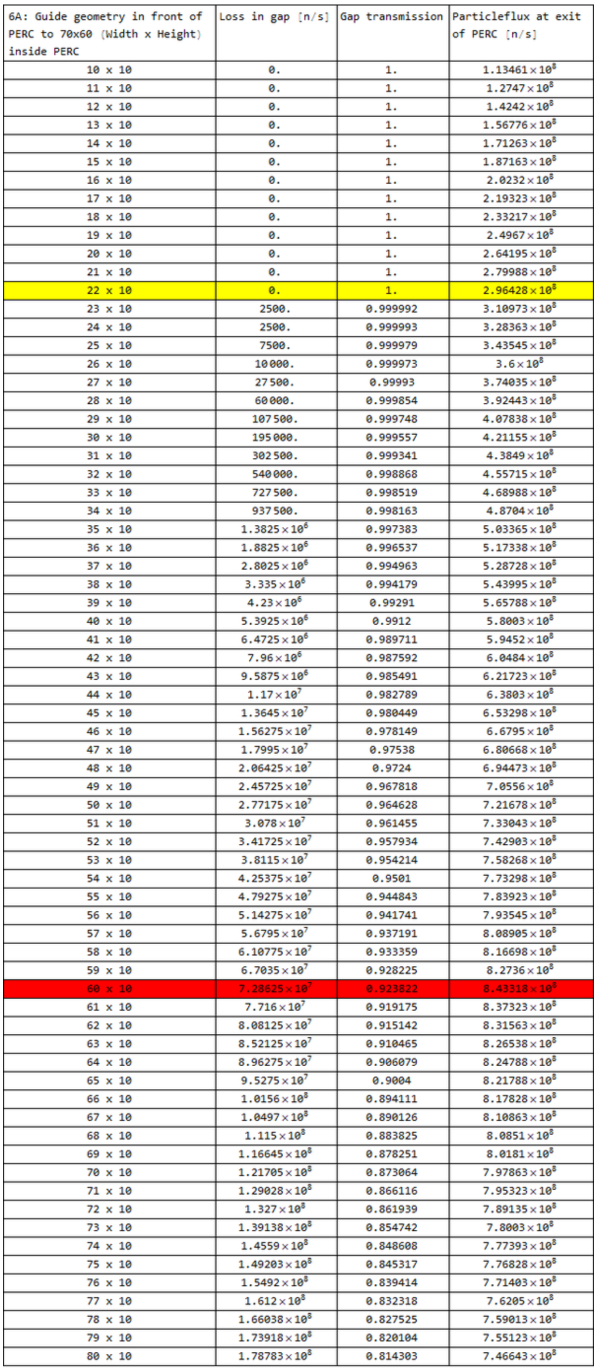

6A: Guide geometry in front of PERC to 70x60 (Width x Height) inside PERC	Loss in gap [n/s]	Gap transmission	Particleflux at exit of PERC [n/s]
10 x 10	0.	1.	1.13461×10^{8}
11 x 10	0.	1.	1.2747×10^{8}
12 x 10	0.	1.	1.4242×10^{8}
13 x 10	0.	1.	1.56776×10^{8}
14 x 10	0.	1.	1.71263×10^{8}
15 x 10	0.	1.	1.87163×10^{8}
16 x 10	0.	1.	2.0232×10^{8}
17 x 10	0.	1.	2.19323×10^{8}
18 x 10	0.	1.	2.33217×10^{8}
19 x 10	0.	1.	2.4967×10^{8}
20 x 10	0.	1.	2.64195×10^{8}
21 x 10	0.	1.	2.79988×10^{8}
22 x 10	0.	1.	2.96428×10^{8}
23 x 10	2500.	0.999992	3.10973×10^{8}
24 x 10	2500.	0.999993	3.28363×10^{8}
25 x 10	7500.	0.999979	3.43545×10^{8}
26 x 10	10 000.	0.999973	3.6×10^{8}
27 x 10	27 500.	0.99993	3.74035×10^{8}
28 x 10	60 000.	0.999854	3.92443×10^{8}
29 x 10	107 500.	0.999748	4.07838×10^{8}
30 x 10	195 000.	0.999557	4.21155×10^{8}
31 x 10	302 500.	0.999341	4.3849×10^{8}
32 x 10	540 000.	0.998868	4.55715×10^{8}
33 x 10	727 500.	0.998519	4.68988×10^{8}
34 x 10	937 500.	0.998163	4.8704×10^{8}
35 x 10	1.3825×10^{6}	0.997383	5.03365×10^{8}
36 x 10	1.8825×10^{6}	0.996537	5.17338×10^{8}
37 x 10	2.8025×10^{6}	0.994963	5.28728×10^{8}
38 x 10	3.335×10^{6}	0.994179	5.43995×10^{8}
39 x 10	4.23×10^{6}	0.99291	5.65788×10^{8}
40 x 10	5.3925×10^{6}	0.9912	5.8003×10^{8}
41 x 10	6.4725×10^{6}	0.989711	5.9452×10^{8}
42 x 10	7.96×10^{6}	0.987592	6.0484×10^{8}
43 x 10	9.5875×10^{6}	0.985491	6.21723×10^{8}
44 x 10	1.17×10^{7}	0.982789	6.3803×10^{8}
45 x 10	1.3645×10^{7}	0.980449	6.53298×10^{8}
46 x 10	1.56275×10^{7}	0.978149	6.6795×10^{8}
47 x 10	1.7995×10^{7}	0.97538	6.80668×10^{8}
48 x 10	2.06425×10^{7}	0.9724	6.94473×10^{8}
49 x 10	2.45725×10^{7}	0.967818	7.0556×10^{8}
50 x 10	2.77175×10^{7}	0.964628	7.21678×10^{8}
51 x 10	3.078×10^{7}	0.961455	7.33043×10^{8}
52 x 10	3.41725×10^{7}	0.957934	7.42903×10^{8}
53 x 10	3.8115×10^{7}	0.954214	7.58268×10^{8}
54 x 10	4.25375×10^{7}	0.9501	7.73298×10^{8}
55 x 10	4.79275×10^{7}	0.944843	7.83923×10^{8}
56 x 10	5.14275×10^{7}	0.941741	7.93545×10^{8}
57 x 10	5.6795×10^{7}	0.937191	8.08905×10^{8}
58 x 10	6.10775×10^{7}	0.933359	8.16698×10^{8}
59 x 10	6.7035×10^{7}	0.928225	8.2736×10^{8}
60 x 10	7.28625×10^{7}	0.923822	8.43318×10^{8}
61 x 10	7.716×10^{7}	0.919175	8.37323×10^{8}
62 x 10	8.08125×10^{7}	0.915142	8.31563×10^{8}
63 x 10	8.52125×10^{7}	0.910465	8.26538×10^{8}
64 x 10	8.96275×10^{7}	0.906079	8.24788×10^{8}
65 x 10	9.5275×10^{7}	0.9004	8.21788×10^{8}
66 x 10	1.0156×10^{8}	0.894111	8.17828×10^{8}
67 x 10	1.0497×10^{8}	0.890126	8.10863×10^{8}
68 x 10	1.115×10^{8}	0.883825	8.0851×10^{8}
69 x 10	1.16645×10^{8}	0.878251	8.0181×10^{8}
70 x 10	1.21705×10^{8}	0.873064	7.97863×10^{8}
71 x 10	1.29028×10^{8}	0.866116	7.95323×10^{8}
72 x 10	1.327×10^{8}	0.861939	7.89135×10^{8}
73 x 10	1.39138×10^{8}	0.854742	7.8003×10^{8}
74 x 10	1.4559×10^{8}	0.848608	7.77393×10^{8}
75 x 10	1.49203×10^{8}	0.845317	7.76828×10^{8}
76 x 10	1.5492×10^{8}	0.839414	7.71403×10^{8}
77 x 10	1.612×10^{8}	0.832318	7.6205×10^{8}
78 x 10	1.66038×10^{8}	0.827525	7.59013×10^{8}
79 x 10	1.73918×10^{8}	0.820104	7.55123×10^{8}
80 x 10	1.78783×10^{8}	0.814303	7.46643×10^{8}

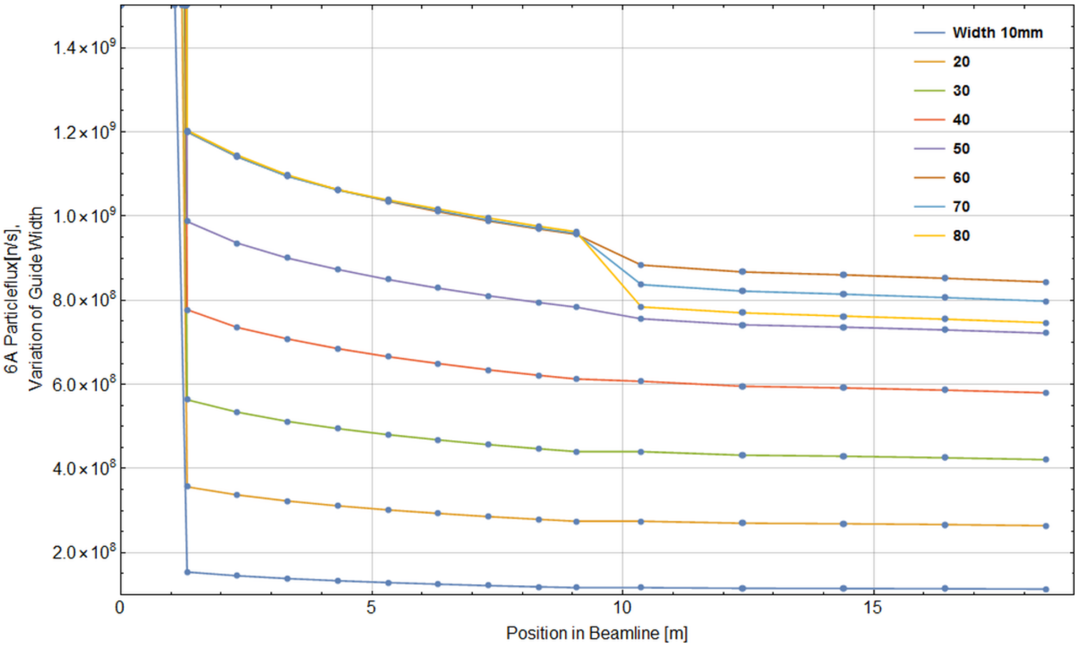

Figure 110: Particle flux in neutrons per second for 6 Å neutrons (y-axis) versus position in beamline (x-axis) for different neutron guide widths in front of PERC. Only every fifth simulation is shown for better visibility.

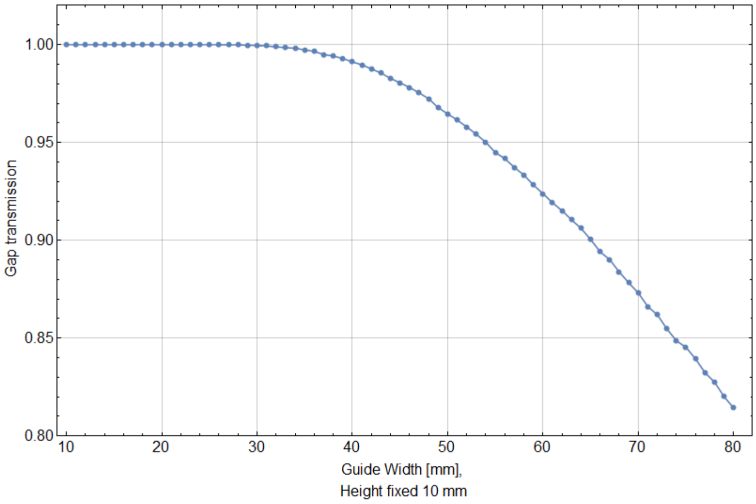

Figure 111: Gap transmission in front of PERC instrument for different guide widths and constant height of 20 mm. Wavelength 6 Å.

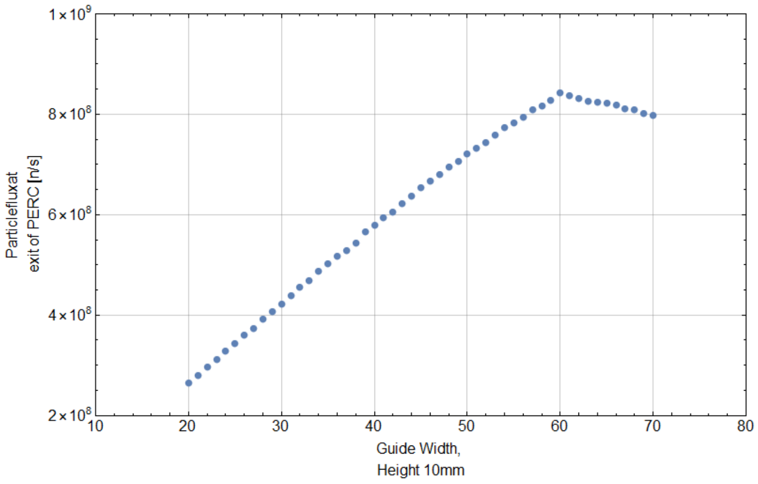

Figure 112: Total flux in neutrons per second at the exit of PERC instrument for different guide widths and constant height of 20 mm. Wavelength 6 Å.

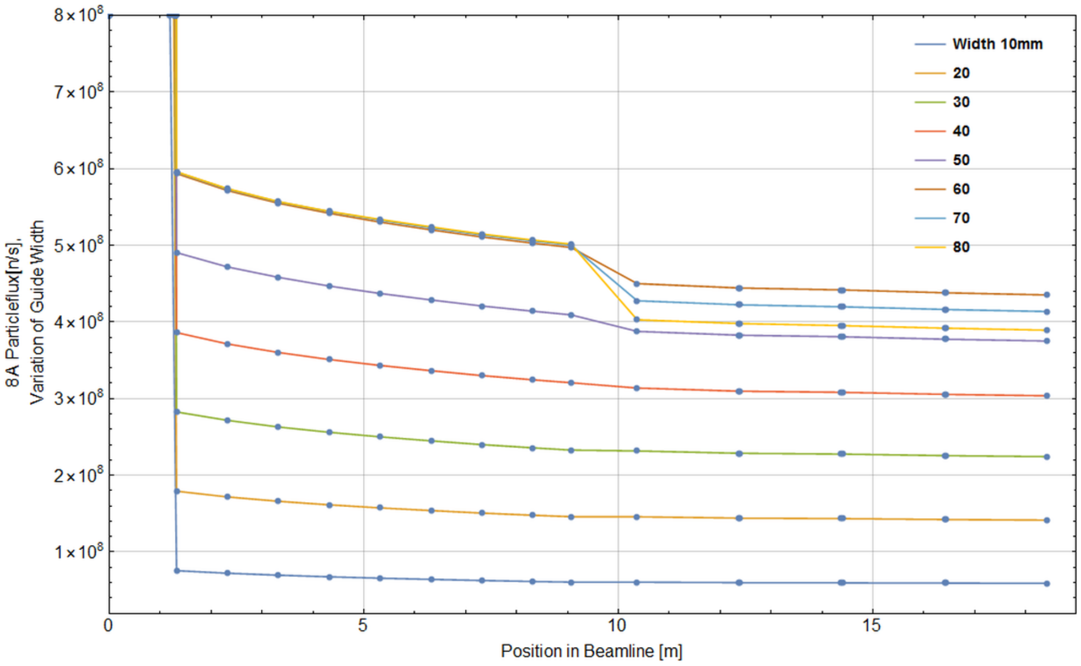

Figure 113: Particleflux in neutrons per second for 8 Å neutrons (y-axis) versus position in beamline (x-axis) for different neutron guide widths in front of PERC. Only every fifth simulation is shown for better visibility.

Table 25: Wavelength 8 Å. List of different guide widths for the guide after velocity selector and in front of PERC. 1.3 m gap between this guide and inner PERC guide is in focus. Loss in this gap is given in neutrons per second and in relativ values. The last column gives the particle flux at the end of the PERC instrument in neutrons per second.

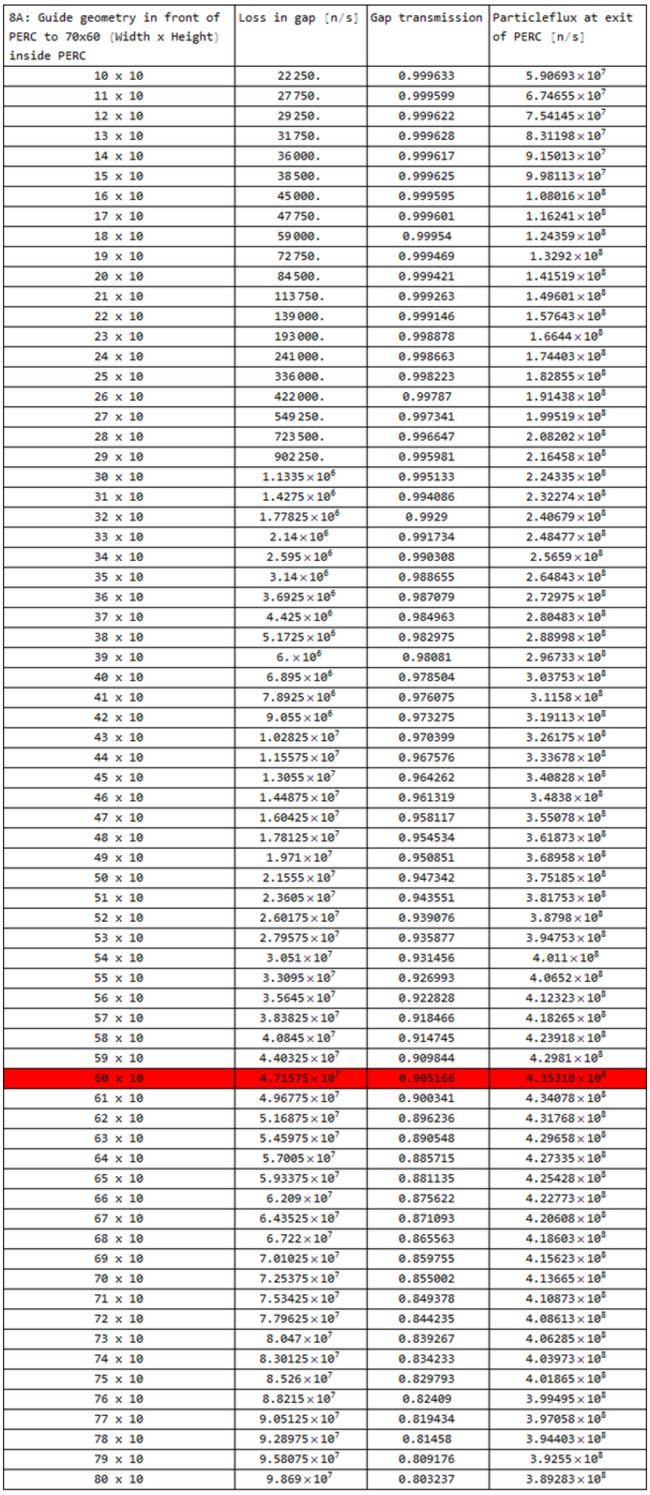

8A: Guide geometry in front of PERC to 70x60 (Width x Height) inside PERC	Loss in gap [n/s]	Gap transmission	Particleflux at exit of PERC [n/s]
10 x 10	22 250.	0.999633	5.90693×10^{7}
11 x 10	27 750.	0.999599	6.74655×10^{7}
12 x 10	29 250.	0.999622	7.54145×10^{7}
13 x 10	31 750.	0.999628	8.31198×10^{7}
14 x 10	36 000.	0.999617	9.15013×10^{7}
15 x 10	38 500.	0.999625	9.98113×10^{7}
16 x 10	45 000.	0.999595	1.08016×10^{8}
17 x 10	47 750.	0.999601	1.16241×10^{8}
18 x 10	59 000.	0.99954	1.24359×10^{8}
19 x 10	72 750.	0.999469	1.3292×10^{8}
20 x 10	84 500.	0.999421	1.41519×10^{8}
21 x 10	113 750.	0.999263	1.49601×10^{8}
22 x 10	139 000.	0.999146	1.57643×10^{8}
23 x 10	193 000.	0.998878	1.6644×10^{8}
24 x 10	241 000.	0.998663	1.74403×10^{8}
25 x 10	336 000.	0.998223	1.82855×10^{8}
26 x 10	422 000.	0.99787	1.91438×10^{8}
27 x 10	549 250.	0.997341	1.99519×10^{8}
28 x 10	723 500.	0.996647	2.08202×10^{8}
29 x 10	902 250.	0.995981	2.16458×10^{8}
30 x 10	1.1335×10^{6}	0.995133	2.24335×10^{8}
31 x 10	1.4275×10^{6}	0.994086	2.32274×10^{8}
32 x 10	1.77825×10^{6}	0.9929	2.40679×10^{8}
33 x 10	2.14×10^{6}	0.991734	2.48477×10^{8}
34 x 10	2.595×10^{6}	0.990308	2.5659×10^{8}
35 x 10	3.14×10^{6}	0.988655	2.64843×10^{8}
36 x 10	3.6925×10^{6}	0.987079	2.72975×10^{8}
37 x 10	4.425×10^{6}	0.984963	2.80483×10^{8}
38 x 10	5.1725×10^{6}	0.982975	2.88998×10^{8}
39 x 10	$6.\times10^{6}$	0.98081	2.96733×10^{8}
40 x 10	6.895×10^{6}	0.978504	3.03753×10^{8}
41 x 10	7.8925×10^{6}	0.976075	3.1158×10^{8}
42 x 10	9.055×10^{6}	0.973275	3.19113×10^{8}
43 x 10	1.02825×10^{7}	0.970399	3.26175×10^{8}
44 x 10	1.15575×10^{7}	0.967576	3.33678×10^{8}
45 x 10	1.3055×10^{7}	0.964262	3.40828×10^{8}
46 x 10	1.44875×10^{7}	0.961319	3.4838×10^{8}
47 x 10	1.60425×10^{7}	0.958117	3.55078×10^{8}
48 x 10	1.78125×10^{7}	0.954534	3.61873×10^{8}
49 x 10	1.971×10^{7}	0.950851	3.68958×10^{8}
50 x 10	2.1555×10^{7}	0.947342	3.75185×10^{8}
51 x 10	2.3605×10^{7}	0.943551	3.81753×10^{8}
52 x 10	2.60175×10^{7}	0.939076	3.8798×10^{8}
53 x 10	2.79575×10^{7}	0.935877	3.94753×10^{8}
54 x 10	3.051×10^{7}	0.931456	4.011×10^{8}
55 x 10	3.3095×10^{7}	0.926993	4.0652×10^{8}
56 x 10	3.5645×10^{7}	0.922828	4.12323×10^{8}
57 x 10	3.83825×10^{7}	0.918466	4.18265×10^{8}
58 x 10	4.0845×10^{7}	0.914745	4.23918×10^{8}
59 x 10	4.40325×10^{7}	0.909844	4.2981×10^{8}
60 x 10	4.71575×10^{7}	0.905166	4.35318×10^{8}
61 x 10	4.96775×10^{7}	0.900341	4.34078×10^{8}
62 x 10	5.16875×10^{7}	0.896236	4.31768×10^{8}
63 x 10	5.45975×10^{7}	0.890548	4.29658×10^{8}
64 x 10	5.7005×10^{7}	0.885715	4.27335×10^{8}
65 x 10	5.93375×10^{7}	0.881135	4.25428×10^{8}
66 x 10	6.209×10^{7}	0.875622	4.22773×10^{8}
67 x 10	6.43525×10^{7}	0.871093	4.20608×10^{8}
68 x 10	6.722×10^{7}	0.865563	4.18603×10^{8}
69 x 10	7.01025×10^{7}	0.859755	4.15623×10^{8}
70 x 10	7.25375×10^{7}	0.855002	4.13665×10^{8}
71 x 10	7.53425×10^{7}	0.849378	4.10873×10^{8}
72 x 10	7.79625×10^{7}	0.844235	4.08613×10^{8}
73 x 10	8.047×10^{7}	0.839267	4.06285×10^{8}
74 x 10	8.30125×10^{7}	0.834233	4.03973×10^{8}
75 x 10	8.526×10^{7}	0.829793	4.01865×10^{8}
76 x 10	8.8215×10^{7}	0.82409	3.99495×10^{8}
77 x 10	9.05125×10^{7}	0.819434	3.97058×10^{8}
78 x 10	9.28975×10^{7}	0.81458	3.94403×10^{8}
79 x 10	9.58075×10^{7}	0.809176	3.9255×10^{8}
80 x 10	9.869×10^{7}	0.803237	3.89283×10^{8}

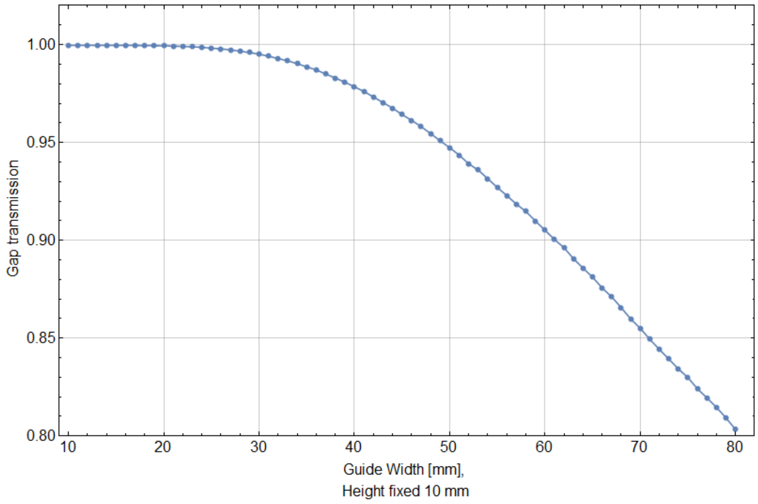

Figure 114: Gap transmission in front of PERC instrument for different guide widths and constant height of 20 mm. Wavelength 8 Å.

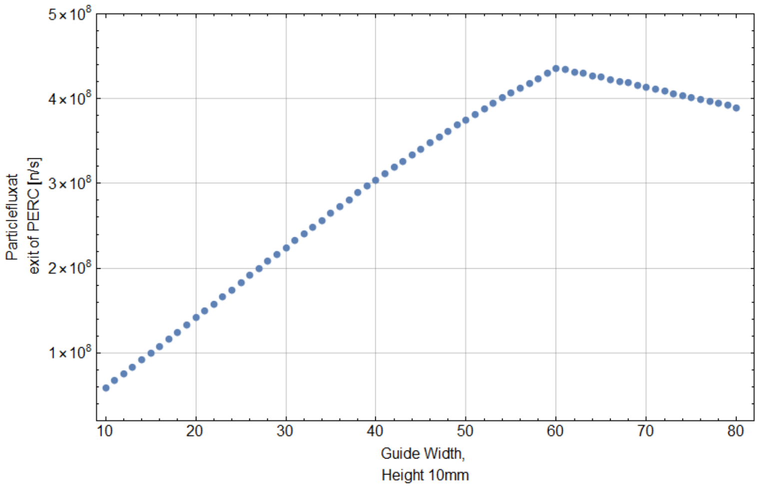

Figure 115: Total flux in neutrons per second at the exit of PERC instrument for different guide widths and constant height of 20 mm. Wavelength 8 Å.

Table 26: Variation of guide width of guide in front of PERC for neutron wavelength 4 Å.

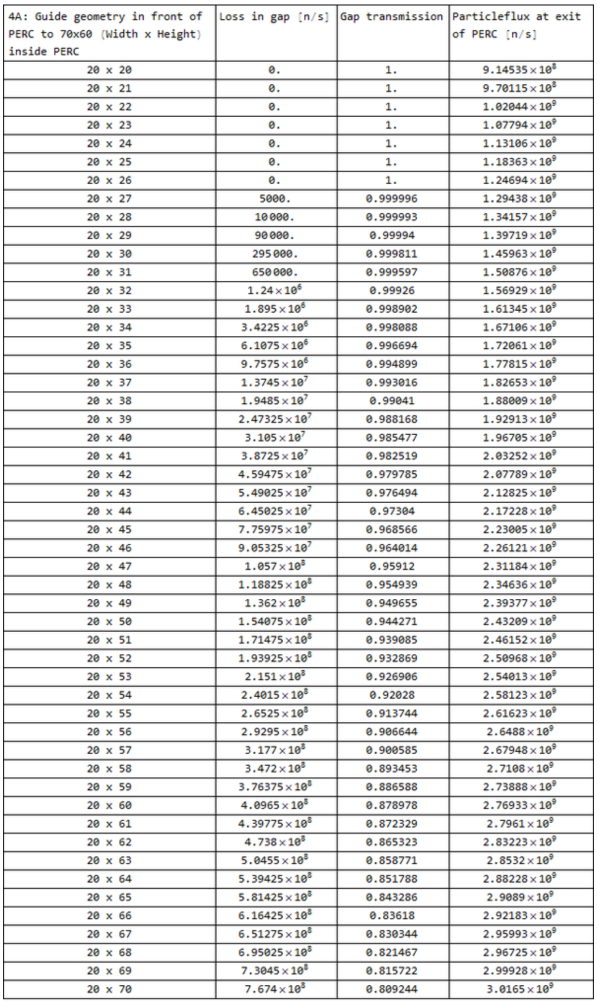

4A: Guide geometry in front of PERC to 70x60 (Width x Height) inside PERC	Loss in gap [n/s]	Gap transmission	Particleflux at exit of PERC [n/s]
20 x 20	0.	1.	9.14535×10^{8}
20 x 21	0.	1.	9.70115×10^{8}
20 x 22	0.	1.	1.02044×10^{9}
20 x 23	0.	1.	1.07794×10^{9}
20 x 24	0.	1.	1.13106×10^{9}
20 x 25	0.	1.	1.18363×10^{9}
20 x 26	0.	1.	1.24694×10^{9}
20 x 27	5000.	0.999996	1.29438×10^{9}
20 x 28	10000.	0.999993	1.34157×10^{9}
20 x 29	90000.	0.99994	1.39719×10^{9}
20 x 30	295000.	0.999811	1.45963×10^{9}
20 x 31	650000.	0.999597	1.50876×10^{9}
20 x 32	1.24×10^{6}	0.99926	1.56929×10^{9}
20 x 33	1.895×10^{6}	0.998902	1.61345×10^{9}
20 x 34	3.4225×10^{6}	0.998088	1.67106×10^{9}
20 x 35	6.1075×10^{6}	0.996694	1.72061×10^{9}
20 x 36	9.7575×10^{6}	0.994899	1.77815×10^{9}
20 x 37	1.3745×10^{7}	0.993016	1.82653×10^{9}
20 x 38	1.9485×10^{7}	0.99041	1.88009×10^{9}
20 x 39	2.47325×10^{7}	0.988168	1.92913×10^{9}
20 x 40	3.105×10^{7}	0.985477	1.96705×10^{9}
20 x 41	3.8725×10^{7}	0.982519	2.03252×10^{9}
20 x 42	4.59475×10^{7}	0.979785	2.07789×10^{9}
20 x 43	5.49025×10^{7}	0.976494	2.12825×10^{9}
20 x 44	6.45025×10^{7}	0.97304	2.17228×10^{9}
20 x 45	7.75975×10^{7}	0.968566	2.23005×10^{9}
20 x 46	9.05325×10^{7}	0.964014	2.26121×10^{9}
20 x 47	1.057×10^{8}	0.95912	2.31184×10^{9}
20 x 48	1.18825×10^{8}	0.954939	2.34636×10^{9}
20 x 49	1.362×10^{8}	0.949655	2.39377×10^{9}
20 x 50	1.54075×10^{8}	0.944271	2.43209×10^{9}
20 x 51	1.71475×10^{8}	0.939085	2.46152×10^{9}
20 x 52	1.93925×10^{8}	0.932869	2.50968×10^{9}
20 x 53	2.151×10^{8}	0.926906	2.54013×10^{9}
20 x 54	2.4015×10^{8}	0.92028	2.58123×10^{9}
20 x 55	2.6525×10^{8}	0.913744	2.61623×10^{9}
20 x 56	2.9295×10^{8}	0.906644	2.6488×10^{9}
20 x 57	3.177×10^{8}	0.900585	2.67948×10^{9}
20 x 58	3.472×10^{8}	0.893453	2.7108×10^{9}
20 x 59	3.76375×10^{8}	0.886588	2.73888×10^{9}
20 x 60	4.0965×10^{8}	0.878978	2.76933×10^{9}
20 x 61	4.39775×10^{8}	0.872329	2.7961×10^{9}
20 x 62	4.738×10^{8}	0.865323	2.83223×10^{9}
20 x 63	5.0455×10^{8}	0.858771	2.8532×10^{9}
20 x 64	5.39425×10^{8}	0.851788	2.88228×10^{9}
20 x 65	5.81425×10^{8}	0.843286	2.9089×10^{9}
20 x 66	6.16425×10^{8}	0.83618	2.92183×10^{9}
20 x 67	6.51275×10^{8}	0.830344	2.95993×10^{9}
20 x 68	6.95025×10^{8}	0.821467	2.96725×10^{9}
20 x 69	7.3045×10^{8}	0.815722	2.99928×10^{9}
20 x 70	7.674×10^{8}	0.809244	3.0165×10^{9}

Table 27: Wavelength 6 Å. List of different guide widths for the guide after velocity selector and in front of PERC. 1.3 m gap between this guide and inner PERC guide is in focus. Loss in this gap is given in neutrons per second and in relativ values. The last column gives the particle flux at the end of the PERC instrument in neutrons per second.

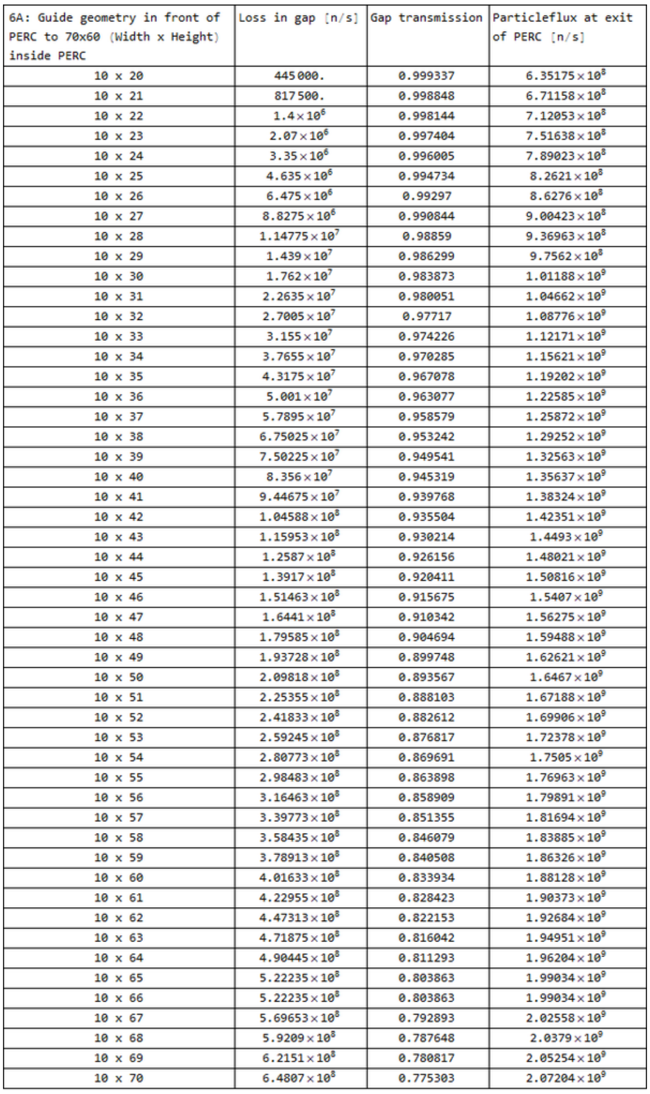

6A: Guide geometry in front of PERC to 70x60 (Width x Height) inside PERC	Loss in gap [n/s]	Gap transmission	Particleflux at exit of PERC [n/s]
10 x 20	445000.	0.999337	6.35175×10^{8}
10 x 21	817500.	0.998848	6.71158×10^{8}
10 x 22	1.4×10^{6}	0.998144	7.12053×10^{8}
10 x 23	2.07×10^{6}	0.997404	7.51638×10^{8}
10 x 24	3.35×10^{6}	0.996005	7.89023×10^{8}
10 x 25	4.635×10^{6}	0.994734	8.2621×10^{8}
10 x 26	6.475×10^{6}	0.99297	8.6276×10^{8}
10 x 27	8.8275×10^{6}	0.990844	9.00423×10^{8}
10 x 28	1.14775×10^{7}	0.98859	9.36963×10^{8}
10 x 29	1.439×10^{7}	0.986299	9.7562×10^{8}
10 x 30	1.762×10^{7}	0.983873	1.01188×10^{9}
10 x 31	2.2635×10^{7}	0.980051	1.04662×10^{9}
10 x 32	2.7005×10^{7}	0.97717	1.08776×10^{9}
10 x 33	3.155×10^{7}	0.974226	1.12171×10^{9}
10 x 34	3.7655×10^{7}	0.970285	1.15621×10^{9}
10 x 35	4.3175×10^{7}	0.967078	1.19202×10^{9}
10 x 36	5.001×10^{7}	0.963077	1.22585×10^{9}
10 x 37	5.7895×10^{7}	0.958579	1.25872×10^{9}
10 x 38	6.75025×10^{7}	0.953242	1.29252×10^{9}
10 x 39	7.50225×10^{7}	0.949541	1.32563×10^{9}
10 x 40	8.356×10^{7}	0.945319	1.35637×10^{9}
10 x 41	9.44675×10^{7}	0.939768	1.38324×10^{9}
10 x 42	1.04588×10^{8}	0.935504	1.42351×10^{9}
10 x 43	1.15953×10^{8}	0.930214	1.4493×10^{9}
10 x 44	1.2587×10^{8}	0.926156	1.48021×10^{9}
10 x 45	1.3917×10^{8}	0.920411	1.50816×10^{9}
10 x 46	1.51463×10^{8}	0.915675	1.5407×10^{9}
10 x 47	1.6441×10^{8}	0.910342	1.56275×10^{9}
10 x 48	1.79585×10^{8}	0.904694	1.59488×10^{9}
10 x 49	1.93728×10^{8}	0.899748	1.62621×10^{9}
10 x 50	2.09818×10^{8}	0.893567	1.6467×10^{9}
10 x 51	2.25355×10^{8}	0.888103	1.67188×10^{9}
10 x 52	2.41833×10^{8}	0.882612	1.69906×10^{9}
10 x 53	2.59245×10^{8}	0.876817	1.72378×10^{9}
10 x 54	2.80773×10^{8}	0.869691	1.7505×10^{9}
10 x 55	2.98483×10^{8}	0.863898	1.76963×10^{9}
10 x 56	3.16463×10^{8}	0.858909	1.79891×10^{9}
10 x 57	3.39773×10^{8}	0.851355	1.81694×10^{9}
10 x 58	3.58435×10^{8}	0.846079	1.83885×10^{9}
10 x 59	3.78913×10^{8}	0.840508	1.86326×10^{9}
10 x 60	4.01633×10^{8}	0.833934	1.88128×10^{9}
10 x 61	4.22955×10^{8}	0.828423	1.90373×10^{9}
10 x 62	4.47313×10^{8}	0.822153	1.92684×10^{9}
10 x 63	4.71875×10^{8}	0.816042	1.94951×10^{9}
10 x 64	4.90445×10^{8}	0.811293	1.96204×10^{9}
10 x 65	5.22235×10^{8}	0.803863	1.99034×10^{9}
10 x 66	5.22235×10^{8}	0.803863	1.99034×10^{9}
10 x 67	5.69653×10^{8}	0.792893	2.02558×10^{9}
10 x 68	5.9209×10^{8}	0.787648	2.0379×10^{9}
10 x 69	6.2151×10^{8}	0.780817	2.05254×10^{9}
10 x 70	6.4807×10^{8}	0.775303	2.07204×10^{9}

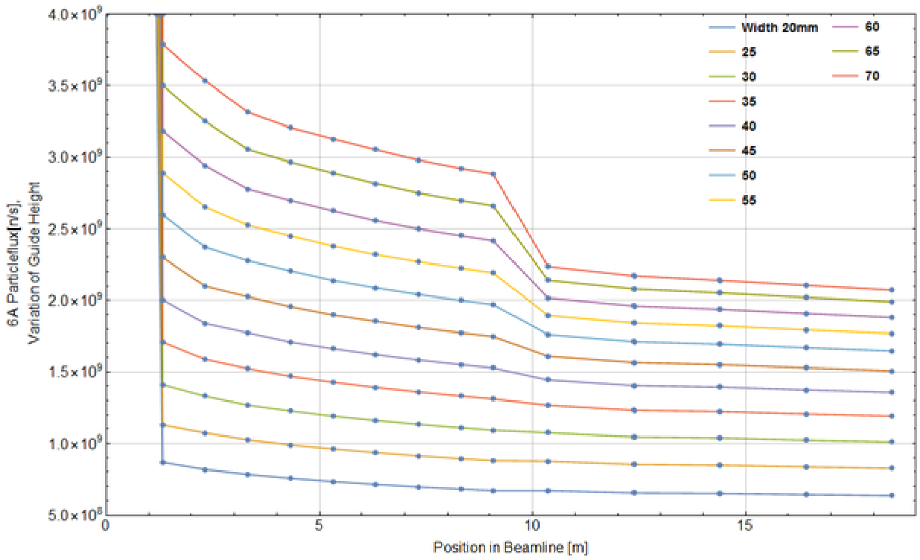

Figure 116: Particleflux in neutrons per second (y-axis) versus position in beamline (x-axis) for different neutron guide widths in front of PERC. Every fifth simulation is shown.

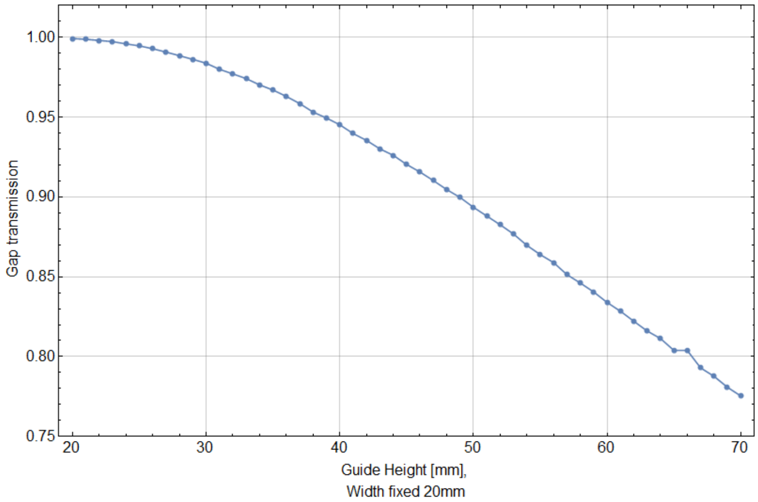

Figure 117: Gap transmission in front of PERC instrument for different guide heights and constant width of 20 mm. Wavelength 6 Å.

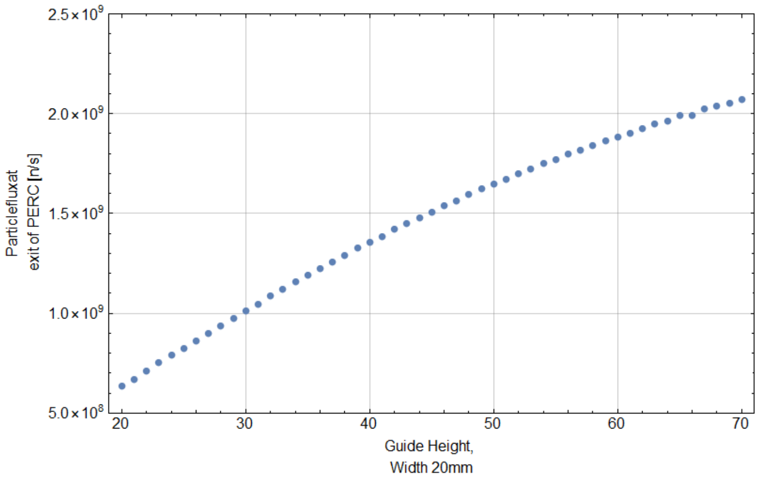

Figure 118: Total flux in neutrons per second at the exit of PERC instrument for different guide heights and constant widths of 20 mm. Wavelength 6 Å.

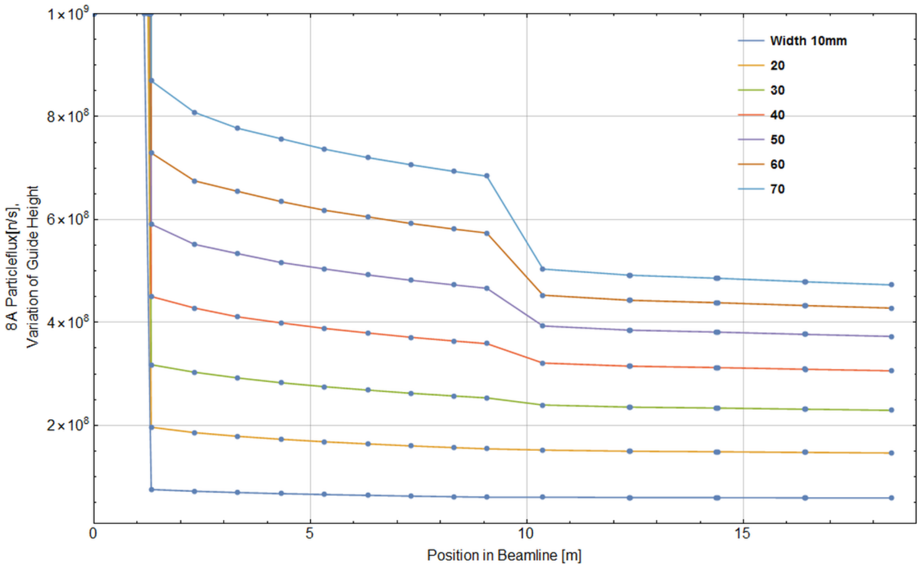

Figure 119: Particle flux in neutrons per second (y-axis) versus position in beamline (x-axis) for different neutron guide heights in front of PERC. Every fifth simulation is shown.

Table 28: Wavelength 8 Å. List of different guide widths for the guide after velocity selector and in front of PERC. 1.3 m gap between this guide and inner PERC guide is in focus. Loss in this gap is given in neutrons per second and in relative values. The last column gives the particle flux at the end of the PERC instrument in neutrons per second.

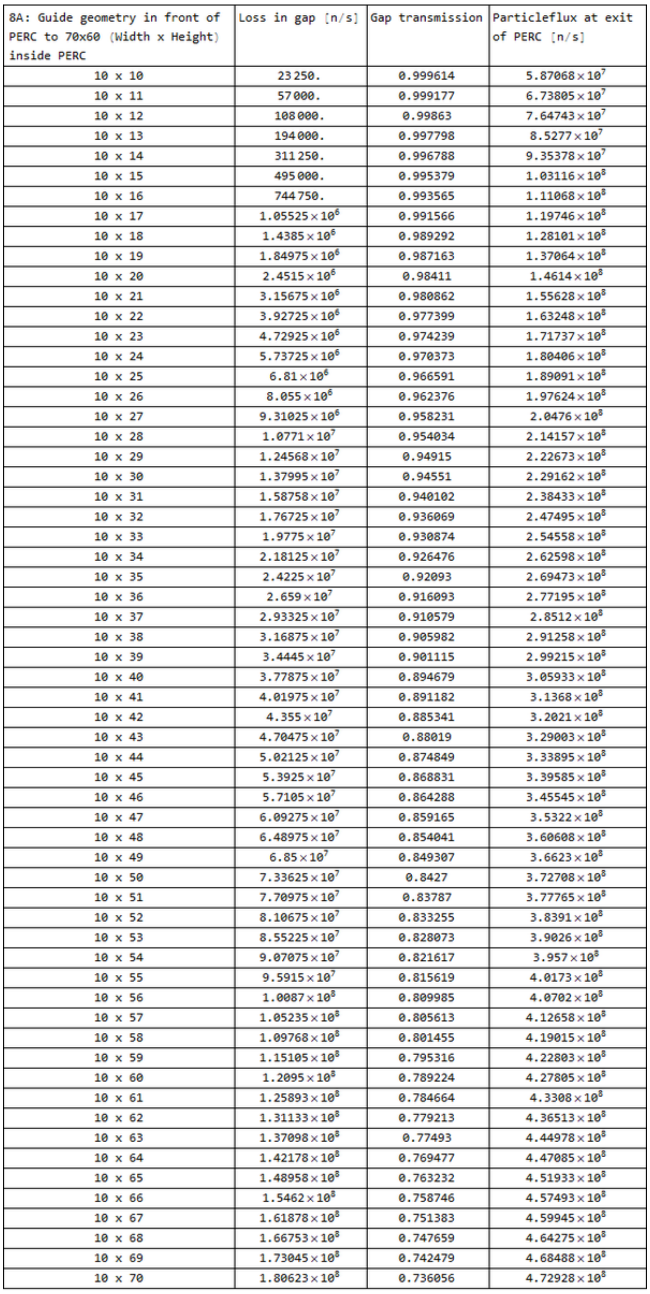

8A: Guide geometry in front of PERC to 70x60 (Width x Height) inside PERC	Loss in gap [n/s]	Gap transmission	Particleflux at exit of PERC [n/s]
10 x 10	23250.	0.999614	5.87068×10^7
10 x 11	57000.	0.999177	6.73805×10^7
10 x 12	108000.	0.99863	7.64743×10^7
10 x 13	194000.	0.997798	8.5277×10^7
10 x 14	311250.	0.996788	9.35378×10^7
10 x 15	495000.	0.995379	1.03116×10^8
10 x 16	744750.	0.993565	1.11068×10^8
10 x 17	1.05525×10^6	0.991566	1.19746×10^8
10 x 18	1.4385×10^6	0.989292	1.28101×10^8
10 x 19	1.84975×10^6	0.987163	1.37064×10^8
10 x 20	2.4515×10^6	0.98411	1.4614×10^8
10 x 21	3.15675×10^6	0.980862	1.55628×10^8
10 x 22	3.92725×10^6	0.977399	1.63248×10^8
10 x 23	4.72925×10^6	0.974239	1.71737×10^8
10 x 24	5.73725×10^6	0.970373	1.80406×10^8
10 x 25	6.81×10^6	0.966591	1.89091×10^8
10 x 26	8.055×10^6	0.962376	1.97624×10^8
10 x 27	9.31025×10^6	0.958231	2.0476×10^8
10 x 28	1.0771×10^7	0.954034	2.14157×10^8
10 x 29	1.24568×10^7	0.94915	2.22673×10^8
10 x 30	1.37995×10^7	0.94551	2.29162×10^8
10 x 31	1.58758×10^7	0.940102	2.38433×10^8
10 x 32	1.76725×10^7	0.936069	2.47495×10^8
10 x 33	1.9775×10^7	0.930874	2.54558×10^8
10 x 34	2.18125×10^7	0.926476	2.62598×10^8
10 x 35	2.4225×10^7	0.92093	2.69473×10^8
10 x 36	2.659×10^7	0.916093	2.77195×10^8
10 x 37	2.93325×10^7	0.910579	2.8512×10^8
10 x 38	3.16875×10^7	0.905982	2.91258×10^8
10 x 39	3.4445×10^7	0.901115	2.99215×10^8
10 x 40	3.77875×10^7	0.894679	3.05933×10^8
10 x 41	4.01975×10^7	0.891182	3.1368×10^8
10 x 42	4.355×10^7	0.885341	3.2021×10^8
10 x 43	4.70475×10^7	0.88019	3.29003×10^8
10 x 44	5.02125×10^7	0.874849	3.33895×10^8
10 x 45	5.3925×10^7	0.868831	3.39585×10^8
10 x 46	5.7105×10^7	0.864288	3.45545×10^8
10 x 47	6.09275×10^7	0.859165	3.5322×10^8
10 x 48	6.48975×10^7	0.854041	3.60608×10^8
10 x 49	6.85×10^7	0.849307	3.6623×10^8
10 x 50	7.33625×10^7	0.8427	3.72708×10^8
10 x 51	7.70975×10^7	0.83787	3.77765×10^8
10 x 52	8.10675×10^7	0.833255	3.8391×10^8
10 x 53	8.55225×10^7	0.828073	3.9026×10^8
10 x 54	9.07075×10^7	0.821617	3.957×10^8
10 x 55	9.5915×10^7	0.815619	4.0173×10^8
10 x 56	1.0087×10^8	0.809985	4.0702×10^8
10 x 57	1.05235×10^8	0.805613	4.12658×10^8
10 x 58	1.09768×10^8	0.801455	4.19015×10^8
10 x 59	1.15105×10^8	0.795316	4.22803×10^8
10 x 60	1.2095×10^8	0.789224	4.27805×10^8
10 x 61	1.25893×10^8	0.784664	4.3308×10^8
10 x 62	1.31133×10^8	0.779213	4.36513×10^8
10 x 63	1.37098×10^8	0.77493	4.44978×10^8
10 x 64	1.42178×10^8	0.769477	4.47085×10^8
10 x 65	1.48958×10^8	0.763232	4.51933×10^8
10 x 66	1.5462×10^8	0.758746	4.57493×10^8
10 x 67	1.61878×10^8	0.751383	4.59945×10^8
10 x 68	1.66753×10^8	0.747659	4.64275×10^8
10 x 69	1.73045×10^8	0.742479	4.68488×10^8
10 x 70	1.80623×10^8	0.736056	4.72928×10^8

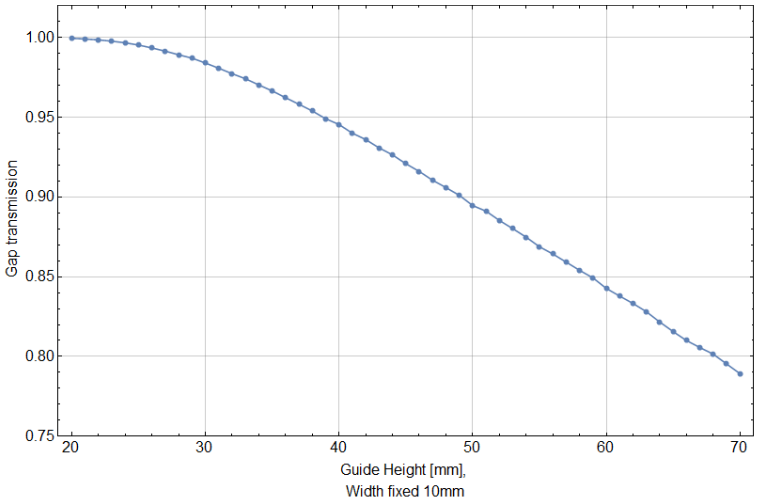

Figure 120: Gap transmission in front of PERC instrument for different guide heights and constant width of 20 mm. Wavelength 8 Å.

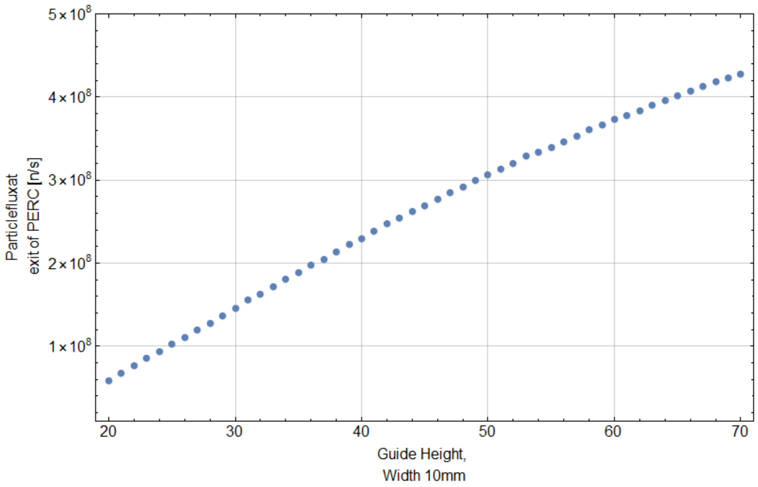

Figure 121: Total flux in neutrons per second at the exit of PERC instrument for different guide heights and constant widths of 20 mm. Wavelength 8 Å.

C.2 Inner Guide Geometries

Table 29: Wavelength 5 Å. Simulations of different geometries of guide in front of PERC. Inside PERC: Entry (60 x 60), 1m pieces, each meter 10 mm pumping gap and 1 mm broadening, Exit (67 x 60)

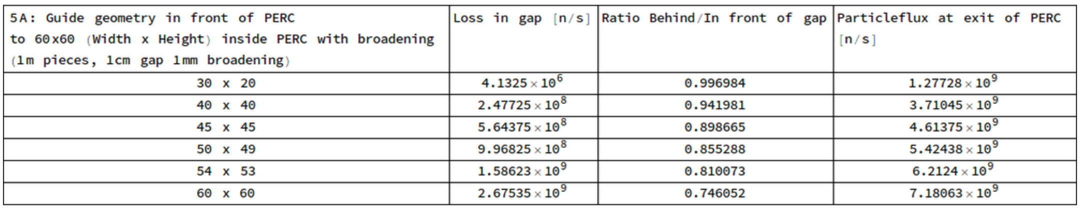

5A: Guide geometry in front of PERC to 60x60 (Width x Height) inside PERC with broadening (1m pieces, 1cm gap 1mm broadening)	Loss in gap [n/s]	Ratio Behind/In front of gap	Particleflux at exit of PERC [n/s]
30 x 20	4.1325×10^6	0.996984	1.27728×10^9
40 x 40	2.47725×10^8	0.941981	3.71045×10^9
45 x 45	5.64375×10^8	0.898665	4.61375×10^9
50 x 49	9.96825×10^8	0.855288	5.42438×10^9
54 x 53	1.58623×10^9	0.810073	6.2124×10^9
60 x 60	2.67535×10^9	0.746052	7.18063×10^9

Table 30: Wavelength 5 Å. Simulations of different geometries of guide in front of PERC, without broadening in PERC. Inside PERC: Entry (60 x 60), 1m pieces, each meter 10 mm pumping gap, Exit (60 x 60)

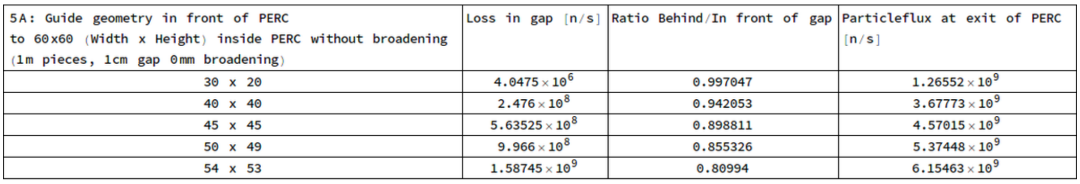

5A: Guide geometry in front of PERC to 60x60 (Width x Height) inside PERC without broadening (1m pieces, 1cm gap 0mm broadening)	Loss in gap [n/s]	Ratio Behind/In front of gap	Particleflux at exit of PERC [n/s]
30 x 20	4.0475×10^6	0.997047	1.26552×10^9
40 x 40	2.476×10^8	0.942053	3.67773×10^9
45 x 45	5.63525×10^8	0.898811	4.57015×10^9
50 x 49	9.966×10^8	0.855326	5.37448×10^9
54 x 53	1.58745×10^9	0.80994	6.15463×10^9

Table 31: Wavelength 5 Å. Simulations of different geometries of guide in front of PERC. Inside PERC: Entry (60 x 60), 2m pieces, each two meters 20 mm pumping gap and 2 mm broadening, Exit (66 x 60)

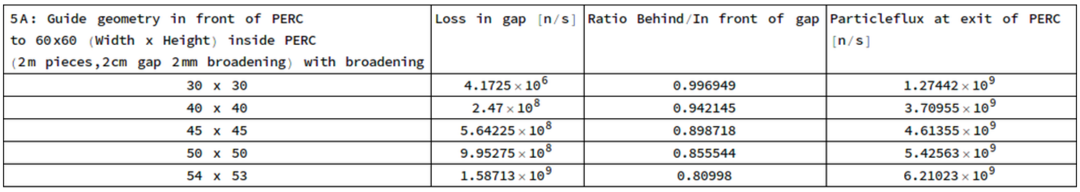

5A: Guide geometry in front of PERC to 60x60 (Width x Height) inside PERC (2m pieces,2cm gap 2mm broadening) with broadening	Loss in gap [n/s]	Ratio Behind/In front of gap	Particleflux at exit of PERC [n/s]
30 x 30	4.1725×10^6	0.996949	1.27442×10^9
40 x 40	2.47×10^8	0.942145	3.70955×10^9
45 x 45	5.64225×10^8	0.898718	4.61355×10^9
50 x 50	9.95275×10^8	0.855544	5.42563×10^9
54 x 53	1.58713×10^9	0.80998	6.21023×10^9

Table 32: Wavelength 5 Å. Simulations of different geometries of guide in front of PERC. Inside PERC: Entry ($70x60$), 2m pieces, each meter 20 mm pumping gap and 2 mm broadening, Exit (76 x 60)

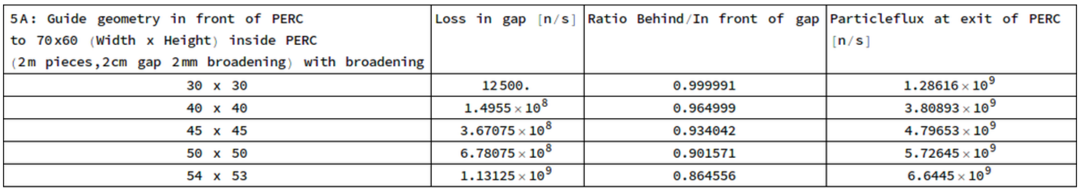

5A: Guide geometry in front of PERC to 70x60 (Width x Height) inside PERC (2m pieces,2cm gap 2mm broadening) with broadening	Loss in gap [n/s]	Ratio Behind/In front of gap	Particleflux at exit of PERC [n/s]
30 x 30	12500.	0.999991	1.28616×10^9
40 x 40	1.4955×10^8	0.964999	3.80893×10^9
45 x 45	3.67075×10^8	0.934042	4.79653×10^9
50 x 50	6.78075×10^8	0.901571	5.72645×10^9
54 x 53	1.13125×10^9	0.864556	6.6445×10^9

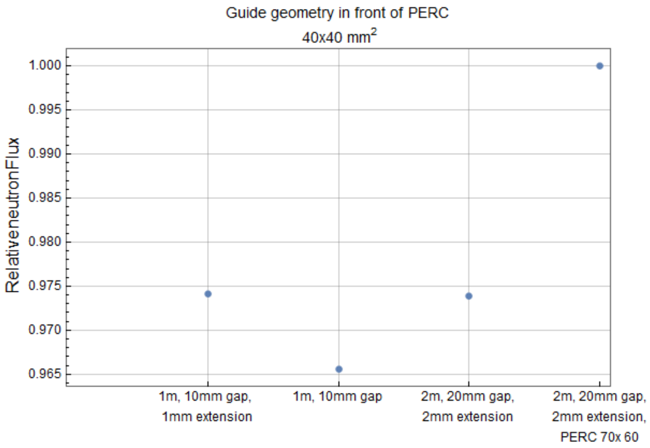

Figure 122: Comparison of neutron flux at end of PERC guide in dependency of PERC guide geometry. With 40 x 40 mm^2 guide in front of PERC.

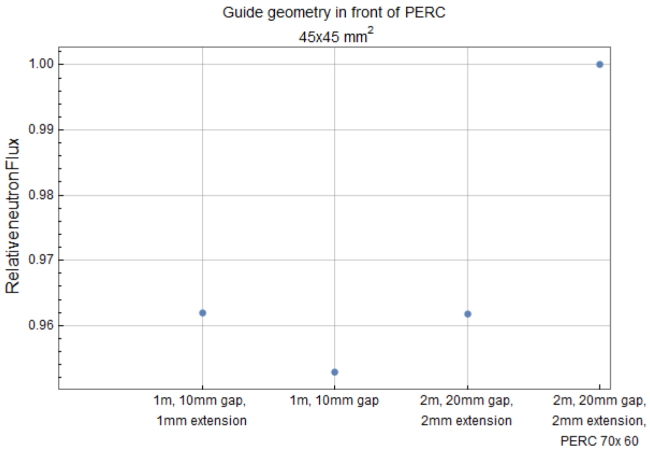

Figure 123: Comparison of neutron flux at end of PERC guide in dependency of PERC guide geometry. With 45 x 45 mm^2 guide in front of PERC.

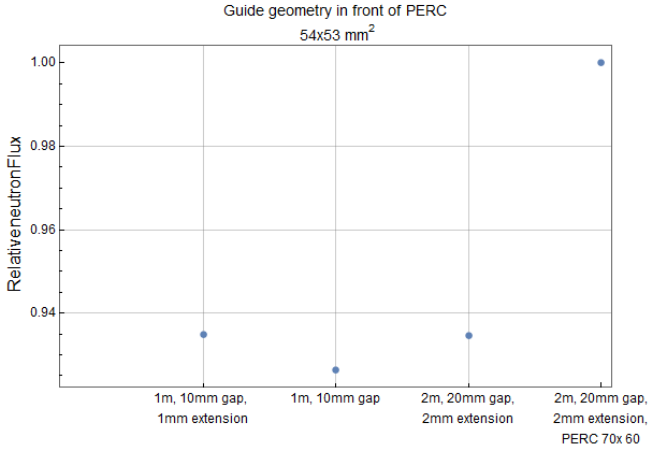

Figure 124: Comparison of neutron flux at end of PERC guide in dependency of PERC guide geometry. With $54\,\mathrm{x}\,53\,\mathrm{mm}^2$ guide in front of PERC.

Acknowledgements

Here, I want to thank all the people who contributed to this work and supported me in what I was doing. I want to thank my supervisor and leader of the PERC project Bastian Märkisch for the opportunity to work in his group. Furthermore, I want to thank him for his support and helpful discussions in the scientific and also the private topics.

I want to thank Ulrich Schmidt for his support and experience in the calculation and simulation of neutron reflectivity curves. Especially, I want to thank Thorsten Lauer from whom I had the chance to learn many things in a wide spectrum of topics. I also want to thank him for his support in the production of neutron optical components.

I want to thank Karina Bernert and Jens Klenke for proofreading my thesis. I want to thank Jens also for supporting me in my work at the FRM II. For answering my questions in technical drawings and for being a kind office colleague, I want to thank Kathrin Lehmann.

Furthermore, I want to thank all other colleagues, who have contributed to this work and made it a successful project.

My heartfelt thanks to my wife Daniela for her never ending support in every condition of life and to my daughters Lea and Liv, who bring a smile to my face every day. Last but not least I want to thank my family for their motivation, sympathy and love.